TSUNAMIS - A MODEL OF THEIR GENERATION AND PROPAGATION

by

Joseph Leonard Hammack, Jr.

In Partial Fulfillment of the Requirements

For the Degree of

Doctor of Philosophy

California Institute of Technology

Pasadena, California

1972

(Submitted April 10, 1972)

ACKNOWLEDGMENTS

The writer wishes to express his sincere gratitude to his thesis advisor, Professor Fredric Raichlen, for his kind guidance and generous assistance "above and beyond the call of duty" throughout every phase of this investigation.

The writer also wishes to thank Professors Vito A. Vanoni, Theodore Y. T. Wu, and Jorg Imberger for many helpful discussions during the development of the theoretical analysis of this study. Dr. Allen T. Y. Chwang also provided many stimulating comments and suggestions for which the writer is extremely grateful.

A special debt of gratitude is owed to Mr. Elton F. Daly, supervisor of the shop and laboratory, whose continuing assistance during the design, construction, and maintainance of the experimental equipment made the laboratory phase of this investigation both possible and pleasurable. Appreciation is also extended to Mr. Robert L. Greenway who assisted in the construction and maintainance of the experimental equipment; to Mr. Carl A. Green who assisted in the laboratory and performed the drafting of all figures appearing in this manuscript; and to Mrs. Arvilla F. Krugh who worked so diligently in typing this manuscript. Mr. Carl T. Eastvedt also assisted in some of the photographic work.

A very special thanks is extended to Mr. John Blair who assisted so ably and without complaint during the many tedious details of data reduction and computations.

For the many years of hard work, patience, kindly advice, and for providing an infinite source of encouragement, the writer offers his sincerest gratitude to his father, Mr. Joseph L. Hammack, and his mother, Mrs. Harry C. Melton.

To his wife, Srisurang, who has suffered the most during the years of this investigation, the writer can only say: "Khob chai mark".

The writer also wishes to thank the California Institute of Technology for financial assistance and for providing a most stimulating environment in which to work. This research was supported by NSF Grants GK-2370 and GK-24716; experiments were conducted at the W. M. Keck Laboratory of Hydraulics and Water Resources.

ABSTRACT

A general solution is presented for water waves generated by an arbitrary movement of the bed (in space and time) in a two-dimensional fluid domain with a uniform depth. The integral solution which is developed is based on a linearized approximation to the complete (nonlinear) set of governing equations. The general solution is evaluated for the specific case of a uniform upthrust or downthrow of a block section of the bed; two time-displacement histories of the bed movement are considered.

An integral solution (based on a linear theory) is also developed for a three-dimensional fluid domain of uniform depth for a class of bed movements which are axially symmetric. The integral solution is evaluated for the specific case of a block upthrust or downthrow of a section of the bed, circular in planform, with a time-displacement history identical to one of the motions used in the two-dimensional model.

Since the linear solutions are developed from a linearized approximation of the complete nonlinear description of wave behavior, the applicability of these solutions is investigated. Two types of nonlinear effects are found which limit the applicability of the linear theory: (1) large nonlinear effects which occur in the region of generation during the bed movement, and (2) the gradual growth of nonlinear effects during wave propagation.

A model of wave behavior, which includes, in an approximate manner, both linear and nonlinear effects is presented for computing wave profiles after the linear theory has become invalid due to the growth of nonlinearities during wave propagation.

An experimental program has been conducted to confirm both the linear model for the two-dimensional fluid domain and the strategy suggested for determining wave profiles during propagation after the linear theory becomes invalid. The effect of a more general time-displacement history of the moving bed than those employed in the theoretical models is also investigated experimentally.

The linear theory is found to accurately approximate the wave behavior in the region of generation whenever the total displacement of the bed is much less than the water depth. Curves are developed and confirmed by the experiments which predict gross features of the lead wave propagating from the region of generation once the values of certain nondimensional parameters (which characterize the generation process) are known. For example, the maximum amplitude of the lead wave propagating from the region of generation has been found to never exceed approximately one-half of the total bed displacement. The gross features of the tsunami resulting from the Alaskan earthquake of 27 March 1964 can be estimated from the results of this study.

TABLE OF CONTENTS

Chapter | Page

1. INTRODUCTION 1

    1.1 Objective and Scope of Present Study 3

2. LITERATURE SURVEY 5

3. THEORETICAL ANALYSIS 21

    3.1 The Two-Dimensional Model - A Linear Theory 22

    3.2 The Two-Dimensional Model - Nonlinear Considerations 35

        3.2.1 Aspects of nonlinearity-generation 36

        3.2.2 Aspects of nonlinearity-propagation 45

    3.3 Relation of the Dam-break Problem to Impulsive Bed Movements 57

    3.4 The Three-Dimensional Model - A Linear Theory 65

4. EXPERIMENTAL EQUIPMENT AND PROCEDURES 70

    4.1 The Wave Tank 70

    4.2 The Wave Generator 75

    4.3 The Response of the Generator 87

    4.4 The Measurement of Wave Amplitudes 98

5. PRESENTATION AND DISCUSSION OF RESULTS 104

    5.1 The Generation Region 105

TABLE OF CONTENTS (Cont'd)

Chapter Page

5.1.1 Maximum wave amplitudes in the generation region 106

5.1.2 Wave profiles in the generation region 128

5.1.3 Wave periods in the generation region 147

5.1.4 Energy dissipation in the generation region 169

5.1.5 The three-dimensional model in the generation region 171

5.2 The Downstream Region 181

5.2.1 Wave propagation 182

5.2.2 Energy dissipation in the downstream region 210

5.3 Oscillating Bed Motions With a Mean Displacement 215

5.4 Application of Results to the Alaskan Earthquake of 27 March 1964 225

6. CONCLUSIONS 241

LIST OF REFERENCES 247

LIST OF SYMBOLS 256

LIST OF FIGURES

Number	Description	Page
3.1	Definition sketch of coordinate system	23
3.2	Exponential time-displacement history of the moving bed	30
3.3	Half-sine time-displacement history of the moving bed	32
3.4	Assumed water surface profile at the end of an impulsive upthrust of the bed	51
3.5	Assumed water surface profile after an impulsive bed upthrust in the region $-\infty < x^* \leq 0$	58
3.6	Regions of the fluid domain after removal of the barrier	60
3.7	Variation of the relative bore amplitude, η_o/ζ_o, as a function of the initial difference in water levels, ζ_o/h	60
3.8	Characteristic-plane solution of a dam-break problem with a reservoir of finite length	62
4.1	Schematic drawing of a typical downstream tank module (after French (1969))	72
4.2	Overall view of wave tank	72
4.3	Schematic drawing of tank module with the wave generator installed	74
4.4	View of the end-tank module and wave generator	76
4.5	Schematic drawing of wave generator system	77
4.6	Exploded view of the moveable bed assembly	79
4.7	View of the hydraulic supply unit	81

LIST OF FIGURES (Cont'd)

Number	Description	Page
4.8	Circuit diagram of the exponential and half-sine function generator	84
4.9	Typical calibration curve of the linear variable differential transformer	86
4.10	Frequency response of the wave generator system	88
4.11	Examples of programmed and actual exponential bed displacements	90
4.12	Examples of programmed and actual half-sine bed displacements	92
4.13	Determination of actual characteristic times; a) exponential bed displacement, b) half-sine bed displacement	96
4.14	Drawing of a typical wave gage (after Raichlen (1965))	99
4.15	Circuit diagram for wave gages (after Raichlen (1965))	99
4.16	Typical calibration curve of a wave gage	101
5.1	Variation of the relative maximum wave amplitude, η_o/ζ_o, with the time-size ratio, $t_c\sqrt{gh}/b$, at $x/h = 0$ for exponential bed displacements	108
5.2	Variation of the relative maximum wave amplitude, η_o/ζ_o, with the time-size ratio, $t_c\sqrt{gh}/b$, at $x/h = 0$ for half-sine bed displacements	112
5.3	Theoretical variation of relative maximum wave amplitude, η_o/ζ_o, with the time-size ratio, $t_c\sqrt{gh}/b$, at $x/h = 0$; a) exponential bed motion, b) half-sine bed motion	115

LIST OF FIGURES (Cont'd)

Number	Description	Page
5.4	Variation of the relative maximum wave amplitude, η_o/ζ_o, with the time-size ratio, $t_c\sqrt{gh}/b$, at $x/h = b/h$ for exponential bed displacements	117
5.5	Variation of the relative maximum wave amplitude, η_o/ζ_o, with the time-size ratio, $t_c\sqrt{gh}/b$, at $x/h = b/h$ for half-sine bed displacements	121
5.6	Theoretical variation of relative maximum wave amplitude, η_o/ζ_o, with the time-size ratio, $t_c\sqrt{gh}/b$, at $x/h = b/h$; a) exponential bed motion, b) half-sine bed motion	123
5.7	Theoretical variation of relative maximum wave amplitude, η_o/ζ_o, with disturbance-size scale, b/h, for impulsive bed displacements	126
5.8	Typical wave profiles in each region of generation at $x/h = 0$ and $x/h = b/h$ generated by exponential bed displacements	130
5.9	Typical wave profiles in each region of generation at $x/h = 0$ and $x/h = b/h$ generated by half-sine bed displacements	133
5.10	Wave profiles generated by the exponential and half-sine bed displacements when the generation parameters for each motion are held constant and the absolute bed size is varied	136
5.11	Wave profiles at $x/h = 0$ and $x/h = b/h$ for a half-sine bed upthrust and downthrow with a large disturbance-amplitude scale, $|\zeta_o/h| = 0.4$	139
5.12	Spatial variations of the water surface elevation in the generation region for exponential bed displacements; a) bed upthrust, b) bed downthrow	142
5.13	Spatial variations of the water surface elevation in the generation region for half-sine bed displacements; a) bed upthrust, b) bed downthrow	146

LIST OF FIGURES (Cont'd)

Number	Description	Page
5.14	Definition sketch of rise time, t_r, fall time, t_f, and nodal time, t_n; a) positive lead wave, b) negative lead wave	147
5.15	Variation in t_r/t_c, t_f/t_c, and t_n/t_c of the lead wave with the time-size ratio, $t_c\sqrt{gh}/b$, at $x/h = 0$ for exponential bed displacements	149
5.16	Variation in t_r/t_c, t_f/t_c, and t_n/t_c of the lead wave with the time-size ratio, $t_c\sqrt{gh}/b$, at $x/h = 0$ for half-sine bed displacements	154
5.17	Variation in t_r/t_c, t_f/t_c, and t_n/t_c of the lead wave with the time-size ratio, $t_c\sqrt{gh}/b$, at $x/h = b/h$ for exponential bed displacements	160
5.18	Variation in t_r/t_c, t_f/t_c, and t_n/t_c of the lead wave with the time-size ratio, $t_c\sqrt{gh}/b$, at $x/h = b/h$ for half-sine bed displacements	163
5.19	Vortex generation at leading edge of moving bed section; a) bed upthrust, b) bed downthrow	170
5.20	Theoretical variation of relative maximum wave amplitude, η_o/ζ_o, with the time-size ratio, $t_c\sqrt{gh}/r_o$; a) at $r/h = 0$, b) at $r/h = r_o/h$	173
5.21	Theoretical variation of relative maximum wave amplitude, η_o/ζ_o, with the disturbance-size scale, b/h and r_o/h, for impulsive bed displacements	175
5.22	Typical wave profiles in each region of generation at $r/h = 0$ and $r/h = r_o/h$ generated by exponential bed displacements	178
5.23	Downstream wave profiles generated by an impulsive exponential bed upthrust; a) measured, b) computed by linear theory, c) computed by KdV equation	188
5.24	Asymptotic wave behavior computed by the KdV equation for waves with a net positive volume	197

LIST OF FIGURES (Cont'd)

Number	Descriptions	Page
5.25	Downstream wave profiles generated by an impulsive, exponential bed downthrow; a) measured, b) computed by linear theory, c) computed by KdV equation	199
5.26	Asymptotic wave behavior computed by the KdV equation for waves with a net negative volume	207
5.27	Amplitude decay of a solitary wave during propagation based on the equation of Keulegan (1948)	212
5.28	Wave breaking in the downstream region for negative bed displacements	215
5.29	Measured wave profiles; a) an impulsive half-sine mean motion, b), c) half-sine mean motion with a superposed oscillation	217
5.30	Measured wave profiles; a) a creeping half-sine mean motion, b) half-sine mean motion with a superposed oscillation	224
5.31	Vertical ground deformations resulting from the Alaskan earthquake of 27 March 1964 (adapted from Plafker (1969))	228

LIST OF TABLES

Number	Description	Page
4.1	Range of generation parameters (and corresponding water depths) used in the experimental investigation.	95
4.2	Wage gage locations for each disturbance-size scale used in the experimental investigation.	100
5.1	Inferred characteristics of the leading wave of the Alaskan tsunami (27 March 1964) near Middleton Island.	236

今は昔
地震を語る
火ばちかな
許六

Tales of earthquakes round the brazier's glow

Are told again: "Now many years ago...."

-KYOROKU-

CHAPTER 1

INTRODUCTION

One of the most destructive water waves occurring in nature is the tsunami. The Japanese word, "tsunami", has been adopted by the scientific community (in lieu of "tidal wave") to describe sea waves generated by seismic disturbances. The principle seismic mechanism responsible for the generation of tsunamis appears to be tectonic earthquakes, e. g., earthquakes which cause a structural deformation of the sea bed. Other activity such as volcanic eruptions and coastal and submarine landslides are also known to have generated tsunamis.

The general features of tsunamis are fairly well known at the present time. In the deep ocean the waves are very long and of sufficiently small amplitude that they are not detectable visually. When these waves approach a coastal region where the water depth decreases rapidly, the wave energy is focused by refraction which, combined with shoaling and local resonance effects, may result in significantly increased wave amplitudes. These large waves then strike the shoreline of exposed areas, presenting a major hazard to life and property in heavily populated regions.

One of the most destructive tsunamis in historical time was generated by an earthquake off the coast of Japan on 15 June 1896. The main wave advanced shoreward to an elevation of 75 to 100 ft above the normal tide level. More than 27,000 people were killed and over 10,000 homes were destroyed. More recently the Chilean earthquake of 23 May 1960 generated a tsunami that killed 1000 people in Chile, 61 persons in Hawaii, and 114 people in Japan (another 90 were lost and presumed drowned). Extensive property damage also occurred in these areas. On 27 March 1964 a major tsunami was generated by an earthquake in the Gulf of Alaska which killed 142 persons in Alaska and along the western coast of the United States and resulted in excess of $100 million property damage in these areas.

The general migration of people to coastal regions in recent years has created a more urgent need for a precise understanding of tsunamis and their potential hazard. Inadequate knowledge of the vulnerability of specific coastal sites to tsunami attack and the lack of precision in predicting probable and possible wave heights may pose severe and costly engineering problems. These problems are especially difficult in the design and construction of nuclear reactors for power generation which require very high standards of safety.

In order to accurately predict the potential tsunami hazard in a specific coastal environment, a more complete understanding of the following processes is required: (1) the generation of the tsunami including the tectonic features of the seismic source and the response of the fluid in the region of generation to the tectonic deformations, (2) the propagation of the tsunami across the variable depth ocean between the generation region and the coast, (3) the response characteristics of the coastal region to the approaching wave system. An understanding of the wave behavior in the region of tsunami generation is especially important to the heavily populated coastal region of Southern California which appears to be largely unaffected by tsunamis generated elsewhere in the Pacific Ocean. The numerous offshore islands and basins adjacent to this region apparently act as a reasonably effective barrier to the wave energy in a tsunami from a distant source; hence, the primary tsunami hazard to this area may originate from a tsunamigenic earthquake occurring between the mainland and these offshore islands and basins.

1.1 OBJECTIVE AND SCOPE OF PRESENT STUDY.

The objective of the present study is to investigate, both theoretically and experimentally, wave behavior in the region of generation resulting from a family of simple and idealized tectonic movements that could be responsible for tsunami generation and the propagation of the generated waves in a fluid domain of uniform depth. Because of a general lack of knowledge regarding actual tectonic features of tsunamigenic earthquakes, a simple model of generation based on a uniform, vertical displacement of a block section of the ocean bed either upward or downward has been adopted. The time-displacement history of the bed movement is varied. A two-dimensional and three-dimensional model of wave generation have been investigated theoretically; laboratory experiments have been conducted to confirm the results of the two-dimensional model. Wave propagation in the two-dimensional model is investigated using a linear theory and a theory which includes both linear and nonlinear effects in an approximate manner.

A limited review of previous mathematical and experimental studies of tsunami generation is presented in Chapter 2. A theoretical analysis based on a linear theory is presented in Chapter 3 for the two-dimensional and three-dimensional models of wave generation. A discussion of the applicability of the linear solutions due to nonlinear effects arising during wave generation and propagation is also presented. In Chapter 4 the experimental equipment and laboratory procedures are described. Experimental and theoretical results are compared in Chapter 5 and applied to the Alaskan earthquake of 27 March 1964 in order to infer probable characteristics of the tsunami which was generated by this earthquake. Conclusions of this study are stated in Chapter 6.

CHAPTER 2

LITERATURE SURVEY

The main body of tsunami research has originated in Japan as a natural consequence of the destruction of life and property this island nation has suffered as a result of these devastating waves. The Japanese apparently began studying tsunamis around 1880 (for a complete listing of tsunami research between 1889 and 1962, see reference (18)); however, most of the early papers are primarily descriptive of tsunami damage and do not attempt to model, either theoretically or experimentally, the generation of tsunamis. This literature survey will be limited to theoretical or experimental studies of tsunamis which are generated by bed displacements that might occur during a tectonic earthquake. Papers which are primarily descriptive or literature in the related fields of waves generated by landslides, explosions, etc., will not be discussed.

The first theoretical investigation of tsunami generation and propagation appears to have been performed by Sano and Hasegawa (1915) who considered a point disturbance at the bed in a three-dimensional domain of fluid. The disturbance was assumed to occur instantaneously in water of uniform depth, h. Based on a linearized description of wave behavior Sano and Hasegawa were able to develop expressions for the wave profile at large distances from the disturbance. Few of the wave properties could be found from their expressions, however, because of the mathematical difficulties encountered in evaluating actual values of the wave amplitudes.

Syono (1936) improved on the model of Sano and Hasegawa by considering the size of the disturbance to be finite. Syono assumed that a section of the sea bed was given the velocity:

$$\frac{\partial\varphi}{\partial z} = f(r)g(t) \cos n\Theta \ , \tag{2.1}$$

where $\varphi = \varphi(r, z;t)$ is the velocity potential, z is the vertical coordinate, r is the radial coordinate, t is time, and $n = 0$ or 1. The spatial and temporal distributions of velocity, i.e., f(r) and g(t), respectively, were given by:

$$f(r) = \frac{Kr^n}{(r^2+R^2)^{n+3/2}} \quad \text{and} \quad g(t) = \frac{L}{t^2+M^2} \ , \tag{2.2}$$

where K, R, M, and L are arbitrary constants. These assumed velocity distributions enabled Syono to determine expressions for the wave structure for the cases of $n = 0$ and $n = 1$ in both deep $(h/R >> 1)$ and shallow $(h/R << 1)$ water. Again the solutions for the wave profile were too complex to elucidate the detailed wave structure and Syono did not calculate wave profiles.

In a series of papers Takahasi (1942, 1945, 1947) considered three different models of tsunami generation. In the first paper a circular disturbance of radius, r_o, in water of uniform depth, h , was assumed to move with a uniform velocity a distance of $\forall/\pi r_o^2$, where $\forall$ is the total volume of the displacement. The bed movement was permitted to occur in a finite time interval, $0 \leq t \leq T$. Using a linear theory Takahasi was able to find expressions for the wave structure in deep ($h/r_o >> 1$), shallow ($h/r_o << 1$), and intermediate ($h/r_o \simeq 1$) water depths. A few wave profiles near the region of generation were computed in an approximate manner for the case of shallow water and for $T = r_o/\sqrt{gh}$ where g is the acceleration of gravity. In the region of generation the water surface followed the bed movement until $t = T$. Annular waves then began to propagate as the water level at the origin ($r = 0$) began to decrease, eventually going below the original still water level to a maximum negative elevation of approximately $-1.5\ \forall/\pi r_o^2$. The water level at $r = 0$ then oscillated about the still water level in a damped manner. The leading wave was found to propagate with a velocity of $\sqrt{gh}$ and the maximum amplitude was found to decay like $r^{-\frac{1}{2}}$. In deep water, sample wave profiles were computed and for $r >> r_o$ the wave height was found to decay like r^{-1}.

In the second paper Takahasi (1945) considered a circular disturbance with azimuthal and radial variations proportional to $r^n \cos n\Theta$ with $n = 1, 2$, and 3. Only simple features of the waves generated by these deformations were determined. Positive leading waves were found to result from bed uplift while negative leading waves resulted from bed downthrow. The velocity of wave propagation was again found to be given for shallow water by $\sqrt{gh}$ and the amplitudes were found to decay like $r^{-\frac{1}{2}}$.

In the third paper Takahasi (1947) considered a bed movement of infinite extent in one coordinate direction so that only a two-dimensional fluid domain was required. The bed deformation was given a velocity in the form:

$$\frac{\partial \varphi}{\partial y} = f(x)g(t) , \tag{2.3}$$

where y is the vertical coordinate, x is the direction of propagation, t is time, and $\varphi = \varphi(x, y; t)$ is the velocity potential. In the first model Takahasi examined, the spatial and temporal variations in the bed velocity were taken to be:

$$f(x) = \begin{cases} \zeta_o & |x| < b \\ 0 & |x| > b \end{cases} , \quad g(t) = \begin{cases} 1/T & 0 < t < T \\ 0 & t > T \end{cases} . \tag{2.4}$$

In the second model the assumed spatial variation was:

$$f(x) = \begin{cases} b \sin \frac{\pi x}{b} & |x| < b \\ 0 & |x| > b \end{cases} , \tag{2.5}$$

and the uniform variation in time as given by Eq. (2.4) was again utilized. The initial wave profiles were found to resemble the bed deformation in both cases. The initial wave then divided into two similar wave systems, propagating in opposite directions, in which the velocity of propagation in shallow water was determined to be given by $\sqrt{gh}$. Mathematical difficulties precluded more definite features of the wave profiles from being determined.

Ichiye (1950) also considered a two-dimensional domain of fluid of uniform depth, h, in which a velocity of the same form as Eq. (2.3) was imparted to bed. Modeling the spatial and temporal distributions of velocity by the functions:

$$f(x) = \begin{cases} \zeta_o & |x| < b \\ 0 & |x| > b \end{cases}, \quad g(t) = \begin{cases} Nte^{-\alpha t} & t > 0 \\ 0 & t < 0 \end{cases}, \qquad (2.6)$$

where N, ζ_o, b, and α are constants, Ichiye was able to determine expressions for the water surface profiles based on a linear description of wave behavior. When the bed motion was rapid, i.e., $b\alpha/\sqrt{gh} >> 1$, these expressions could be simplified so that numerical computation was possible. Water surface profiles in the region of generation were found to approximate the bed movement for this case and the velocity of propagation of the leading wave was found to be $\sqrt{gh}$. At large distances from the generation region the wave profiles were evaluated by the method of stationary phase and found to yield a leading wave followed by a dispersive train of oscillatory waves. The amplitude of the trailing waves was found to grow like $t^{\frac{1}{4}}$. For very slow movements of the bed, i.e., $b\alpha/\sqrt{gh} << 1$, the largest waves were found to propagate with a velocity greater than $\sqrt{gh}$ and at large distances from the disturbance only a single wave was observed.

Honda and Nakamura (1951) also investigated a two-dimensional model of tsunami generation for a fluid domain of uniform depth, h, in which the spatial and temporal variations in velocity of the deforming bed were given by:

$$f(x) = Ae^{-x^2/x_1^2}, \quad g(t) = e^{-t^2/t_1^2}, \qquad (2.7)$$

where A, x_1, and t_1 are arbitrary constants (see Eq. (2.3)). The final elevation of the deformed bed, ζ, is given by:

$$\zeta = \sqrt{\pi}\, t_1\, A e^{-x^2/x_1^2} \; . \tag{2.8}$$

For a shallow sea, i.e., $h/x_1 << 1$, the initial wave profiles were determined from Takahasi's general solution and computed numerically for the special case of $h = 4$ km, $x_1 = 50$ km, $t_1 = 2$ sec, and $\sqrt{\pi}\, t_1 A = 3$ m. The water surface in the region of generation was found to rise like the deforming bed and then divide into two wave systems (moving in the opposite direction) whose maximum amplitude was one-half the maximum bed deformation. The propagation velocity of the leading wave was again found to be given by $\sqrt{gh}$. The magnitude of x_1 and t_1 was then varied and the effect on the wave behavior at the origin, $x = 0$, was observed. As x_1 increased the time required for the water to return to its original still water level also increased; as t_1 increased the maximum water surface movement was found to eventually become less than the total bed movement.

In a later paper Nakamura (1953) extended the previous work of Hondo and Nakamura (1951) to a three-dimensional domain of fluid with a uniform depth, h, in which the spatial and temporal variation in velocity of the deforming bed was assumed to be:

$$f(r) = A e^{-r^2/R^2}, \quad g(t) = e^{-t^2/t_1^2} \; . \tag{2.9}$$

Again the wave behavior at the origin was evaluated assuming a shallow sea such that $h/R << 1$. As the time constant, t_1, was varied, the same general behavior of the maximum water surface elevation observed in the two-dimensional model again was found, i.e., for small t_1 the maximum water elevation became equal to the total bed displacement while for large t_1 the maximum water surface movement was less than the bed movement.

Ichiye (1958) again considered a two-dimensional fluid domain of uniform depth, h, in which the bed velocity was given by:

$$f(x) = \begin{cases} \zeta_o & |x| < b \\ 0 & |x| > b \end{cases}, \quad g(t) = \begin{cases} \frac{1}{2}T & |t| < T \\ 0 & |t| > T \end{cases}, \qquad (2.10)$$

where ζ_o, b, and T are arbitrary constants. Using numerical computations to evaluate the expressions for the resulting wave motion in a shallow sea, Ichiye was able to construct the wave profiles near the region of generation. In his examples the water movement in the generation region approximated the bed deformation during the interval $0 \leq t \leq T$, after which time the water collapsed into two similar dispersive wave trains; one moving in the positive x-direction and one moving in the negative x-direction. In Ichiye's examples the bed movement was so rapid that the maximum water movement at the origin was equal to the total bed movement, ζ_o.

Keller (1963) determined the far-field wave signatures using the method of stationary phase for waves generated in a three-dimensional fluid domain of uniform depth, h, by axially symmetric bed deformations. He found that the leading wave amplitude decayed like r^{-1} in the far-field, where r is the radial coordinate and the leading wave was found to travel with a velocity of $\sqrt{gh}$. Keller also investigated the change in wave behavior based on the methods of geometrical optics when the water waves approached a coastal region where the depth became nonuniform. No computations of actual wave profiles resulting from a specific disturbance were given by Keller to more clearly elucidate the wave structure.

Webb (1962) investigated a simple model of tsunami generation in a two-dimensional domain of fluid of uniform depth in which the assumed spatial and temporal velocities of the moving bed were:

$$f(x) = \begin{cases} \zeta_o & |x| < b \\ 0 & |x| > b \end{cases}, \quad g(t) = \begin{cases} \alpha e^{-\alpha t} & t > 0 \\ 0 & t < 0 \end{cases}, \qquad (2.11)$$

where α, b, and ζ_o are arbitrary constants. (This model of tsunami generation is of special interest since it is also one of the models to be considered in the present study.) Webb invoked the Fourier Integral Theorem in order to represent the prescribed bed movement in terms of a sum of sine and cosine functions. Since the spatial movement is symmetric about $x = 0$, the sine portion of the representation may be ignored; however, the temporal variation is not an even function of t and cannot be represented as a sum of cosine functions as is done by Webb. Webb's solution was thus found to be in error. (The correct solution will be derived shortly.) Since the argument of the sine terms omitted by Webb are functions of time, the incomplete solution fortunately yields a reasonable approximation of the wave profiles near $t = 0$, i.e., the initial waves. These wave profiles were numerically computed by Webb for the special case of $h = 10,000$ ft, $b = 5,000$ ft, and $\alpha = 0.1\ \text{sec}^{-1}$. The maximum water elevation reached during the bed movement occurred at the origin and was equal to 21% of the total bed movement, ζ_o. A positive leading wave propagated from the generation region and gradually decreased in amplitude. A train of damped oscillatory waves formed behind the leading wave during propagation. The velocity of the leading wave was found to exceed $\sqrt{gh}$ initially, decrease to a value below $\sqrt{gh}$ during propagation, and then increase asymptotically to $\sqrt{gh}$. Hendrickson (1962) in the same report developed expressions for the asymptotic behavior of these waves; however, since his analysis was based on an incorrect solution by Webb, the asymptotic solution would also be invalid.

Kajiura (1963) developed general solutions for waves generated by an instantaneous movement of a section of the bed in both a two and three-dimensional domain of fluid of uniform depth, h. Kajiura was specifically interested in the decay of the leading wave during propagation. A parameter, $P_b = (6\sqrt{h/g}\,/t)^{\frac{1}{3}}(b/h)$, was found to be important in determining the decay rate of the leading wave; g is the acceleration of gravity, t is the time, and b is the half-width of the source region. In a three-dimensional model the wave was found to decay like $r^{-\frac{2}{3}}$ for $P_b > 3$ and r^{-1} for $P_b < 1$ where r is the distance of propagation. In the two-dimensional model the leading wave was found to decay like r^0 for $P_b > 3$ and $r^{-\frac{1}{3}}$ for $P_b < 1$. Kajiura also investigated the maximum wave elevation reached at the origin of an instantaneous bed deformation when the half-width of the deformation was varied. For a uniform deformation in a two-dimensional fluid domain the maximum wave amplitude, η_o, was found to be equal to the total bed movement, ζ_o, for $b/h > 3$. For $b/h < 3$ the ratio η_o/ζ_o decreased and tended to zero as $b/h \rightarrow 0$. For a circular deformation in a three-dimensional domain of fluid the ratio, η_o/ζ_o, was equal to unity for $b/h > 4$ and tended to zero as b/h tended to zero. Kajiura also investigated the far-field behavior for waves generated by a bed movement in a three-dimensional fluid domain in which the bed deformation was not axially symmetric. The directivity of the leading wave generated by these disturbances was found to disappear at a very large distance from the source region.

Momoi (1964) has used a high-speed computer to evaluate numerically the wave profiles resulting from a uniform circular uplift of radius, r_o, in a three-dimensional domain of fluid with a uniform depth, h. The computations were based on the equation developed by Takahasi (1942) for an instantaneous bed movement. (Recall that Takahasi was able to find only crude approximations of the wave profile for the limiting cases of a shallow or deep sea.) Momoi computed the wave profiles for the case of $r_o/h = 10$ from $t = 0$ to the nondimensional time $t\sqrt{g/h} = 20$. At $t = 0$ the water assumed the shape of the bed deformation except near $r = r_o$ where a smooth transition occurred between the raised level of fluid and the original still water level. A wave then began to propagate from the region of generation forming a positive leading wave whose maximum amplitude was approximately 50% of the total bed movement, ζ_o. At $t\sqrt{g/h} = 6$

the water level at $r = 0$ began to decrease from its raised level until at $t\sqrt{g/h} = 13$ the water level reached its maximum negative value of approximately $-1.5\ \zeta_o$. (A similar behavior was also observed by Takahasi.) The water level at $r = 0$ then returned to the still water level about which it oscillated in a damped manner.

Carrier (1965) investigated the propagation of waves in a fluid domain with a variable depth which were generated by the bed displacement:

$$\frac{\partial \varphi}{\partial y} = \begin{cases} 0 & t < 0 \\ 0 & x > 0 \\ ae^{ax} c^2 te^{-ct} & x < 0,\ t > 0\ , \end{cases} \qquad (2.12)$$

where a and c are arbitrary constants. The limiting case of $a \to \infty$ and $c \to \infty$ was solved by Carrier. Since Carrier's primary interest was in the wave behavior at large distances from the generation region where the long waves approached a sloping beach, the exponential functions in Eq. (2.12) were chosen purely for mathematical convenience. No wave profiles were computed by Carrier; however, his simple method of solution of the linearized generation problem based on the use of integral transforms is of particular interest since this is also the method which will be adopted in this study.

Hwang and Divoky (1970) have taken an entirely different approach to the tsunami problem; instead of the linearized model of tsunami generation used by previous researchers, they adopt a first-order-nonlinear theory which ignores completely the vertical motion of the water and thus all effects of frequency dispersion. In order to solve the resulting equations in a three-dimensional fluid domain, a finite-difference scheme was adopted which permits an arbitrary bed displacement and a variable water depth to be incorporated into the model. The model was then applied to a prototype bed displacement which occurred during the Alaskan earthquake of 1964. Wave profiles were computed at various locations near the region of generation; the accuracy of these computed wave profiles could not be determined since no actual wave records were available. At one offshore position the computed profile was compared with water movements observed onshore and found to be in reasonable agreement. In a later report Hwang, et al (1971) adapted this model to also consider the curvature of the ocean by expressing the governing equations in spherical coordinates. In light of the results of the present study, the approach of Hwang and Divoky appears to be quite limited in its ability to accurately model tsunami propagation over very large distances. (The limitations are in effect similar to those which depend on a purely linear theory of wave propagation.)

Tuck and Hwang (1972) have most recently considered the waves generated by a bed movement on a uniformly sloping beach by adopting the linear-long-wave equations as a description of wave behavior. The equations were solved analytically for arbitrary bed movements which were assumed to occur instantaneously at the shoreward edge of a two-dimensional fluid domain. The generated waves propagated into a fluid domain whose depth increased linearly. Wave profiles were computed for the special case of a maximum bed displacement, ζ_o, occurring at $x = 0$ and decaying exponentially for $x > 0$. The wave shape was observed to be independent of x while the wave heights decayed like $x^{-\frac{1}{4}}$ or $t^{-\frac{1}{2}}$. The region of validity of the long wave description was also investigated since frequency dispersion is expected to eventually become important during propagation. Considering only the increase in the importance of frequency dispersion due to the increasing depth, Tuck and Hwang found the region of validity to be given by $b_o << x << b_o/\alpha_o^2$ where b_o is a characteristic size of the disturbance and α_o is the slope of the bed. It should be noted that the presence of nonlinear effects and frequency dispersion which are omitted in Tuck's and Hwang's analysis would most probably restrict the applicability of their solution to a region of propagation which is much smaller than they suggest. Certainly as the bed slope, α_o, tends to zero so that the fluid domain becomes uniform in depth, the range of validity of the linear-long-wave equations (which reduce to the simple wave equation for this case) would not tend to infinity. The importance and interaction of nonlinearities and frequency dispersion will be discussed in detail in this study.

Experimental studies of tsunami generation by bed movements appear to be very rare. Takahasi (1963) reported on earlier experiments which were conducted in a three-dimensional wave tank. In his 1933 experiment a small wave basin was used (2 m x 1.5 m x 0.3 m) in which a cylinder housing a moveable piston was fitted to the bottom of the tank. The piston could be moved suddenly through several centimeters by a spring-fly-wheel assembly. Wave measurements were made photographically and indicated that the water initially rose in a bell shape over the uplifted piston after which annular waves begin to propagate. A negative wave elevation was observed to occur at the center of the piston followed by oscillations about the original still water level. The propagation velocity of the leading wave was found to be equal to $\sqrt{gh}$ or slightly less while the amplitude appeared to decay like $r^{-0.6}$ or r^{-1}.

The 1957 experiments of Takahasi (1963) were conducted in a large, outdoor basin in which circular membranes were installed at the tank bottom. The membranes could be mechanically raised or lowered impulsively by piston rods connected to the center of the membrane and installed below the tank. Experiments were conducted using one, two, and six membranes. With one membrane Takahasi found the generated waves to be dispersive with the leading wave propagating with a celerity of $\sqrt{gh}$ and decaying in amplitude like $r^{-5/6}$. Interpretation of wave records was admittably difficult due to the presence of wind generated waves and vibration of the rubber membranes at the end of a movement.

Takahasi and Hatori (1962) experimentally investigated the waves generated by the sudden uplift of an elliptical membrane in a three-dimensional fluid domain of uniform depth, h. A large outdoor basin was used and the rubber membrane was installed at the bottom level of the basin. The movement of the membrane was created by the introduction of compressed air below the membrane which caused the membrane to swell. Wave measurements again indicated the formation of a dispersive wave train whose leading wave propagated with a velocity of $\sqrt{gh}$. The ratio of the wave heights at the ends of the long and short axes of the elliptical region of generation was observed to be one-third which was also the length ratio of the elliptical axes. During propagation this ratio decreased. The amplitude of the initial crest was observed to decay like $r^{-0.5}$ or $r^{-0.74}$ depending on the water depth used.

Although numerous authors have investigated the tsunami problem none appear to have thoroughly defined the wave signatures generated over a full range of characteristic size and time scales of a specific bed deformation. No authors appear to have considered the effect of large amplitude movements relative to the water depth. Previous analyses have approximated the equations governing the fluid motion by ignoring the nonlinear terms except in one study where the nonlinear terms have been partially retained but the linear effects were ignored.

In this investigation a linear theory will be adopted to describe the waves generated over a full range of generation characteristics by a simple family of bed movements; however, the applicability of this linearized approximation will also be investigated. Experimental measurements will be presented to confirm the theoretical analysis.

A strategy will also be demonstrated for finding the wave profiles during wave propagation when the linear theory is found to be no longer applicable. A theory for this case is presented which includes in an approximate manner both nonlinearities and the linear effects of frequency dispersion.

CHAPTER 3

THEORETICAL ANALYSIS

In this chapter a linear theory is presented for waves generated by a moving bed in a fluid initially with a constant depth. An integral solution for an arbitrary bed movement (in space and time) is obtained. Two general solutions are found, one for a two-dimensional fluid domain, and a second for a three-dimensional domain. For the three-dimensional model the bottom deformation is restricted to displacements which are axially symmetrical. The integral solutions are applied to two specific bed displacements. In both deformations the spatial variation is taken to be a simple block upthrust or downthrow; the time-displacement history of the block movement is varied.

Since the solutions obtained from the linear theory are only approximations to the complete nonlinear description of the problem of wave generation, the applicability of the linear solutions is discussed. Two classes of bed deformations, termed impulsive and creeping, are found for which the linear solutions are applicable near the region of wave generation. The nonlinear effects, which are initially small for these two classes of bed displacements, grow in importance during wave propagation. Eventually the linear and nonlinear effects become of the same order of magnitude. Once this condition is reached, the equation of Korteweg and deVries (1895) is discussed as an appropriate model of further wave behavior.

The analogy between the classical dam-break problem, with a semi-infinite and finite length reservoir, and the uniform upthrust of a bed section occurring impulsively for the two-dimensional fluid domain is discussed. From the dam-break analogy certain aspects of the waves generated by this type of bed deformation can be deduced.

3.1 THE TWO-DIMENSIONAL MODEL - A LINEAR THEORY

Consider a fluid domain D as shown in Fig. 3.1 bounded above by the free surface, S_f, below by the solid boundary, S_b, and unbounded in the direction of wave propagation, i.e., $-\infty < x < \infty$. Initially the fluid is at rest with the free surface and the solid boundary defined by the curves $y = 0$ and $y = -h$, respectively. For $t > 0$ the bed (or solid boundary) is permitted to move in a prescribed manner given by $y = -h + \zeta(x;t)$ such that: $\lim_{|x| \to \infty} \zeta(x;t) = 0$. The resulting deformation of the free surface which is to be determined is given by $y = \eta(x;t)$.

The problem can be solved by assuming the fluid to be incompressible and the flow irrotational. Thus, a velocity potential $\varphi = \varphi(x, y;t)$ is known to exist such that $\vec{q} = \nabla\varphi$ where $\vec{q} = (u, v)$ is the velocity vector and ∇ is the gradient operator $(\partial/\partial x,\ \partial/\partial y)$, and Laplace's equation is obtained from the continuity equation of an incompressible fluid, $\nabla \cdot \vec{q} = 0$:

$$\nabla^2\varphi = 0 \text{ in D.} \tag{3.1}$$

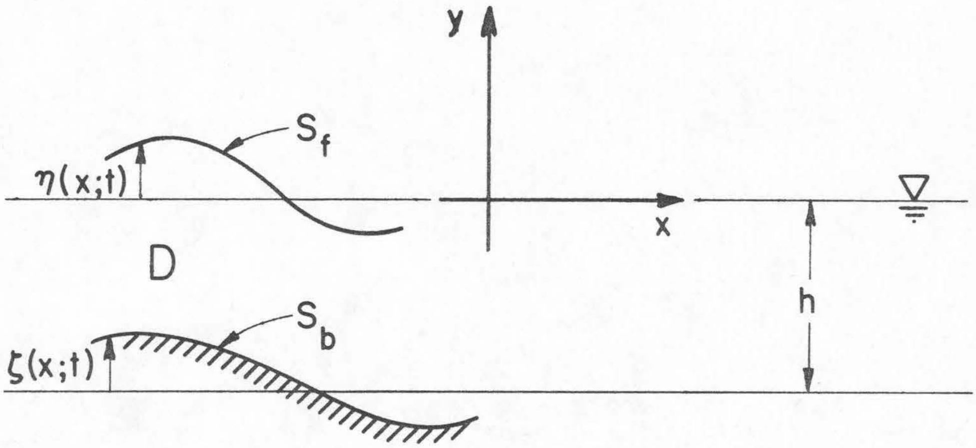

Fig. 3.1 Definition sketch of coordinate system.

The kinematic conditions to be satisfied on the free surface, S_f, and the bottom, S_b, are respectively:

$$\varphi_y = \eta_t + \varphi_x \eta_x \text{ on } y = \eta(x;t) , \tag{3.2}$$

$$\varphi_y = \zeta_t + \varphi_x \zeta_x \text{ on } y = -h + \zeta(x;t). \tag{3.3}$$

By further assuming the flow to be inviscid and surface energy effects to be negligible, the dynamic condition to be satisfied by fluid particles on the free surface, S_f, becomes:

$$\varphi_t + \tfrac{1}{2}(\nabla\varphi)^2 + g\eta = 0 \text{ on } y = \eta(x;t) , \tag{3.4}$$

where g is the acceleration of gravity. It is also assumed in Eq. (3.4) that the pressure on the free surface is constant and for convenience it has been taken to be zero.

The solution of the boundary value problem given by Eqs. (3.1), (3.2), (3.3), and (3.4) is inherently difficult due to the nonlinear terms in the boundary conditions and the fact that the position of the free surface, on which the boundary conditions given by Eqs. (3.2) and (3.4) are to be applied, is unknown prior to the solution of the problem. The usual procedure in solving problems of this type is to circumvent these difficulties by substituting for the complete problem a linear approximation. In this approximation the nonlinear terms are omitted and the boundary conditions are applied both on the undeformed free surface and the solid boundary. The linearized problem is given by:

$$\nabla^2\varphi = 0 \text{ in } D, \tag{3.5}$$

$$\varphi_y = \eta_t \text{ on } y = 0, \tag{3.6a}$$

$$\varphi_t + g\eta = 0 \text{ on } y = 0, \tag{3.6b}$$

and

$$\varphi_y = \zeta_t \text{ on } y = -h. \tag{3.7}$$

Eqs. (3.6a) and (3.6b) are usually combined to give the single free surface condition:

$$\varphi_{tt} + g\varphi_y = 0 \text{ on } y = 0. \tag{3.8}$$

A formal basis for using this linear approximation can be found by expanding the dependent variables $\varphi(x, y;t)$ and $\eta(x;t)$ as a power series in terms of a small parameter ϵ. Collecting terms of the lowest order in ϵ yields the linear problem given by Eqs. (3.5), (3.7) and (3.8). Therefore the accuracy of the linear approximation is dependent on the size of the parameter ϵ. A physical interpretation of ϵ can sometimes be found by scaling the dependent and independent variables of the problem with quantities which characterize the motion. A discussion of the effects of nonlinearities will be given in Section 3.2.

The solution of the initial and boundary value problem given by Eqs. (3.5), (3.7), and (3.8) is most easily obtained by the methods of operational calculus using integral transforms. An integral transform $\overline{f}(p)$ of a function $f(x)$ is defined by:

$$\overline{f}(p) = \int_{a_1}^{a_2} K(p,x)\, f(x)\, dx \;, \tag{3.9}$$

where the limits of integration a_1 and a_2 are known as well as the kernal $K(p,x)$. The use of an integral transform often reduces a partial differential equation in n independent variables to one of (n-1) variables. Successive use of transforms can ultimately reduce the equation to an ordinary differential equation or even to an algebraic equation. An outline of the strategy to be used in applying integral transforms to the solution of initial and boundary value problems is given by Tranter (1966, p. 18). For the problem under discussion there exists three independent variables x, y, and t. Thus, the use of transforms on two of these variables should reduce the problem to the solution of an ordinary differential equation. A further reduction to an algebraic equation is not worthwhile if the ordinary differential equation can be solved readily. An appropriate transform for the independent variable x whose limits are from minus to plus infinity is the complex Fourier transform (Sneddon, 1951) given by:

$$\overline{f}(k) = \int_{-\infty}^{\infty} e^{ikx} f(x)\, dx . \qquad (3.10)$$

where i is the imaginary number $\sqrt{-1}$. The appropriate transform for the time variable t, for which functions are defined only for $t \geq 0$, is the Laplace transform (Churchill, 1958) given by:

$$\tilde{f}(s) = \int_{0}^{\infty} e^{-st} f(t)\, dt. \qquad (3.11)$$

(The bar superscript will be used throughout this chapter to denote the Fourier transform of a function and the tilda superscript will be used to denote the Laplace transform.) Applying both transforms to a function $f(\mathbf{x};t)$ yields:

$$\tilde{\overline{f}}(k;s) = \int_{-\infty}^{\infty} dx \int_{0}^{\infty} e^{ikx} e^{-st} f(x;t)\, dt . \qquad (3.12)$$

To transform Eq. (3.5), the field equation is first multiplied through by the kernals e^{ikx} and e^{-st} and then integrated twice with respect to x and t over the limits indicated by Eqs. (3.10) and (3.11), respectively. Performing these operations yields:

$$\int_{-\infty}^{\infty} dx \int_{0}^{\infty} e^{ikx} e^{-st} \varphi_{xx}(x,y;t)dt + \int_{-\infty}^{\infty} dx \int_{0}^{\infty} e^{ikx} e^{-st} \varphi_{yy}(x,y;t)dt = 0. \quad (3.13)$$

Eq. (3.13) may also be written:

$$\int_{-\infty}^{\infty} e^{ikx} \frac{\partial^2}{\partial x^2}\left[\int_{0}^{\infty} e^{-st} \varphi(x,y;t)\, dt\right]dx$$

$$+ \frac{\partial^2}{\partial y^2}\left[\int_{-\infty}^{\infty} dx \int_{0}^{\infty} e^{ikx} e^{-st} \varphi(x,y;t)dt\right] = 0 , \qquad (3.14)$$

where all integrals have been assumed to be sufficiently well-behaved to permit the indicated operations, i. e., uniformly convergent. Comparing the bracketed terms with Eqs. (3. 11) and (3. 12), Eq. (3. 14) may be rewritten as:

$$\int_{-\infty}^{\infty} e^{ikx} \frac{\partial^2 \bar{\varphi}(x,y;s)}{\partial x^2}\, dx + \frac{\partial^2 \tilde{\bar{\varphi}}(k,y;s)}{\partial y^2} = 0 \,. \tag{3.15}$$

The above integral can be evaluated using integration by parts to yield:

$$\tilde{\bar{\varphi}}_{yy}(k,y;s) - k^2 \tilde{\bar{\varphi}}(k,y;s) = 0 \text{ in D.} \tag{3.16}$$

In a similar manner Eqs. (3. 7) and (3. 8) may be transformed to:

$$\tilde{\bar{\varphi}}_{y}(k,-h;s) = s\tilde{\bar{\zeta}}(k;s) \,, \tag{3.17}$$

$$\tilde{\bar{\varphi}}_{y}(k,0;s) + \frac{s^2}{g} \tilde{\bar{\varphi}}(k,0;s) = 0 \,. \tag{3.18}$$

In deriving Eqs. (3. 17) and (3. 18) use has been made of the fact that $\varphi(x,y;0) = \varphi_t(x,y;0) = 0$ which is a consequence of the initial conditions imposed on the boundary value problem.

The transformed field equation, Eq. (3. 16), is an ordinary differential equation which may be solved directly for $\tilde{\bar{\varphi}}(k,y;s)$. The solution is:

$$\tilde{\bar{\varphi}}(k,y;s) = A(k;s) \cosh ky + B(k;s) \sinh ky \,, \tag{3.19}$$

where A and B are functions of k and s alone. Substituting $\tilde{\bar{\varphi}}(k,y;s)$, as given by Eq. (3. 19), into Eq. (3. 18) gives:

$$B(k;s) = -\frac{s^2}{gk} A(k;s) . \qquad (3.20)$$

Substituting Eqs. (3.19) and (3.20) into Eq. (3.17) one obtains:

$$A(k;s) = \frac{-gs\,\tilde{\bar{\zeta}}(k;s)}{(s^2 + gk \tanh kh) \cosh kh} . \qquad (3.21)$$

Combining Eqs. (3.19), (3.20), and (3.21) the transformed velocity potential is found to be:

$$\tilde{\bar{\varphi}}(k,y;s) = \frac{-gs\,\tilde{\bar{\zeta}}(k;s)}{(s^2+\omega^2) \cosh kh} \left[\cosh ky - \frac{s^2}{gk} \sinh ky \right] . \qquad (3.22)$$

where for convenience ω^2 is defined as:

$$\omega^2 \equiv gk \tanh kh. \qquad (3.23)$$

It is noted that Eq. (3.23) is identical to the dispersion relationship found in water wave problems with a stationary bottom and without surface energy effects; however, this is not to imply that Eq. (3.23) is the dispersion relation for this problem.

The free surface location $\eta(x;t)$ is related to the velocity potential $\varphi(x,y;t)$ by Eq. (3.6b). Thus, the transformed relationship is:

$$\tilde{\bar{\eta}}(k;s) = -\frac{s}{g} \tilde{\bar{\varphi}}(k,0;s) . \qquad (3.24)$$

Substituting Eq. (3.22) into Eq. (3.24) the following is obtained:

$$\tilde{\bar{\eta}}(k;s) = \frac{s^2\,\tilde{\bar{\zeta}}(k;s)}{(s^2+\omega^2) \cosh kh} . \qquad (3.25)$$

The transformation of $\tilde{\bar{\eta}}(k;s)$ to $\eta(x;t)$, i.e., to the original independent variables $(x;t)$, is accomplished using the inversion formulae for the Fourier and Laplace transforms. The inversion integral for the Fourier transform is given by:

$$f(x) = \frac{1}{2\pi}\int_{-\infty}^{\infty} e^{-ikx}\bar{f}(k)\,dk, \tag{3.26}$$

and for the Laplace transform:

$$f(t) = \lim_{\Gamma\to\infty}\frac{1}{2\pi i}\int_{\mu-i\Gamma}^{\mu+i\Gamma} e^{st}\tilde{f}(s)\,ds\ , \tag{3.27}$$

where μ is a positive constant; hereafter, the inversion integral for the Laplace transform will be written as:

$$f(t) = \frac{1}{2\pi i}\int_{Br.} e^{st}\tilde{f}(s)\,ds\ , \tag{3.28}$$

where $\int_{Br.} \equiv \lim_{\Gamma\to\infty}\int_{\mu-i\Gamma}^{\mu+i\Gamma}$ is the Bromwich contour. Therefore, the surface elevation becomes:

$$\eta(x;t) = \frac{1}{2\pi}\int_{-\infty}^{\infty}\left\{\frac{1}{2\pi i}\int_{Br.}\frac{s^2 e^{-ikx}\, e^{st}\tilde{\bar{\zeta}}(k;s)}{(s^2+\omega^2)\cosh kh}\,ds\right\}dk\ . \tag{3.29}$$

Eq. (3.29) gives the free surface elevation as a function of space and time in the fluid domain D (shown in Fig. 3.1) resulting from a bed displacement described by $\zeta(x;t)$. Before a further simplification of Eq. (3.29) can be made, specific bed deformations must be prescribed. Of special interest in the present study are two bed displacements whose spatial variation is taken to be a block section of the bed, symmetric about $x = 0$, moving in the positive or negative vertical direction. Two different time-displacement histories of the block upthrust or downthrow will be used. The first displacement is described mathematically by:

$$\zeta(x;t) = \zeta_o(1 - e^{-\alpha t})\,H(b^2 - x^2), \qquad t \geq 0 . \tag{3.30}$$

$H(b^2-x^2)$ is the Heavyside step function defined by:

$$H(b^2-x^2) = \begin{cases} 1, & b^2-x^2 > 0 \\ 0, & b^2-x^2 < 0 \end{cases} . \tag{3.31}$$

The Heavyside step function used in Eq. (3.30) confines the spatial deformation of the bed to a uniform movement with time in the interval $-b < x < b$. The time-displacement history of the bed section is shown in Fig. 3.2. The bed deformation can be characterized by three

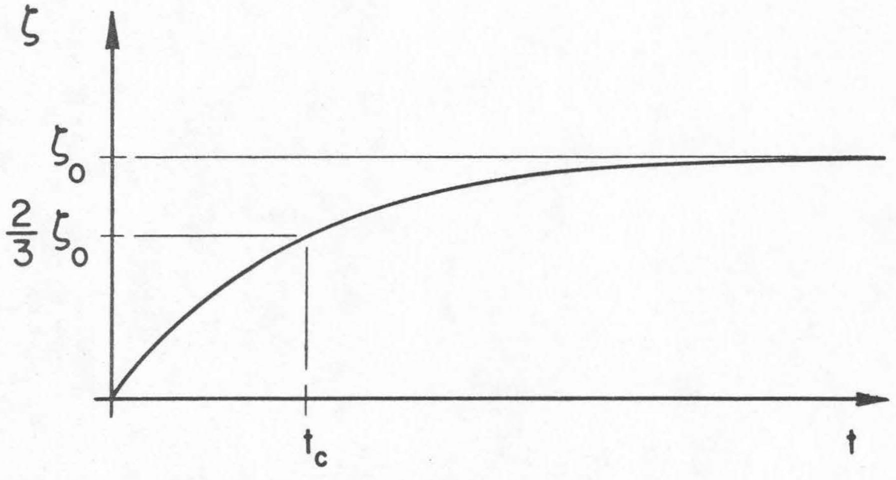

Fig. 3.2 Exponential time-displacement history of the moving bed.

parameters: ζ_o, the amplitude of the vertical displacement (either positive or negative); b, the halfwidth of the block section; and t_c, a characteristic time of the displacement, e.g., $t_c = 1/\alpha$. For reasons to be discussed in Chapter 4, the characteristic time of movement used will be the time required for two-thirds of the motion to be completed, i.e., $t = t_c$ when $\zeta/\zeta_o = 2/3$ or $t_c = 1.11/\alpha$ (see Fig. 3.2). Of particular interest for this displacement is the initial discontinuity in velocity, $\partial\zeta/\partial t$, and the asymptotic approach of the block section to ζ_o. (The exponential bed displacement given by Eq. (3.30) will hereafter be referred to as $\zeta_e(x;t)$.)

The second bed deformation of interest is given by:

$$\zeta(x;t) = \zeta_o\left[\tfrac{1}{2}(1-\cos\frac{\pi t}{T})\,H(T-t) + H(t-T)\right]H(b^2-x^2)\ , \qquad t \geq 0\,. \qquad (3.32)$$

Again, the Heavyside step function $H(b^2-x^2)$ is used to confine the displacement to the interval $-b < x < b$. Step functions are also employed in the temporal variation. For $t < T$, $H(T-t) = 1$ and $H(t-T) = 0$, so the block section moves according to the function $\zeta_o\left[1-\cos(\pi t/T)\right]/2$. For $t > T$, $H(T-t) = 0$ and $H(t-T) = 1$ so the bed unit remains at the constant elevation ζ_o. The time-displacement history of the block section is shown in Fig. 3.3. This movement has a continuous velocity, $\partial\zeta/\partial t$, and is completed in a finite period, T. Again three parameters are required to characterize the motion: ζ_o, b, and a characteristic time, t_c. An obvious choice for the characteristic time is the total time of movement, T. (Henceforth, the half-sine bed displacement given in Eq. (3.32) will be referred to as $\zeta_s(x;t)$.)

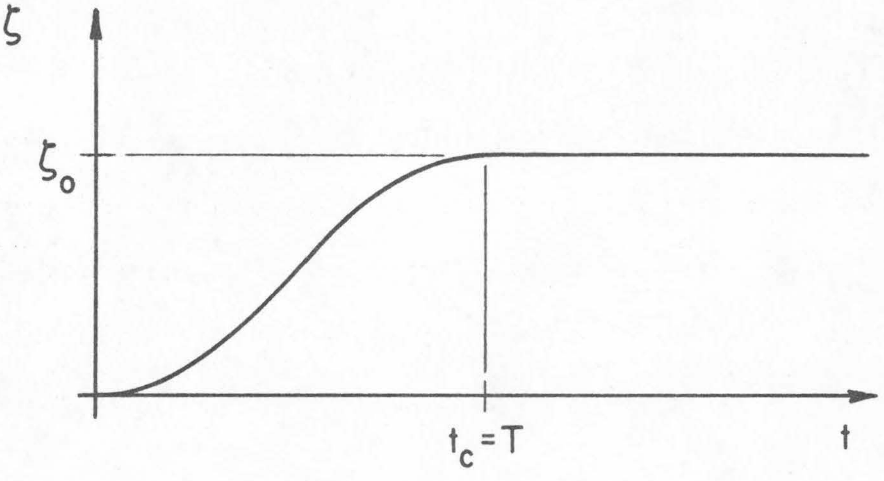

Fig. 3.3 Half-sine time-displacement history of the moving bed.

Eq. (3.29) can now be specialized using the particular bed displacements given in Eqs. (3.30) and (3.32). However, before the wave amplitude can be obtained from Eq. (3.29), the bed deformations must be transformed by the Laplace and Fourier transforms. Performing the operations indicated by Eq. (3.12) the following is obtained for the exponential bed displacement:

$$\overline{\tilde{\zeta}}_e(k;s) = 2\zeta_o \frac{\sin kb}{k}\left[\frac{\alpha}{s(s+\alpha)}\right] \tag{3.33}$$

Substituting Eq. (3.33) into Eq. (3.29) the following is obtained:

$$\eta(x;t) = \frac{\zeta_o}{\pi}\int_{-\infty}^{\infty} e^{-ikx}\,\frac{\sin kb}{k\cosh kh}\left\{\frac{1}{2\pi i}\int_{Br.}\frac{\alpha s e^{st}}{(s+\alpha)(s^2+\omega^2)}\,ds\right\} dk\,. \tag{3.34}$$

The Laplace inversion with respect to s, shown in brackets above, can be integrated in closed form using the residue theorem and noting that all poles appearing in the integrand are simple. Performing this integration yields:

$$\eta(x;t) = -\frac{\zeta_o}{\pi}\int_{-\infty}^{\infty} e^{-ikx}\,\frac{\sin kb}{k\cosh kh}\left(\frac{\alpha^2}{\alpha^2+\omega^2}\right)\left[e^{-\alpha t} - \cos\omega t - \frac{\omega}{\alpha}\sin\omega t\right]dk. \quad (3.35)$$

Taking the real part of Eq. (3.35), and since the integrand is even in k, the surface elevation can be expressed as:

$$\eta(x;t) = -\frac{2\zeta_o}{\pi}\int_{0}^{\infty} \frac{\cos kx\,\sin kb}{k\cosh kh}\left(\frac{\alpha^2}{\alpha^2+\omega^2}\right)\left[e^{-\alpha t} - \cos\omega t - \frac{\omega}{\alpha}\sin\omega t\right]dk. \quad (3.36)$$

The integration over k cannot be computed in closed form and thus must be approximated by numerical integration. A removable singularity exists in the integrand of Eq. (3.36) at the lower limit of integration, k = 0. Letting I represent the integrand of Eq. (3.36), then by L'Hospital's rule:

$$\lim_{k\to 0} I = b(e^{-\alpha t} - 1)\,. \quad (3.37)$$

This limiting value is required for the numerical integration.

When the half-sine bed displacement given by Eq. (3.32) is transformed by the Laplace and Fourier transforms the following is obtained:

$$\tilde{\bar{\zeta}}_s(k;s) = \zeta_o\frac{\sin kb}{k}\left[\left(1+e^{-sT}\right)\left(\frac{\varkappa^2}{s(s^2+\varkappa^2)}\right)\right], \quad (3.38)$$

where $\varkappa = \pi/T$. When Eq. (3.38) is substituted into Eq. (3.29) one obtains the following:

$$\eta(x;t) = \frac{\zeta_o}{2\pi}\int_{-\infty}^{\infty} e^{-ikx}\,\frac{\sin kb}{k\cosh kh}\,\cdot$$

$$\left\{\frac{1}{2\pi i}\int_{Br.} e^{st}\left[\frac{s^2}{s^2+\omega^2}\right]\left[\frac{\varkappa^2}{s(s^2+\varkappa^2)}\right]\left[1+e^{-sT}\right]ds\right\}dk\,. \qquad (3.39)$$

As for the exponential bed displacement, the integration with respect to s can be performed in closed form. Performing the integration indicated by the bracketed integral in Eq. (3.39) yields:

$$\eta(x;t) = \frac{\zeta_o}{2\pi}\int_{-\infty}^{\infty} e^{-ikx}\,\frac{\sin kb}{k\cosh kh}\left\{\frac{\varkappa^2}{\varkappa^2-\omega^2}\right\}\Big\{\cos\omega t$$

$$-\cos\varkappa t + H(t-T)[\cos\omega(t-T)+\cos\varkappa t]\Big\}dk\;, \qquad (3.40)$$

where H(t-T) is the Heavyside step function. Noting that the integrand of Eq. (3.40) is an even function of k and taking only the real part yields:

$$\eta(x;t) = \frac{\zeta_o}{\pi}\int_{0}^{\infty}\frac{\cos kx\,\sin kb}{k\cosh kh}\left\{\frac{\varkappa^2}{\varkappa^2-\omega^2}\right\}\Big\{\cos\omega t$$

$$-\cos\varkappa t + H(t-T)[\cos\omega(t-T)+\cos\varkappa t]\Big\}dk\,. \qquad (3.41)$$

Again the integral over the wave number k cannot be computed in closed form thus necessitating the use of numerical integration. The integrand of Eq. (3.41) has a removable singularity at the lower limit of integration, k = 0. The limiting value of the integrand, I, as k → 0 is:

$$\lim_{k\to 0} I = b\Big\{1-\cos\varkappa t + H(t-T)[1+\cos\varkappa t]\Big\}\,, \qquad (3.42)$$

which, as before, is required for the numerical integration.

3.2 THE TWO-DIMENSIONAL MODEL - NONLINEAR CONSIDERATIONS

The linear theory presented in Section 3.1 is only an approximation to the complete nonlinear problem; thus, it is of major importance to determine the conditions necessary for the linear model to provide an accurate description of the actual wave behavior. As mentioned in Section 3.1, a rational basis for using the linear model is usually found by expressing all independent variables as a power series in terms of a "small" parameter ϵ. The collection of lowest order terms of ϵ normally yields the linearized problem as a first approximation to the complete description of wave behavior. Physically the parameter ϵ indicates the relative importance of nonlinear terms compared to the linear terms. As also mentioned in Section 3.1, a physical interpretation of the parameter ϵ can sometimes be found by scaling the dependent and independent variables of the problem by quantities which characterize the motion. In the two following sections (Section 3.2.1 and 3.2.2) it will be shown that more than one parameter ϵ is required to adequately define the limitations of the linear model. The discussion of nonlinear effects is conveniently divided into two parts. In Section 3.2.1 nonlinear effects occurring during the time of bed deformation will be discussed. In Section 3.2.2 the effects of nonlinearities that arise during wave propagation are discussed. Both types of nonlinearities limit the applicability of the linearized model.

3.2.1 Aspects of Nonlinearity-Generation

During the time of bed displacement, it would seem appropriate to scale the motion of a water particle in the fluid domain with respect to the motion of the deforming solid boundary. It was indicated in Section 3.1 that the specific bed deformations given by Eqs. (3.30) and (3.32) each can be characterized by three parameters: an amplitude of displacement, ζ_o, a time, t_c, and a size, b. The two other independent variables of the problem are the water depth, h, and the acceleration of gravity, g. These five independent variables are available to scale the dimensional variables of the problem. Buckingham (1914) showed that if the magnitude of a physical quantity, Q_1, is a function of (n-1) other independent physical quantities, and if Q_1 and these (n-1) quantities include j fundamental dimensions, then the functional equation:

$$Q_1 = f(Q_2, Q_3, \ldots, Q_n) , \tag{3.43}$$

may be replaced by

$$\Pi_1 = f(\Pi_2, \Pi_3, \ldots, \Pi_{n-j}) , \tag{3.44}$$

where each Π term is an independent dimensionless ratio of the various Q's. In the present problem the dependent quantity of interest is the water surface displacement, η, which can be related functionally to the five independent variables in the following way:

$$\eta = f(\zeta_o, b, t_c, h, g). \tag{3.45}$$

Since the five independent quantities involve only two physical dimensions, length and time, the normalized water surface displacement should be a function of three dimensionless ratios (or Π terms). A possible choice of these Π terms is:

$$\frac{\eta}{\zeta_o} = f\,(\zeta_o/h,\ b/h,\ t_c\sqrt{g/h})\,. \tag{3.46}$$

The ratio ζ_o/h represents an amplitude scale of the bed movement, b/h represents a size scale, and $t_c\sqrt{g/h}$ represents a time scale. The significance of this choice of nondimensional numbers, and combinations thereof, will be shown shortly.

In order to gain some insight into the parameters which must be small during generation in order for the linear theory to be applicable, it is more convenient to use the nonintegrated equations of motion. It is well known in fluid mechanics that under the assumptions given in Section 3.1 the equations of motion are:

$$(u^*)_{t^*} + u^*(u^*)_{x^*} + v^*(u^*)_{y^*} + \frac{1}{\rho}(P^*)_{x^*} = 0, \quad \text{(x-momentum)}, \tag{3.47}$$

$$(v^*)_{t^*} + u^*(v^*)_{x^*} + v^*(v^*)_{y^*} + \frac{1}{\rho}(P^*)_{y^*} + g = 0, \quad \text{(y-momentum)}, \tag{3.48}$$

where the asterisk is used temporarily to denote a dimensional variable and the notation $(\ )_{t^*}$ implies the differentation of the bracketed quantity with respect to t^*. The quantity $P^* = P^*(x^*, y^*; t^*)$ is the pressure in the fluid field, ρ is the density of the fluid, and g is the acceleration of gravity. If the velocity vector (u^*, v^*) is written in terms of the velocity potential φ in Eqs. (3.47) and (3.48), and the irrotationality condition: $(u^*)_{y^*} = (v^*)_{x^*}$ is used, the equations may be integrated once to yield Eq. (3.4) on the free surface, i.e., on $y^* = \eta^*(x^*; t^*)$. The continuity equation and boundary conditions are the same as indicated previously but they are repeated here for convenience:

$$(u^*)_{x^*} + (v^*)_{y^*} = 0 \; , \tag{3.49}$$

$$v^* = (\eta^*)_{t^*} + u^*(\eta^*)_{x^*} \qquad \text{on } y^* = \eta^* \; , \tag{3.50}$$

$$v^* = (\zeta^*)_{t^*} + u^*(\zeta^*)_{x^*} \qquad \text{on } y^* = -h + \zeta^* \, . \tag{3.51}$$

The choice of scaling for each dimensional variable appearing in Eqs. (3.47) through (3.51) must be based on a reasonable physical interpretation of the problem. Assume for the moment that the bed displacement occurs so rapidly that the water surface profile is similar in shape to the deformed bed at any time during the movement. Bed movements of this type will hereafter be referred to as impulsive. Then the water volume displaced by the deforming boundary has a length scale, Λ, of the order of the length of the bed deformation, i.e., $\Lambda = 0(b)$. The amplitude scale, χ, of the displaced water volume is of order, ζ_o, the amplitude of the bed deformation. (This can easily be seen by equating the volume of displaced fluid per unit width, $\zeta_o b$, to the volume per unit width in the wave, i.e., $\chi b = \zeta_o b$ or $\chi = \zeta_o$.) In addition, time variations of the wave must scale with the characteristic time of bed displacement, t_c. A characteristic vertical velocity based on the bed deformation characteristics is ζ_o/t_c. The velocity in the direction of wave propagation and the fluid pressure should be scaled by $\sqrt{gh}$ and ρgh, respectively, in the normal manner for problems of this type. The following scaling of variables thus seems appropriate when the wave is generated impulsively:

$$x = \frac{x^*}{b},\ y = \frac{y^*}{h},\ t = \frac{t^*}{t_c},\ u = \frac{u^*}{\sqrt{gh}},$$
$$v = \frac{v^*}{(\zeta_o/t_c)},\ \eta = \frac{\eta^*}{\zeta_o},\ \zeta = \frac{\zeta^*}{\zeta_o},\ P = \frac{P^*}{\rho gh}. \tag{3.52}$$

Note that two length scales have been used in the vertical scaling. The boundary deformations have been scaled by the characteristic amplitude scale $\chi = \zeta_o$ while the position coordinate y^* has been scaled by the water depth h. Rewriting Eqs. (3.47) through (3.51) in terms of the nondimensional variables yields:

$$u_t + \frac{t_c\sqrt{g/h}}{b/h}(uu_x + P_x) + \frac{\zeta_o}{h}(vu_y) = 0\ , \tag{3.53}$$

$$v_t + \frac{t_c\sqrt{g/h}}{b/h}(uv_x) + \frac{\zeta_o}{h}(vv_y) + (t_c\sqrt{g/h})^2\left(\frac{\zeta_o}{h}\right)^{-1}(P_y+1) = 0\ , \tag{3.54}$$

$$\frac{t_c\sqrt{g/h}}{b/h}u_x + \frac{\zeta_o}{h}v_y = 0\ , \tag{3.55}$$

$$v = \eta_t + \frac{t_c\sqrt{g/h}}{b/h}u\eta_x \qquad \text{on } y = \frac{\zeta_o}{h}\eta\ , \tag{3.56}$$

$$v = \zeta_t + \frac{t_c\sqrt{g/h}}{b/h} u\zeta_x \qquad \text{on } y = -1 + \frac{\zeta_o}{h}\zeta \, . \tag{3.57}$$

The stretching of variables given by Eq. (3.52) has made each term in Eqs. (3.53) through (3.57) of the same order as its coefficient. Thus, if the coefficients of the nonlinear terms in Eqs. (3.53) through (3.57) are required to be much less than unity, i.e., if:

$$\frac{t_c\sqrt{g/h}}{b/h} < < 1, \quad \zeta_o/h < < 1 \quad , \tag{3.58}$$

then the nonlinear terms may be neglected as a first approximation, resulting in a system of linear equations. Since ζ_o/h is taken to be much less than unity, the linearized boundary conditions on the free surface and on the bed may be applied at $y = 0$ and $y = -1$, respectively, with little error. The continuity equation, Eq. (3.55), depends only on the relative size of $t_c\sqrt{gh}/b$ and ζ_o/h. If both parameters are small and of the same order then both terms must be used in the first approximation. If one coefficient is much smaller than the other (with both still much less than unity) then the term with the smaller coefficient may be neglected in the first approximation.

Thus, two parameters are found that must be small in order for the linear theory to be applicable. These parameters consist of the three ratios found previously by dimensional analysis. An interesting combination of two of these numbers is given by the ratio of $t_c\sqrt{g/h}$

and b/h which may be written $t_c\sqrt{gh}/b$. The quantity $t_c\sqrt{gh}$ is simply the distance a long gravity wave will travel in a time t_c. Thus if $t_c\sqrt{gh}/b$ is much less than unity a major portion of the bed movement occurs before elevations (or depressions) of the water surface have an opportunity to leave the generating region. This results in a displaced water surface near the end of the bed movement similar in shape to the deformed bed as was assumed in deriving the scaling of variables given by Eq. (3.52). It should be noted that no restriction must be placed on the magnitude of b/h alone in order to maintain the applicability of the linear theory; the disturbance-size scale is unlimited as long as $t_c\sqrt{gh}/b$ remains much less than unity.

Now consider the case of a wave generated by a very slow bed movement, i.e., $t_c\sqrt{gh}/b$ is much greater than unity; hence, the water surface elevations (or depressions) that occur have sufficient time to leave the generation region during the time of bed displacement. Bed displacements of this type will hereafter be referred to as creeping. Near the end of the bed deformation process the displaced volume of water is distributed over a length in the direction of wave propagation proportional to $t_c\sqrt{gh}$. Thus an appropriate length scale, Λ, would appear to be $t_c\sqrt{gh}$. A characteristic amplitude, χ, of the displaced water volume can be found as before by equating the wave volume per unit width to the displaced volume per unit width:

$$\chi t_c\sqrt{gh} = b\zeta_o \text{ or } \chi = \frac{b\zeta_o}{t_c\sqrt{gh}} . \tag{3.59}$$

The time variations of this wave form are assumed to be proportional to the travel time of a long gravity wave across the deforming bed section, i.e., $b/\sqrt{gh}$, and the remaining variables, i.e., u^*, v^*, y^*, and P^*, scale as before. It would seem appropriate to scale the water surface deformation, $\eta^*(x^*;t^*)$, and the bed deformation, $\zeta^*(x^*;t^*)$, by the same characteristic amplitude, χ, as was done for the previous case. Thus a reasonable choice for the scaling of variables when $t_c\sqrt{gh}/b >> 1$ is:

$$\begin{gathered} x = \frac{x^*}{t_c\sqrt{gh}}, \quad y = \frac{y^*}{h}, \quad t = \frac{t^*}{(b/\sqrt{gh})}, \quad u = \frac{u^*}{\sqrt{gh}}, \\ v = \frac{v^*}{(\zeta_o/t_c)}, \quad \eta = \frac{\eta^*}{\zeta_o}\frac{t_c\sqrt{gh}}{b}, \quad \zeta = \frac{\zeta^*}{\zeta_o}\frac{t_c\sqrt{gh}}{b}, \quad P = \frac{P^*}{\rho gh} . \end{gathered} \tag{3.60}$$

Rewriting Eqs. (3.47) through (3.51) in terms of the nondimensional variables presented in Eq. (3.60) yields:

$$u_t + \frac{b/h}{t_c\sqrt{g/h}}(uu_x + P_x) + \frac{b/h}{t_c\sqrt{g/h}}\left(\frac{\zeta_o}{h}\right)vu_y = 0 , \tag{3.61}$$

$$v_t + \frac{b/h}{t_c\sqrt{g/h}}(uv_x) + \frac{b/h}{t_c\sqrt{g/h}}\left(\frac{\zeta_o}{h}\right)(vv_y) + t_c\sqrt{g/h}\left(\frac{b}{h}\right)\left(\frac{\zeta_o}{h}\right)^{-1}(P_y+1) = 0, \tag{3.62}$$

$$u_x + \frac{\zeta_o}{h}(v_y) = 0 , \tag{3.63}$$

$$v = \eta_t + \frac{b/h}{t_c\sqrt{g/h}}(u\eta_x) \qquad \text{on } y = \frac{b/h}{t_c\sqrt{g/h}}\left(\frac{\zeta_o}{h}\right)\eta\,, \tag{3.64}$$

$$v = \zeta_t + \frac{b/h}{t_c\sqrt{g/h}}(u\zeta_x) \qquad \text{on } y = -1 + \frac{b/h}{t_c\sqrt{g/h}}\left(\frac{\zeta_o}{h}\right)\zeta\,. \tag{3.65}$$

Since, the original assumption in this development was:

$$\frac{t_c\sqrt{gh}}{b} = \frac{t_c\sqrt{g/h}}{b/h} >> 1\,, \tag{3.66}$$

the nonlinear terms, as a first approximation, may again be neglected when compared to the linear terms. This statement is true regardless of the value of the relative bed displacement, ζ_o/h, since this ratio is always less than or equal to unity. Hence, the linearized boundary conditions $v = \eta_t$ on the free surface and $v = \zeta_t$ on the bed may be applied on $y = 0$ and $y = -1$, respectively, even when ζ_o/h approaches unity. Again no restriction must be placed on the relative size of the disturbance, b/h , alone in order for the linear approximation to be applicable as long as $t_c\sqrt{gh}/b >> 1$.

If the quantities ζ_o/h, b/h, and $t_c\sqrt{g/h}$ are indeed the proper dimensionless generation parameters and if these ratios remain constant, the wave generated should be similar regardless of the actual values of ζ_o, b, t_c, h or g. To see if this indeed is the case, consider the linear solution given by Eq. (3.36) which describes the variation of the wave amplitude as a function of space and time for the exponential bed displacement given by Eq. (3.30). The definition of the characteristic time, t_c, for this motion, as mentioned previously, is taken as $t_c = 1.11/\alpha$ where α is the arbitrary constant appearing in Eq. (3.30). Introducing the nondimensional variable $\lambda = kh$, Eq. (3.36) may be rewritten as:

$$\frac{\eta\left(\frac{x}{h}, t\sqrt{g/h}\right)}{\zeta_o} = -\frac{2}{\pi}\int_0^\infty \frac{\cos\lambda\left(\frac{x}{h}\right)\sin\lambda\left(\frac{b}{h}\right)}{\lambda\cosh\lambda}\left[\frac{\left(\frac{1.11}{t_c\sqrt{g/h}}\right)^2}{\left(\frac{1.11}{t_c\sqrt{g/h}}\right)^2 + \lambda\tanh\lambda}\right] \cdot$$

$$\left[\exp\left(-1.11\frac{t\sqrt{g/h}}{t_c\sqrt{g/h}}\right) - \cos\left(\sqrt{\lambda\tanh\lambda}\; t\sqrt{g/h}\right)\right.$$

$$\left. - \frac{t_c\sqrt{g/h}\sqrt{\lambda\tanh\lambda}}{1.11}\sin\left(\sqrt{\lambda\tanh\lambda}\; t\sqrt{g/h}\right)\right]d\lambda. \quad (3.67)$$

From Eq. (3.67) it can be seen that if b/h and $t_c\sqrt{g/h}$ are constant, then the same nondimensional wave form, η/ζ_o, results at the same nondimensional distance downstream, x/h, and at the same nondimensional time, $t\sqrt{g/h}$. Note that the generation parameter, ζ_o/h, does not appear in Eq. (3.67). In general, this parameter is assumed to be much less than unity by the linear model and is thus eliminated from consideration. In a similar manner the wave form given by Eq. (3.41) for the half-sine bed displacement may be expressed as:

$$\begin{aligned}\frac{\eta\left(\frac{x}{h}, t\sqrt{g/h}\right)}{\zeta_o} = \frac{1}{\pi}\int_0^{\infty} \frac{\cos \lambda\left(\frac{x}{h}\right) \sin \lambda\left(\frac{b}{h}\right)}{\lambda \cosh \lambda} & \left[\frac{\left(\frac{\pi}{t_c\sqrt{g/h}}\right)^2}{\left(\frac{\pi}{t_c\sqrt{g/h}}\right)^2 - \lambda \tanh \lambda}\right] \cdot \\ & \left\{\cos\left(\sqrt{\lambda \tanh \lambda}\, t\sqrt{g/h}\right) - \cos\left(\pi \frac{t\sqrt{g/h}}{t_c\sqrt{g/h}}\right) + H\left[(t-t_c)\sqrt{g/h}\right] \cdot \right. \\ & \left.\left[\cos\left(\sqrt{\lambda \tanh \lambda}\,(t-t_c)\sqrt{g/h}\right) + \cos\left(\pi \frac{t\sqrt{g/h}}{t_c\sqrt{g/h}}\right)\right]\right\} d\lambda, \qquad (3.68)\end{aligned}$$

where again $\lambda = kh$ and the characteristic time has been set equal to the total time of displacement, i.e., $t_c = T$. Eq. (3.68) also shows that a similar nondimensional wave results when the nondimensional generation parameters, b/h and $t_c\sqrt{g/h}$, are held constant.

In summary, it has been shown that during the time of bed displacement, the linear theory appears to be applicable when the generation parameters satisfy the conditions given by either Eq. (3.58) or Eq. (3.66). From these conditions it can be seen that no restriction need be placed on the size scale, b/h, alone as long as the time scale, $t_c\sqrt{g/h}$, is such that Eqs. (3.58) or (3.66) are satisfied.

3.2.2 Aspects of Nonlinearity - Propagation.

In the preceding section the effects of nonlinearities introduced during the bed deformation process were discussed. Parameters characterizing the generation and ranges of these parameters for which the linear theory appeared to be applicable were determined.

Once a wave has been generated and propagates into the fluid region of constant depth a different scaling of the dimensional variables is required in Eqs (3.47) through (3.51). It is well known for long waves, i.e., waves whose lengths are large compared to the water depth, that the magnitude of the nonlinear terms is given by the ratio of the maximum wave amplitude, η_o, and the water depth, h, i.e., η_o/h. The magnitude of the linear terms is indicated by the square of the ratio of the water depth, h, to a characteristic length, ℓ, of the wave in its direction of propagation, i.e., $(h/\ell)^2$. The characteristic length, ℓ, is a measure of the distance over which significant changes in water surface elevation occur. More discussion of this characteristic length will be given later. The importance of the nonlinear terms relative to the linear terms is thus proportional to:

$$\frac{\text{nonlinear effects}}{\text{linear effects}} \propto \frac{\eta_o/h}{(h/\ell)^2} = \frac{\eta_o \ell^2}{h^3} = \underline{U}. \tag{3.69}$$

Although this ratio was pointed out by several authors (see, e.g., Stokes (1847)), Ursell (1953) first discussed the significance of the ratio in characterizing water waves of different types thus resolving what had come to be known as the long wave paradox (see Stokes (1891) or Lamb (1932, § 252)). Hence the ratio given by Eq. (3.69) will hereafter be referred to as the Ursell Number. For the nonlinear effects (also termed amplitude dispersion by Lighthill and Whitham (1955)) to be negligible during wave propagation the Ursell Number must be much less than unity, i.e., $\eta_o/h << (h/\ell)^2$. When the Ursell Number is of order unity or greater, the linear theory is no longer applicable. Waves for which the Ursell Number is much greater than unity can be approximated very well by ignoring the linear effects (or frequency dispersion) and retaining only the nonlinear effects.

When amplitude and frequency dispersion are of the same order such at $\underline{U} = 0(1)$ the description of the wave motion must retain all terms. Approximations to the complete solution of the water wave problem for this special case can be made when linear and nonlinear effects are assumed to be small and of the same order, i.e., $\eta_o/h = 0[(h/\ell)^2] << 1$. Equations governing the wave motion for this special case have been developed by several authors including Boussinesq (1872) and Korteweg and deVries (1895). Since this discussion of nonlinear effects occurring during wave propagation only applies to long waves, the ratio h/ℓ must always remain much less than unity. It will also be tacitly assumed throughout this discussion that $\eta_o/h << 1$ in order to avoid the phenomenon of wave breaking which is known to occur when η_o/h approaches unity. Hence, the special case of $\eta_o/h = 0[(h/\ell)^2] << 1$ is of major importance in this study and will be discussed in more detail shortly.

The Ursell Number provides an excellent indicator for tracing the evolution of wave behavior during propagation. Suppose for the moment that a bed deformation occurs such that the wave generated is initially predicted accurately by the linear theory. Then for the wave $\eta_o/h << (h/\ell)^2$, i.e., the Ursell Number is much less than unity.

It is well known that as the wave propagates the nonlinear effects will grow and eventually they will become of the same order of magnitude as the linear effects. If the bed deformation is such that the Ursell Number for the resulting wave form is initially much greater than unity, the linear theory is invalid for all time. For this case, however, the importance of the linear effects increases relative to the amplitude dispersion terms during propagation and the Ursell Number decreases until it is again of order unity. Thus, regardless of the initial wave, the wave always evolves into a state in which the Ursell Number is of order unity during propagation in a fluid of uniform depth.

Once the Ursell Number becomes of order unity, it remains constant during further wave propagation. The region of space in the direction of wave propagation for which the Ursell Number is of order unity will be referred to as the far-field. (A discussion of wave behavior in the far-field will be given shortly.) The region of space, including the generation region, over which the Ursell Number is much less or much greater than unity will be termed the near-field. In addition, a linear near-field will be said to exist when the Ursell Number is much less than unity, and a nonlinear near-field will exist when initially the Ursell Number is much greater than unity. The existence of a linear near-field is determined by the generation parameters discussed in Section 3.2.1. The length of a linear near-field is a function of the rate of growth of nonlinearities during wave propagation.

As suggested earlier, the length, ℓ, required to characterize the linear effects of frequency dispersion, is a measure of the distance over which significant changes in wave amplitude occur. When the length is chosen properly for a wave, the ratio $(h/\ell)^2$ becomes proportional to the vertical accelerations a water particle experiences as the wave passes (see, e.g., Lamb (1932, § 172)). An excellent physical description of wave dispersion caused by vertical accelerations of fluid particles is given by Peregrine (1966) and Madsen and Mei (1969). In a periodic wave the characteristic length, ℓ, is proportional to the wave length. In a wave of complex shape, i.e., non-periodic, the characteristic length is no longer well defined and in fact no single length may exist which adequately describes the entire wave. In a wave of this type the length, ℓ, becomes a local property of various regions of the wave profile. An appropriate definition for the characteristic length, ℓ, in a region of a complex wave form is:

$$\ell = 0(\eta/\eta_x) , \tag{3.70}$$

where η_x is the slope of the wave profile. When computation requires a specific value for the length, ℓ, it may be taken as:

$$\ell = \frac{\eta_o}{\|\eta_x\|} , \tag{3.71}$$

where η_o is the maximum wave amplitude in the region of the wave under consideration and $||\eta_x||$ is defined as the maximum value of the slope of the profile in that region. Thus, the local Ursell Number for a complex wave shape may be given as:

$$\underline{U} = \frac{\eta_o^3}{h^3 \, ||\eta_x||^2} \quad . \tag{3.72}$$

In Section 3.2.1 the linear theory was found to be applicable during the interval of the bed deformation when the conditions on the generation parameters given by Eqs. (3.58) and (3.66) were satisfied. As indicated previously, the length of time after wave generation for which the linear theory remains applicable depends on the rate of growth of the nonlinear effects during wave propagation. This rate of growth depends on the generated wave form which is a function of the generation parameters discussed in the previous section.

Consider the bed deformation whose generation parameters satisfy the conditions given by Eq. (3.58). For these deformations the bed displacement can be considered to be impulsive; hence, at the end of the displacement little wave propagation has taken place. The water surface will have assumed a profile near the end of the bed movement similar to the shape of the deformed bed. Due to the elliptic nature of the fluid's response to an impulsive boundary displacement, the water surface will not move exactly as the solid boundary. This is especially true for small disturbance-size scales, b/h, as will be demonstrated in Chapter 5. It is useful, however, to assume for the moment that for small-amplitude-impulsive-displacements of the bed, the water surface at the end of the displacement is identical to the bed deformation. For a block upthrust of the bed section, the assumed water surface at the end of the displacement is shown in Fig. 3.4. If the step in the bed profile is ignored, the

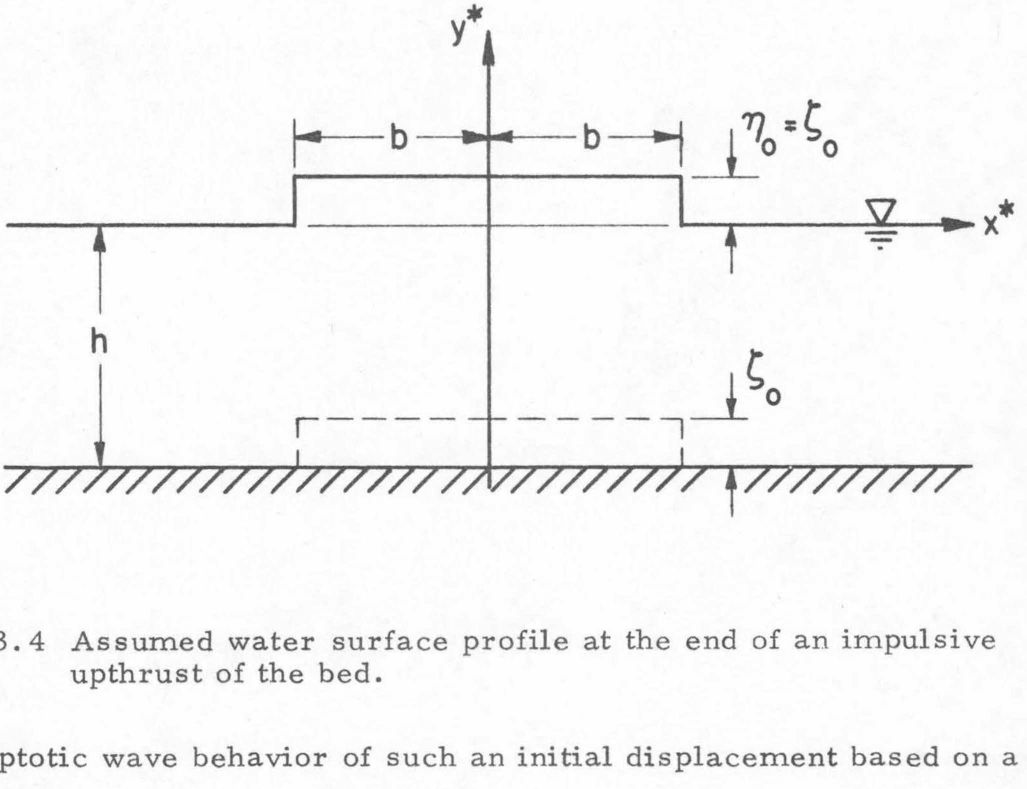

Fig. 3.4 Assumed water surface profile at the end of an impulsive upthrust of the bed.

asymptotic wave behavior of such an initial displacement based on a linear theory has been found by Jeffreys and Jeffreys (1946) to be:

$$\frac{\eta^*(x^*,t^*)}{\zeta_o} = \left[b\left(\frac{2}{t^* g^{1/2} h^{5/2}}\right)^{\frac{1}{3}}\right] \mathrm{Ai}\left[\left(\frac{2}{t^* g^{1/2} h^{5/2}}\right)^{\frac{1}{3}}\left(x^* - t^*\sqrt{gh}\right)\right], \quad (3.73)$$

where Ai [ ] is the Airy integral and all variables are dimensional. The Airy function for its argument less than zero, i. e., for $x < t^*\sqrt{gh}$, is a damped oscillation where the spacing of the nodes or the wave length decreases as the argument becomes more negative. From Eq. (3. 73) it is seen that a convenient choice of a characteristic amplitude of the wave form, η_o, and a characteristic length, ℓ, are:

$$\eta_o = 0\left[\zeta_o\left(\frac{b}{h}\right)\left(t^*\sqrt{g/h}\right)^{-\frac{1}{3}}\right] \text{ and } \ell = 0\left[h\left(t^*\sqrt{g/h}\right)^{\frac{1}{3}}\right], \qquad (3.74)$$

where t^* is the elapsed time after generation. It is noted that the choice of length, ℓ, given by Eq. (3. 74) differs from that suggested by Eq. (3. 71); however, either choice should yield values of the same order of magnitude for the Airy integral. Thus the Ursell Number behaves as:

$$\underline{U} = 0\left[\left(\frac{\zeta_o}{h}\right)\left(\frac{b}{h}\right)\left(t^*\sqrt{g/h}\right)^{\frac{1}{3}}\right]. \qquad (3.75)$$

From Eq. (3. 75) nonlinear effects are seen to grow with time as $(t^*)^{\frac{1}{3}}$. (This discussion of the growth rate of nonlinearities is essentially that presented by Ursell (1953).)

The time required for the Ursell Number to reach a specified value can be approximated from Eq. (3. 75). For instance, when the Ursell Number equals unity the linear theory is no longer applicable. The nondimensional time, ψ, after generation for this to occur is of order:

$$\psi = 0\left[\left(\frac{\zeta_o}{h}\right)^{-3}\left(\frac{b}{h}\right)^{-3}\right], \tag{3.76}$$

and the corresponding nondimensional distance, β, from the generation region is of order:

$$\beta = 0\left[\left(\frac{\zeta_o}{h}\right)^{-3}\left(\frac{b}{h}\right)^{-3}\right]. \tag{3.77}$$

Therefore, the extent of the linear near-field decreases very rapidly as the amplitude scale, ζ_o/h, or the size scale, b/h, of the deforming boundary increases. It is interesting to note that although the magnitude of the size scale alone is unimportant in determining the applicability of the linear theory, it is extremely important in determining the distance over which the linear approximation remains useful.

The far-field has been previously defined as the region of wave propagation in which amplitude dispersion has become equal in importance to frequency dispersion, i.e., the Ursell Number is of order unity. In a positive wave ($\eta_o > 0$) amplitude dispersion tends to hold the wave form together while frequency dispersion is acting to disperse the wave. Since both effects are equal in magnitude, a balance is achieved and permanent wave forms are possible. In a negative wave ($\eta_o < 0$) both amplitude and frequency dispersion act together to disperse the wave; hence, no permanent form waves are possible.

As pointed out earlier, when $\eta_o/h << 1$ and $(h/\ell)^2 << 1$ such that $\eta_o/h = 0[(h/\ell)^2]$, approximate equations governing the wave motion have been developed by several authors [see, e.g., Boussinesq (1872), Rayleigh (1876), McCowan (1891), and Korteweg and deVries (1895)].

The permanent form waves found by these authors are the solitary or cnoidal waves. The equation which Korteweg and deVries found to govern a wave propagating in the direction of increasing x^* in water of constant depth, h, is:

$$(\eta^*)_{t^*} + \sqrt{gh}\left(1+\frac{3}{2}\frac{\eta^*}{h}\right)(\eta^*)_{x^*} + \frac{1}{6}\sqrt{gh}\,h^2(\eta^*)_{x^*x^*x^*} = 0 \ , \qquad (3.78)$$

where the asterisk is again used to denote dimensional variables. (Eq. (3.78) will hereafter be referred to as the KdV equation.) Letting $\eta = \eta^*/h$, $x = x^*/h$, and $t = t^*\sqrt{g/h}$ the KdV equation may also be written:

$$\eta_t + (1+\frac{3}{2}\eta)\,\eta_x + \frac{1}{6}\eta_{xxx} = 0 \ . \qquad (3.79)$$

Another form of the KdV equation which was used by Peregrine (1966) is given as:

$$u_t + (1+\frac{3}{2}u)u_x - \frac{1}{6}u_{xxt} = 0 \ , \qquad (3.80)$$

where $u = u^*/\sqrt{gh}$ and $u^*(x^*;t^*)$ is the mean horizontal velocity of the water. The water surface elevation, η, is related to the velocity, u, to the same order of approximation by:

$$\eta = u + \frac{1}{4}u^2 - \frac{1}{6}u_{xx} \ . \qquad (3.81)$$

From the preceding discussion it is seen that when $\eta_o/h << 1$ and $(h/\ell)^2 << 1$ such that $\eta_o/h = 0[(h/\ell)^2]$ in the far-field, the KdV equation provides an appropriate description of the future wave behavior. In this investigation, a possible strategy to use when wave forms are required in the far-field is to take the linear solution which is applicable in the near-field as the input to the KdV equation. The far-field wave forms can then be found by solving the initial value problem for the KdV equation, either numerically or analytically. Due to the complexity of the algorithm of the exact solution a numerical solution has been used based on the work of Peregrine using Eqs. (3.80) and (3.81). A similar input-output approach to the solution of the KdV equation has recently been used by Zabusky and Galvin (1971).

When nonlinear and linear effects are each of order unity the above strategy fails since the KdV equation applies to small (but finite) waves only. Fortunately, this case is of little importance in the current study.

As indicated previously, when the Ursell Number is of order unity for a wave of complex shape, permanent form waves are possible. The evolution of permanent wave forms has been recently demonstrated by an extensive amount of research on the properties of the KdV equation by several authors. In a numerical study of the KdV equation Zabusky and Kruskal (1965) were able to show that solitary waves (termed solitons by the authors) of different amplitudes, and thus travelling with different celerities, were able to "pass through" one another without losing their identity. The only effect of the nonlinear interaction of two solitons was a slight shift in phase (an acceleration) of the two waves. The ability of solitons to emerge from the nonlinear interaction suggests that a complex wave form may be thought of as consisting of a finite number of interacting solitons of different amplitudes. This surprising behavior of a nonlinear physical process has been confirmed analytically by Gardner, et al (1967) who discovered a nonlinear transformation which relates the solutions of the KdV equation to the eigenvalues of the inverse scattering problem. They showed that for an initial wave profile whose net volume is finite and positive, a train of solitons will eventually evolve with decreasing amplitude toward the rear of the train followed by a spreading tail of oscillatory waves. (For an initial wave profile whose net volume is finite but negative, no solitons emerge; this case will be discussed in more detail in Chapter 5.) The amplitude and number of solitons that emerge is a function of the initial condition $\eta(x;0)$. Lax (1968) has investigated this same behavior for a class of nonlinear equations of evolution one of which is the KdV equation. A more complete discussion of the KdV equation and its properties has appeared in a series of papers authored by researchers at the Plasma Physics Laboratory, Princeton University, which are indicated by references (24), (31), (32), and (46).

3.3 RELATION OF THE DAM-BREAK PROBLEM TO IMPULSIVE BED MOVEMENTS.

In Section 3.2.1 a class of bed movements was discussed in which the deformation occurred so rapidly that the free surface near the end of the movement assumed a shape almost identical to that of the deformed bed. For a small-amplitude-bed-uplift, i.e., $0 < \zeta_o/h << 1$, a solution for the asymptotic wave behavior was presented which was based on a linear theory. Now consider the case where the uplifting bed section lies in the region $-\infty < x^* \leq 0$, and the bed displacement occurs impulsively through a distance ζ_o which is small but no longer much less than the water depth, h. The discussion of the generation parameters in Section 3.2.1 suggests that a nonlinear theory is required to describe the wave behavior. Again assuming the water surface to be identical to the deformed bed at the end of the movement, the initial water surface profile is shown in Fig. 3.5. (If the relative bed displacement, ζ_o/h, is small (but finite) then the presence of the step in the deformed bed may be ignored as a first approximation.) The wave form shown in Fig. 3.5 resembles the initial water surface profile commonly used in the classical dam-break problem; hence, further behavior of waves generated in this manner should be analogous to the waves predicted by the solution of the dam-break problem.

The dam-break problem (Stoker (1957), p. 333) consists of finding the wave generated when a barrier separating two regions of fluid of depth h and $h + \zeta_o$ is suddenly removed; thus, resulting in an initial wave profile identical to that shown in Fig. 3.5. (Note that the origin of the coordinate system is now at the bed.) The equations which are assumed to govern the motion are given by:

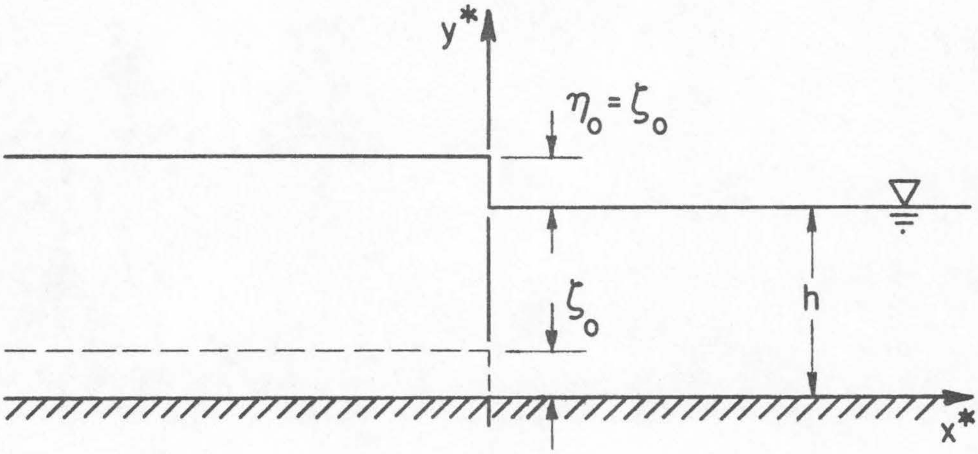

Fig. 3.5 Assumed water surface profile after an impulsive bed upthrust in the region $-\infty < x^* \leq 0$.

$$(u^*)_{t^*} + u^*(u^*)_{x^*} + g(\eta^*)_{x^*} = 0 , \tag{3.82}$$

$$[u^*(h+\eta^*)]_{x^*} + (\eta^*)_{t^*} = 0 , \tag{3.83}$$

where $\eta^*(x^*;t^*)$ is the water surface elevation above the downstream water level given by h. Eqs. (3.82) and (3.83) neglect vertical water particle motions thus eliminating the linear effects of frequency dispersion and implying a hydrostatic pressure distribution everywhere. An analytical solution of Eqs. (3.82) and (3.83) for the initial water profile shown in Fig. 3.5 is available based on the method of characteristics (see Stoker (1957)). The solution assumes that a bore (or shock) of amplitude η_o forms immediately upon removal of the barrier and then moves downstream with a constant velocity V. At the same time a negative wave moves upstream into the reservoir. Fig. 3.6 shows the water surface profile at a time t_o^* after the removal of the barrier. The fluid domain in Fig. 3.6 is divided into four regions: zone (1) downstream of the advancing bore, zone (2) containing the constant amplitude bore, zone (3) where the transition between the upstream water surface elevation and the bore occurs, and zone (4) which is the upstream quiet zone. Since regions (1) and (4) are quiet zones, the water surface elevations are the same as the initial state and the horizontal fluid velocities are zero. In regions (2) and (3) the bore amplitude, η_o, the particle velocities under the bore, u_2^*, and the bore velocity, V, are related (see Stoker (1957)) by the equations:

$$1+\frac{\eta_o}{h} = \frac{1}{2}\left(\sqrt{1+8\,(V/\sqrt{gh})^2}-1\right) \qquad (3.84)$$

$$u_2^* + 2\sqrt{gh\left(1+\frac{\eta_o}{h}\right)} = 2\sqrt{gh\left(1+\frac{\zeta_o}{h}\right)} \quad , \qquad (3.85)$$

$$u_2^* = V + \frac{1}{4}\frac{gh}{V}\left(1-\sqrt{1+8(V/\sqrt{gh})^2}\right) \; , \qquad (3.86)$$

while the water surface elevation in zone (3) is given by

$$h+\eta^*(x^*;t^*) = \frac{1}{9g}\left(2\sqrt{gh\left(1+\frac{\zeta_o}{h}\right)}-\frac{x^*}{t^*}\right)^2 . \qquad (3.87)$$

The negative wave retreating upstream is thus parabolic in form. Eqs. (3.84), (3.85), and (3.86) may be solved simultaneously for η_o, u_2^*, and V as a function of ζ_o/h. The solution of these equations for the relative bore amplitude, η_o/ζ_o, as a function of ζ_o/h is shown

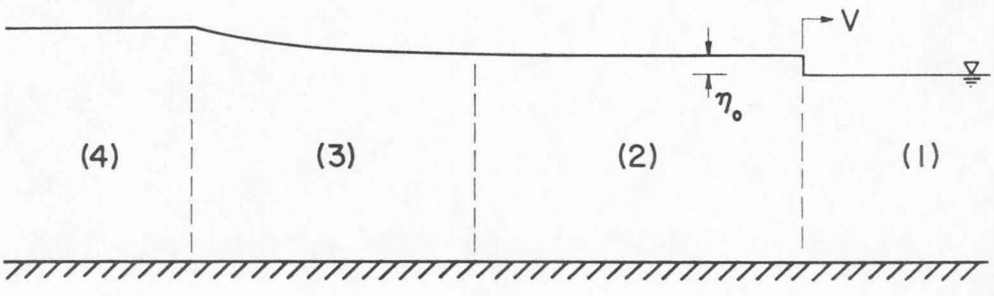

Fig. 3.6 Regions of the fluid domain after removal of the barrier.

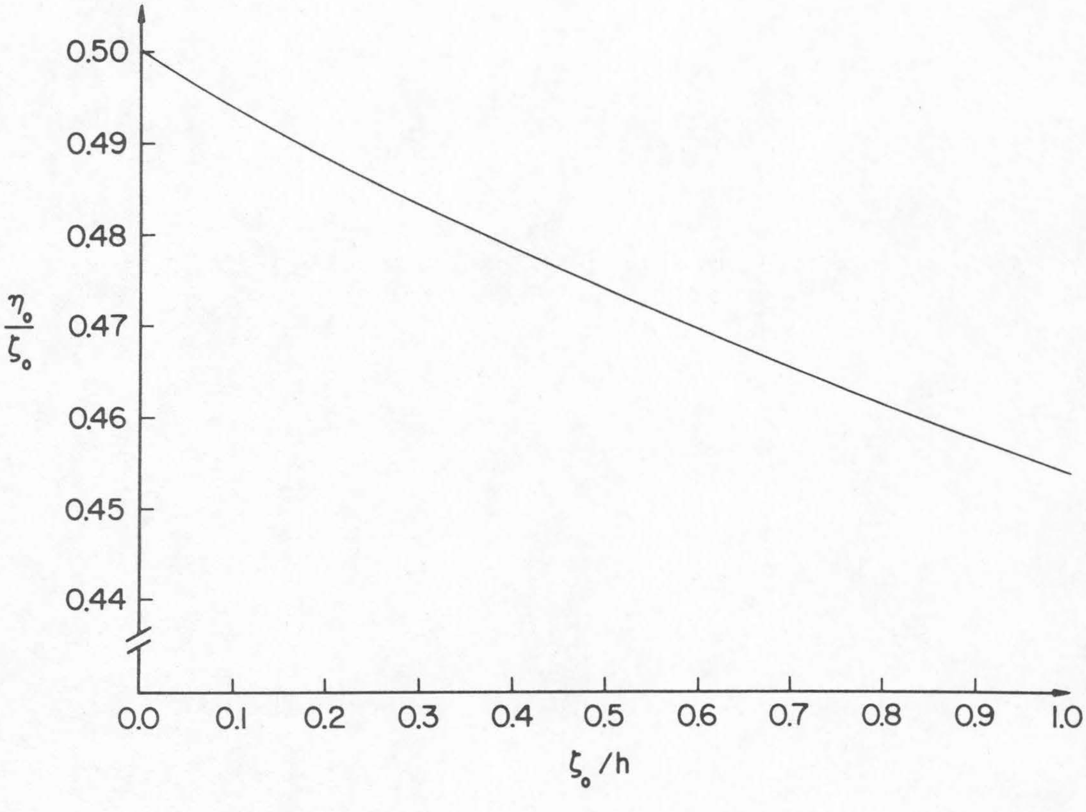

Fig. 3.7 Variation of the relative bore amplitude, η_o/ζ_o, as a function of the initial difference in water levels, ζ_o/h.

in Fig. 3.7. As the amplitude scale, ζ_o/h, becomes small, the bore amplitude becomes equal to one-half of the initial difference in water levels, i.e., $\eta_o/\zeta_o \rightarrow 0.5$ as $\zeta_o/h \rightarrow 0$. As ζ_o/h increases to unity, the relative bore amplitude decreases from 0.5 to 0.454. Since the uplifted bed section is not present in the dam-break problem, the two problems are no longer approximately analogous for large values of ζ_o/h.

When a reservoir of finite length, b, exists behind the barrier the previous discussion is limited to the time interval occurring before the negative wave, which propagates upstream from the original location of the barrier, reaches the end of the reservoir. Assuming for convenience that a vertical wall exists at the upstream end of the channel, i.e., at $x^* = -b$, the negative wave is reflected and propagates downstream in the positive x^*-direction after striking the wall. A characteristic-plane solution for this problem is shown in Fig. 3.8 where the coordinate x^* is scaled by the reservoir length, b, and time is scaled by the time required for the negative wave to reach the backwall, i.e., $t = t^*\sqrt{g(h+\zeta_o)}/b$. The water particle velocities, u_2^*, and the phase velocities, $\sqrt{g(h+\eta^*)}$, (from which the water surface elevations, $\eta^*(x^*;t^*)$, can be found) at the labelled nodes in Fig. 3.8 have been determined using standard techniques of the method of characteristics. (These values are shown in the table inset in Fig. 3.8.) The shock which is generated at the instant the barrier is removed, travels downstream along the straight characteristic C_1. The negative wave

NODE	$\frac{u_2^*}{\sqrt{g(h+\zeta_o)}}$	$\frac{\sqrt{g(h+\eta^*)}}{\sqrt{g(h+\zeta_o)}}$
1	0	1
2	$4/3d\theta$	$1-2/3d\theta$
3	0	$1-4/3d\theta$
4	$8/3d\theta$	$1-4/3d\theta$
5	$4/3d\theta$	$1-2d\theta$
6	0	$1-8/3d\theta$
7	$4d\theta$	$1-2d\theta$
8	$8/3d\theta$	$1-8/3d\theta$
9	$4/3d\theta$	$1-10/3d\theta$
10	0	$1-4d\theta$

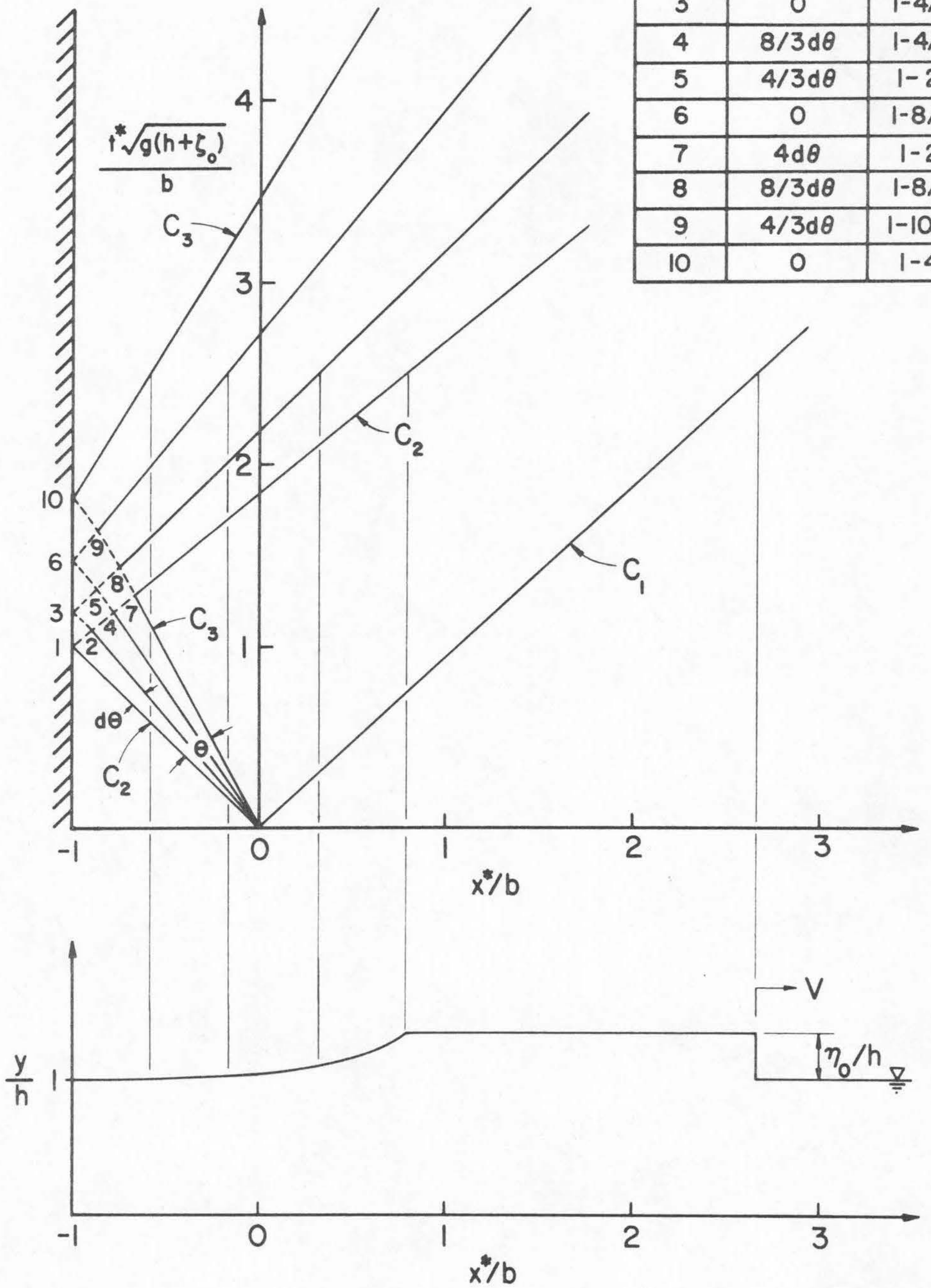

Fig. 3.8 Characteristic-plane solution of a dam-break problem with a reservoir of finite length.

propagating upstream is bounded by an expansion fan of angle θ by the characteristics C_2 and C_3. Once u_2^* and η_o are found from Eqs. (3.84) through (3.86), the angle, θ, of the expansion fan can be found. The characteristic C_2 is reflected from the backwall and interacts in a nonlinear manner with the incoming negative wave. The nonlinear interaction is evident by the curvature of the characteristics which indicate an acceleration of the negative wave until the interaction is completed. The region of the nonlinear interaction in Fig. 3.8 is indicated by the dashed portion of the characteristics. When the characteristic C_3 strikes the backwall the reflection of the negative wave has been completed. It is interesting to note that once the reflected characteristic C_2 clears the region of nonlinear interaction, at node (7), it moves downstream at a constant velocity slightly larger than the bore velocity; thus the negative wave will eventually overtake the shock front. This is true for all initial differences in water level over the range $0 < \zeta_o/h \leq 1$. (For a discussion of an expansion wave overtaking a shock see Courant and Friedrichs (1967, p. 180).)

A typical water surface profile after the reflection process has been completed, but before the negative wave overtakes the shock front, is also shown in Fig. 3.8. The bore now has a finite length, as it must, since the volume of water in the reservor is finite. The profile shown in Fig. 3.8 should be typical of waves generated by bed movements for which the dam-break analogy is applicable, at least near the generation region.

Thus, the dam-break analogy provides a convenient mechanism for investigating the effect of the bed displacement, ζ_o, and the disturbance length, b, on the generated waves for a class of deformations termed impulsive. It should be remembered that the nonlinear theory used to solve the dam-break problem is limited in its ability to predict the detailed wave structure due to the omission of frequency dispersion and viscous effects. The vertical acceleration experienced by a fluid particle is directly proportional to the curvature of the water surface. At an abrupt discontinuity in the water surface (the shock front) the curvature is infinite thus the omission of the effects of frequency dispersion is not justified. In a real (viscous) fluid diffusion of vorticity by viscosity will smooth this discontinuity. Furthermore, Binnie and Orkney (1955) have shown experimentally that when the ratio of bore amplitude, η_o, to water depth, h, exceeds 0.75 the front of the bore breaks and becomes turbulent as in the hydraulic jump. For $0.35 < \eta_o/h < 0.75$ they found that undulations formed on the bore and at least one of these broke; the undulations are the result of frequency dispersion. No breaking was observed in their experiments when $\eta_o/h < 0.35$, however, the undulations were still present.

3.4 THE THREE-DIMENSIONAL MODEL - A LINEAR THEORY.

In the previous discussions in this chapter attention has been given primarily to a simple two-dimensional model of tsunami generation, i.e., waves generated and propagating between parallel orthogonals. The real tsunami problem is generally three-dimensional with waves emanating in all directions from the disturbance. Therefore, it is of interest to investigate certain aspects of a simple three-dimensional model in order to relate the general properties of waves propagating in that type of system to those in the two-dimensional case.

Consider a three-dimensional fluid domain D with cylindrical coordinates r, z, and Θ. The fluid region is bounded above by a free surface, S_f, below by a solid boundary, S_b, and unbounded in the radial direction, i.e., $0 \leq r < \infty$. Initially the free surface and bed are located at $z = 0$ and $z = -h$, respectively. The prescribed bed movement for $t > 0$ is given by $z = -h + \zeta(r;t)$ where the bed deformation has been assumed to be axially symmetrical. The resulting water surface displacement will also be independent of the coordinate Θ and is given by $z = \eta(r;t)$. The fluid flow is again assumed to be incompressible, irrotational, inviscid, and surface energy effects are neglected. Since the flow is axially symmetrical the velocity potential, φ, is independent of the coordinate Θ. Under these conditions the mathematical description of the problem is as follows:

$$\nabla^2\varphi = \varphi_{rr} + \frac{1}{r}\varphi_r + \varphi_{zz} = 0 \qquad \text{in D,} \qquad (3.88)$$

$$\varphi_t + \frac{1}{2}(\varphi_r^2 + \varphi_z^2) + g\eta = 0 \qquad \text{on } z = \eta(r;t) , \qquad (3.89)$$

$$\varphi_z = \eta_t + \varphi_r \eta_r \qquad \text{on } z = \eta(r;t), \qquad (3.90)$$

$$\varphi_z = \zeta_t + \varphi_r \zeta_r \qquad \text{on } z = -h + \zeta(r;t) . \qquad (3.91)$$

In a manner which is similar to that presented in Section 3.1 the nonlinear problem given by Eqs. (3.88) through (3.91) is replaced by its linear approximation:

$$\varphi_{rr} + \frac{1}{r}\varphi_r + \varphi_{zz} = 0 \qquad \text{in D,} \qquad (3.92)$$

$$\varphi_{tt} + g\varphi_z = 0 \qquad \text{on } z = 0 , \qquad (3.93)$$

$$\varphi_z = \zeta_t \qquad \text{on } z = -h . \qquad (3.94)$$

The linearized equations are most easily solved using transform techniques similar to those described in Section 3.1. The appropriate transform for the radial coordinate (which ranges from zero to infinity) is the Hankel transform of zeroth order. The Hankel transform of a function f(r) is given by:

$$\hat{f}(k) = \int_0^\infty r\, J_o(kr)\, f(r)\, dr , \qquad (3.95)$$

where $J_o(kr)$ is the Bessel function of the first kind and of order zero. (The caret superscript will be used here to denote the Hankel transform.) The time variable, t, is again transformed by the Laplace transform (Eq. 3.11). Performing the necessary operations on Eqs.

(3.92), (3.93), and (3.94), the transformed problem becomes:

$$\tilde{\hat{\varphi}}_{zz}(k, z;s) - k^2\,\tilde{\hat{\varphi}}(k, z;s) = 0 \ , \tag{3.96}$$

$$\tilde{\hat{\varphi}}_{z}(k, 0;s) + \frac{s^2}{g}\,\tilde{\hat{\varphi}}(k, 0;s) = 0 \ , \tag{3.97}$$

$$\tilde{\hat{\varphi}}(k, -h;s) = s\tilde{\hat{\zeta}}(k;s) \ . \tag{3.98}$$

Solving Eqs. (3.96), (3.97), and (3.98) yields:

$$\tilde{\hat{\varphi}}(k, z;s) = \frac{-gs\tilde{\hat{\zeta}}(k;s)}{(s^2+\omega^2)\cosh kh}\left[\cosh kz - \frac{s^2}{gk}\sinh kz\right] \tag{3.99}$$

where ω^2 again is defined as: $\omega^2 \equiv gk \tanh kh$. The water surface variation is found from Eq. (3.89) after that expression has been linearized and transformed to be:

$$\tilde{\hat{\eta}}(k;s) = \frac{s^2\,\tilde{\hat{\zeta}}(k;s)}{(s^2+\omega^2)\cosh kh} \ . \tag{3.100}$$

Application of the inversion integral for the Hankel transform of zeroth order, i.e.:

$$f(r) = \int_0^\infty kJ_0(kr)\hat{f}(k)\,dk \ , \tag{3.101}$$

and the Laplace inversion integral, Eq. (3.28), to Eq. (3.100) yields:

$$\eta(r;t) = \int_0^\infty \left\{\frac{1}{2\pi i}\int_{Br.} \frac{s^2 e^{st} kJ_0(kr)\,\tilde{\hat{\zeta}}(k;s)}{(s^2+\omega^2)\cosh kh}\,ds\right\} dk \ . \tag{3.102}$$

To use Eq. (3.102) a specific bed displacement-time history must be given. For example, consider a block upthrust or downthrow of a section of the bed which is circular in planform and moves in the same exponential manner as shown in Fig. 3.2. If the radius of the moving bed section is given by r_o, then the movement is described mathematically by:

$$\zeta(r;t) = \zeta_o(1-e^{-\alpha t})H(r_o-r), \quad t \geq 0 , \tag{3.103}$$

where $H(r_o-r)$ is the Heavyside step function defined by Eq. (3.31). Transforming the bed movement by the Hankel and Laplace transforms given by Eq. (3.101) and (3.11), respectively, one obtains:

$$\tilde{\hat{\zeta}}(k;s) = \zeta_o \frac{r_o J_1(kr_o)}{k}\left[\frac{\alpha}{s(s+\alpha)}\right] , \tag{3.104}$$

where $J_1(kr_o)$ is the Bessel function of first kind and order one. Substituting Eq. (3.104) into Eq. (3.102) yields:

$$\eta(r;t) = \zeta_o r_o \int_0^{\infty} \frac{J_1(kr_o)J_o(kr)}{\cosh kh}\left\{\frac{1}{2\pi i}\int_{Br.} \frac{\alpha s e^{st} ds}{(s^2+\omega^2)(s+\alpha)}\right\} dk . \tag{3.105}$$

The integration of the bracketed quantity above is identical to the Laplace inversion integral appearing in Eq. (3.34); hence, the following expression for the wave amplitude distribution results:

$$\eta(r;t) = -\zeta_o r_o \int_0^{\infty} \frac{J_1(kr_o)J_o(kr)}{\cosh kh}\left[\frac{\alpha^2}{\alpha^2+\omega^2}\right]\left[e^{-\alpha t} - \cos \omega t - \frac{\omega}{\alpha}\sin \omega t\right] dk. \tag{3.106}$$

The integration over wave number space in Eq. (3.106) cannot be performed in closed form. Thus, numerical integration again must be used.

CHAPTER 4

EXPERIMENTAL EQUIPMENT AND PROCEDURES

In order to model the bed deformations given by Eqs. (3.30) and (3.32) in the laboratory, a wave generation system was required in which both the time-displacement history of a block section of the bed in a wave tank and the motion characteristics, i.e., ζ_o, b, and t_c, could easily be varied. A hydraulic servo-system was developed to meet these requirements. Since the wave behavior for the simple two-dimensional model of generation described in Chapter 3 is symmetric about the position $x = 0$, this position was replaced in the laboratory model by a vertical wall; hence, only one-half of the disturbance and fluid domain were modeled. In this chapter the wave tank, the hydraulic servo-system, the associated instrumentation, the actual time-displacement histories and dynamics of the moving bed section, and the range of the generation parameters (ζ_o/h, b/h, $t_c\sqrt{g/h}$ or $t_c\sqrt{gh}/b$) for which experiments were conducted are described in detail.

4.1 THE WAVE TANK.

A wave tank measuring 103.8 ft (31.6 m) long, 2 ft (61 cm) deep, and 15-1/2 in. (39.4 cm) wide was used for the experimental program. The tank is constructed of eleven separate modules, ten of which are identical; the additional module is located at one end of the wave tank and contains the moveable block section of the bed which is used to generate the waves. A schematic drawing of one of the ten similar modules of the wave tank is shown in Fig. 4.1. Details of the construction of these modules have been given previously by French (1969) and will only be discussed briefly here. The side walls of each of these ten modules are constructed of glass panels measuring 5 ft long, 25 in. high, and 1/2 in. thick. The instrument carriage rails are made of 1 in. diameter stainless steel rod and are mounted on the top flanges of the tank sidewalls with studs spaced at 2 ft intervals. The rails were carefully leveled to within 0.001 ft of a still water surface in the wave tank. A photograph of an overall view of the wave tank taken from the downstream end, i.e., the end of the tank furthest from the wave generator, is shown in Fig. 4.2.

A wave-energy dissipation system which consists of twelve individual units is located at the downstream end of the wave tank. Each unit is constructed of a sheet of rubberized hair (commonly used in the manufacture of furniture) measuring 2 in. thick with the dimensions of the tank cross-section, and held in a rack made of 1/8 in. stainless steel rod. The units are approximately equally spaced over the last 5 ft of length of the wave tank (see Fig. 4.2). Two sheets of rubberized hair are also attached to the downstream end-wall of the tank. The efficiency of this system as an energy dissipator varied appreciably over the range of water depths used in the experiments. No detailed reflection coefficients were obtained for the system, since

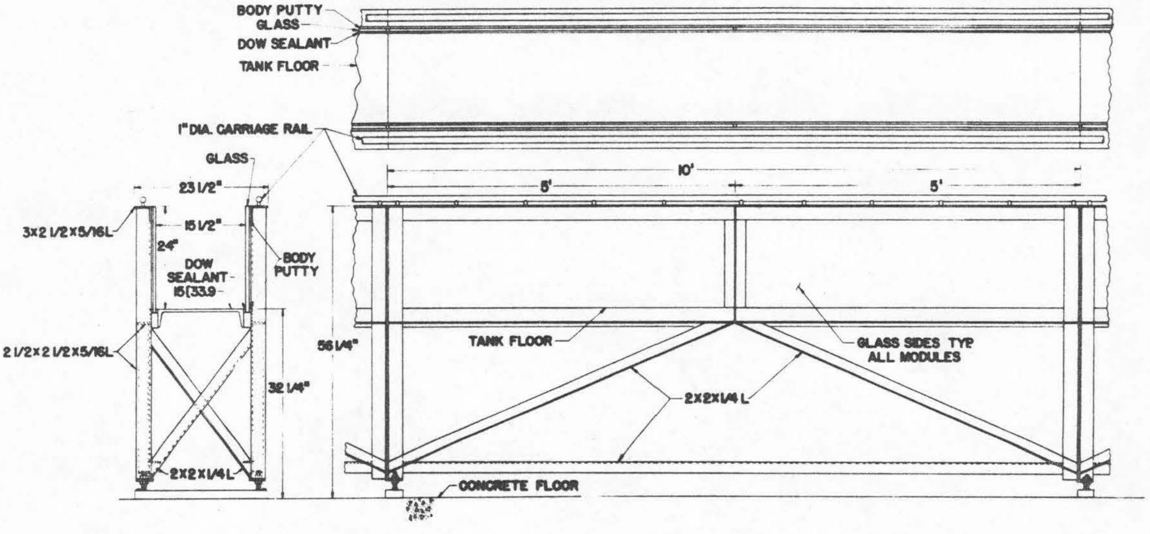

Fig. 4.1 Schematic drawing of a typical downstream tank drawing (after French (1969))

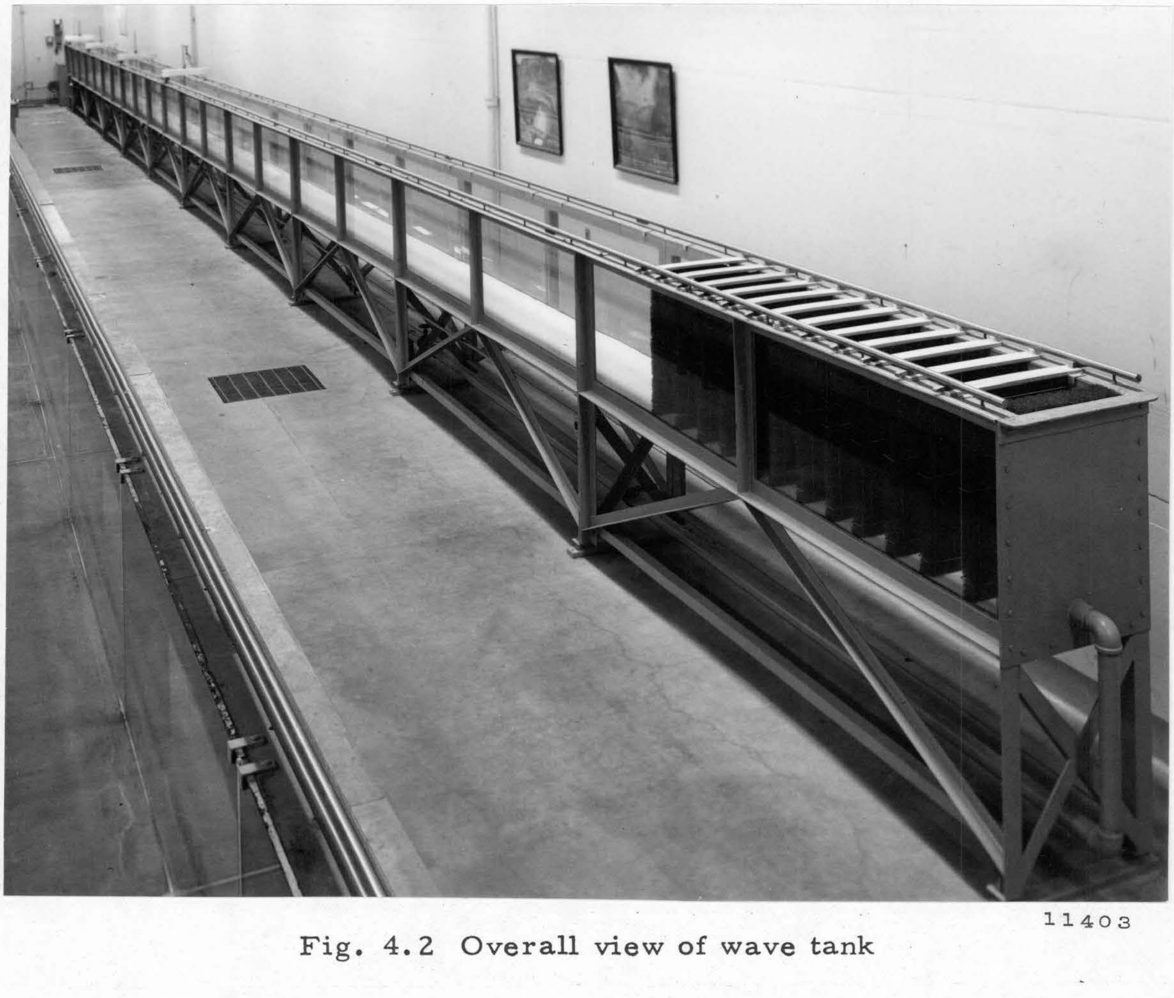

Fig. 4.2 Overall view of wave tank

the main purpose of the dissipators was to attenuate the reflected wave energy in the tank in the shortest possible time.

A schematic drawing of the tank module which was constructed to house the moveable bed section is shown in Fig. 4.3. The upstream end-wall of this module (corresponding to the position $x = 0$ in the theoretical model presented in Chapter 3) is constructed of 15 in. aluminum channel with a machined face and is mounted on four cadmimum-plated studs. Using these studs, the end-wall can be adjusted for proper vertical alignment. Adjacent to the upstream end-wall is an open section (or chamber) in the bottom of the module where the moveable bed section of the wave generator is located. (Note that the moveable bed section is shown installed in this chamber in Fig. 4.3.) The length of this chamber corresponds to the half-length, b, of the modeled bed deformation. The downstream wall of the chamber is a 1/2 in. machined aluminum plate which is also mounted to adjustable studs to facilitate alignment. The fixed portion of the bed section in this tank module, which connects to the remaining wave tank, is constructed of 15 in. aluminum channel. (All aluminum was anodized to reduce corrosion.) The fixed bed section and the downstream chamber wall are designed so that alterations in the chamber length can be made; hence, the half-length, b, of bed deformation may be varied.

The side walls of the end module shown in Fig. 4.3 are made of glass panels measuring 48 in. long, 41 in. high, and 3/4 in. thick. Thicker glass is used in this module than in the downstream tank

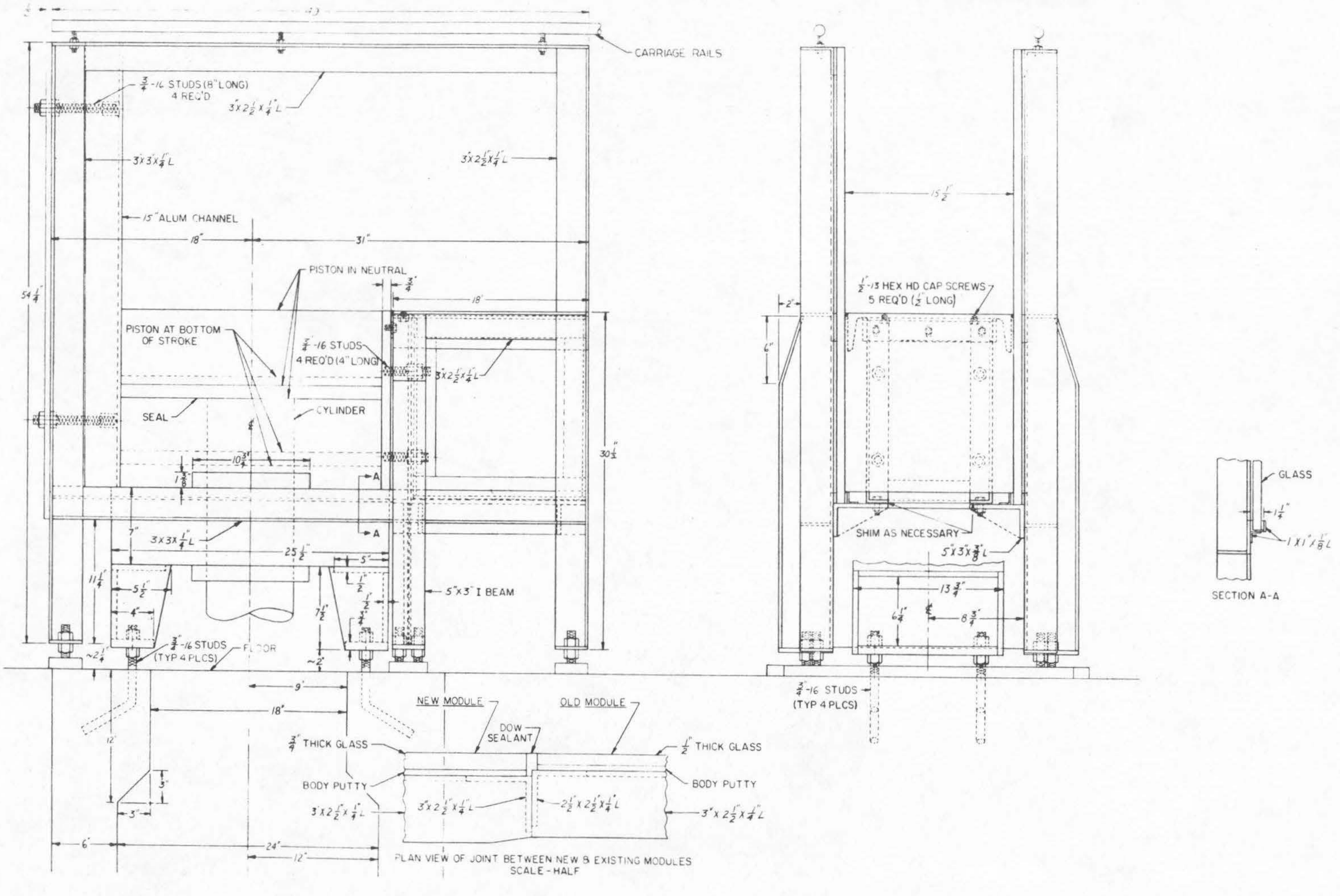

Fig. 4.3 Schematic drawing of tank module with the wave generator installed.

modules because of the larger hydrodynamic forces which occur during rapid movements of the bed section. After construction, this tank module was bolted to the existing wave tank with each leg of the module supported on bolts which were fastened to a flat steel bar bolted to the laboratory floor (see Fig. 4.3). Hence, the portion of the tank bed in this module just downstream of the chamber for the moveable bed unit could be aligned with the bed of the remaining wave tank. Instrument carriage rails were also mounted on the top flanges of this module and aligned with the rails of the main wave tank. A photograph of the end tank module after installation is shown in Fig. 4.4 with the moveable bed unit in place in the chamber.

4.2 THE WAVE GENERATOR.

The wave generator which was designed and constructed to accurately model the bed deformations discussed in Chapter 3 is driven by a hydraulic servo-system. This system accepts an input voltage and converts the input electrical signal into a mechanical displacement (which is directly proportional to the magnitude of the voltage); hence, the time-displacement history of the mechanical movement is proportional to the time-voltage history of the input signal. (A brief description of this generation system has been given by Raichlen (1970).) The system can be conveniently divided into the following sections: a moveable bed assembly, the hydraulic supply unit, and the servo-system. A schematic drawing of the entire system is shown in Fig. 4.5.

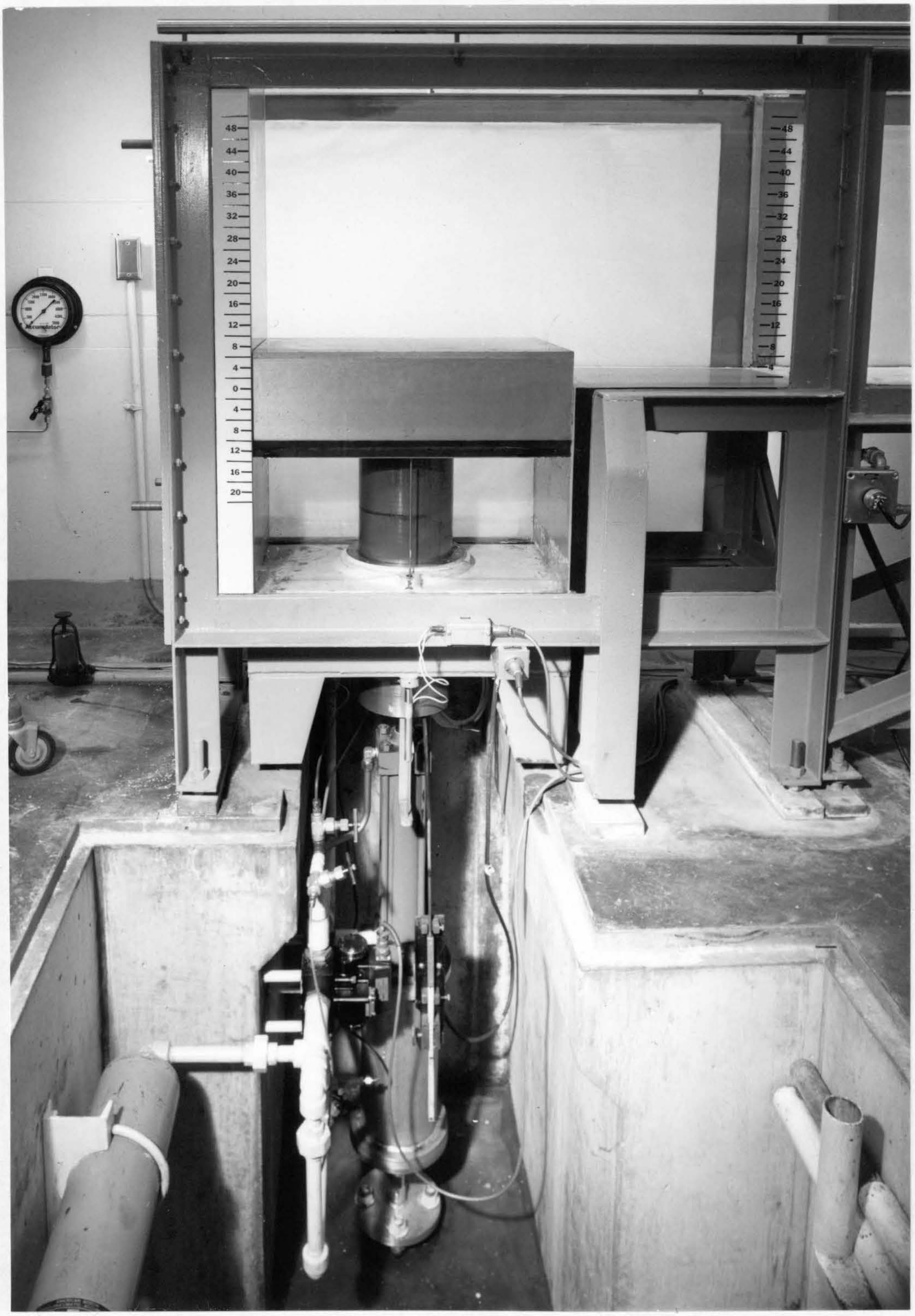

Fig. 4.4 View of the end-tank module and wave generator.

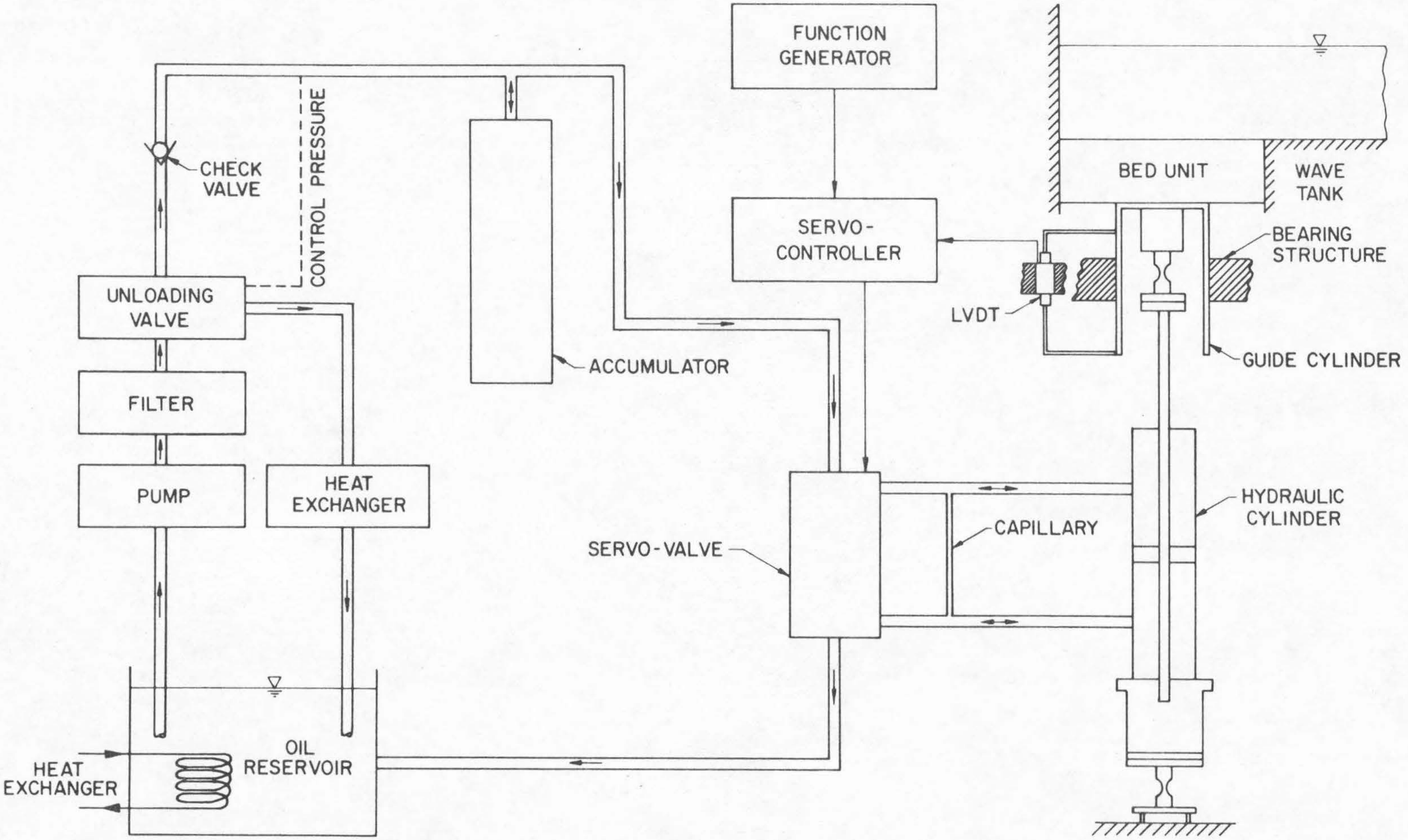

Fig. 4.5 Schematic drawing of wave generator system.

The moveable bed assembly consists of a hydraulic cylinder, its supporting structure, two flexures, a load cell, a guide cylinder, the bearing support structure, and the bed unit with its attached seal. The assembly is located in a pit beneath the end module of the wave tank (see Fig. 4.4); an "exploded" view of the assembly is shown in Fig. 4.6. The hydraulic cylinder which drives the bed unit is a double-throw type (Miller Model DH62) with a stroke of ±7 in. (±17.78 cm) and has a net piston area of 6.811 sq.in. The hydraulic cylinder is mounted vertically and attached by means of two stainless steel flexures to the floor of the pit and to the load cell. The flexures provide a means to correct for any small vertical misalignments occurring during installation. The upper portion of a load cell (BLH Electronics, Type U361) is attached to the bed unit and measures the total force applied to the bed unit. (This transducer was not used in the current study.) To insure the proper vertical movement of the bed unit, a stainless steel cylinder with a length of 2 ft and a 7-1/2 in. outside diameter was used as a guide. The guide cylinder moves between two bronze bearings located in the bearing support structure. The bearing support structure is firmly anchored to the laboratory floor beneath the end tank module as shown in Fig. 4.3. The bed unit is positioned inside the chamber of the end module of the wave tank and is bolted to the upper portion of the guide cylinder. A seal is attached to the bottom perimeter of the bed unit (see Fig. 4.3). The seals which were designed and fabricated are a single-piece unit, molded of relatively flexible material and mounted to an aluminum frame.

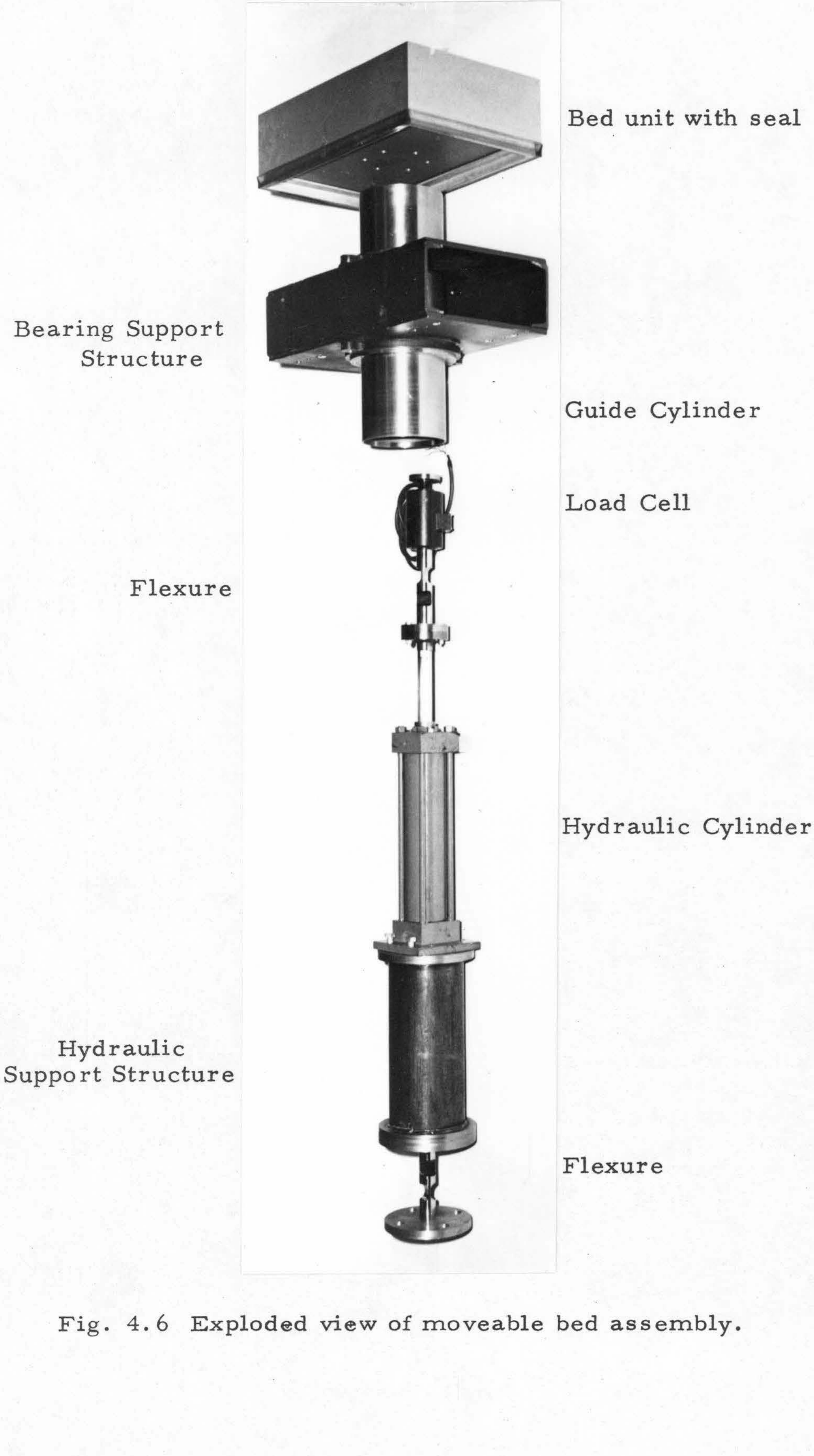

Fig. 4.6 Exploded view of moveable bed assembly.

Two bed units were used in the experimental program in order to vary the half-length, b, of the bed deformation. The longer bed unit (shown in Figs. 4.3, 4.4, and 4.6) measures 2 ft (61 cm) in length, 8 in. high, 15-1/4 in. wide, and is constructed of machined cast aluminum except for the upper lid which is made of 1/2 in. aluminum plate. The second bed unit is 1 ft (30.5 cm) in length, 8 in. high, 15-1/4 in. wide, and is constructed entirely of 1/2 in. machined aluminum plating. Both units were anodized to protect against corrosion. A seal was fabricated for each bed unit.

The hydraulic supply unit consists of a hydraulic fluid reservoir, pump, filter, unloading valve, two heat exchange units, check valve, and an accumulator. A photograph of the main portion of the hydraulic supply unit is shown in Fig. 4.7; the accumulator which is located in the pit beneath the wave tank and the water cooled heat exchanger which is located in the hydraulic fluid reservoir are not shown in this photograph. (A schematic drawing of this assembly has been shown in Fig. 4.5.) The reservoir is filled with hydraulic fluid and contains a sight gage which indicates the fluid level and temperature. A Denison, constant volume, axial-piston-type pump, rated at 2.9 gpm at 3000 psi and 2.8 gpm at 3500 psi is mounted above the reservoir; the pump is powered by a 7.5 hp, 1800 rpm electric motor. Immediately downstream of the pump is a filter constructed of stainless steel wire cloth with a nominal and absolute particle diameter rating of 5 microns and 15 microns, respectively. Downstream of the filter is an unloading valve which is followed by a check valve. The unloading

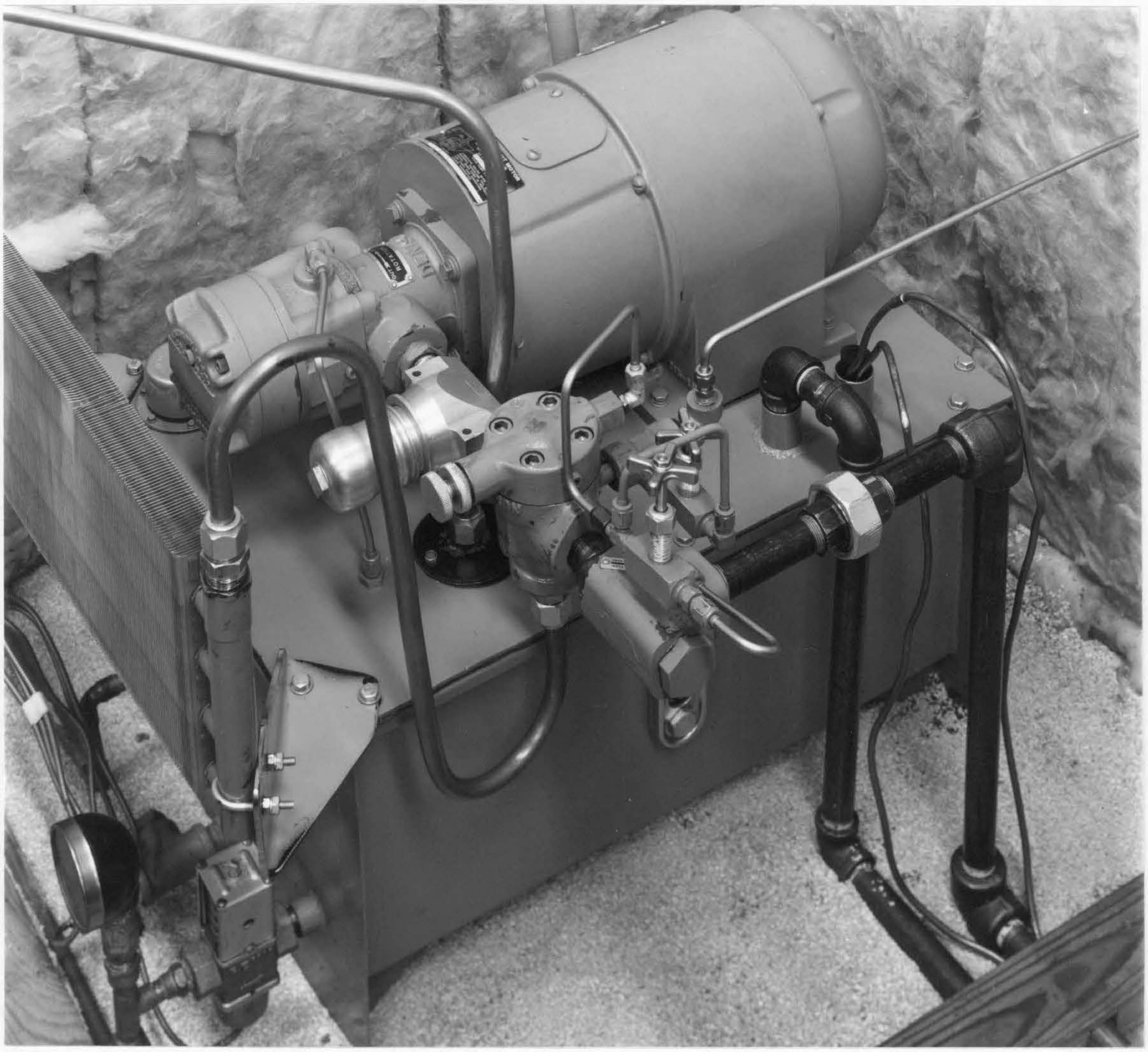

Fig. 4.7 View of the hydraulic supply unit.

valve senses the system pressure at a position downstream of the check valve; when the system pressure is below a preset value (3200 psi during normal operation) the unloading valve directs the flow of hydraulic fluid into the system. Once the desired system pressure is reached, the system side of the valve closes and the flow is diverted through an air-cooled heat exchanger (the radiator structure shown in Fig. 4.7) and back to the reservoir. The check valve prevents a reverse flow through the pump from the pressurized system when power to the pump is turned off. During normal operation the assembly shown in Fig. 4.7 is enclosed in an acoustically insulated housing that contains a fan which is used to increase the air flow through the heat exchanger.

An accumulator was installed downstream of the check valve in order to provide a sufficient volume of hydraulic fluid at high pressure to drive the moving bed unit when flow rates greater than 2.9 gpm (the pump capacity) are required. The accumulator (partially shown in Fig. 4.4 horizontally mounted to the wall of the pit) is precharged with nitrogen at 1500 psi on one side of a moveable piston. Under a system pressure of 3200 psi the nitrogen is compressed behind the piston thus permitting approximately 2-1/2 gallons of hydraulic fluid to be stored. This volume is sufficient to supply the required flow rates which occasionally reach an instantaneous value of 60 gpm for very short intervals of time.

One of the most important parts of the wave generator is the servo-system which controls the time-displacement history of the moving bed. The servo-system consists of a Moog AC/DC servo-controller (Model 82-151) and power pack (Model 82-152), a Moog servovalve (Model 72-103), a function generator designed and constructed by Dr. Haskell Shapiro, and a linear variable differential transformer.

The function generator provides a DC voltage which varies with time and is directly proportional to the desired time-displacement history of the moveable bed unit; the circuit required to produce a time-voltage history proportional to the exponential and half-sine bed movements given by Eqs. (3.30) and (3.32), respectively, is shown in Fig. 4.8. When the two selector switches in Fig. 4.8 are in position A, the output voltage varies in an exponential manner given by Eq. (3.30). The variable capacitor, CX_3, permits changes in the time scale of the exponential movement; the capacitance in microfarads corresponds approximately to the time in seconds required for two-thirds of the motion to be completed. (This relationship is the reason for the definition of the characteristic time, t_c, adopted in Chapter 3.) The maximum voltage which is approached asymptotically by the exponential time history (which corresponds to the maximum bed displacement, ζ_o) is controlled by the variable resistor, R_1. When the two selector switches are in the position, B, the output voltage varies in a half-sine manner described by Eq. (3.32). The matching variable capacitors, CX_1 and CX_2, may be adjusted to control the

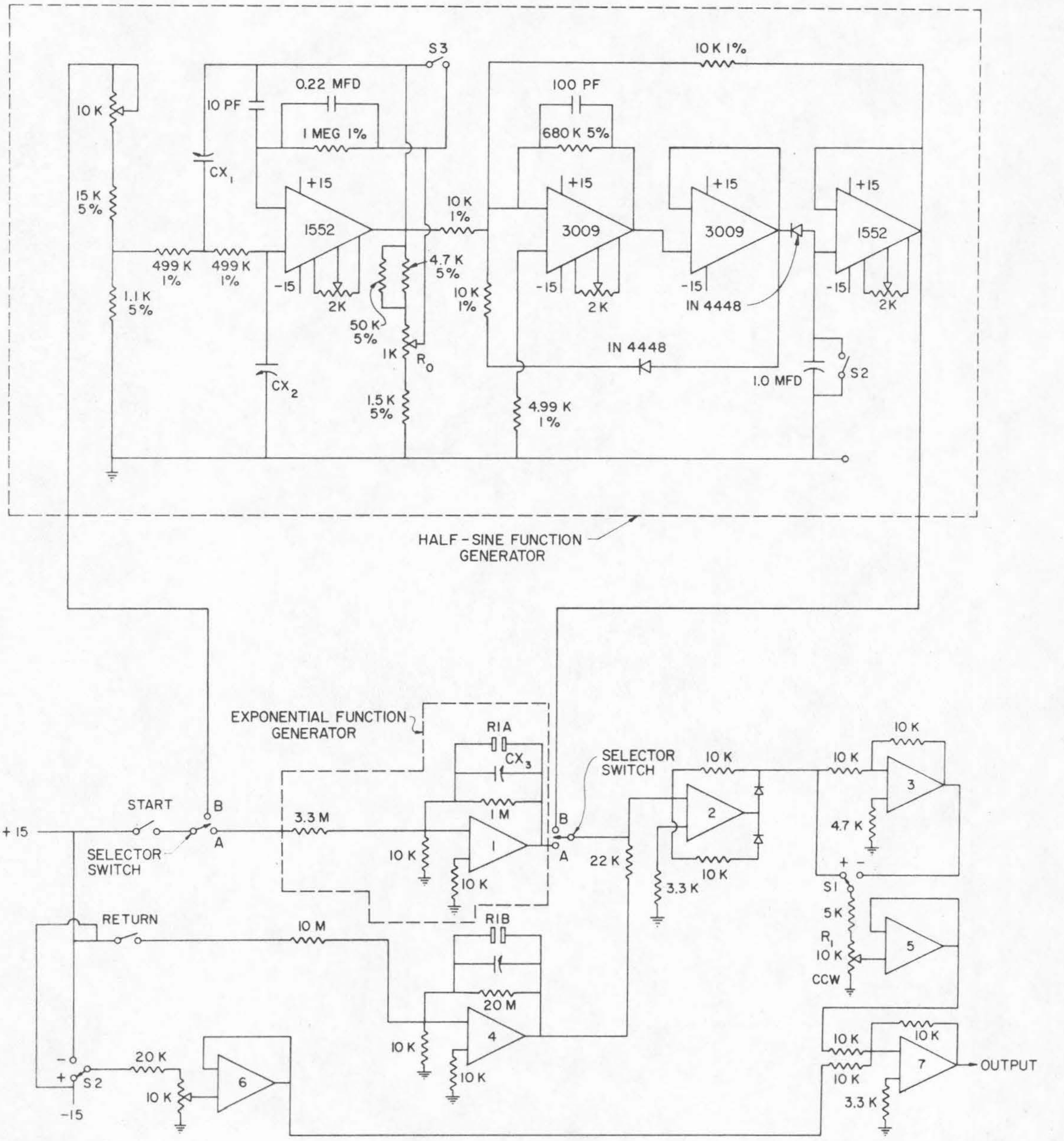

Fig. 4.8 Circuit diagram of the exponential and half-sine function generator.

total time of the movement in seconds. The total amplitude of the movement may be adjusted in the same manner as for the exponential motion by changing the variable resistor, R_1.

The servocontroller receives the electrical signal from the function generator and actuates the servovalve to vary the flow of hydraulic fluid to either side of the piston in the hydraulic cylinder; the imbalance of pressure across the hydraulic piston results in the displacement of the bed unit. The LVDT is used in conjunction with the servo-system to monitor the actual bed displacement. The servocontroller compares the actual bed displacement with the programmed motion and makes corrections in the electrical signal to the servovalve if the bed unit is not moving properly. In this manner the time history of the mechanical displacement is corrected within the limitations of the ability of the mechanical system to respond to the electrical signal. (This response will be discussed in Section 4.3.)

The electrical signal from the LVDT is also recorded on a multi-channel Consolidated Electronics Corporation (Model 5-124A) recording oscillograph after first being amplified by a Dynamics (Model 6450) differential DC amplifier. (The recording speeds of the oscillograph range from 0.625 cm/sec to 160 cm/sec; hence, detailed measurements of very rapid bed movements are possible.) The LVDT was calibrated by moving the bed a known distance and recording the electrical signal from the LVDT on the oscillograph. A typical calibration curve of the LVDT is shown in Fig. 4.9. The LVDT was

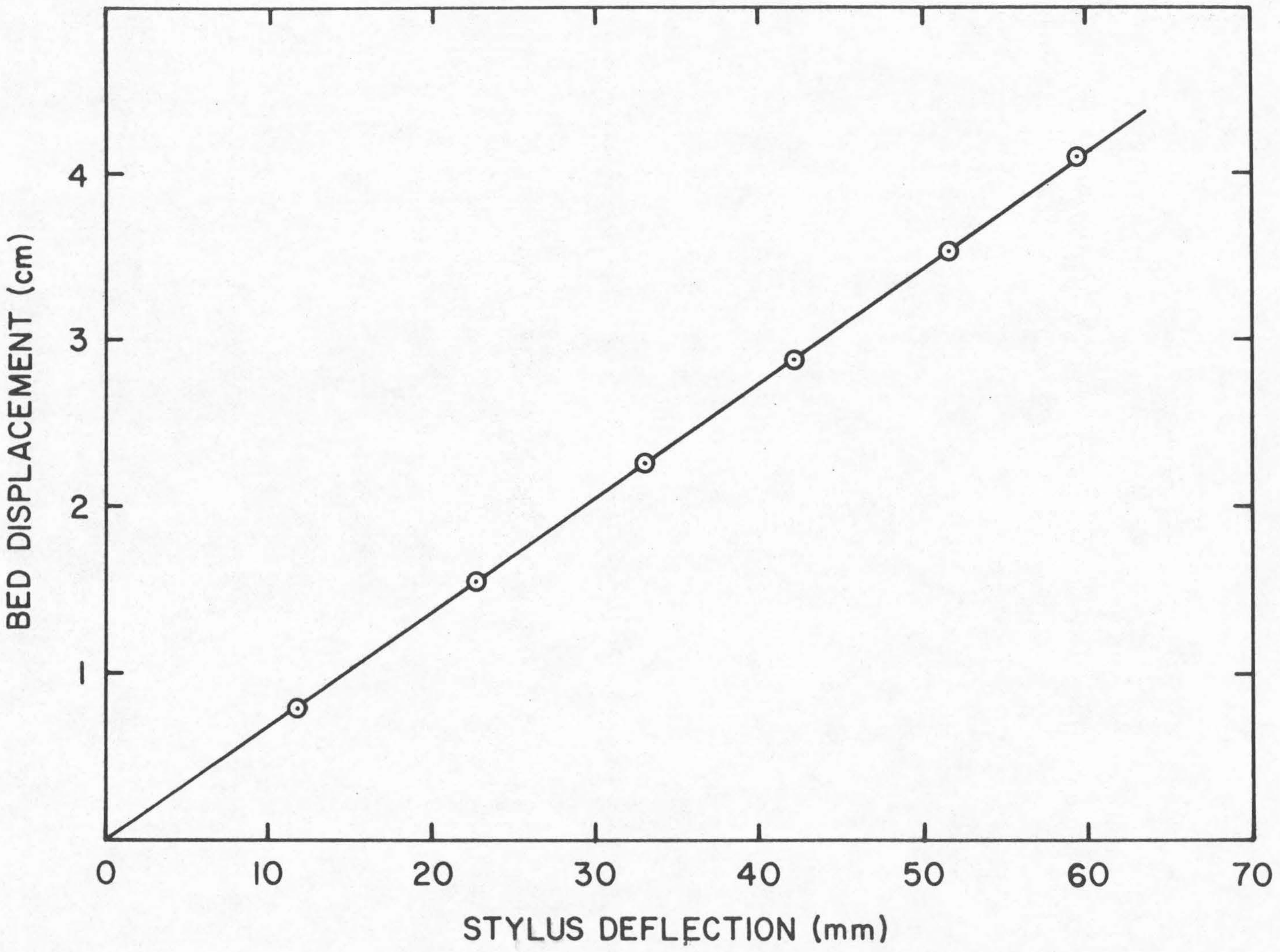

Fig. 4.9 Typical calibration curve of the linear variable differential transformer.

found to be a highly reliable motion transducer maintaining its linearity over the full range of displacements used in this study.

4.3 THE RESPONSE OF THE WAVE GENERATOR.

The hydraulic servo-system is limited in its performance by the ability of the mechanical system to respond to the programmed electrical signal. In order to check the performance of the wave generator over a wide range of programmed time scales, the frequency response of the mechanical-electrical system was determined. A sinusoidal voltage of constant maximum amplitude and variable frequency (up to a maximum of 40 cps) was used as input to the servo-controller. The response of the moveable bed unit to this signal was then determined from the recorded output of the LVDT. The damping in the system may be varied electrically to change the response characteristics of the entire wave generator. Response curves obtained at three different values of the electrical damping are shown in Fig. 4.10 where the total bed displacement, ζ_t, normalized with respect to the total bed displacment for a frequency approaching zero, ζ_{t_0}, is shown as a function of the forcing frequency. (The experimental curves placed through the measured data are to be considered only as suggested response curves.) The short-dashed curve represents the system response for the smallest electrical damping; amplification of the bed motion appears to occur at 1.5 cps and 20 cps for this damping. As the electrical damping is increased, these resonant peaks disappear. The solid curve shown in Fig. 4.10 represents the system behavior at

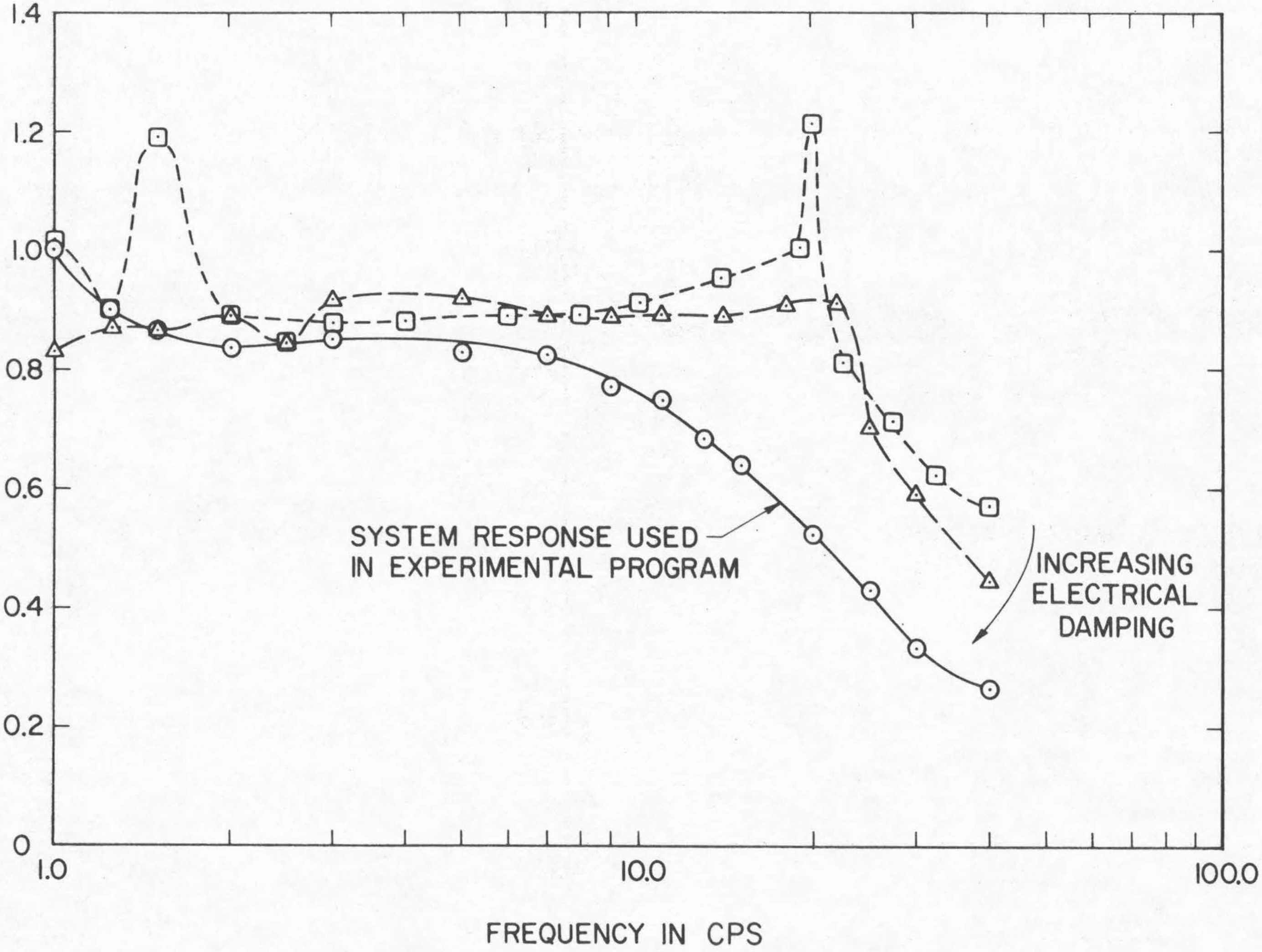

Fig. 4.10 Frequency response of the wave generator system.

a damping which was found to yield the best overall performance of the wave generator; this damping was adopted for use throughout the experimental program.

In addition to monitoring the bed unit displacement on the recording oscillograph, the electrical signal from the function generator was also monitored. Since the calibration curve of the LVDT output is linear, the side-by-side measurement of programmed and actual bed movement provides an easy performance check of the wave generation system. Two examples of the system performance for the exponential bed displacement are shown in Figs. 4.11a and 4.11b where the programmed and actual bed displacements, ζ, are shown as a function of time. (Note that the electrical signals from the LVDT and function generator in each figure have been scaled so that they cause the same total stylus deflection.) The characteristic time, t_c, of the programmed movement shown in Fig. 4.11a is 0.250 secs. (Recall that $t = t_c$ when $\zeta/\zeta_o = 2/3$ for the exponential bed displacement; the manner in which t_c is determined from the LVDT output will be discussed shortly.) The actual bed movement in Fig. 4.11a appears to lag the programmed signal by approximately 0.01 secs. The actual bed motion in Fig. 4.11a closely resembles the programmed movement except initially where some discrepancies are observed. These discrepancies are caused by the discontinuity in the bed velocity of the exponential time history at $t = 0$. The mechanical system smoothes this discontinuity in accordance with the response shown in Fig. 4.10.

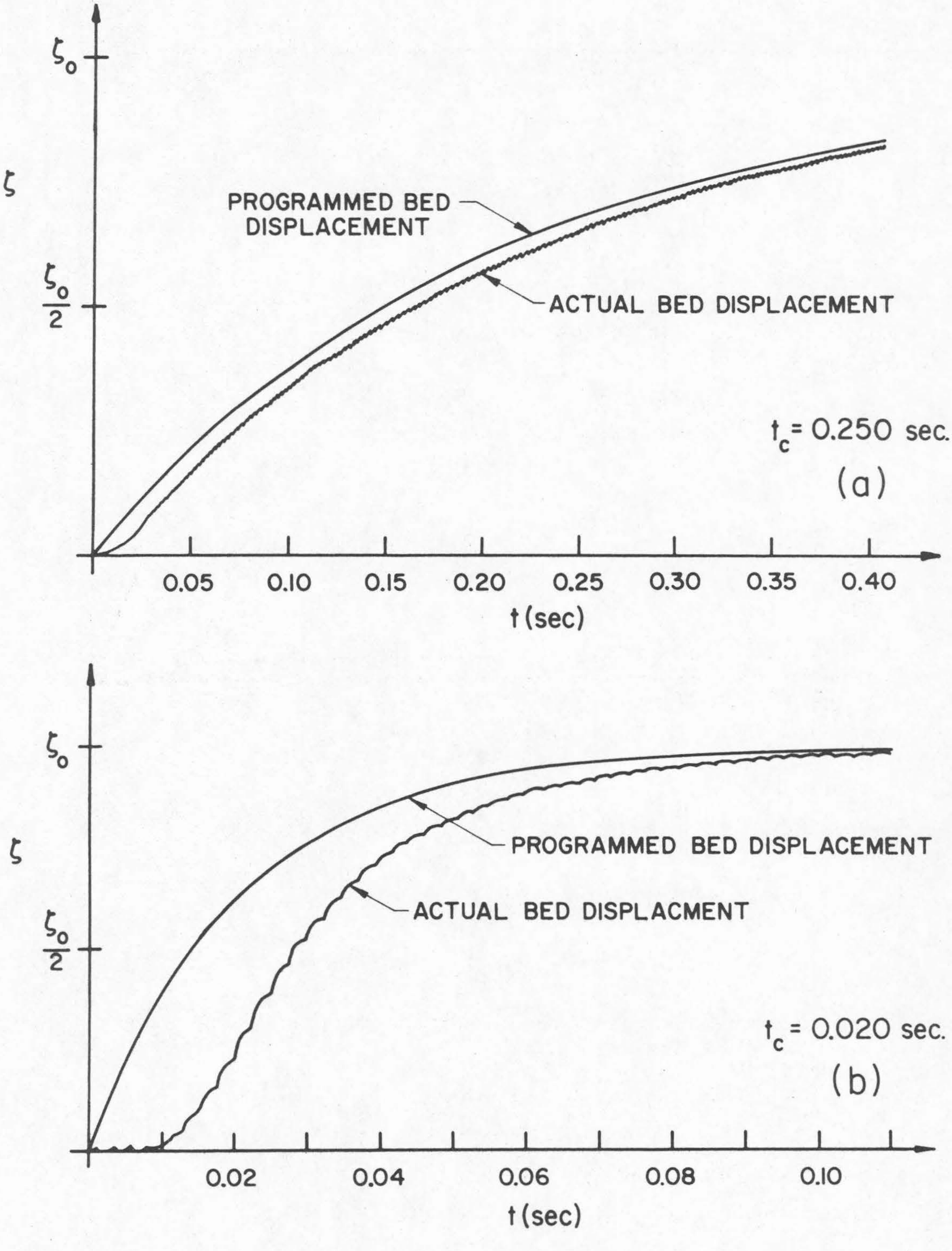

Fig. 4.11 Examples of programmed and actual exponential bed displacements.

This smoothing process requires approximately 0.01 secs after motion of the bed has begun. The high frequency oscillation in the electrical signal from the LVDT (the actual bed displacement) is a result of the 400 cps electrical signal used to excite the LVDT. The presence of this signal did not affect the bed movement since the mechanical system cannot respond to a frequency of this magnitude.

As the characteristic time of the exponential bed displacement is increased to values larger than $t_c = 0.250$ secs, the agreement between the programmed and actual bed displacements improves. As the characteristic time decreases, the differences between programmed and actual motions become more pronounced since the initial smoothing of the discontinuity requires a larger period of time relative to t_c. This type of behavior is demonstrated in Fig. 4.11b where simultaneous measurements of the LVDT and function generator output for an exponential bed displacement with $t_c = 0.020$ secs are shown. For this movement the smoothing of the initial discontinuity requires approximately 0.012 secs; hence, the programmed and actual bed movements are dissimilar for more than 50% of the characteristic time. Because of this behavior no experiments were conducted for the exponential bed displacements with a characteristic time, t_c, less than 0.073 secs.

Side-by-side measurements of actual and programmed time histories of two half-sine bed displacements are shown in Figs. 4.12a and 4.12b. The characteristic time, t_c, of the programmed motion

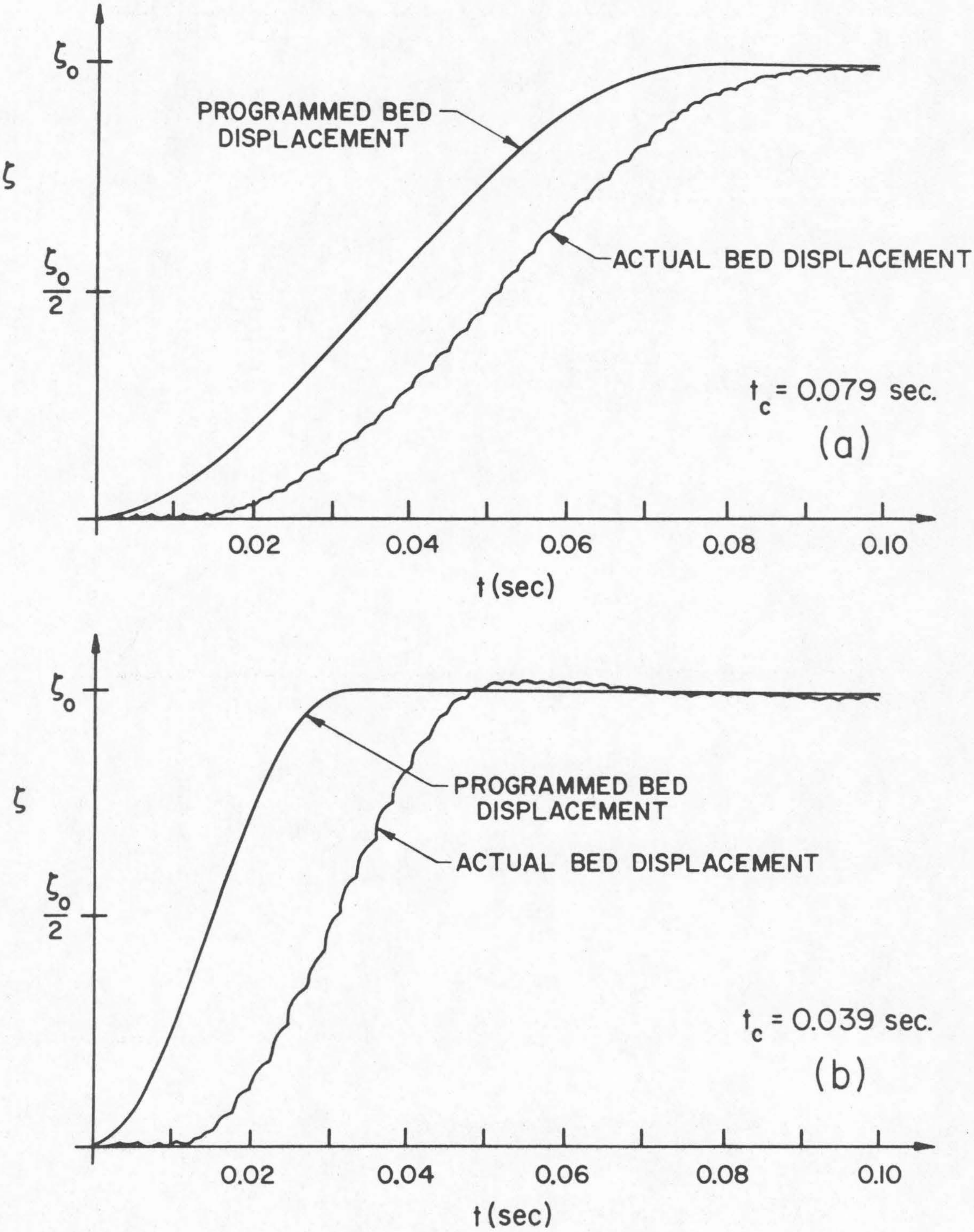

Fig. 4.12 Examples of programmed and actual half-sine bed displacements.

in Fig. 4.12a is 0.079 secs. (Recall that the characteristic time of the half-sine motion has been taken as the total time of movement; the determination of this time from an actual motion record will be discussed shortly.) The bed movement is again observed to lag the programmed movement by approximately 0.01 secs. Except for the presence of this lag, the actual and programmed motion appear to be similar. (The oscillations observed on the actual bed motion are caused again by the 400 cps electrical signal used to excite the LVDT.)

No discontinuity exists in the slope of the half-sine bed displacement given by Eq. (3.32); however, in accordance with the system response, the actual motion of the bed becomes distorted as the characteristic time of the displacement becomes very small. This is illustrated in Fig. 4.12b where the simultaneous recordings of the programmed and actual bed motion are shown for a programmed motion with a characteristic time of 0.039 secs. The bed unit is not able to reach the velocities required by the programmed motion and the bed unit overshoots the total programmed displacement. In order to avoid this behavior, no experiments with half-sine bed displacements were conducted with a characteristic time of less than 0.043 secs.

In addition to the frequency limitations of the wave generator, the response is also limited by the total displacement, ζ_o, of the programmed motion. Although a maximum stroke of ±17.78 cm is provided by the hydraulic cylinder, it was found that the actual bed displacements deviated from the programmed movements when ζ_o

exceeded ±6 cm for rapid bed motions. This type of behavior is caused by the increase in the required velocities and accelerations as the total displacement increases for a constant characteristic time. Hence, a maximum bed displacement of ±6 cm was used in the experimental program for rapid movements. Larger total displacements could be used for slow bed movements; however, the total displacement never exceeded ±10 cm.

In accordance with the limitations of the experimental equipment, the range of the generation parameters (ζ_o/h, b/h, $t_c\sqrt{g/h}$ or $t_c\sqrt{gh}/b$) used in the experimental program are shown in Table 4.1 for both the exponential and half-sine bed displacements. The disturbance-amplitude scale never exceeds ±0.2, i.e., $|\zeta_o/h| \leq 0.2$, for the three smaller disturbance-size scales of $b/h = 0.61$, 1.22, and 2.03. For $b/h = 6.10$ a bed displacement up to 50% of the water depth was used; for the largest size scale, i.e., $b/h = 12.2$, the bed unit could be displaced over the full depth, i.e., $|\zeta_o/h| \leq 1.0$.

Although the characteristic time of the programmed exponential or half-sine bed movement could be determined approximately from the capacitance used in the circuit (see Fig. 4.8), the actual characteristic time was computed from the LVDT output for each movement. In order to determine t_c for the exponential motion, the actual time-displacement history is plotted on semi-log paper as shown in Fig. 4.13a where the ordinate is given by $1 - \zeta/\zeta_o$ and the abscissa represents the time elapsed from the beginning of the bed displacement.

b/h	b	h	EXPONENTIAL						HALF-SINE					
			$\|\zeta_o/h\|$		$t_c\sqrt{g/h}$		$t_c\sqrt{gh}/b$		$\|\zeta_o/h\|$		$t_c\sqrt{g/h}$		$t_c\sqrt{gh}/b$	
	(cm)	(cm)	MIN	MAX	MIN	MAX	MIN	MAX	MIN	MAX	MIN	MAX	MIN	MAX
0.61	30.5	50	0.100	0.100	0.270	12.3	0.443	20.18	0.100	0.100	0.470	6.38	0.771	10.45
1.22	30.5	25	0.100	0.200	0.450	22.2	0.369	18.20	0.040	0.100	0.477	2.04	0.395	1.67
	61.0	50	0.010	0.200	0.208	55.8	0.171	45.80	0.010	0.200	0.323	79.00	0.265	64.80
2.03	61.0	30	0.010	0.200	0.274	70.8	0.135	34.90	0.010	0.200	0.417	92.90	0.208	45.70
6.10	30.5	5	0.400	0.500	0.853	95.0	0.140	15.58	0.200	0.400	69.300	185.00	11.400	30.40
	61.0	10	0.050	0.500	0.424	118.0	0.070	19.35	0.050	0.500	0.671	176.00	0.110	28.80
12.2	61.0	5	0.100	1.000	0.756	168.0	0.062	13.80	0.100	1.000	1.092	275.00	0.090	22.50

Table 4.1 Range of generation parameters (and corresponding water depths) used in the experimental investigation.

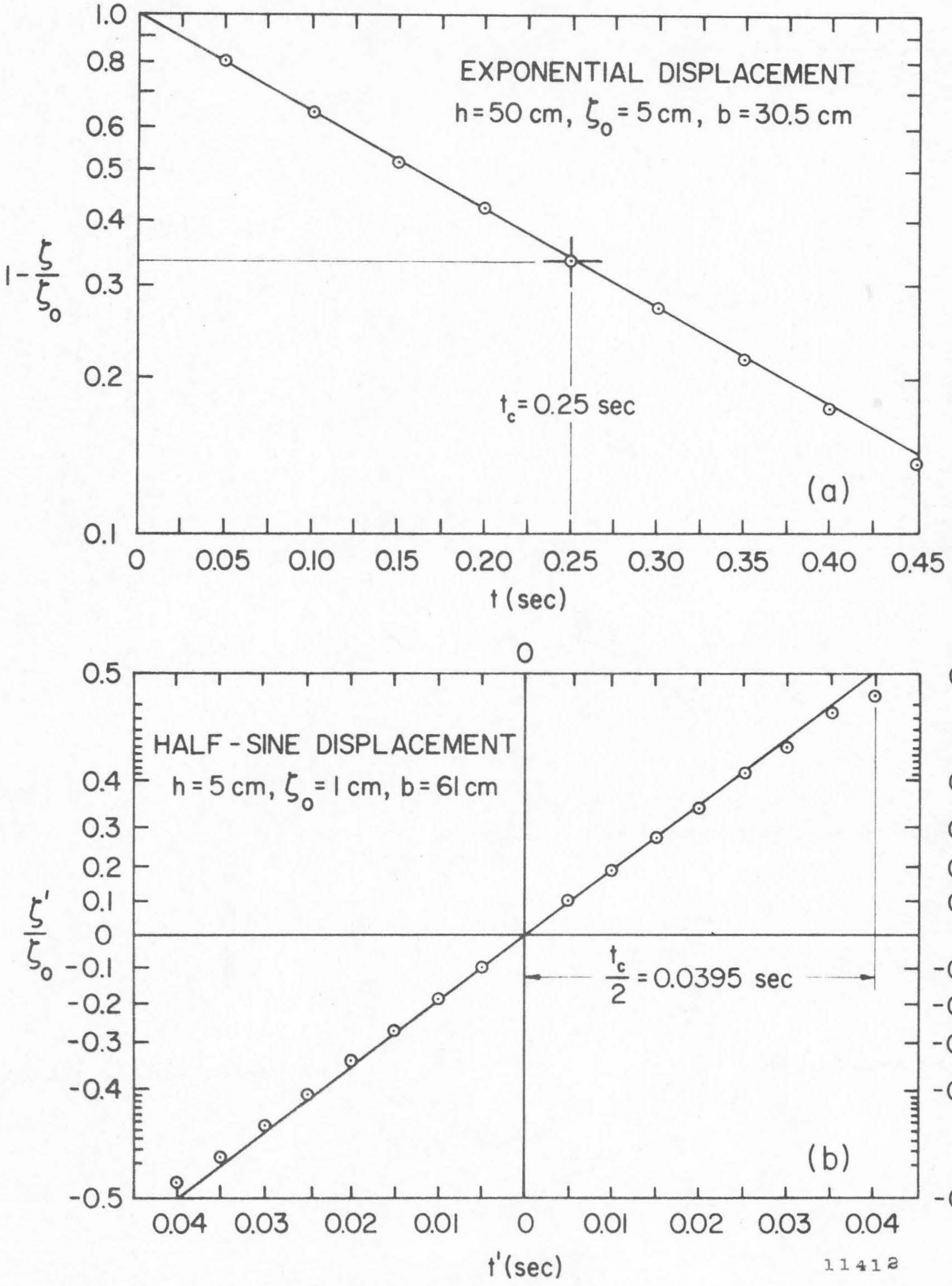

Fig. 4.13 Determination of actual characteristic times; a) exponential bed displacement, b) half-sine bed displacement.

The data shown in Fig. 4.13a have been determined from the actual bed movement shown in Fig. 4.11a; note that a large water depth, $h = 50$ cm, a large total displacement, $\zeta_o = +5$ cm, and the smaller bed unit ($b = 30.5$ cm) were used for this movement. Once the data for the actual motion are determined, a straight line is fit to the data and the characteristic time, t_c, is found at $\zeta/\zeta_o = 2/3$ or $1 - \zeta/\zeta_o = 1/3$ (see Fig. 4.13a).

For the half-sine bed displacement, the characteristic time is determined by plotting the actual motion on a special paper where the half-sine motion between $t = 0$ and $t = T$ plots as a straight line. Fig. 4.13b shows the half-sine movement of the experimental record shown in Fig. 4.12a plotted in this manner. (Note that a small water depth, $h = 5$ cm, a small total displacement, $\zeta_o = +1$ cm, and the larger bed unit ($b = 61$ cm) have been used in this experiment.) The data in Fig. 4.13b are determined by first finding the position on the actual experimental record at which one-half of the motion has been completed (see Fig. 4.12a). This position becomes the origin from which the bed displacement, ζ', and time, t', are measured; hence, ζ' and t' are negative for the motion which occurs during the first half of the displacement. Once ζ' has been normalized with respect to the total bed displacement, ζ_o, and plotted as a function of t', a straight line is fit to the data from which the characteristic time, t_c, is easily determined (see Fig. 4.13b).

4.4 THE MEASUREMENT OF WAVE AMPLITUDES.

Resistance wave gages are used in conjunction with the Sanborn (150 Series) recorder in order to measure wave amplitudes as a function of time at a specific location in the wave tank. A drawing of a typical wave gage is shown in Fig. 4.14. The wave gage consists of two stainless steel wires 3.25 in. long with a diameter of 0.01 in., and spaced 0.16 in. apart. The wires are stretched taut and parallel in a frame constructed of 1/8 in. diameter stainless steel rod. The wires are insulated electrically from each other in the frame, however, a current can pass between the wires when they are immersed in a conducting fluid. The wave gage is mounted on a point gage which is attached to an instrument carriage resting on the stainless steel rails which are mounted to the walls of the wave tank. A Sanborn Carrier Preamplifier (Model 150-1100 AS) is used to supply the 2400 cps/4.5 volt excitation for the gages as indicated by the circuit diagram in Fig. 4.15. The output signal from the wave gage is also received by the Carrier Preamplifier which after demodulation and amplification is displayed on the recording unit. As the immersion of a wave gage is varied in a conducting solution, the resistance in the circuit changes proportionally, causing an imbalance in the full bridge circuit shown in Fig. 4.15; this imbalance is recorded as a change from the balanced position.

Before the wave gage is calibrated the full bridge circuit must be balanced at a fixed gage immersion. The gage is then immersed

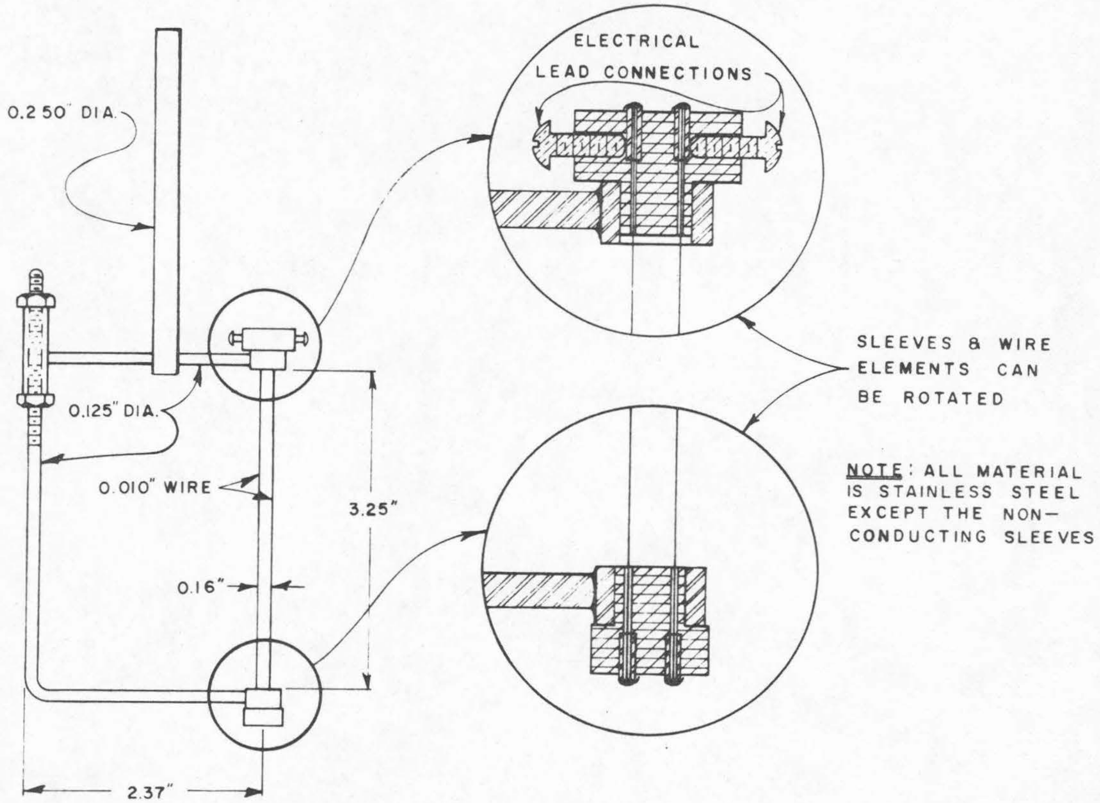

Fig. 4.14 Drawing of a typical wave gage (after Raichlen (1965)).

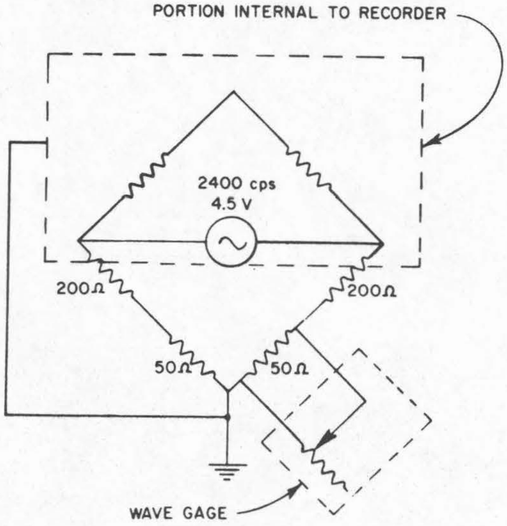

Fig. 4.15 Circuit diagram for wave gages (after Raichlen (1965)).

and withdrawn a known distance from the balanced position and the deflection of the stylus is noted. This procedure is repeated for various immersions and withdrawals, and a typical calibration curve which results is shown in Fig. 4.16. Every wave gage is calibrated before each experiment; however, no calibration curves were obtained at the end of the experiment, since each experiment was completed within minutes of the initial calibration.

Wave profiles were normally recorded at five locations in the wave tank during the experiments; two wave gages were positioned over the moving bed section and three gages were located downstream of the bed section. Over the bed unit the waves were measured at the end-wall ($x/h = 0$) and at the leading edge of the moving bed section ($x/h = b/h$). The downstream positions were varied according to the water depth such that the entire wave profile could be recorded at each position before the wave reflected from the end of the tank and returned to distort the generated wave pattern. Table 4.2 shows the wave gage

b/h	(x-b)/h				
0.61	-b/h	0	10	20	30
1.22	-b/h	0	10	20	30
2.03	-b/h	0	20	30	60
6.10	-b/h	0	20	60	180
12.22	-b/h	0	20	180	400

Table 4.2 Wave gage locations for each disturbance-size scale used in the experimental investigation.

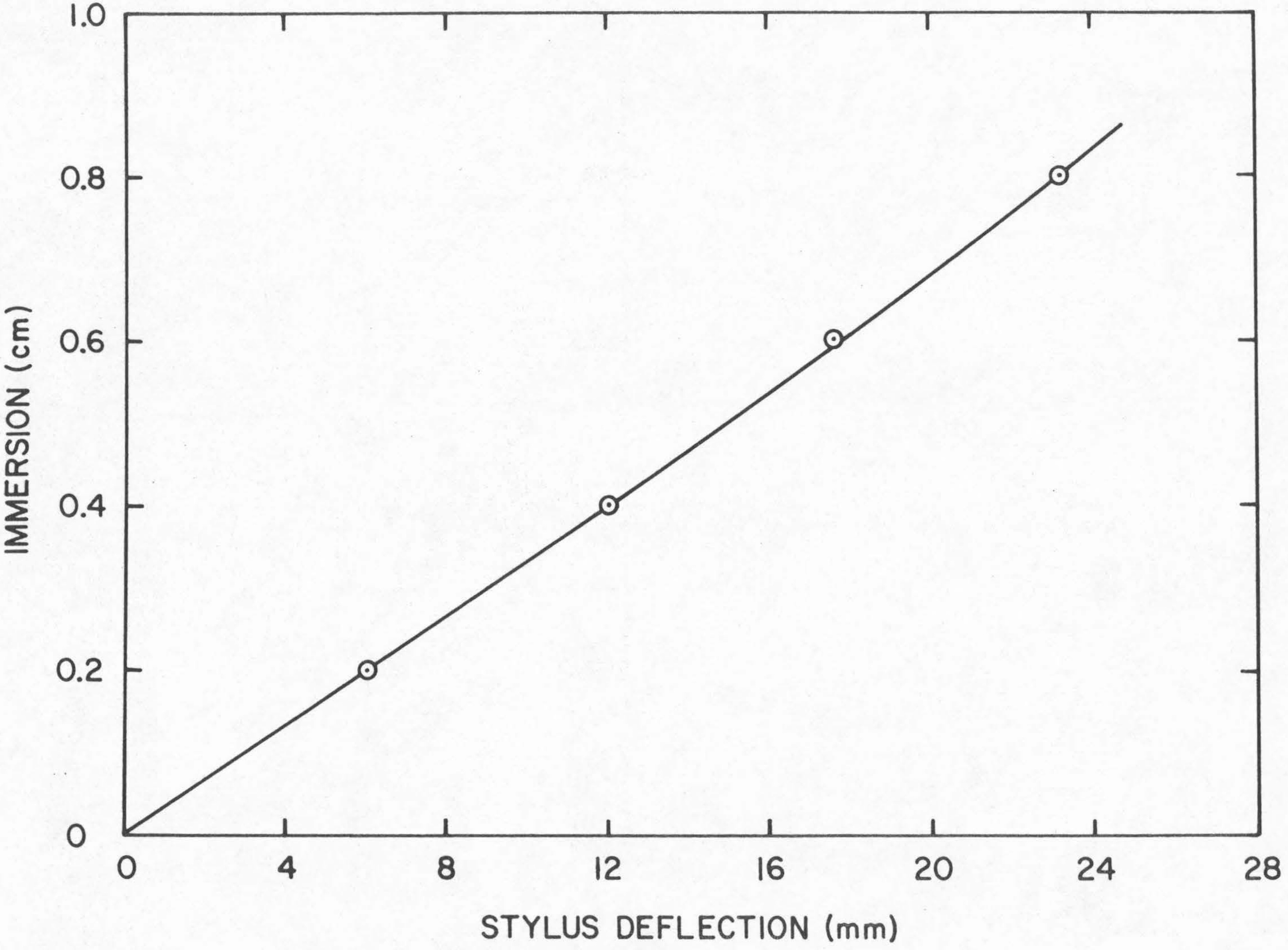

Fig. 4.16 Typical calibration curve of a wave gage.

positions for each of the five disturbance-size scales, b/h, for which experiments were conducted. Note that the wave gage locations are arranged such that two adjacent values of disturbance-size scale have four positions in common. The wave measurements at $x/h = 0$ (or $(x-b)/h = -b/h$) were by necessity obtained approximately 1 cm in front of the tank end-wall. Obviously, measurements at this position could not be made in experiments for which the bed unit displacement was positive and equal to the water depth. For this case, also, wave recordings at the leading edge of the bed section were made about 1 cm downstream of the uplifting bed unit.

In addition to these Eulerian measurements of wave profiles, i.e., the observation of the change in wave height with time at a fixed spatial location, a photographic system was constructed to enable Lagrangian measurements of the water surface movement to be made near the moveable bed section. These Lagrangian measurements permitted the spatial distribution of the wave amplitudes to be observed at a fixed time.

The photographic system consists of an adjustable point gage with an attached micro-switch, a time-delay mechanism, two gas-discharge flash lamps, and a camera. The point gage is mounted on the support structure of the moveable bed assembly in a manner such that a cam attached to the guide cylinder could trip the micro-switch when the cylinder movement reaches a preset position of the point gage. The micro-switch closes an electrical circuit which activates the time-delay device. The time-delay device could be adjusted to activate the lamps after a time interval of zero to three seconds; adjustments of this mechanism could be made in 0.05 sec intervals. A camera is positioned in front of the generation region with the shutter open so that the lamp flash imprints the picture on the film. Hence, the water surface location in the region of generation can be photographed at any time after the bed movement begins.

CHAPTER 5

PRESENTATION AND DISCUSSION OF RESULTS

In the first section of this chapter (Section 5.1) results are presented for the region of the fluid domain in which the bed deformation occurs; both the two-dimensional (2-D) and three-dimensional (3-D) models of wave generation which were described in Chapter 3 are examined. The region of the fluid domain in which the bed movement occurs is termed the generation region and is given by $|x| \leq b$ and $r \leq r_o$ for the two and three-dimensional models, respectively. In the discussion of the two-dimensional model, theoretical and experimental results are presented for the maximum amplitudes and characteristic periods of the generated waves as well as the detailed wave structure at different locations in the region of generation. Possible energy dissipation mechanisms present in the experimental measurements for the 2-D model are also briefly discussed. Section 5.1 is concluded with a presentation of the theoretical results for the maximum wave amplitudes and the general wave structure in the generation region of the 3-D model.

In Section 5.2 theoretical and experimental results are presented for wave propagation in the two-dimensional model which occurs outside the region of generation. The fluid domain outside the region of generation, i.e., $|x| > b$, is termed the downstream region. Wave propagation in this region is investigated by both the linear theory developed in Chapter 3 and the nonlinear description of wave motion based on the KdV equation which was also discussed in Chapter 3. The effects of energy dissipation that occur in the downstream region of the experimental model are also discussed.

Experimental wave profiles are presented in Section 5.3 which result when an oscillating motion is superposed on the half-sine bed displacement. Changes in the wave profiles caused by varying both the frequency and amplitude of the oscillating motion are investigated.

This chapter is concluded in Section 5.4 with a discussion of the practical application of the theoretical and experimental results to the Alaskan earthquake of 27 March 1964. Characteristic values of appropriate generation parameters are found for the tectonic deformations occurring during this disastrous earthquake; from these values certain features of the resulting tsunami are inferred.

5.1 THE GENERATION REGION

For the two and three-dimensional models the generation region is defined as the region of fluid extending over the moving bed section which is given by $|x| \leq b$ and $r \leq r_o$, respectively. There are two positions in the generation region of the two-dimensional model which have been investigated both experimentally and theoretically; these positions are: $x/h = 0$, which will be referred to as the backwall, and $x/h = b/h$ termed the leading edge (or the leading edge of the disturbance). In the experiments the plane $x = 0$ corresponds to the upstream limit of both the wave generator and the wave tank. The positions corresponding to $x/h = 0$ and $x/h = b/h$ in the three-dimensional model are $r/h = 0$ and $r/h = r_o/h$; wave structure at these positions has only been investigated theoretically.

The range of the generation parameters (ζ_o/h, b/h, and $t_c\sqrt{g/h}$) for which experiments have been conducted for the exponential and half-sine bed displacements were presented in Chapter 4. These generation parameters will be referred to in this chapter as:

$\zeta_o/h \equiv$ disturbance-amplitude scale,
$b/h \equiv$ disturbance-size scale,
$t_c\sqrt{g/h} \equiv$ disturbance-time scale.

(The ratio of the disturbance-time scale to the disturbance-size scale will hereafter be referred to as the time-size ratio.) It should be recalled that the characteristic time, t_c, for the exponential bed displacement is the time required for two-thirds of the movement to occur, i.e., $t = t_c$ when $\zeta/\zeta_o = 2/3$. For the half-sine bed displacement the total time of movement, T, is taken as the characteristic time.

5.1.1 Maximum Wave Amplitudes in the Generation Region.

One of the more important characteristics of the waves generated by a moving boundary is the maximum water surface elevation reached by the wave at a particular location. The maximum amplitude of the leading wave generated by the exponential and half-sine bed displacements will be referred to herein as η_o. (Other characteristics of the generated waves, e.g., wave profiles and periods, will be discussed in Sections 5.1.2 and 5.1.3, respectively.)

Experimental and theoretical results for the variation of the ratio of the maximum wave amplitude to the maximum bed displacement, i.e., η_o/ζ_o, as a function of the time-size ratio, $t_c\sqrt{gh}/b$, at the backwall ($x/h = 0$) are shown in Fig. 5.1 for the exponential bed displacement. (Recall that the time-size ratio, $t_c\sqrt{gh}/b$, was found in Section 3.2.1 to be important as an indicator of the type of wave which is generated.) In Fig. 5.1 the data are presented separately for each disturbance-size scale; hence, changes in the relative wave amplitude, η_o/ζ_o, are the result of changes in only the disturbance-time scale, $t_c\sqrt{g/h}$. In Fig. 5.1 hollow circles are used to indicate experiments in which the bed displacement is positive ($\zeta_o > 0$) while solid circles correspond to experiments for negative bed displacements ($\zeta_o < 0$). The symbols have also been identified to indicate the absolute value of the disturbance-amplitude scale, $|\zeta_o/h|$, of the bed movement; the symbols and the corresponding amplitude scale are shown in the legend of Fig. 5.1. (It should be noted from the legend that no experiments were conducted for the case of $|\zeta_o/h| = 0.7$.) The arrows which are adjacent to certain data points indicate experiments for which the smaller bed unit, $b = 30.5$ cm, was used; for all other experiments the length of the bed unit was 61 cm.

The curves for each disturbance-size scale indicate the theoretical values of the maximum wave amplitude which were found by numerically integrating Eq. (3.67). In the numerical integration the integral of Eq. (3.67) rapidly converged so that the computation could

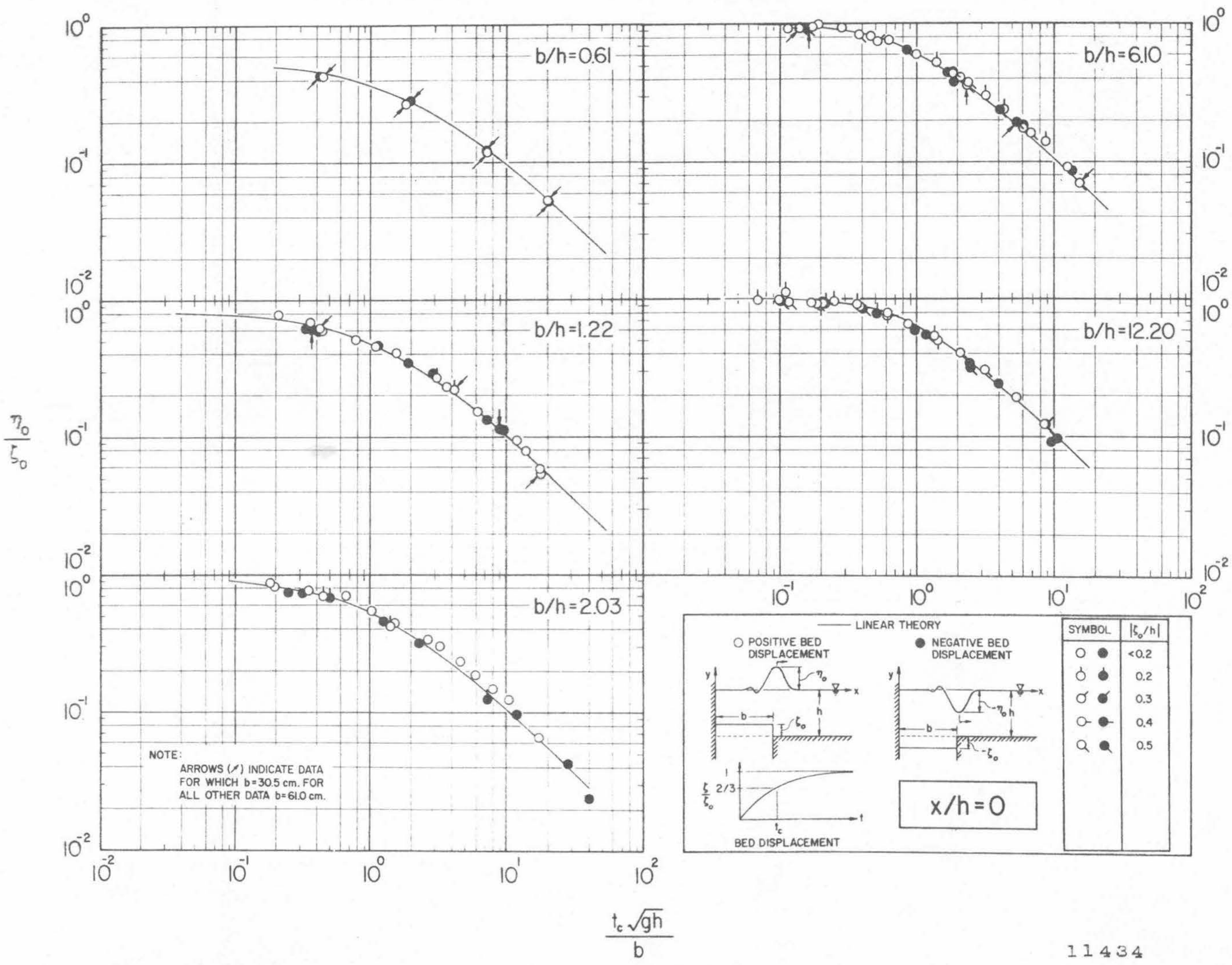

11434

Fig. 5.1 Variation of the relative maximum wave amplitude, η_o/ζ_o, with the time-size ratio, $t_c\sqrt{gh}/b$, at $x/h = 0$ for exponential bed displacements.

be terminated quickly. The variation of the integrand as a function of the integration variable, i.e., the quantity $\lambda = kh$, was used to determine the limits of the integration such that an accurate approximation to the integral was obtained. All computations were performed on an IBM 360/75 or 370/155 high-speed digital computer.

Examination of the results in Fig. 5.1 for each disturbance-size scale shows that the linear theory accurately predicts the relative wave amplitude for both positive and negative bed motions and for the full range of the generation parameters which were investigated. In the discussion of Chapter 3 regarding nonlinear effects occurring during a bed movement, it was suggested that the linear theory was only applicable over the full range of disturbance-amplitude scales, i.e., $0 < |\zeta_o/h| \leq 1$, when the time-size ratio was much greater than unity. For bed movements which occurred so rapidly that the time-size ratio was much less than unity, the analysis in Chapter 3 indicated that the linear theory was applicable only for small disturbance-amplitude scales, i.e., $|\zeta_o/h| << 1$. Surprisingly, the linear theory shown in Fig. 5.1 appears to accurately predict the relative wave amplitude, η_o/ζ_o, at the backwall for the full range of amplitude scales even when the time-size ratio is much less than unity. This behavior is demonstrated best by the data for the largest size scale studied, i.e., $b/h = 12.2$, where data with disturbance-amplitude scales up to ± 0.5 appear near $t_c\sqrt{gh}/b = 10^{-1}$.

Fig. 5.1 clearly shows the variation of the relative wave height, η_o/ζ_o, as a function of the time scale, $t_c\sqrt{g/h}$, for a constant disturbance-size scale. Consider again the results for the largest size scale, i.e., $b/h = 12.2$, where the maximum wave amplitude becomes essentially equal to the total bed displacement, i.e., $\eta_o/\zeta_o \simeq 1$, for a time scale such that the time-size ratio is less than 10^{-1}. As the time scale increases (or equivalently, as the time-size ratio increases) the relative wave height decreases until the theoretical curve approaches a slope of minus unity on the log-log representation for very large values of $t_c\sqrt{gh}/b$; hence, η_o/ζ_o becomes inversely proportional to the time-size ratio as $t_c\sqrt{gh}/b$ becomes large. This behavior was suggested previously in Chapter 3 where it was found that the characteristic wave amplitude for bed movements such that $t_c\sqrt{gh}/b >> 1$ was inversely proportional to the parameter, $t_c\sqrt{gh}/b$, now termed the time-size ratio. The results for the smaller disturbance-size scales shown in Fig. 5.1 shows the same general behavior as that for $b/h = 12.2$. However, the asymptotic value of η_o/ζ_o approached by the theoretical curves for the smaller size scales (e.g., $b/h = 1.22$) when the time-size ratio becomes very small is now less than unity. More discussion of this behavior for small size scales will be given shortly.

For the two disturbance-size scales: $b/h = 1.22$ and 6.10, data are shown in Fig. 5.1 for which two different bed unit lengths, b, were used. No difference in the relative wave amplitude, η_o/ζ_o, is apparent from the data regardless of the bed unit length as long as b/h remains constant; hence, the disturbance-size scale appears to be a proper scaling parameter for characterizing the wave generation process.

In Chapter 3 bed movements which occurred so rapidly that the water surface nearly followed the bed deformation were described as impulsive. Thus for the largest size scale in Fig. 5.1, i.e., $b/h = 12.2$, the region of the time-size ratio for which the maximum wave amplitude equals the bed displacement, i.e., $t_c\sqrt{gh}/b < 10^{-1}$, may be termed the impulsive region of generation. For the smaller disturbance-size scales in which the maximum wave amplitude, η_o, never becomes equal to the total bed displacement, ζ_o, a region does exist in which the ratio η_o/ζ_o becomes constant, i.e., η_o/ζ_o is independent of the time-size ratio; this region will hereafter be referred to as the impulsive region of generation. The region which corresponds to time-size ratios much greater than unity for which the relative wave amplitude, η_o/ζ_o, becomes inversely proportional to the time-size ratio will be referred to as the creeping region of wave generation as suggested previously in Chapter 3. (The word "creeping" is adopted due to its general use in seismology to describe slow adjustments along faults occurring after a major earthquake.) The range of time-size ratios between the impulsive and creeping regions will be referred to as the transition zone of generation.

Fig. 5.2 shows the variation of the relative wave amplitude, η_o/ζ_o, as a function of the time-size ratio, $t_c\sqrt{gh}/b$, at the backwall

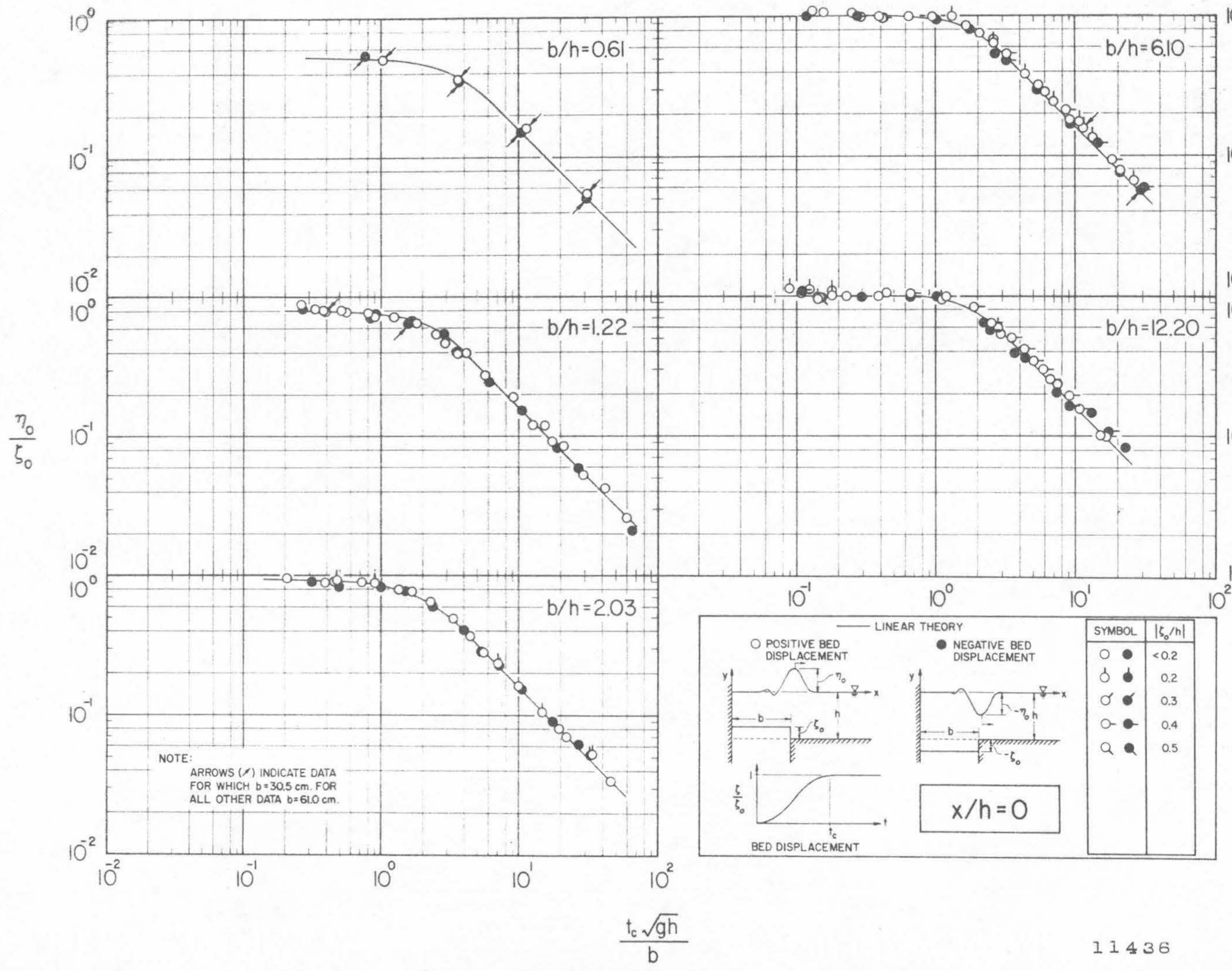

Fig. 5.2 Variation of the relative maximum wave amplitude, η_o/ζ_o, with the time-size ratio, $t_c\sqrt{gh}/b$, at $x/h = 0$ for half-sine bed displacements.

for the case of the half-sine bed displacement. The notation used is the same as that shown in Fig. 5.1 and is described again in the legend of Fig. 5.2. The theoretical curves for each size scale have been computed from Eq. (3.68). Again the linear theory appears to accurately predict the relative wave amplitude for all of the time scales, $t_c\sqrt{g/h}$, amplitude scales, ζ_o/h, and size scales, b/h, which have been investigated. The general behavior of the results shown in Fig. 5.2 is the same as that observed for the data presented in Fig. 5.1 for the exponential bed displacement. As the disturbance-time scale decreases for a constant size scale, a maximum wave amplitude is reached which then remains constant with further reductions of the time scale. For two size scales: b/h = 6.10 and 12.2, the maximum wave amplitude, η_o, is equal to the total bed displacement, ζ_o. Smaller relative wave amplitudes are reached in the impulsive regions of the other disturbance-size scales: b/h = 0.61, 1.22, and 2.03. (This behavior will be discussed shortly.) Upon leaving the impulsive region of generation for any size scale, the relative wave amplitude quickly becomes inversely proportional to the time-size ratio; the transition region for each size scale shown in Fig. 5.2 is smaller in extent than the corresponding region for the exponential bed displacement shown in Fig. 5.1.

Data are also shown in Fig. 5.2 for the disturbance-size scales b/h = 1.22 and 6.10 in which the smaller bed unit length (b=30.5 cm) was used. The agreement of these data with that for the larger bed unit again indicates that b/h is a proper scaling parameter for the wave generation process.

The theoretical curves at the backwall are shown for all size scales in Fig. 5.3 for both the exponential (Fig. 5.3a) and the half-sine bed displacement (Fig. 5.3b). In addition to the five size scales for which experiments have been conducted, a theoretical curve has also been computed for $b/h = 100$. Only a small difference in relative wave amplitude, η_o/ζ_o, is observed for the exponential bed displacement between the curves for $b/h = 12.2$ and $b/h = 100$. This slight difference occurs only in the transition region of generation as the two curves are coincident in the impulsive and creeping regions. For the half-sine bed displacement the theoretical curves for $b/h = 12.2$ and $b/h = 100$ are coincident for all time-size ratios. This lack of dependence of the relative wave amplitude on the size scale at $x/h = 0$ for large values of b/h (e.g., $b/h > 12.2$) is important in the application of these data to practical problems.

It can be seen from Fig. 5.3a and Fig. 5.3b that the theoretical curves for η_o/ζ_o collapse into a single curve when the creeping region of generation is reached for each disturbance-size scale. As the size scale decreases, the magnitude of the time-size ratio required before the creeping region is reached also increases. This behavior is consistent between the theoretical results for the exponential and half-sine bed displacements. Fig. 5.3a and Fig. 5.3b also show that as the impulsive region is reached for each disturbance-size scale, the maximum value of η_o/ζ_o that is achieved in this region decreases as the size scale decreases; a discussion of this behavior will be given shortly.

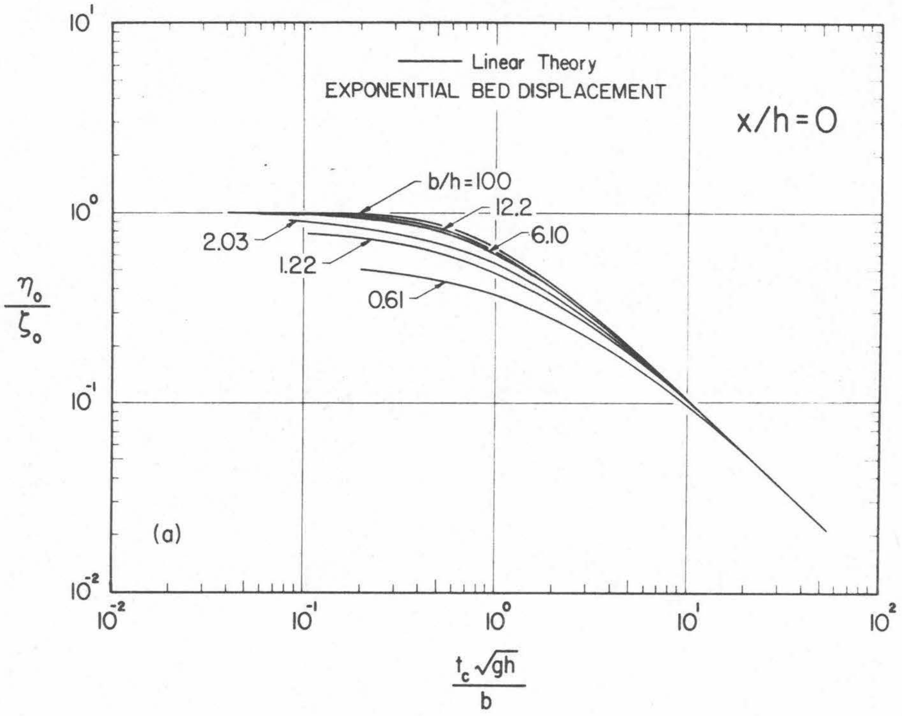

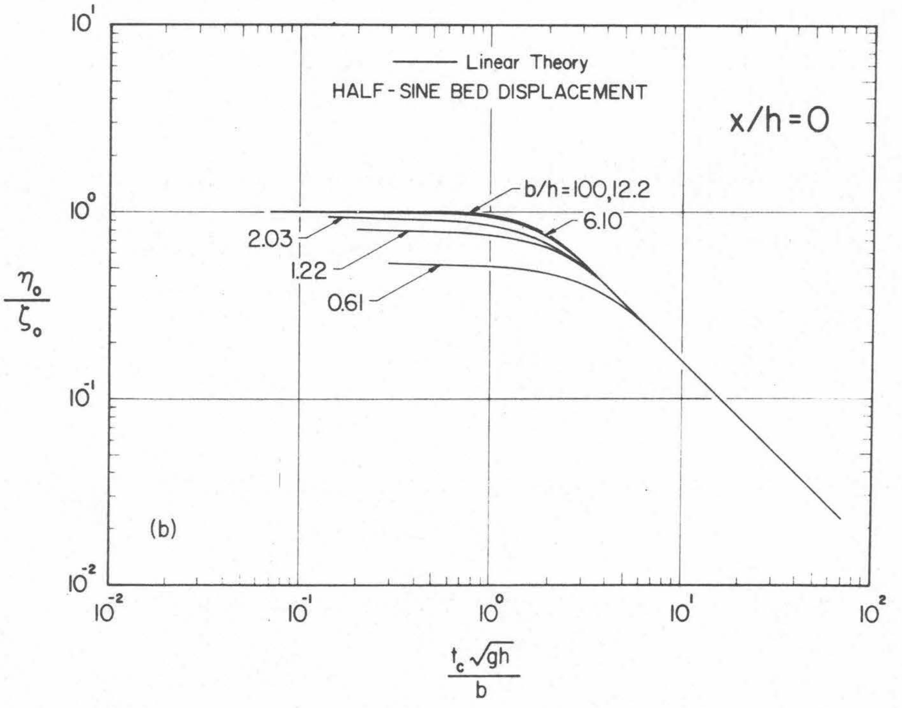

Fig. 5.3 Theoretical variation of relative maximum wave amplitude, η_o/ζ_o, with the time-size ratio, $t_c\sqrt{gh}/b$, at $x/h = 0$; a) exponential bed motion, b) half-sine bed motion.

The second position of interest in the generation region is the leading edge of the moving bed section, i.e., $x = b$ or $x/h = b/h$. Experimental and theoretical results for the variation of the relative wave amplitude, η_o/ζ_o, as a function of the time-size ratio, $t_c\sqrt{gh}/b$, when the bed moves in an exponential manner are shown in Fig. 5.4. Again the results for each size scale are shown separately so that changes in the time-size ratio (plotted as the abscissa) only represent changes in the disturbance-time scale. The notation used in Fig. 5.4 is the same as used previously and is again noted in the legend of the figure.

Before discussing the agreement between theory and experiment, it is more convenient to look at the general behavior of η_o/ζ_o that is predicted by the linear theory. For the largest size scale, $b/h = 12.2$, the maximum wave amplitude at the leading edge of the bed section, η_o, becomes equal to one-half the total bed displacement, ζ_o, as the time scale becomes small, i.e., in the impulsive region of generation. This is the same value as predicted by the dam-break analogy in Chapter 3 for small initial differences in the water level between the reservoir and the downstream region. (Recall that the initial difference in water levels in the dam-break problem is analogous to the disturbance-amplitude scale in the problem now under discussion.) As the disturbance-time scale is increased for $b/h = 12.2$ the relative wave amplitude decreases and approaches a slope of minus unity on the log-log representation again indicating that the relative wave amplitude is

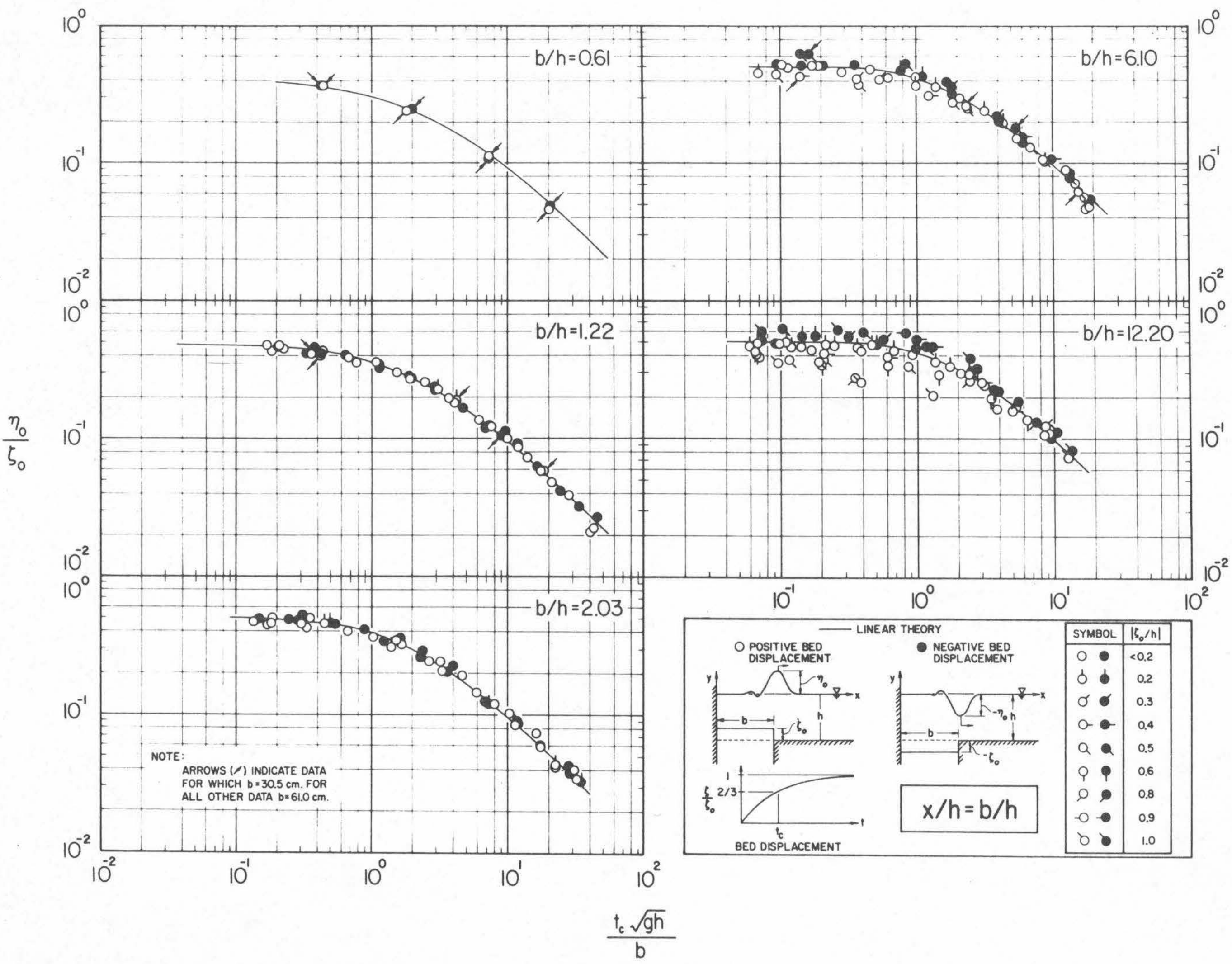

NOTE:
ARROWS (↗) INDICATE DATA FOR WHICH b = 30.5 cm. FOR ALL OTHER DATA b = 61.0 cm.

Fig. 5.4 Variation of the relative maximum wave amplitude, η_o/ζ_o, with the time-size ratio, $t_c\sqrt{gh}/b$, at $x/h = b/h$ for exponential bed displacements.

inversely proportional to the time scale. This same general behavior is found for the other size scales shown except for the smallest, i.e., $b/h = 0.61$, where the maximum wave amplitude reached in the impulsive region of generation is less than one-half the total bed displacement. (Again, an explanation of this behavior will be given shortly.)

The agreement between theory and experiment in Fig. 5.4 is no longer as good for the larger disturbance-size scales, i.e., $b/h = 6.10$ and 12.2, as was observed at the backwall. The data for these size scales in Fig. 5.4 indicate that η_o/ζ_o is consistently less than the value predicted by the linear theory in the transition and impulsive regions of generation for positive bed displacements (hollow circles) with amplitude scales greater than 0.2. The larger the disturbance-amplitude scale, the more the linear theory deviates from the experimental results. Near $t_c\sqrt{gh}/b = 0.4$ for $b/h = 12.2$ the linear theory predicts a relative wave amplitude, η_o/ζ_o, approximately twice as large as that observed experimentally when the amplitude scale approaches unity. A similar finite-amplitude effect was suggested by the dam-break analogy in Chapter 3 where the amplitude of the generated bore, η_o, relative to the initial difference in water levels (termed ζ_o) decreased as ζ_o increased for a fixed downstream water depth. When the initial difference in water levels was equal to the downstream water depth, a decrease in the relative bore amplitude, η_o/ζ_o, of approximately 6% was calculated. The much stronger nonlinear effect evident from the data in Fig. 5.4 for positive bed movements in the impulsive region of generation for $b/h = 12.2$ is probably due to the presence of the large step in the channel at the end of the impulsive bed movement. No step is present in the bed profile for the dam-break problem; hence, the analogy with the waves generated by the bed movement no longer exists. When an impulsive movement of the bed unit occurs such that ζ_o/h is of order unity, the flow of water near $x/h = b/h$ more closely resembles flow over a broad-crested weir as it spills out of the generation region into the downstream domain of fluid. It should be noted that as the time scale, $t_c\sqrt{g/h}$, decreases in the impulsive region of generation for $b/h = 12.2$, the difference between the predicted and the measured values of maximum amplitudes for positive bed movements of large amplitude appears to decrease; this is indeed the case and is due to a major change in the general wave profile which occurs. (This behavior will be discussed in Section 5.1.2.)

For $b/h = 6.10$ and 12.2 the relative wave amplitude, η_o/ζ_o, for negative bed displacements increases in the impulsive and transition regions as the absolute value of the disturbance-amplitude scale becomes greater than 0.2; however, this finite-amplitude effect of the bed movement is not as pronounced as observed for positive bed displacements. It can be seen from the data for $b/h = 12.2$ that when $0.5 \le |\zeta_o/h| \le 1$ the measured relative wave amplitude is only 20% larger than that predicted by the linear theory. As the time scale becomes very small, these data for negative bed movements do not appear to approach the linear theory as indicated by the data for positive bed displacements.

The linear theory agrees well with the data shown in Fig. 5.4 over the full range of the time-size ratio investigated for b/h = 6.10 and 12.2, when the disturbance-amplitude scale is less than 0.2. For the smaller size scales: b/h = 0.61, 1.22, and 2.03, the linear theory agrees well with all the data shown. It should be noted that for these smaller disturbance-size scales, no amplitude scale greater than 0.2 could be used in any experiments.

From Fig. 5.4 it can be seen that in the creeping region of generation the data agree well with the linear theory for each disturbance-size scale regardless of the amplitude scale of the bed movement. This behavior for creeping bed movements was suggested previously in Chapter 3.

For the size scales: b/h = 1.22 and 6.10, experiments are indicated for which the smaller bed unit length ($b \simeq 30.5$ cm) was used. No differences between these data and the data for the larger bed unit are observed; hence, b/h does appear to be a proper generation parameter.

Fig. 5.5 shows the experimental and theoretical results for the relative wave amplitude, η_o/ζ_o, as a function of the time-size ratio, $t_c\sqrt{gh}/b$, at x/h = b/h when the bed moves in a half-sine manner. The notation is the same as used previously and is again noted in the legend of Fig. 5.5. As for the exponential bed displacement, the linear theory accurately predicts η_o/ζ_o for all time-size ratios and disturbance-size scales when the absolute value of the disturbance-amplitude scale

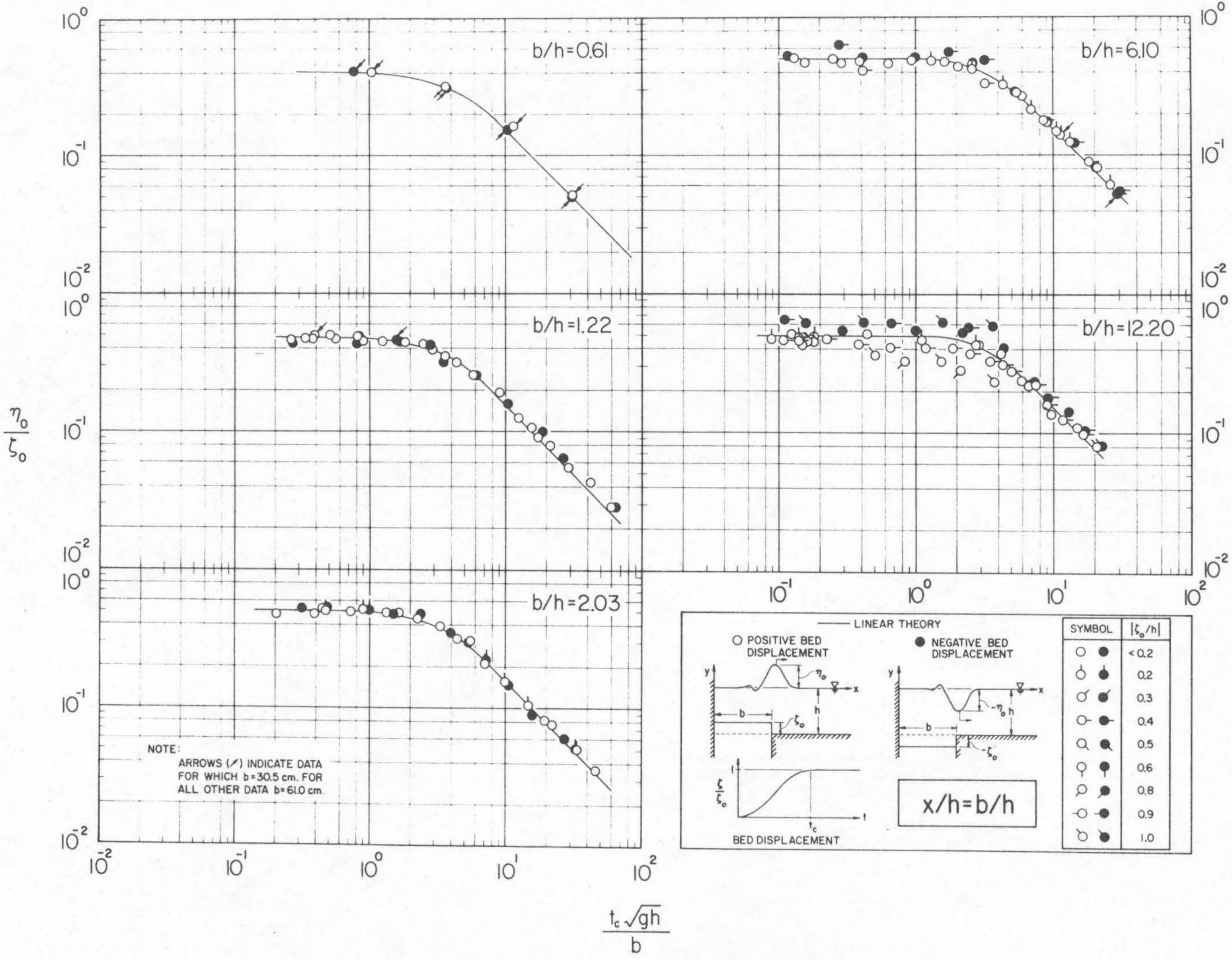

Fig. 5.5 Variation of the relative maximum wave amplitude, η_o/ζ_o, with the time-size ratio, $t_c\sqrt{gh}/b$, at $x/h = b/h$ for half-sine bed displacements.

is less than 0.2. For $|\zeta_o/h| > 0.2$ the same nonlinear behavior of the relative wave amplitude in the impulsive and transition regions for $b/h = 6.10$ and 12.2 is observed as was discussed previously for the exponential bed displacement in Fig. 5.4. In the creeping region of each size scale, the linear theory agrees well with the data over the full range of amplitude scales.

Fig. 5.6a and Fig. 5.6b show the theoretical results for the relative wave amplitude as a function of the time-size ratio for the exponential and half-sine bed displacements, respectively. In addition to the five disturbance-size scales discussed previously, a theoretical curve has been computed for $b/h = 100$ for each time-displacement history of the bed unit. The curves for $b/h = 100$ predict a slightly larger relative wave amplitude in the transition region of generation than that predicted for the smaller size scale, $b/h = 12.2$. The theoretical curves for these two size scales are coincident in the impulsive region of generation where the relative wave amplitude becomes constant at a value of 0.5 and in the creeping region where η_o/ζ_o is inversely proportional to the time-size ratio. In Fig. 5.6a and Fig. 5.6b the relative wave amplitude, η_o/ζ_o, appears to become independent of the disturbance-size scale for size scales greater than $b/h = 12.2$; this behavior was also observed for the relative wave amplitude measurements at the backwall (see Fig. 5.3).

For the smaller disturbance-size scales in Fig. 5.6a and 5.6b, the maximum value of the relative wave amplitude, η_o/ζ_o, reached in the impulsive region of generation is less than 0.5. A similar

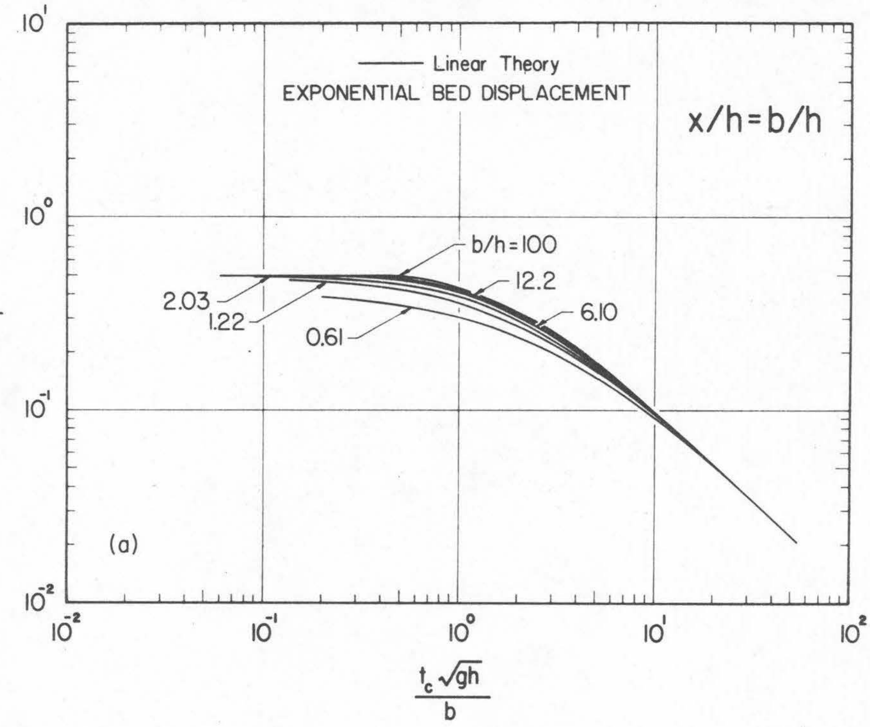

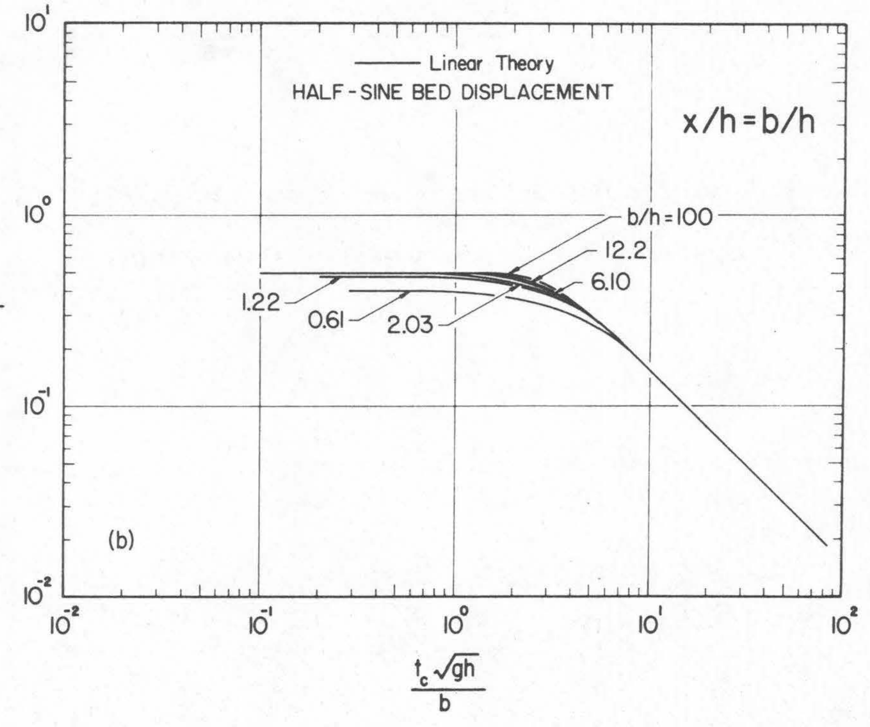

Fig. 5.6 Theoretical variation of relative maximum wave amplitude, η_o/ζ_o, with the time-size ratio, $t_c\sqrt{gh}/b$, at $x/h = b/h$; a) exponential bed motion, b) half-sine bed motion.

behavior was also exhibited by η_o/ζ_o for the smaller size scales in the impulsive region of generation at the backwall (see Fig. 5.3a and 5.3b). The decrease in the maximum wave amplitude that can be reached in the generation region for small size scales is a result of the elliptic nature of the partial differential equation, $\nabla^2\varphi = 0$, governing the response of the fluid medium to the impulsive boundary condition. In order to understand this "elliptic behavior" of the fluid medium, it is useful to first discuss an analogous problem from the theory of elasticity where elliptic equations are also found to describe the response of an elastic solid to a system of applied forces.

Consider an elastic solid which is experiencing a complex system of forces over a section of its boundary of length, Ω, whose resultant force is zero. Saint-Venant's principle (which is used extensively in the study of the elastic behavior of solids) states that the strains produced by the system of forces are negligible at distances from the force system which are large compared to Ω (see, e.g., Fung, 1965). Hence, the complex system of forces may be replaced by any other system which is statically equivalent in order to determine the behavior of the solid at distances from the force system which are large compared to Ω.

Saint-Venant's principle may also be applied to the current problem since the governing equations are elliptic. Hence, the response of the fluid at distances much greater than 2b (the disturbance length) from the impulsive boundary deformation would not be expected to behave differently during any impulsive boundary deformation in which the same amount of water volume is displaced. (Requiring the deformations to displace the same total water volume is analogous to requiring the force systems on the elastic solid to be statically equivalent.) When the water depth is such that $h >> 2b$ then the water surface over the impulsively moving bed is included in this part of the fluid domain and would no longer be expected to resemble the deformed bed at the end of the deformation.

The effect of this elliptic behavior on the wave amplitudes at $x/h = 0$ and $x/h = b/h$ at the end of the impulsive bed displacement is shown in Fig. 5.7 where the maximum wave amplitude, η_o/ζ_o, is shown as a function of the disturbance-size scale, b/h. The curves shown have been computed by the linear theory for both half-sine and exponential bed displacements when the time-size ratio was less than 10^{-2}. The same curves result independent of the time-displacement history of the bed movement as would be anticipated for impulsive bed displacements.

The maximum wave amplitude, η_o, at the position $x/h = 0$ becomes equal to the total bed displacement for all disturbance-size scales greater than about four. As the size scale becomes less than four the relative wave amplitude, η_o/ζ_o, decreases from unity until it becomes directly proportional to the size scale for $b/h < 0.1$, i.e.:

$$\eta_o/\zeta_o = b/h \quad \text{for } b/h < 0.1. \tag{5.1}$$

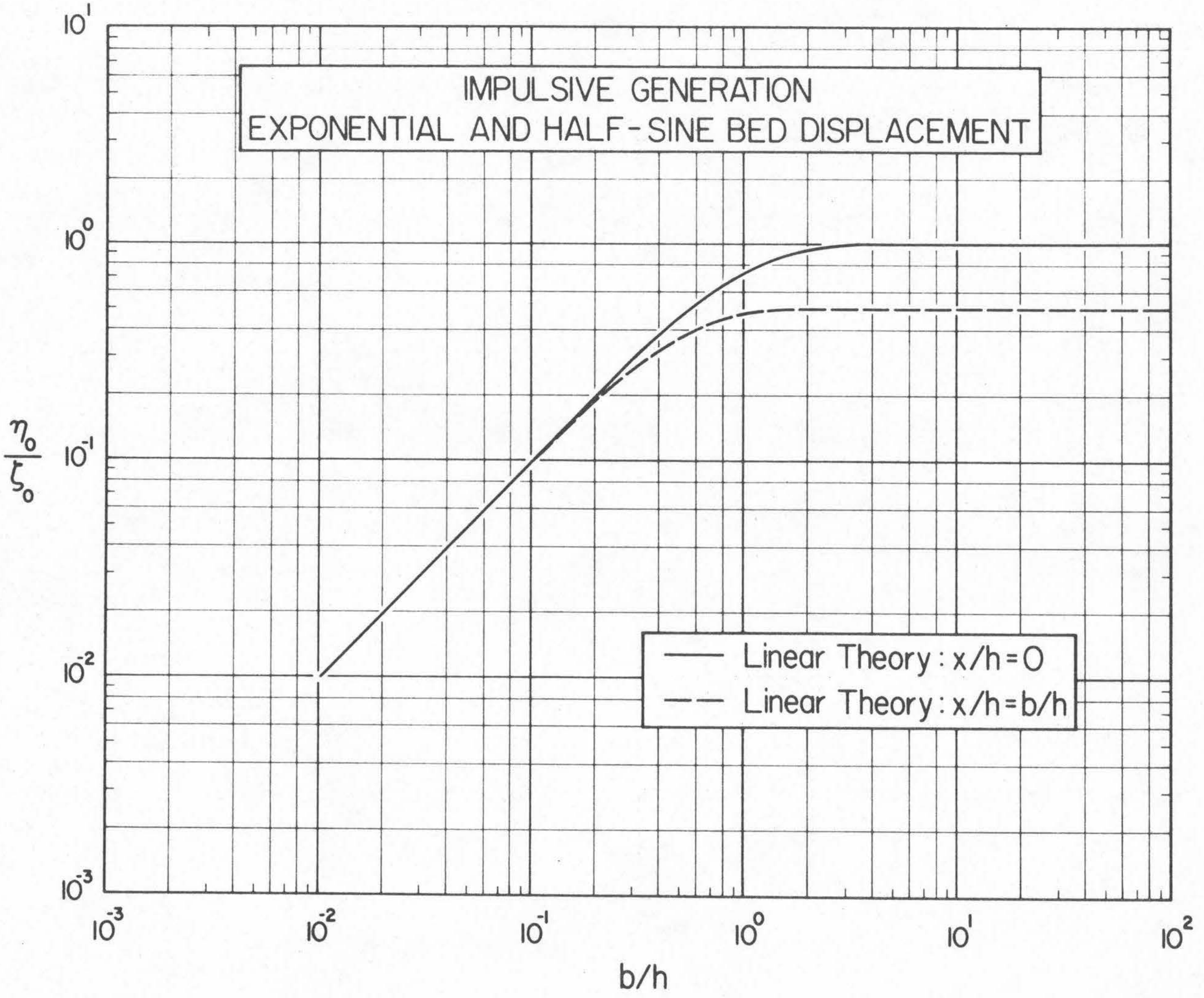

Fig. 5.7 Theoretical variation of relative maximum wave amplitude, η_o/ζ_o, with disturbance-size scale, b/h, for impulsive bed displacements.

(The constant of proportionality can be seen from Fig. 5.7 to be equal to unity.)

The maximum wave amplitude, η_o, occurring at the edge of the moving bed section, i.e., $x/h = b/h$, is equal to one-half the total bed displacement for all disturbance-size scales greater than approximately two. The maximum wave amplitude then decreases as the size scale decreases until, near $b/h = 0.1$, the wave amplitude at the leading edge becomes equal to the wave amplitude at the center of the deformed bed section ($x/h = 0$). These amplitudes remain equal for smaller size scales; hence, the relative wave amplitudes at $x/h = b/h$ is also given by Eq. (5.1) for $b/h < 0.1$.

Eq. (5.1) may also be written as:

$$\frac{\eta_o b}{\zeta_o b} = \frac{b}{h} , \tag{5.2}$$

where $\eta_o b$ represents the amount of the displaced water volume remaining in the generation region during the impulsive bed displacement and $\zeta_o b$ is equal to the displaced water volume. Hence, for the disturbance-size scales less than 0.1 most of the displaced water volume is already in the downstream region at the end of the impulsive bed displacement.

Still another form of Eq. (5.1) is:

$$\frac{\eta_o h}{\zeta_o b} = 1 \quad \text{for } b/h < 0.1 , \tag{5.3}$$

which appears to indicate that the displaced water volume is contained in a region at the end of the impulsive bed movement which resembles a semi-circular-cylindrical shell of radius h, a thickness η_o, and unit width.

It is interesting to note that Sokolnikoff (1946, p. 90) in his treatise on elasticity states that it is commonly assumed in problems regarding beams that Saint-Venant's principle becomes applicable at a distance of approximately five times the characteristic length of the applied force system. In the present problem the water surface directly over the disturbance is at a distance of five times the disturbance length (2b) when $b/h = 0.1$. This is indeed the largest disturbance-size scale for which the water surface behavior in the generation region becomes independent of location.

In summary, it appears that the linear theory developed in Chapter 3 for the two-dimensional model predicts reasonably well the relative wave amplitude, η_o/ζ_o, in the generation region. Major differences between the linear theory and experiments appear to be limited primarily to the impulsive and transitional region of generation for large disturbance-amplitude scales, i.e., $|\zeta_o/h| > 0.2$. In the creeping region of generation the linear theory agrees well with experiments over the full range of amplitude scales, i.e., $0 < |\zeta_o/h| \leq 1$.

5.1.2 Wave Profiles in the Generation Region.

In the previous section only one characteristic of the waves in the generation region was discussed, i.e., the maximum amplitude, η_o, of the leading wave. In general the linear theory was found to predict this amplitude well. A more complete confirmation of the linear theory in the region of generation requires a detailed comparison between theory and experiment of the entire wave profile; such a comparison will be made in this subsection.

In the discussion of maximum wave amplitudes it was found that the bed displacements for a specific size scale could be conveniently divided into three regions of generation according to the magnitude of the time-size ratio, $t_c\sqrt{gh}/b$. An impulsive region of generation was said to exist when the maximum wave amplitude remained constant for a decreasing time-size ratio; a creeping region was defined for large $t_c\sqrt{gh}/b$ when the wave amplitude became inversely proportional to the time-size ratio and independent of b/h; and a zone of transition was defined between the impulsive and creeping regions. Since the wave structure is similar within each of these three regions, a convenient method for determining the accuracy of the linear theory in predicting the wave structure is to examine in detail typical wave profiles in each region.

Typical theoretical and experimental wave profiles which occur in each region of generation for exponential bed displacements are shown in Fig. 5.8 where the normalized wave amplitude, η/ζ_o, is shown as a function of the nondimensional time, $t\sqrt{g/h}$. The size scale for each wave profile shown is $b/h = 12.2$; recorded and computed wave profiles are shown at the backwall $(x/h = 0)$ and at the leading

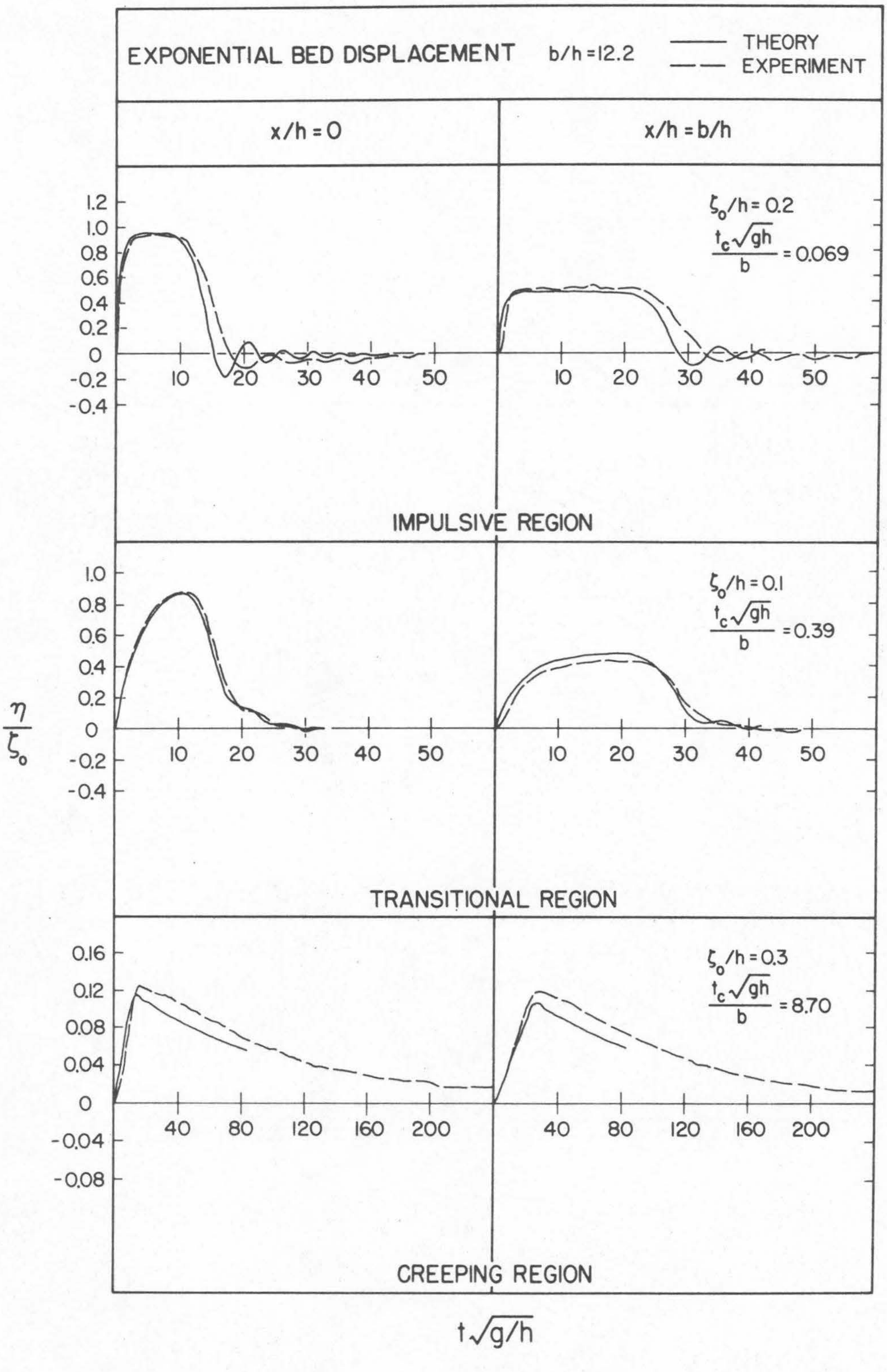

Fig. 5.8 Typical wave profiles in each region of generation at x/h = 0 and x/h = b/h generated by exponential bed displacements.

edge of the disturbance (x/h = b/h). (The generation parameters for each profile are indicated in the figure. Note that an amplitude scale, ζ_o/h, for which the linear theory should be applicable has been chosen in each region.) Experimental curves are shown dashed in Fig. 5.8 while theoretical curves are shown as solid lines.

In the impulsive region the water surface at both the backwall and the leading edge of the disturbance rapidly rises to an amplitude of ζ_o and $\zeta_o/2$, respectively. The wave amplitude then remains constant for a limited interval of time after which the water surface rapidly decreases to the still water level (also referred to as SWL) and then oscillates in a damped manner about this mean level. The amplitude of each oscillation is small compared with the amplitude of the leading wave. The experimental profiles and the linear theory in Fig. 5.8 agree well at both the backwall and the leading edge except for the trailing portion of the leading wave. The time required for the leading wave to rise and then return to the SWL (hereafter referred to as the nodal time) appears to be somewhat larger in the experiments than in the computed profiles. This behavior of the experimental and the theoretical profiles was consistent for all runs in which the disturbance-amplitude scale was small, i.e., $\zeta_o/h \le 0.2$, and the disturbance-size scale, b/h, was equal to 12.2. As b/h decreased, the linear theory agreed more closely with the experimental profiles. (Nodal times of the wave profiles will be discussed in the following section (Section 5.1.3).)

The waves at the backwall and at the leading edge in the transition region shown in Fig. 5.8 rise at a slower rate than those in the impulsive region and reach a maximum amplitude which is less than ζ_o and $\zeta_o/2$, respectively. Immediately upon reaching this maximum amplitude, the water elevation begins to decrease toward the SWL. The rate of fall decreases before reaching the still water level and slight oscillations occur; these oscillations do not appear to go below the SWL. In this region the theoretical and experimental profiles agree well over the entire wave signature.

In the creeping region of generation the waves at both the backwall and leading edge slowly rise to a maximum amplitude and then fall very slowly back toward the SWL. (Note the change in abscissa and ordinate scales for this profile.) The rate of fall is so slow that the profile resembles a bore. The theoretical profiles agree well in shape with the experimental waves but fail to reach the same amplitudes; maximum experimental wave amplitudes are on the order of 10% higher than the computed amplitudes. Dimensional wave heights for this experiment were less than 2 mm; hence, a 10% error in measurement is within the normal error expected for measurements with a resistance wave gage (see Section 4.4) for waves of this amplitude.

Typical experimental and theoretical profiles for waves generated by a half-sine bed displacement in each of the three regions of generation are shown in Fig. 5.9 where η/ζ_o is again shown as a function of $t\sqrt{g/h}$. Wave profiles for both a positive and negative bed

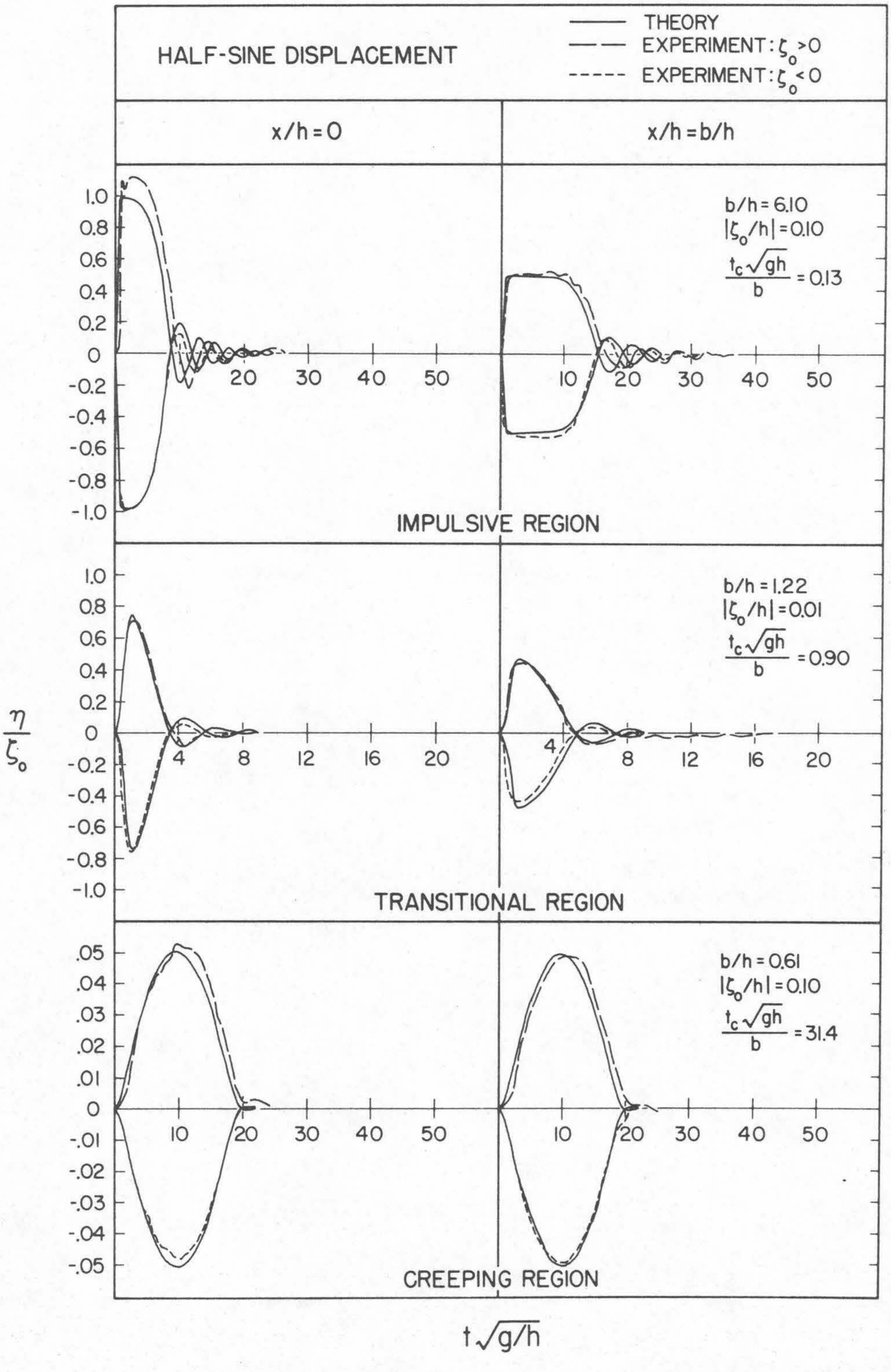

Fig. 5.9 Typical wave profiles in each region of generation at x/h = 0 and x/h = b/h generated by half-sine bed displacements.

displacement are shown in each region and the disturbance-size scale is varied among the regions. For the negative bed displacements the generation parameters are the same as for the corresponding positive cases. (Recall that the linear theory predicts that a negative bed displacement will generate a wave which is the mirror image of the wave created by a positive bed displacement.)

In the impulsive region of generation the experimental and theoretical profiles for the negative displacement ($\zeta_0 < 0$) agree well in detailed structure at both the backwall and leading edge. The agreement between the theoretical and experimental wave profiles generated by a positive bed displacement does not appear to be quite as good at either position. At the backwall the measured wave profile reaches an amplitude greater than the total bed displacement. This behavior of the measured profile may be caused by observed leakage of air around the seal of the moveable bed unit during very fast bed displacements. This leakage could cause the measured water surface to exceed the theoretical amplitude, ζ_o, and possibly oscillate as shown by the experimental profile for small nondimensional times. (The entrainment of air due to leakage around the seal will be discussed in more detail shortly.) As for the exponential case in the impulsive region, the nodal times of the leading wave for the experimental wave profiles are greater than those predicted by the linear theory. In the transition and creeping regions of generation, both the positive and negative wave profiles of the linear theory agree well with the experimental wave profiles in detailed structure.

Comparison of the waves for each region between Fig. 5.8 for the exponential bed displacement and Fig. 5.9 for the half-sine bed displacement shows that, in general, the wave profiles in the impulsive and transition regions of generation are similar while the wave profiles are quite different in the creeping region of generation. For the exponential bed displacement a wave resembling a bore is generated in the creeping region of generation while the wave generated by the half-sine bed displacement is much more symmetrical and has a finite nodal time.

Eqs. (3.67) and (3.68) demonstrated that similar wave profiles result when the generation parameters b/h and $t_c\sqrt{g/h}$ remain constant, regardless of the individual values of b, h, t_c, and g. This suggested behavior could be investigated experimentally by using the two bed units of different lengths and varying the generation characteristics such that the nondimensional generation parameters remained constant. Fig. 5.10 shows a sequence of measured wave profiles for both an exponential and half-sine bed displacement for bed lengths, b, of 30.5 cm and 61 cm. The wave amplitude, η, has been normalized by the total bed displacement, ζ_o, and shown as a function of the nondimensional time $t\sqrt{g/h} - (x-b)/h$. Since the wave motion at both $x/h = 0$ and $x/h = b/h$ begins at $t = 0$, the wave profile at the backwall must begin at the abscissa value of b/h. In addition to these two positions in the generation region, three wave measurements are also shown in the downstream region. For the half-sine bed displacement the downstream

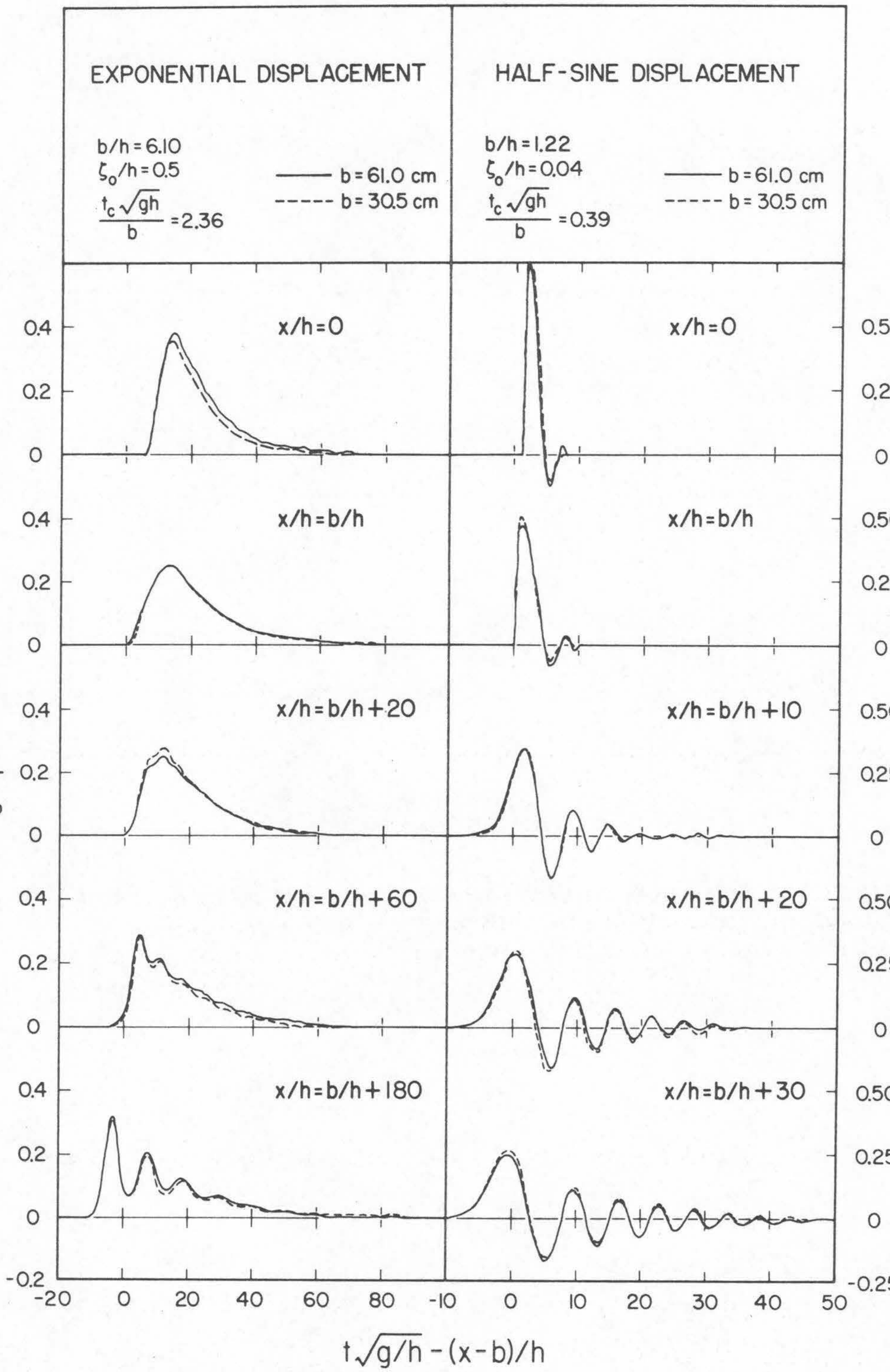

Fig. 5.10 Wave profiles generated by the exponential and half-sine bed displacements when the generation parameters for each motion are held constant and the absolute bed size is varied.

locations are at 10, 20, and 30 depths from the leading edge of the disturbance; for the exponential bed movement measurements were made at 20, 60, and 180 depths from the leading edge. The solid curves in Fig. 5.10 represent the experimental profiles recorded using the larger bed unit (b = 61 cm); the dashed curves represent the profiles recorded at similar locations when the smaller bed unit (b = 30.5 cm) was used. The values of the nondimensional generation parameters (which were held constant for the experiments) are indicated in Fig. 5.10. Various aspects of the propagation characteristics of such waves will be discussed completely in Section 5.2; some of these are presented in Fig. 5.10 only to indicate the similarity of profiles for a change in absolute bed size.

The time-size ratio for the exponential bed displacement lies in the transition region of generation and has a large amplitude scale of $\zeta_o/h = 0.5$. It can be seen that at each location the recorded profiles for this experiment are almost identical for each of the bed unit sizes.

The time-size ratio for the half-sine experiment also lies in the transition region of generation but has a very small amplitude scale of $\zeta_o/h = 0.04$. Again the recorded profiles are almost identical for each bed unit. This, to some extent, confirms the validity of the choice of the generation parameters which were determined in Chapter 3.

The general wave structure in the impulsive region illustrated in Figs. 5.8 and 5.9 for the exponential and half-sine bed movements is typical of the experiments for small disturbance-amplitude scales, i.e., $|\zeta_o/h| \leq 0.2$. For larger amplitude scales, however, the general wave structure in the generation region is altered when the bed movement is impulsive. Wave profiles recorded at $x/h = 0$ and $x/h = b/h$ for a disturbance with $|\zeta_o/h| = 0.4$ are shown in Fig. 5.11 for a positive and negative half-sine bed movement which is impulsive. Again the wave amplitude, η, has been normalized by the bed displacement, ζ_o, and shown as a function of the normalized time, $t\sqrt{g/h}$. The linear theory is again shown as a solid curve with the experimental profiles shown dashed.

For the positive movement in Fig. 5.11, the recorded wave at the backwall has a much larger nodal period than that predicted by the linear theory. At $x/h = 0$ the leading wave is now followed by a single negative wave with a nodal period of the same order of magnitude as that of the leading wave. At the leading edge of the disturbance $(x/h = b/h)$ the water level rapidly rises to a maximum elevation, η_o, where it remains constant for an interval of time after which the amplitude decreases to the SWL. This results in a long negative wave trailing the positive disturbance. The only feature of this wave structure which appears to be predicted reasonably well by the linear theory is the maximum amplitude, η_o, which occurs momentarily in the measured profile. It was found that η_o/ζ_o approached one-half as the

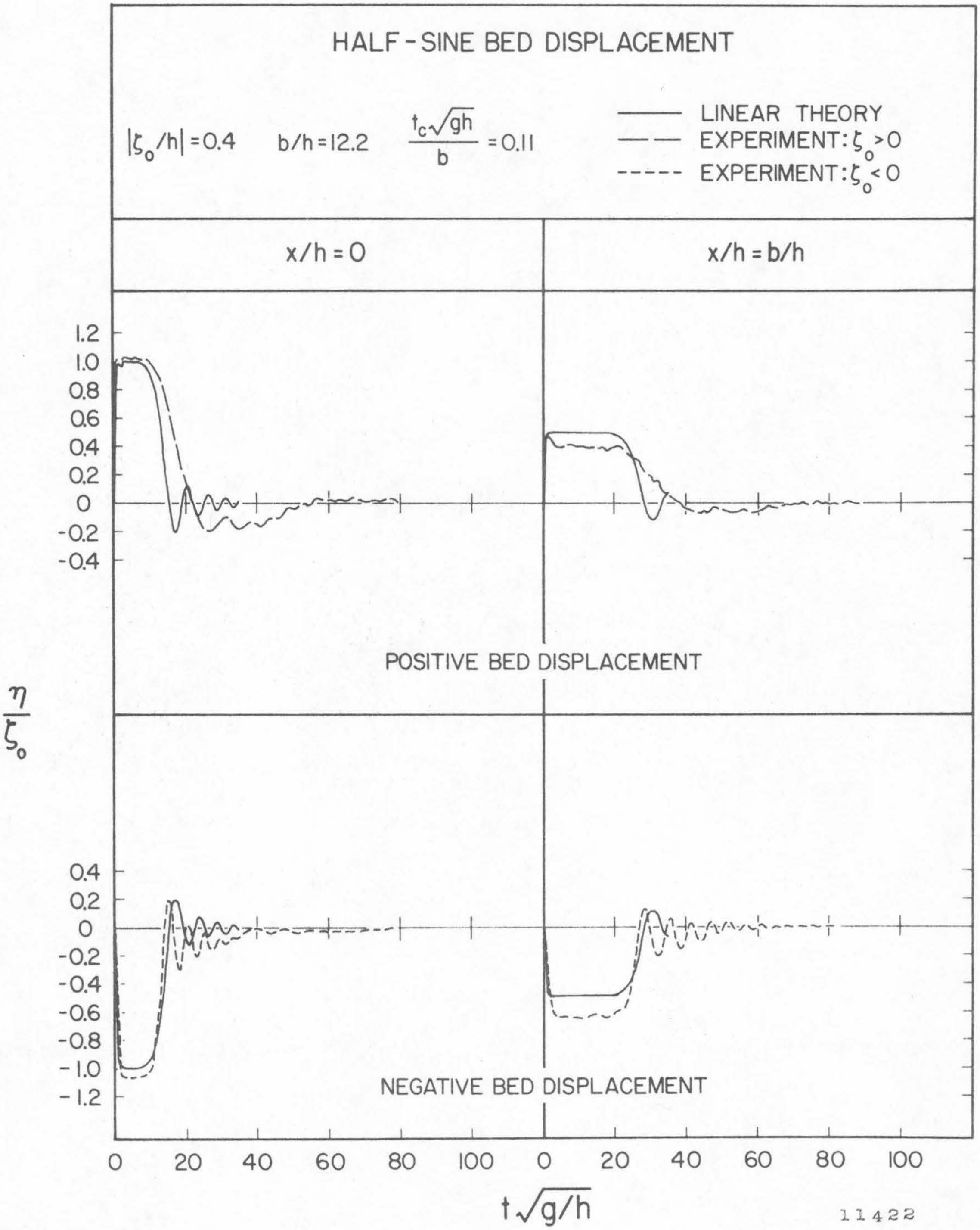

Fig. 5.11 Wave profiles at x/h = 0 and x/h = b/h for a half-sine bed upthrust and downthrow with a large disturbance-amplitude scale, $|\zeta_o/h| = 0.4$.

time-size ratio was decreased within the impulsive region of generation. (This behavior was demonstrated by the data presented in Fig. 5.4 and 5.5.)

The theoretical profiles for the negative bed displacement at $x/h = 0$ and $x/b = b/h$ in Fig. 5.11 appear to predict the temporal variation of the experimental profiles more accurately than for the positive bed displacements. The maximum wave amplitude, η_o, at the leading edge of the disturbance for the measured profile is approximately 20% greater than that predicted by the linear theory.

In other experiments it was noted that as the disturbance-amplitude scale was increased, the temporal variation of the waves shown in Fig. 5.11 was maintained while the differences increased between the measured amplitudes and those computed by the linear theory.

In the preceding discussion the wave forms have been viewed from an Eulerian point of view, i.e., the position of observation has been fixed and variations with respect to time have been observed. It is also useful to observe the wave structure in the generation region by fixing the time of observation and examining the water surface spatially. Lagrangian measurements of this type have been performed in the laboratory photographically in order to fix the motion at a specific time. The experimental arrangement permitted pictures of the water surface to be taken at predetermined times during and after the bed displacement yielding a time sequence of photos showing the temporal evolution of the water surface behavior. (For a full description of the photographic system the reader is referred to Chapter 4.)

The two experiments photographed to illustrate the spatial water surface deformation in the region of generation for the exponential bed displacement had the following generation characteristics: $\zeta_o = \pm 5$ cm, $b = 61$ cm, $t_c = 0.116$ secs, and $h = 10$ cm thus:

$$\zeta_o/h = \pm 0.5, \quad b/h = 6.10, \quad \frac{t_c\sqrt{gh}}{b} = 0.188 \ . \tag{5.4}$$

From Fig. 5.1 this displacement is seen to lie in the transition region of generation. A large disturbance-amplitude scale and small time scale were chosen in order to enable the water surface movements to be easily observed. As indicated by Eq. (5.4), both a positive and a negative bed displacement were investigated; the sequence of photographs obtained for each displacement is presented in Fig. 5.12a and 5.12b. The bed position and times are indicated beneath each photo; the SWL has been marked by a black line in each photo and a vertical scale is indicated on each photograph (in centimeters).

Fig. 5.12a shows the sequence of photographs for the positive bed displacement with photo # 1 showing the undisturbed fluid. In photos #2 and #3 the water surface is essentially following the moving bed section except near the leading edge where a smooth transition occurs between the SWL and rising water surface. In this case, the transitional length between the downstream water depth and the rising water surface in the generation region is due to wave propagation rather than

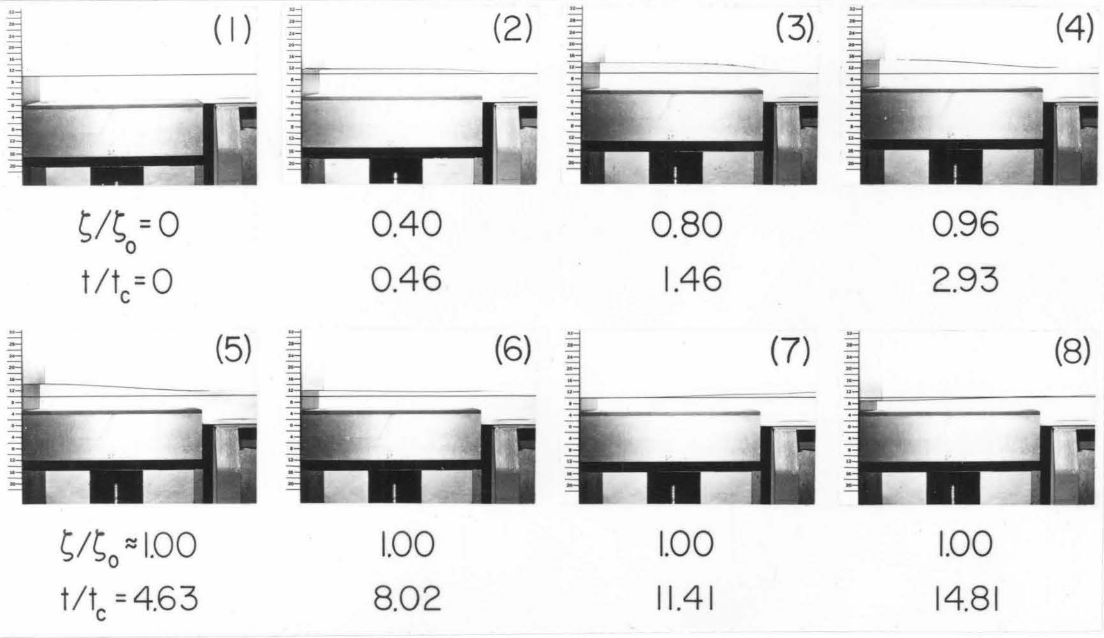

(a)

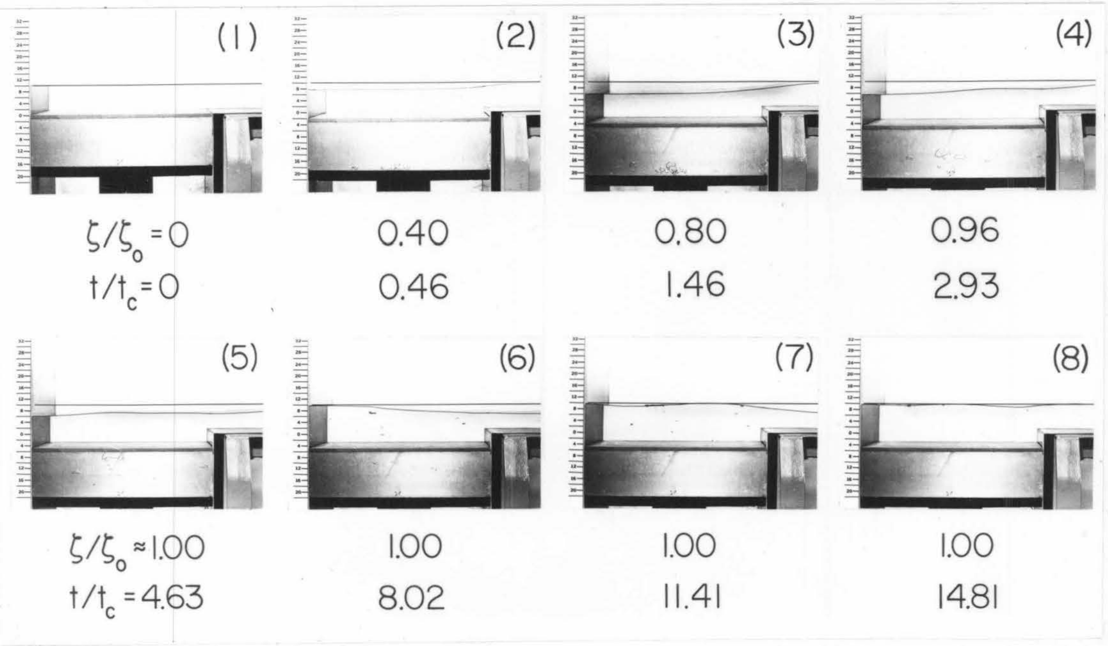

(b)

Fig. 5.12 Spatial variations of the water surface elevation in the generation region for exponential bed displacements; a) bed upthrust, b) bed downthrow.

the elliptic response of the fluid. A long wave traveling with a velocity of $\sqrt{gh} = 99$ cm/sec has had an opportunity to propagate a distance of approximately 17 cm upstream and downstream of the leading edge in photo #3, yielding a transition length of 34 cm which is approximately the length of the transition scaled from the photograph. In photo #4 a positive wave can definitely be seen leaving the generation region while a negative wave is retreating over the bed unit. In photo #5 the negative wave has reached the backwall where the water level is now decreasing. This continues in photo #7 until in photo #8 the water at the backwall has returned to the still water level. A small negative wave forms in photo #8 trailing the positive leading wave.

The corresponding sequence of photographs for the negative exponential bed displacement is shown in Fig. 5.12b; again photo #1 shows the undisturbed fluid. In photo #2 and #3 the water surface is deforming in the same manner as the bed unit except near the leading edge where a smooth transition with a length of approximately 34 cm occurs between the two water levels. Photos #4 and #5 show a positive wave entering the generation region which has reached the backwall in photo #6 where the water level has returned to the SWL. In photo #7 the trailing portion of the negative leading wave is shown leaving the generation region while photo #8 shows small amplitude oscillations forming behind the leading wave.

The presence of air entrained around the seal of the bed unit during rapid bed movements is illustrated by the sequence of photos shown in Fig. 5.12b. Examination of the area just above the seal in photo #2 shows that air bubbles have formed between the moving bed unit and the glass sidewalls of the wave tank. The bubbles increase in size and begin to rise into the fluid during the displacement and reach the free surface of the fluid domain in photo #7. As suggested earlier, the leakage of air around the seal for rapid bed displacements may account for some of the differences which were noted between the experimental and theoretical wave profiles shown in Fig. 5.9 (especially at the backwall).

A comparison of the photographs in Fig. 5.12a and Fig. 5.12b for bed upthrust and downthrow is also of interest. Since the photos were taken at identical positions during the bed displacement, a direct comparison of wave behavior is possible. As stated previously, the linear theory suggests that wave profiles, whether Eulerian or Lagrangian, are mirror images about the still water level for positive and negative bed movements with the same generation parameters. In photos #2 and #3 the corresponding water surfaces do indeed appear to be mirror images of each other. Slight discrepancies begin to appear in photo #4 which increase in magnitude in the remaining photos. These discrepancies are probably caused by the nonlinear effects introduced by the large amplitude scale of the bed displacement.

The experiment which was photographed to illustrate the water surface deformation in the region of generation for the half-sine bed displacement had the characteristics: $\zeta_o = \pm 5$ cm, b = 61 cm,

$t_c = 0.20$ secs, and $h = 10$ cm with the following generation parameters:

$$\zeta_o/h = \pm 0.5,\ b/h = 6.10,\ \frac{t_c\sqrt{gh}}{b} = 0.324. \qquad (5.5)$$

Fig. 5.2 indicates that this time-size ratio lies in the impulsive region of generation near the boundary of the transition region. The sequence of photos for the case of bed uplift is shown in Fig. 5.13a. Again a black line is used to indicate the SWL and a vertical scale graduated in centimeters is shown in each photograph. Beneath each photograph the position of the bed unit in space and time is indicated.

The evolution of the water surface shown in Fig. 5.13a is very similar to that shown for the exponential bed displacement in Fig. 5.12a. The water surface essentially follows the bed unit in photos #2 and #3. In photo #4 a wave can be seen leaving the generation region and in photo #5 the water level at the backwall has begun to decrease. The trailing portion of the leading wave can be seen developing in the remaining photos.

The photographic sequence for bed downthrow for a half-sine bed displacement program is shown in Fig. 5.13b. The wave behavior is similar to that shown in Fig. 5.12b for the exponential time history of the bed displacement. Comparison of the individual photos between the case of positive bed movement shown in Fig. 5.13a and the negative movement of Fig. 5.13b again demonstrates that the detailed wave profiles are not the mirror image of each other due to the large amplitude scale used in this experiment ($\zeta_o/h = \pm 0.4$).

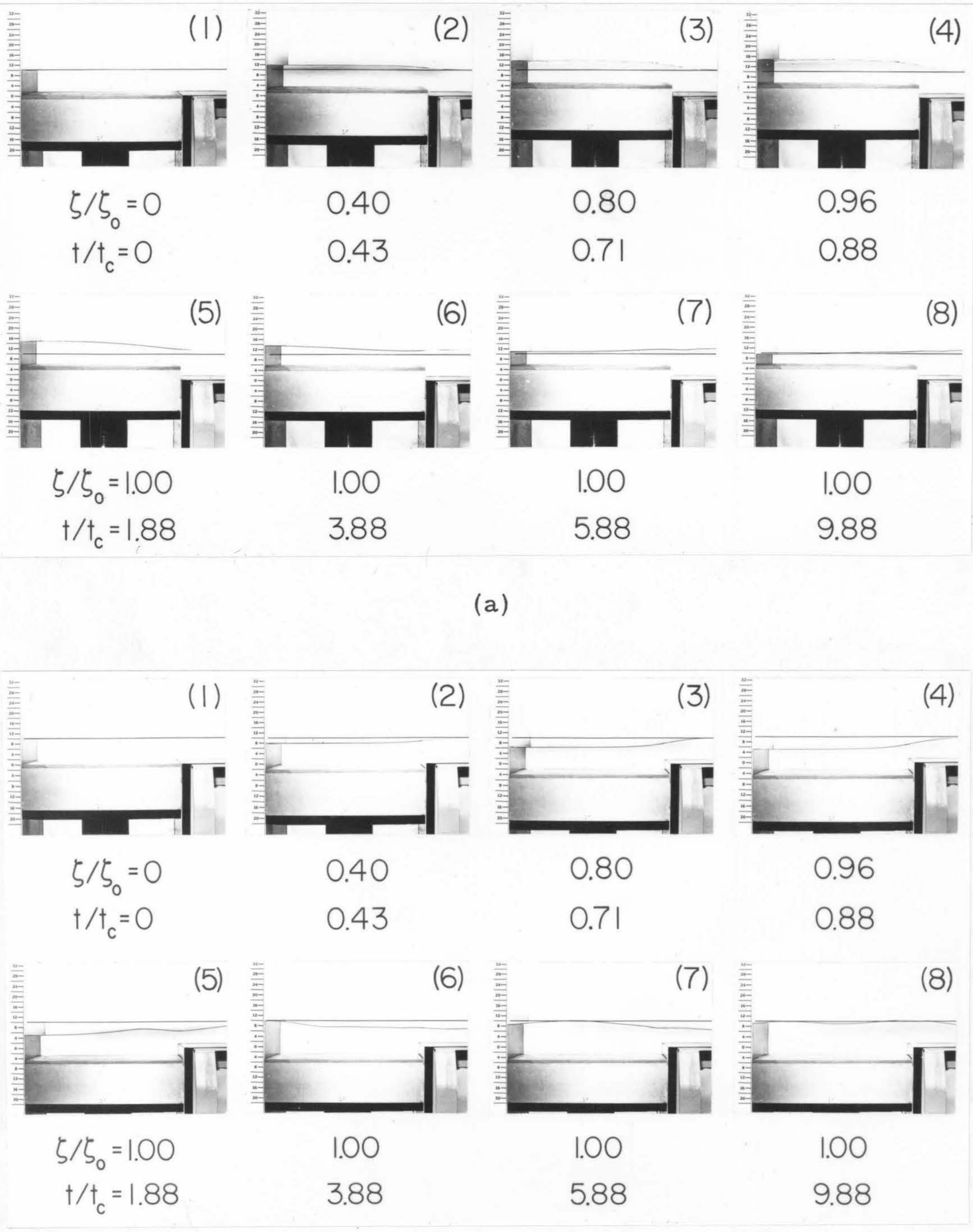

(b)

Fig. 5.13 Spatial variations of the water surface elevation in the generation region for half-sine bed displacements; a) bed upthrust, b) bed downthrow.

5.1.3 Wave Periods in the Generation Region.

All wave profiles occurring in the region of generation and described in the preceding section were complex in shape, i.e., nonperiodic, over the full ranges of the generation parameters (b/h, ζ_o/h, and $t_c\sqrt{g/h}$) which were investigated. For these complex wave shapes, no single period exists which adequately describes the temporal variation of the entire wave profile. Fortunately, most of the displaced volume of water (and wave energy) for the wave profiles illustrated in Section 5.1.2 is contained in the leading wave. Three periods appear to adequately describe the temporal variation for most of the various complex shapes of the lead waves found in the region of generation.

Consider the typical profile of the leading wave in the generation region illustrated by the sketch in Fig. 5.14a and Fig. 5.14b for an impulsive, positive and negative bed displacement, respectively. For

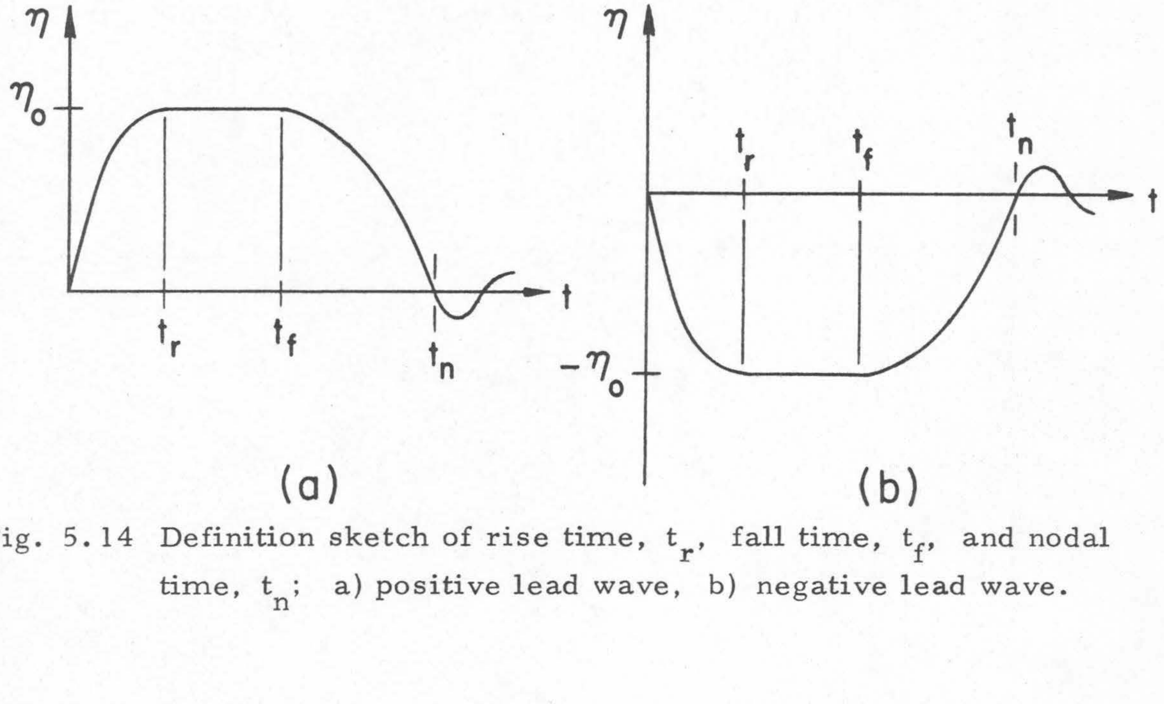

Fig. 5.14 Definition sketch of rise time, t_r, fall time, t_f, and nodal time, t_n; a) positive lead wave, b) negative lead wave.

the positive bed displacement the water rises to a maximum height, η_o, in a period t_r, remains at this amplitude until the time t_f, and then begins to decrease to the still water level which is reached at the time, t_n. Similar time intervals are shown in Fig. 5.14b for the leading wave generated by a negative bed displacement. (The times t_r, t_f, and t_n will hereafter be referred to as the rise time, fall time, and nodal time, respectively.

It should be noted that the shape of the leading wave shown in Fig. 5.14a for an impulsive positive bed displacement is not characteristic of all the profiles at the leading edge of the disturbance. When the disturbance-amplitude scale is large, i.e., $\zeta_o/h > 0.2$, and the bed displacement is impulsive, a typical wave profile of the leading wave recorded at the leading edge is shown in Fig. 5.11. The water surface for this case requires at least one more amplitude, (corresponding to the constant height which the water surface maintains over some time interval) and time interval (corresponding to the interval before the constant wave height is reached) to describe the temporal variation of these waves. No effort will be made in this section to describe the temporal variation of these wave profiles at $x/h = b/h$ except in terms of the notation shown in Fig. 5.14a.

Fig. 5.15 shows the experimental and theoretical periods: t_r, t_f, and t_n, for leading waves at the backwall ($x/h = 0$) which were generated by an exponential bed displacement. The wave periods have been normalized by the characteristic time of the bed movement, t_c,

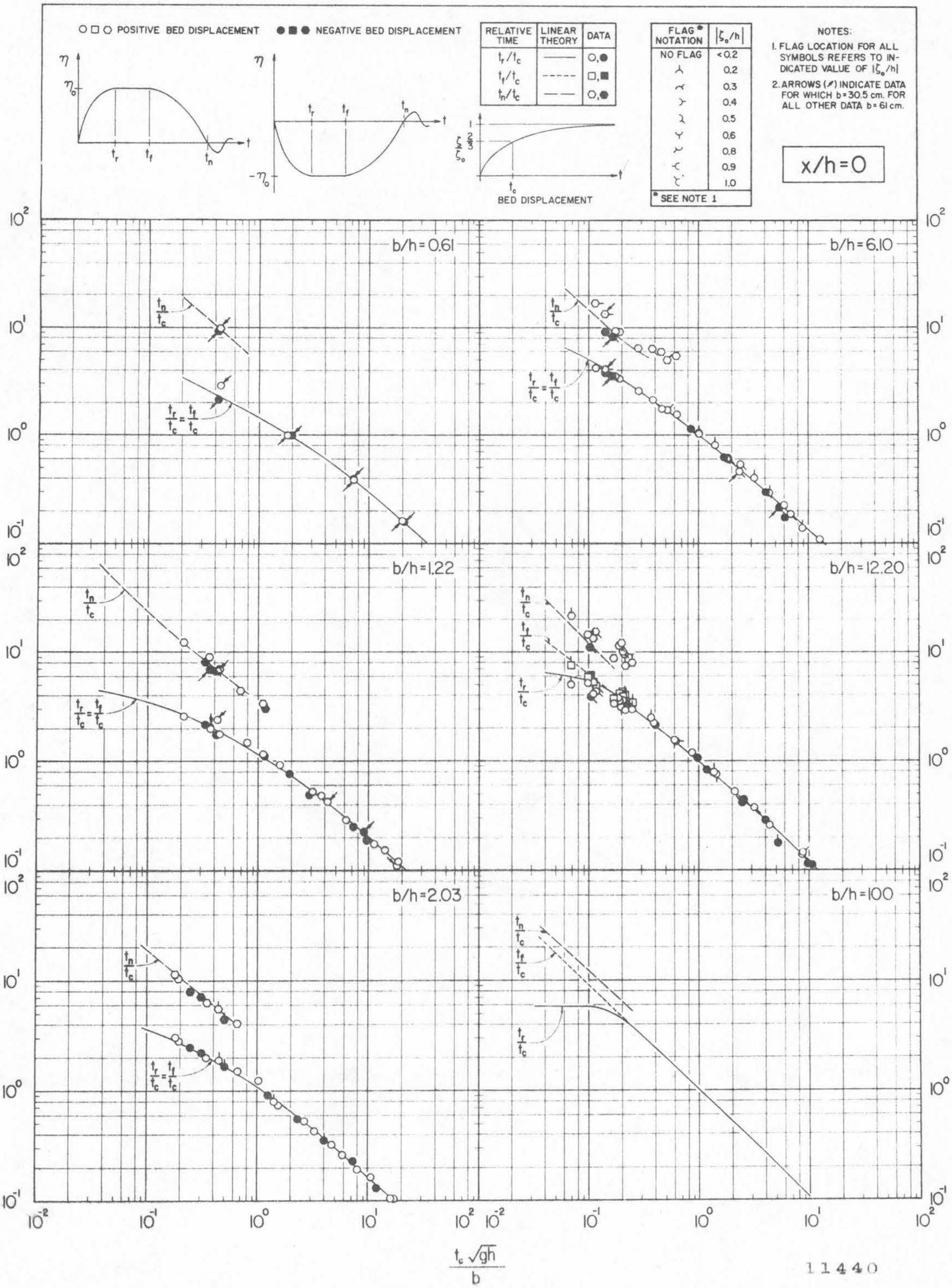

Fig. 5.15 Variation in t_r/t_c, t_f/t_c, and t_n/t_c of the lead wave with the time-size ratio, $t_c\sqrt{gh}/b$, at $x/h = 0$ for exponential bed displacements.

and shown separately for each disturbance-size scale, b/h, as a function of the time-size ratio, $t_c\sqrt{gh}/b$. The theoretical curves shown for each period have been computed from the linear theory given by Eq. (3.67). Hollow symbols are again used to indicate data for positive bed displacements while solid symbols indicate data for which a negative movement of the bed occurred. Three different symbols (see the legend of Fig. 5.15) are used to indicate the normalized rise time, fall time, and nodal times for each wave. The notation for the disturbance-amplitude scale for each experiment is shown in the table in the legend of Fig. 5.15. Arrows adjacent to certain data again indicate experiments for which the smaller bed unit, b = 30.5 cm, was used; for all other experiments b = 61 cm.

Typical wave profiles in the generation region for an exponential bed displacement have been previously shown in Fig. 5.8. The rise and fall times of the lead wave are observed to be equal in this figure for both the transition and creeping regions of generation. When the rise and fall times for a wave profile are equal, only the rise time symbol and the theoretical curve for rise times are shown in Fig. 5.15. It is also observed from Fig. 5.8 that the wave forms at both the back-wall and the leading edge in the creeping region of generation resemble a bore; hence, the nodal time becomes a meaningless measurement. No data or theory are indicated in Fig. 5.15 for the nodal times in this region of generation. It should be noted that measurements of the rise times for experimental wave forms became more difficult for very fast bed movements (t_c < 0.1 secs) due to the relatively slow speed at which the wave forms were recorded (1 cm/sec). Some difficulty was also experienced in defining the rise times for very slow bed movements in which the maximum wave elevation was approached at a very slow rate. (Theoretical computations have also been made for the disturbance-size scale of $b/h = 100$ for which no experimental data exist.)

The theoretical results presented in Fig. 5.15 for the rise, fall, and nodal-time ratios for the size scales: $b/h = 0.61$, 1.22, and 2.03, agree well with the experimental data for both positive and negative bed displacements. For these three disturbance-size scales, no amplitude scale greater than 0.2 was used and the rise and fall times are equal for the full range of time-size ratios investigated.

For $b/h = 6.10$ the theoretical results agree well with the experimental data for the rise and fall-time ratios which are equal over the full range of $t_c\sqrt{gh}/b$ which was investigated. Some of the data have disturbance-amplitude scales as large as 0.5; hence, the amplitude scale appears to have little effect on the rise and fall times at the backwall. (Recall from Section 5.1.1 that the relative wave amplitude, η_o/ζ_o, at the backwall also appeared to be predicted by the linear theory over the full range of disturbance-amplitude scales.) The theoretical nodal times for $b/h = 6.10$ no longer agree as well with the data as for the smaller size scales. Measured nodal times for positive bed displacements are consistently larger than those predicted by the linear theory, with a possible weak dependence on the amplitude scale; this behavior was also shown in Fig. 5.8 by the wave profiles in the impulsive region of generation. The nodal time data for negative bed displacements which have an amplitude scale of $\zeta_o/h = -0.5$ are slightly smaller than those predicted by the linear theory.

For the disturbance-size scale: $b/h = 12.2$, in Fig. 5.15, a region of the time-size ratio exists which is given approximately by $t_c\sqrt{gh}/b < 10^{-1}$ where the rise and fall times are no longer equal. This region is indicated by both the experimental and theoretical results. The linear theory for the fall-time ratio, t_f/t_c, agrees well with all data in this region; however, the theory for the rise times, t_r/t_c, appears to predict a larger rise-time ratio than observed in the experiments for the data with an amplitude scale greater than 0.2. No definite conclusions can be stated regarding a possible disturbance-amplitude scale effect on rise or fall times in this region due to the limited amount of data available.

The linear theory for $b/h = 12.2$ in Fig. 5.15 predicts a smaller nodal-time ratio, t_n/t_c, than indicated by the data for positive bed displacements, regardless of the disturbance-amplitude scale; this same behavior was also observed for $b/h = 6.10$ in Fig. 5.15. It does appear from the experimental data that t_n/t_c increases as ζ_o/h increases. The single data point for a negative bed displacement with $\zeta_o/h = -0.5$ is only slightly smaller than the value predicted by the linear theory.

The theoretical results for $b/h = 100$ presented in Fig. 5.15 indicate that the rise-time ratio becomes approximately constant for a time-size ratio less than 10^{-1}, i.e., in the impulsive region of generation. For $t_c\sqrt{gh}/b > 0.2$ the rise-time ratio appears to become inversely proportional to the time-size ratio, i.e., $t_r/t_c \propto (t_c\sqrt{gh}/b)^{-1}$. The fall-time ratio, t_f/t_c, is inversely proportional to $t_c\sqrt{gh}/b$ over the full range of the time-size ratio investigated and is equal to t_r/t_c for $t_c\sqrt{gh}/b > 0.2$. The theoretical curve for the nodal-time ratio is slightly above and approximately parallel to the curve for the fall-time ratio; hence, the temporal variation of the wave forms generated for $b/h = 100$ at the backwall when $t_c\sqrt{gh}/b < 0.1$ may be found by extrapolating the curves. Since the curves for t_n/t_c and t_f/t_c appear to be parallel in the impulsive region of generation, the ratio t_n/t_f is approximately constant. Note that the theoretical curves for t_n/t_c do not vary appreciably between $b/h = 12.2$ and $b/h = 100$.

Fig. 5.16 shows the theoretical and experimental time ratios: t_r/t_c, t_f/t_c, and t_n/t_c, as a function of $t_c\sqrt{gh}/b$ at the backwall ($x/h = 0$) for the half-sine bed displacement. The notation used is identical to that shown in Fig. 5.15 for the exponential bed displacement and is repeated in the legend of Fig. 5.16. Theoretical curves for t_r/t_c, t_f/t_c, and t_n/t_c have been computed by the linear theory, Eq. (3.68), for each disturbance-size scale investigated experimentally and for $b/h = 100$.

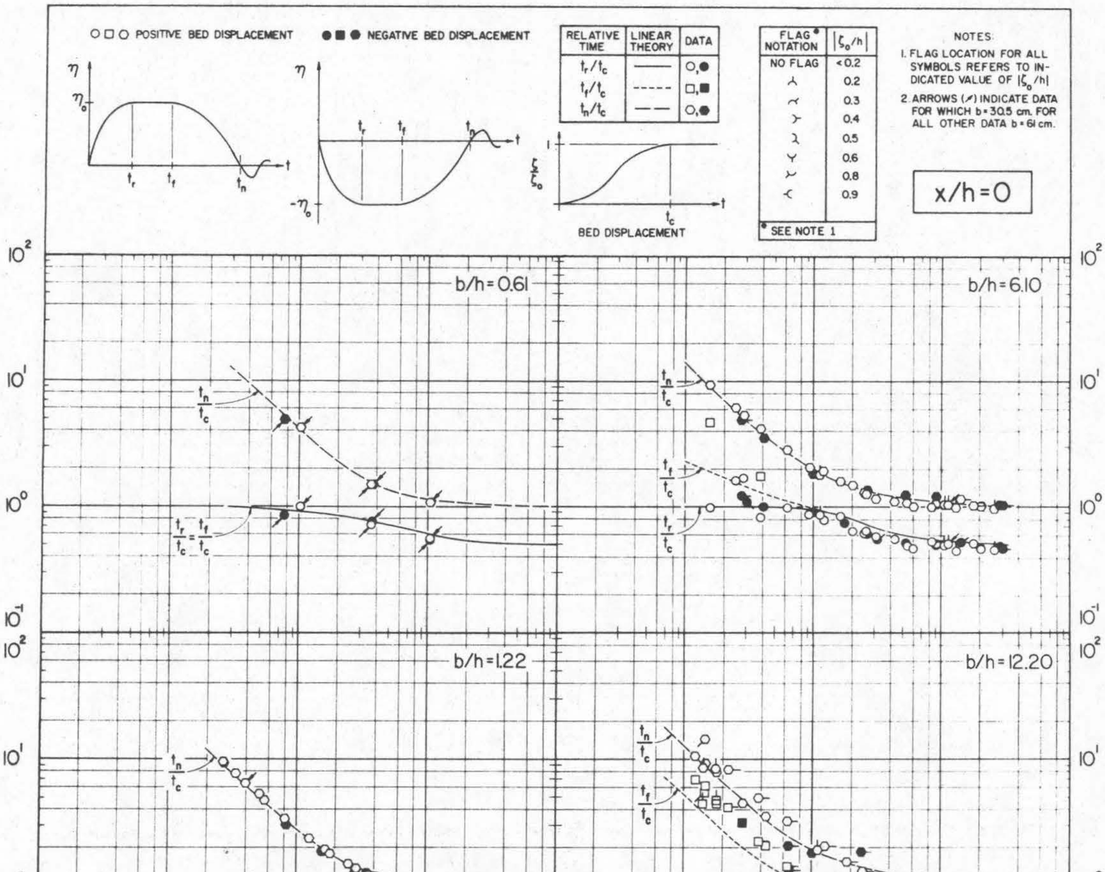

Fig. 5.16 Variation in t_r/t_c, t_f/t_c, and t_n/t_c of the lead wave with the time-size ratio, $t_c\sqrt{gh}/b$, at x/h = 0 for half-sine bed displacements.

The linear theory for t_r/t_c, t_f/t_c, and t_n/t_c presented in Fig. 5.16 appears to agree well with the data for $b/h = 0.61$ for both positive and negative bed displacements. The rise and fall times for this disturbance-size scale are equal over the full range of the time-size ratio which was investigated. For a time-size ratio less than 0.4, i.e., the impulsive region of generation, the rise and fall-time ratio approaches unity; hence, the water rises at the backwall until the bed movement is completed and immediately begins to decrease to the still water level. The nodal-time ratio in the impulsive region of generation increases as the time-size ratio decreases. In the creeping region of generation, i.e., $t_c\sqrt{gh}/b > 40$, the rise and fall-time ratios become equal to 0.5 indicating that the water level at the backwall begins to decrease once the bed has moved through one-half of its total displacement. The nodal-time ratio in the creeping region of generation, becomes asymptotic to unity. Since, the rise and fall-time ratios are equal to 0.5 in this region, the rise and fall times occur midway the nodal-time interval thus indicating a symmetrical wave shape (see, e.g., Fig. 5.9).

For $b/h = 1.22$ and 2.03 the rise and fall-time ratios in Fig. 5.16 remain equal over the full range of $t_c\sqrt{gh}/b$ investigated. The behavior of $t_r/t_c = t_f/t_c$, and t_n/t_c suggested by the linear theory for these size scales in the impulsive, transition, and creeping regions of generation is similar to that observed for $b/h = 0.61$. The agreement of the linear theory with the data for these two disturbance-size scales is reasonably good except for several experiments for negative bed displacements in the impulsive region of generation when $b/h = 2.03$. These measurements indicate a smaller nodal time than the other data and the linear theory in this region; hence, these data are probably erratic points. The linear theory appears to consistently indicate a slightly larger rise, fall, and nodal time for these size scales over the full range of the time-size ratio investigated.

For $b/h = 6.10$ the linear theory in Fig. 5.16 suggests the same general behavior for t_r/t_c and t_n/t_c in each region of generation as found for the smaller disturbance-size scales. However, the fall-time ratio is now larger than the rise-time ratio in the region $t_c\sqrt{gh}/b < 1$; hence, for this region, the amplitude of the leading wave reaches a maximum at the time t_r and remains constant for the time interval given by t_f-t_r. As the time-size ratio becomes greater than unity the rise and fall times are equal and approach a value of one-half the characteristic time, t_c. For $t_c\sqrt{gh}/b > 10$ the nodal-time ratio becomes equal to unity; hence, a symmetrical wave shape results in the creeping region of generation as discussed previously. In the region $t_c\sqrt{gh}/b < 1$ where the linear theory indicates that the fall time is no longer equal to the rise time, the agreement of the linear theory with the data is reasonably good except for the fall-time ratio, t_f/t_c. The data for t_r/t_c and t_f/t_c in this region are somewhat inconsistent with several experiments indicating equal rise and fall times while others result in different values; this behavior may simply be due to experimental error.

The linear theory for the nodal-time ratio appears to agree well with all data for both positive and negative bed displacements. It should be noted that an insufficient amount of data are available to indicate any possible nonlinear effects due to large disturbance-amplitude scales.

The data presented for $b/h = 12.2$ in Fig. 5.16 cover a larger range of disturbance-amplitude scales given by $0 < |\zeta_o/h| \leq 0.8$, and are thus more indicative of any nonlinear effects caused by large amplitude scales. No nonlinear effect is evident for the rise-time ratio, t_r/t_c, over the full range of $t_c\sqrt{gh}/b$ which was investigated; however, all of the data for the rise times consistently indicate a smaller rise time than that predicted by the linear theory independent of the disturbance-amplitude scale. The fall-time ratio becomes larger than the rise-time ratio in the region $t_c\sqrt{gh}/b < 1$. The data for the fall times in this region indicate a larger fall time than that predicted by the linear theory, apparently independent of the disturbance-amplitude scale and the direction of the bed movement. (Note that all of the data in this region have a fall time different from the rise time; hence, the data in the impulsive region of $b/h = 6.10$ in which the rise and fall times were equal and greater than unity do indeed appear to be erroneous.) The linear theory for the nodal-time ratio agrees well with the data which correspond to $|\zeta_o/h| \leq 0.2$; however, the data for positive bed displacements with $\zeta_o/h > 0.2$ have a larger nodal time in the impulsive and transition region of generation than that predicted by the linear theory. This nonlinear behavior of the nodal times at the backwall was also shown in Fig. 5.11 for a positive bed movement. An insufficient amount of data is available for negative bed movements to suggest a corresponding nonlinear behavior. In the creeping region of generation, i.e., $t_c\sqrt{gh}/b > 4$ (see Fig. 5.2), the linear theory for t_n/t_c agrees well with the experimental data over the full range of disturbance-amplitude scales.

The linear theory for the rise, fall, and nodal-time ratios when $b/h = 100$ is similar to that described for $b/h = 6.10$ and 12.2. For $t_c\sqrt{gh}/b < 1$ the rise-time ratio is equal to unity and the fall-time ratio (t_f/t_c) is larger than t_r/t_c and increases as the time-size ratio decreases. The nodal-time ratio is slightly larger than t_f/t_c and the difference between these two ratios appears to decrease as $t_c\sqrt{gh}/b$ decreases. For $t_c\sqrt{gh}/b > 10$ the nodal-time ratio is asymptotic to unity and the rise and fall-time ratios (which are now equal) become asymptotic to 0.5. All curves appear to be linear on the log-log representation for the asymptotic conditions of large and small time-size ratios; hence, extrapolation to smaller $t_c\sqrt{gh}/b$ may be possible. However, extrapolation of the curves for t_f/t_c and t_n/t_c to time-size ratios less than 10^{-1} would appear to eventually yield a point at which these two ratios became equal; no further extrapolation should then be made. Note that the theoretical curves for t_r/t_c and t_n/t_c do not vary appreciably between $b/h = 12.2$ and $b/h = 100$. It also appears that the fall-time ratio approaches the nodal-time as the size scale increases for a constant value of $t_c\sqrt{gh}/b$ in the impulsive region of generation.

Fig. 5.17 shows the theoretical and experimental results for the time ratios: t_r/t_c, t_f/t_c, and t_n/t_c, as a function of $t_c\sqrt{gh}/b$ at the leading edge of the bed section for an exponential bed displacement; i.e., at $x/h = b/h$. The notation for the data and theory is the same as used in Figs. 5.15 and 5.16 and is described again in the legend of Fig. 5.17. No data or theory are shown for the nodal-time ratio, t_n/t_c, in the creeping region for each disturbance-size scale since the wave profile in this region resembles a bore (see, e.g., Fig. 5.8). In addition, the rise and fall times are equal as shown in Fig. 5.8 and only data symbols for the rise times are presented.

For the three size scales: $b/h = 0.61$, 1.22, and 2.03, the rise and fall-time ratios shown in Fig. 5.17 are equal over the full range of the time-size ratio, $t_c\sqrt{gh}/b$, which was investigated. The theory for each of these size scales agrees well with the data. (Recall that no disturbance-amplitude scale greater in absolute value than 0.2 was used for these size scales.)

For $b/h = 6.10$, 12.2, and 100 the linear theory shown in Fig. 5.17 suggests that the rise and fall times are no longer equal for $t_c\sqrt{gh}/b < 0.4$; Fig. 5.6 showed that this region corresponded to the impulsive region of generation for these size scales. In the impulsive region of $b/h = 6.10$ the linear theory for the rise-time ratio agrees fairly well with all data for negative bed movements regardless of amplitude scale and with the data for positive bed movements for which $\zeta_o/h < 0.2$. The data for positive bed displacements with amplitude

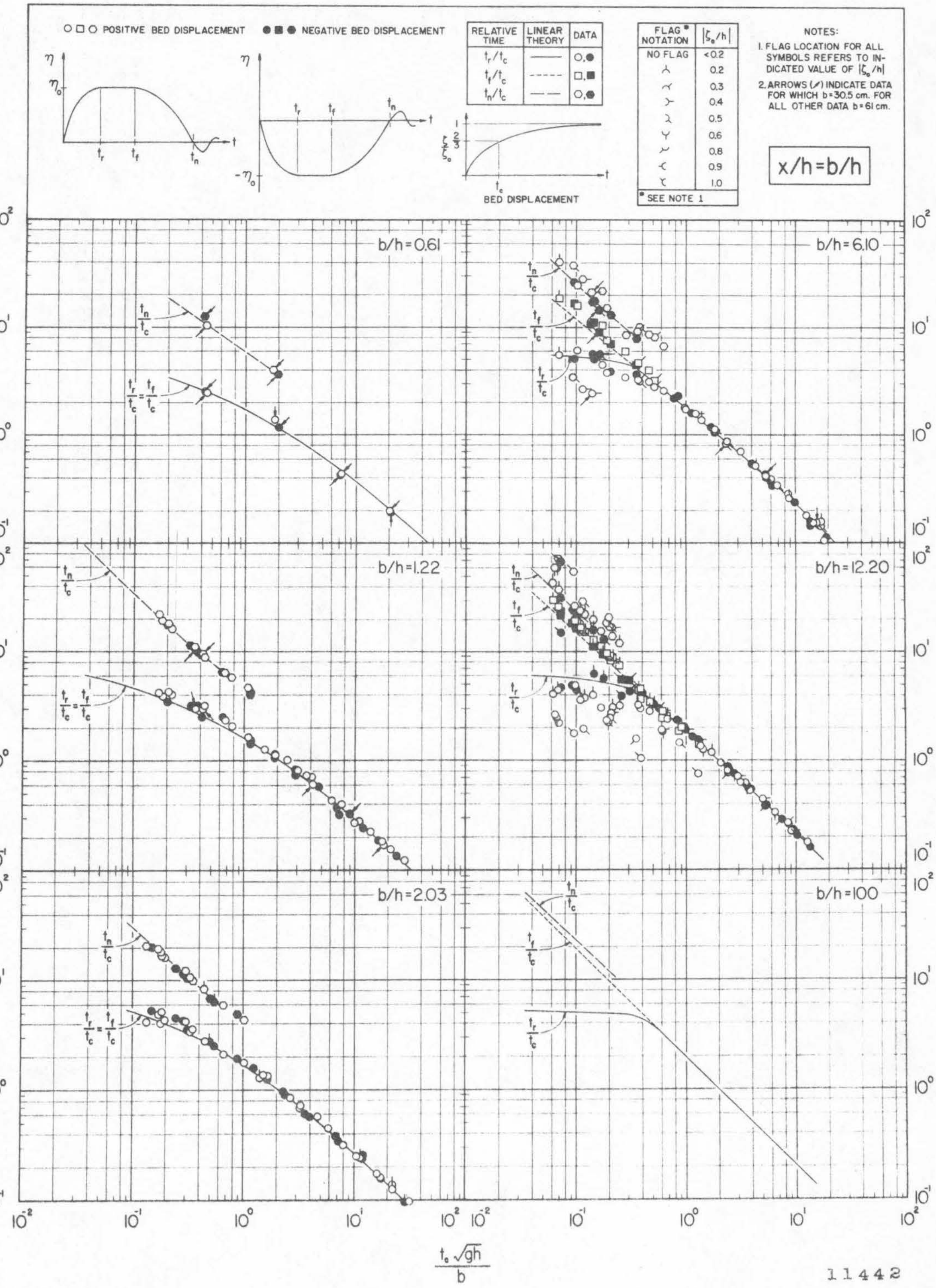

Fig. 5.17 Variation in t_r/t_c, t_f/t_c, and t_n/t_c of the lead wave with the time-size ratio, $t_c\sqrt{gh}/b$, at $x/h = b/h$ for exponential bed displacements.

scales greater than 0.2 show a much smaller rise time than that predicted by the linear theory. This nonlinear behavior of the rise times for large amplitude scales and positive bed movements is more dramatically demonstrated by the data for $b/h = 12.2$ where the maximum amplitude scale is unity. Here this nonlinear effect is also evident in the transition region of generation, i.e., $0.4 < t_c\sqrt{gh}/b < 4$. In the creeping region for $b/h = 6.10$ and 12.2, the linear theory for the rise-time ratio (which is also equal to the fall-time ratio) agrees well with the data regardless of the amplitude scale of the disturbance and the direction of the bed movement.

The linear theory for the fall-time ratio in the region $t_c\sqrt{gh}/b < 0.4$ for $b/h = 6.10$ and 12.2 appears to be slightly smaller than the values indicated by the experiments, regardless of the disturbance-amplitude scale or the direction of bed movement. No nonlinear effects due to large amplitude scales are apparent for the fall times; however, it should be noted that, for some experiments, positive amplitude scales greater than 0.2 result in waves resembling those shown in Fig. 5.11. For those wave profiles the rise and fall times are equal and fall-time data for these experiments are not shown in Fig. 5.17. The theoretical results for the nodal times appear to agree well with the data for negative bed displacements and the theory consistently predicts a nodal time slightly less than the observed values for positive bed displacements regardless of the amplitude scale. This behavior can also be seen in the profiles presented in Fig. 5.8.

It is evident from the experimental results for the nodal times for these two size scales that a nonlinear effect due to large bed displacements is present, i.e., as the amplitude scale increases, the nodal-time ratio also increases thus deviating more from the value predicted by the linear theory.

The theoretical computations for $b/h = 100$ in Fig. 5.17 again show that the rise and fall-time ratios become different for $t_c\sqrt{gh}/b < 0.4$. In this region the rise-time ratio becomes constant at a value of approximately five compared to a value of six at the backwall. The fall-time ratio in this region (and also for $t_c\sqrt{gh}/b > 0.4$) is inversely proportional to the time-size ratio, i.e., $t_f/t_c \propto (t_c\sqrt{gh}/b)^{-1}$. The curve for t_n/t_c (shown only for $t_c\sqrt{gh}/b < 0.1$) is only slightly above the curve for the fall-time ratio; the difference between these curves seems to decrease as $t_c\sqrt{gh}/b$ decreases on the log-log representation. (This behavior for $b/h = 100$ is similar to that observed in Fig. 5.15 at the backwall.) Note that the theoretical curves for t_r/t_c and t_n/t_c do not differ appreciably between $b/h = 12.2$ and $b/h = 100$. The theoretical curve for t_f/t_c appears to be approaching t_n/t_c on this log-log representation as the size scale increases for a constant value of $t_c\sqrt{gh}/b$ in the impulsive region of generation; hence, the ratio t_n/t_f is decreasing toward unity as b/h increases.

The temporal variations of the leading wave profiles generated by a half-sine bed displacement at $x/h = b/h$ are shown in Fig. 5.18 where the ratios: t_r/t_c, t_f/t_c, and t_n/t_c are presented as a function of

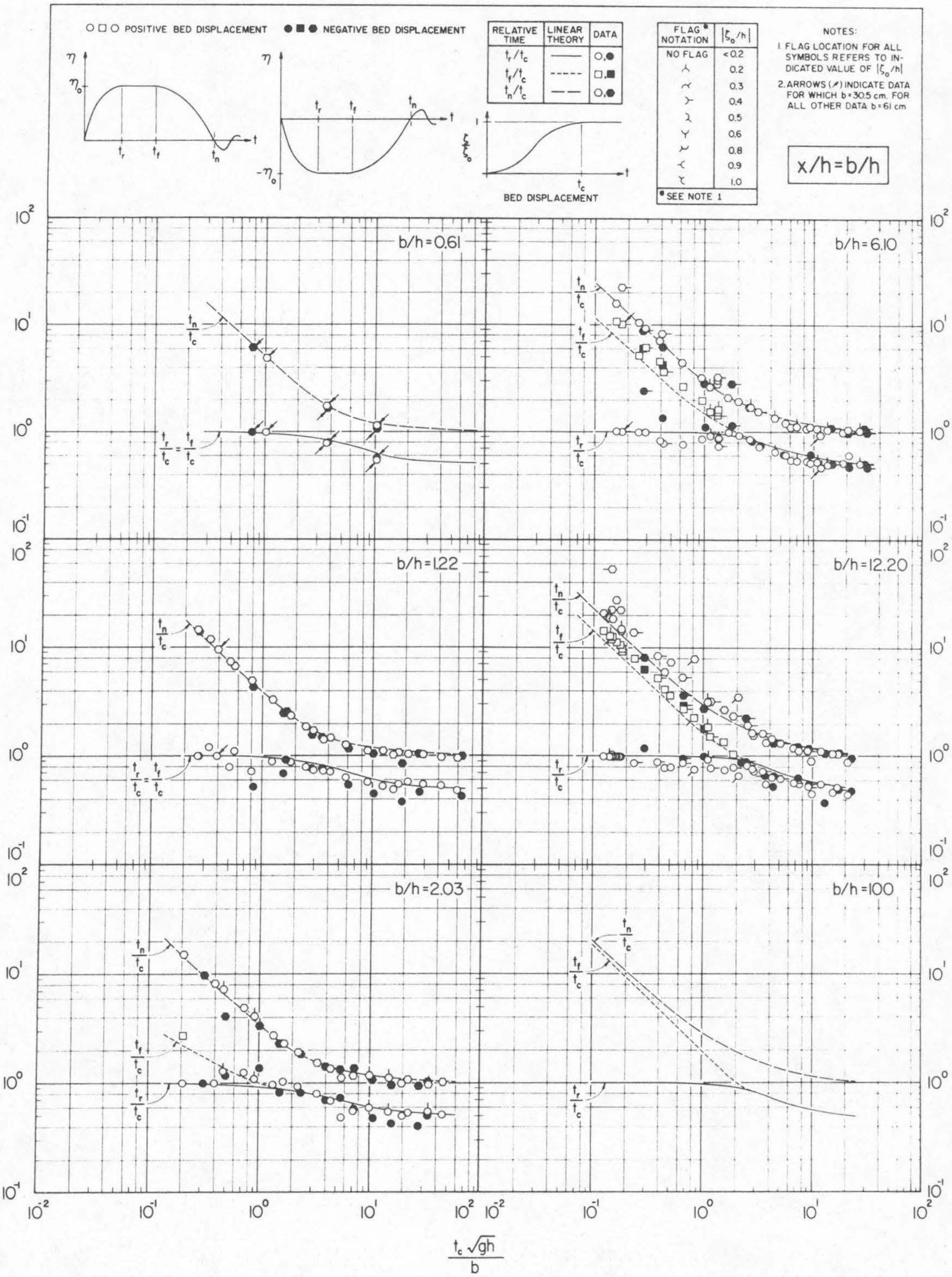

Fig. 5.18 Variation in t_r/t_c, t_f/t_c, and t_n/t_c of the lead wave with the time-size ratio, $t_c\sqrt{gh}/b$, at $x/h = b/h$ for half-sine bed displacements.

$t_c\sqrt{gh}/b$. The same notation is used in this figure for the theoretical and experimental results as was used previously in Figs. 5.15, 5.16, and 5.17 and a summary of this notation appears in the legend of Fig. 5.18. (It should be mentioned again that in the experiments where the fall times and the rise times are equal only the rise times are shown.)

For the two smallest size scales ($b/h = 0.61$ and 1.22) the rise and fall-time ratios shown in Fig. 5.18 are equal over the full range of $t_c\sqrt{gh}/b$ investigated. This behavior is indicated by both the experimental data and the theoretical computations. The linear theory appears to agree reasonably well with the experimental data, especially for the smaller size scale ($b/h = 0.61$). A tendency does appear to exist, however, for the linear theory to slightly over-estimate the rise-time ratio for $b/h = 1.22$. For $t_c\sqrt{gh}/b < 1$ the rise and fall-time ratios (which are equal for these two size scales) become asymptotic to unity while the nodal-time ratio increases rapidly as $t_c\sqrt{gh}/b$ decreases. For $t_c\sqrt{gh}/b > 40$ the rise and fall-time ratios become asymptotic to 0.5 while the nodal-time ratio approaches unity; hence, a symmetric wave shape is generated similar to the profile shown in Fig. 5.9. These asymptotic conditions for large and small time-size ratios for the theory and data at the leading edge are similar to those observed in Fig. 5.16 at the backwall.

For $b/h = 2.03$ the linear theory shown in Fig. 5.18 indicates that the rise and fall-time ratio are no longer equal in the region $t_c\sqrt{gh}/b < 1$; however, all data do not appear to confirm this suggested behavior. A similar inconsistency was observed in data for experiments at the backwall in Fig. 5.16 for $b/h = 6.10$. In the discussion of Fig. 5.16 it was suggested that this inconsistency was probably caused by anomalities in the experimental measurements; this may also be true of the experimental data shown in Fig. 5.18. In general, it can be seen that there is fairly good agreement between theory and experiment. The nodal-time ratio for this size scale appears to be accurately predicted by the linear theory over the full range of $t_c\sqrt{gh}/b$ which was investigated. It should be noted that no disturbance-amplitude scale greater than 0.2 (in absolute value) was investigated.

The linear theory presented in Fig. 5.18 for the rise-time ratio of the two size scales: $b/h = 6.10$ and 12.2, agrees reasonably well with the data for all amplitude scales shown. However, there is considerable scatter of the data, the majority of which indicates a smaller rise-time ratio than that predicted by the linear theory. This is true of the data for both the positive and negative bed displacements over the full range of the time-size ratio investigated. The rise-time data in the impulsive and transition regions of generation for which $\zeta_o/h > 0.2$ indicate no large or consistent nonlinear effects as was found for the exponential bed movements in Fig. 5.17. Any weak nonlinear effects present for the half-sine bed displacements are masked by the scatter in the data. The linear theory suggests that the rise and fall-time ratios are different in the region $t_c\sqrt{gh}/b < 2$, similar to the behavior for $b/h = 2.02$ in the region $t_c\sqrt{gh}/b < 1$. For these larger size scales the linear theory agrees with the data in predicting the region in which the rise and fall-time ratios are no longer equal; however, the data consistently indicate a larger value of t_f/t_c than predicted by the linear theory. In the case of the nodal-time ratio for $b/h = 6.10$ and 12.2 the linear theory agrees well with the data for negative bed motions and with the data for positive bed movements where the disturbance-amplitude scale is less than 0.2. As the amplitude scale for positive bed movements increases, the data deviate more from the theory; a similar nonlinear effect was observed in the data for the nodal-time ratio shown in Fig. 5.17 for the exponential bed motion.

The theoretical curves for the temporal variation of the leading waves shown in Fig. 5.18 for $b/h = 100$ are similar to those presented at the backwall in Fig. 5.16 for the same disturbance-size scale. For $t_c\sqrt{gh}/b < 1$ the rise-time ratio is asymptotic to unity and the fall-time ratio increases at a rate inversely proportional to the time-size ratio, i.e., $t_f/t_c \propto (t_c\sqrt{gh}/b)^{-1}$. The curve for t_n/t_c in this region is only slightly above the curve for the fall-time ratio and these curves appear to be converging as $t_c\sqrt{gh}/b$ decreases. Hence, the rear portion of the leading wave appears to become steeper at $x/h = b/h$ as the time scale decreases. In the region $t_c\sqrt{gh}/b > 20$ the rise and fall-time ratios are equal and are asymptotic to the value 0.5 while the nodal-time ratio approaches unity. The theoretical curves for t_r/t_c and t_n/t_c do not appear to vary appreciably between $b/h = 12.2$ and $b/h = 100$. The curve for the fall-time ratio appears to be approaching the curve for the nodal-time ratio as the size scale increases for a constant value of $t_c\sqrt{gh}/b$ in the impulsive region of generation; hence, the ratio, t_n/t_f, is approaching unity.

In summary, the linear theory appears to predict the rise-time ratio, t_r/t_c, at the backwall reasonably well over the full range of the time-size ratios investigated for both the exponential and half-sine bed movements. The rise-time ratio at the backwall also appears to be relatively independent of the disturbance-amplitude scale. The linear theory consistently under-estimates the fall-time ratio, t_f/t_c, obtained from experiments whenever this quantity was different from the rise-time ratio for both types of bed displacements; nonlinear effects due to large disturbance-amplitude scales were not evident. The nodal-time ratio, t_n/t_c, at the backwall also appeared to be slightly under-estimated by the linear theory for the larger disturbance-size scales and for amplitude scales less than 0.2. As the amplitude scale increased the observed nodal-time ratios increased with the discrepancy between the linear theory and the experiments also increasing.

At the leading edge of the disturbance, $x/h = b/h$, the linear theory for a positive exponential bed movement appeared to predict the rise-time ratio fairly well only for small amplitude scales. As the amplitude scale increased in the impulsive and transition region of generation, the observed values of t_r/t_c were much smaller than those predicted by the linear theory. In the creeping region of generation the linear theory appeared to be applicable over the full range of disturbance-amplitude scale. The linear theory for t_r/t_c agreed well with the data for negative exponential bed movements over the full range of disturbance-amplitude and size scales which were investigated.

For the half-sine bed displacement the linear theory at $x/h = b/h$ appeared to predict a slightly larger rise-time ratio than observed over the full range of $t_c\sqrt{gh}/b$ which was investigated. Strong nonlinear effects due to the disturbance-amplitude scale were not apparent in the rise-time data for the half-sine bed displacement.

The linear theory appeared to predict a smaller fall-time ratio at $x/h = b/h$ than observed in the region of the time-size ratio where t_r/t_c and t_f/t_c were not equal for both types of bed movement. The data do not appear to depend on the disturbance-amplitude scale.

The nodal time ratio, t_n/t_c, was also under-estimated by the linear theory at $x/h = b/h$ for the larger size scales investigated for both the exponential and half-sine bed displacements. The nodal-time ratio also was observed to increase as the disturbance-amplitude scale increased for both bed motions.

Theoretical curves for t_r/t_c and t_n/t_c do not appear to vary appreciably in the generation region for size scales greater than 12.2 when the time-displacement history of the bed is not varied. The ratio, t_n/t_f appears to approach unity in the impulsive region of generation as the size scale increases for both the exponential and half-sine bed movements. This behavior of the time ratios is extremely important in the practical application of these results.

5.1.4 Energy Dissipation in the Generation Region.

In the linear theory presented in Chapter 3 the effect of fluid viscosity was neglected; however, the experimental measurements are all affected to some degree by viscosity. Boundary layers are formed in the fluid domain during wave propagation at the bed and sidewalls of the wave tank as well as at the free surface due to the local effects of surface tension. In fact one major difference between the experimental model and the theoretical model is the condition which exists at $x/h = 0$. In the former there is a no-slip condition at this location whereas in the latter $x/h = 0$ is simply a plane of symmetry. The boundary resistance to flow reduces the amplitude and velocity of the centroid of the propagating wave (see, e.g., Benjamin and Mahony (1971)). Since the length of wave propagation in the generation region never exceeded 24.4 water depths, energy losses from wave propagation in this region are probably small. (Energy losses during downstream wave propagation will be discussed in detail in Section 5.2.)

The major effect of fluid viscosity in the generation region appears to be the creation of a vortex near the leading edge of the rising or falling bed section. Fig. 5.19 shows the vortex structure for both a positive and negative half-sine bed displacement with generation parameters identical to those given by Eq. (5.5) which were used in the photographic sequence shown in Fig. 5.13a and 5.13b. The effect of this vortex on the wave amplitudes and temporal variations in the generation region appears to be small as evidenced by the agreement

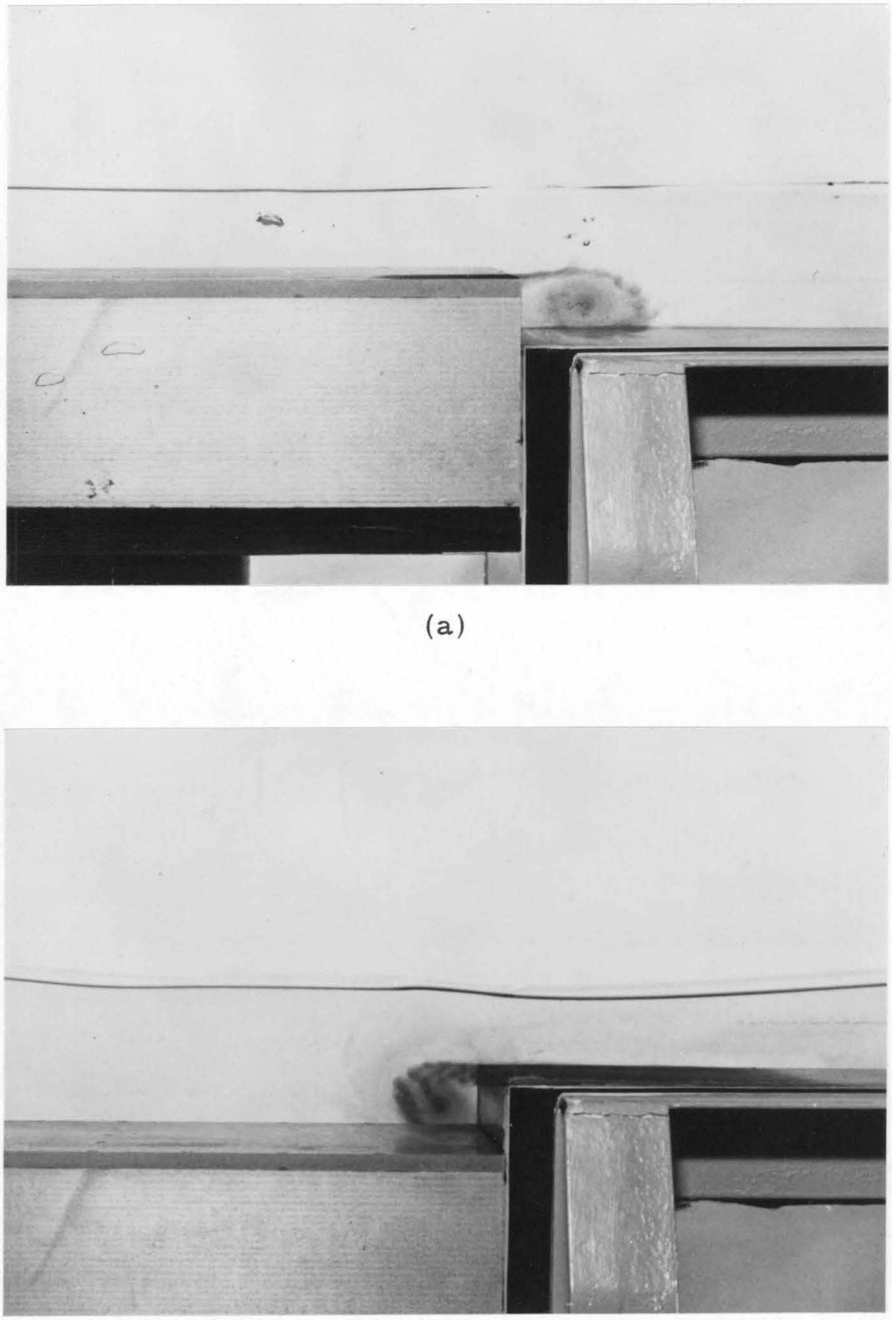

(a)

(b)

Fig. 5.19 Vortex generation at leading edge of moving bed section;
a) bed upthrust, b) bed downthrow.

of theory and experiment in this region which was discussed in Sections 5.1.1 and 5.1.2.

5.1.5 The Three-Dimensional Model in the Generation Region.

Generally, waves created in nature by moving boundaries involve a more complex pattern of wave propagation than described by the simple two-dimensional model presented in Chapter 3. In the two-dimensional model wave propagation occurs in one coordinate direction while in the most general case, surface wave propagation occurs in two coordinate directions; hence, the fluid domain must be described three dimensionally.

A simple three-dimensional model was presented in Section 3.4 in which the fluid domain was described by the coordinates (r, Θ, z), and a linear solution for a class of bed deformations which were axially symmetrical was developed. The general solution, Eq. (3.102), was then applied to the specific bed deformation given by Eq. (3.103) which consisted of a block upthrust or downthrow, circular in planform with a radius r_o, which moved exponentially in time (see Fig. 3.2). The size scale, amplitude scale, and time scale for this deformation are defined as: r_o/h, ζ_o/h, and $t_c\sqrt{g/h}$, respectively. Assuming the bed deformation to be axially symmetric led to a wave system propagating radially into a three-dimensional fluid domain.

The generation region for the three-dimensional (3-D) model is defined as the fluid region over the moving bed section, i.e., $r \leq r_o$.

The positions in this region corresponding to the "backwall" and the "leading edge" in the two-dimensional model are $r/h = 0$ and $r/h = r_o/h$, respectively. It is useful to compare the theoretical results at these two positions to the results obtained from the linear theory in the two-dimensional (2-D) model. Figs. 5.20a and 5.20b show the variation of the relative maximum wave amplitudes, η_o/ζ_o, computed at $r/h = 0$ and $r/h = r_o/h$ for a disturbance-size scale of $r_o/h = 12.2$ as a function of the parameter $t_c\sqrt{gh}/r_o$ which will be termed the time-size ratio. (The characteristic time is again chosen as the time required for two-thirds of the bed movement to be completed.) Also shown in Figs. 5.20a and 5.20b are corresponding wave amplitude computations for the two-dimensional model at $x/h = 0$ and $x/h = b/h$; these curves from Figs. 5.1 and 5.4 are for the disturbance-size scale: $b/h = 12.2$.

At $r/h = 0$, the same general behavior for the relative wave amplitude, η_o/ζ_o, is observed in Fig. 5.20a as for the two-dimensional case. As the parameter $t_c\sqrt{gh}/r_o$ becomes less than 10^{-1} the wave height at the center of the disturbance becomes constant and equal to the total bed displacement, ζ_o. As the time-size ratio approaches a value near 10, the relative wave amplitude becomes inversely proportional to the time-size ratio, $t_c\sqrt{gh}/r_o$, just as in the analogous two-dimensional model. Thus an impulsive, transition, and creeping region of generation based on the time-size ratio, $t_c\sqrt{gh}/r_o$, again may be defined for the three-dimensional model in the same manner as was done in

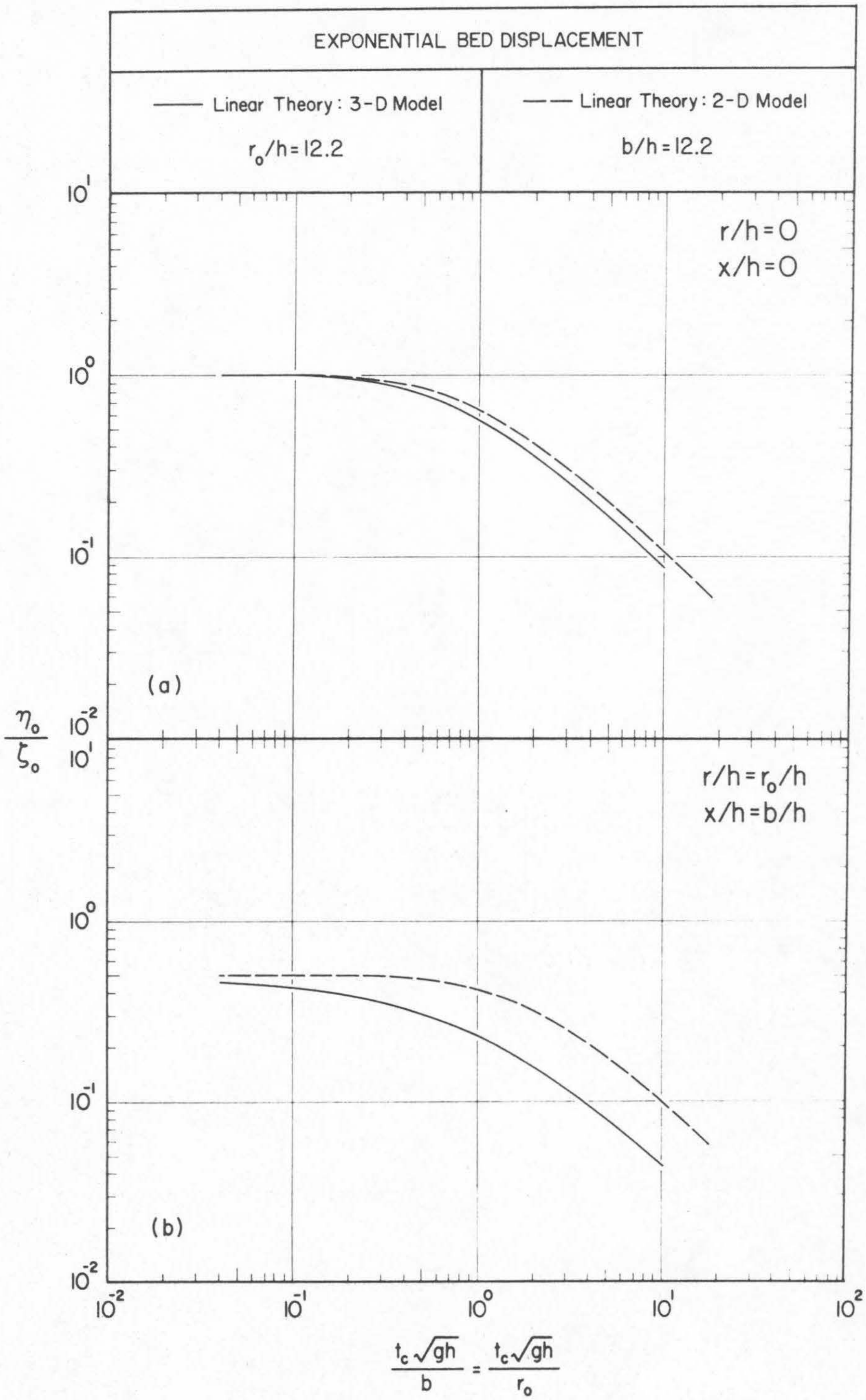

Fig. 5.20 Theoretical variation of relative maximum wave amplitude, η_o/ζ_o, with the time-size ratio, $t_c\sqrt{gh}/r_o$; a) at $r/h = 0$, b) at $r/h = r_o h$.

Section 5.1.1 for the 2-D case. The only difference observed between the two and three-dimensional wave amplitudes at $x/h = 0$ and $r/h = 0$ is that a slightly smaller maximum wave amplitude results in the transition and creeping region of generation for the 3-D model for a fixed value of the time-size ratio.

At the leading edge of the disturbance, $r/h = r_o/h$, the relative wave amplitude, η_o/ζ_o, observed in Fig. 5.20b for the 3-D model is similar in its general behavior to the analogous curve for $b/h = 12.2$ for the two-dimensional model; however, a smaller wave results for the 3-D model over the full range of time-size ratios which were investigated. This behavior in the impulsive region of generation for $r_o/h = 12.2$ suggests that at the leading edge of the disturbance the elliptic response of the three-dimensional fluid domain to an impulsive bed movement affects larger size scales than in the 2-D model.

Fig. 5.21 shows the maximum value of the ratio, η_o/ζ_o, that can be reached in the impulsive region of generation at $r/h = 0$ and $r/h = r_o/h$ as a function of the size scale r_o/h. Similar results for the two-dimensional model which were shown previously in Fig. 5.7 are shown in Fig. 5.21 for comparison. (The curves shown for the 3-D model were computed for an exponential bed displacement only; however, no difference in the indicated behavior would be expected for a half-sine time-displacement history of the bed movement as was found previously for the 2-D model. Computations for these curves were made for a time-size ratio, $t_c\sqrt{gh}/r_o$, less than or equal to 10^{-3}.)

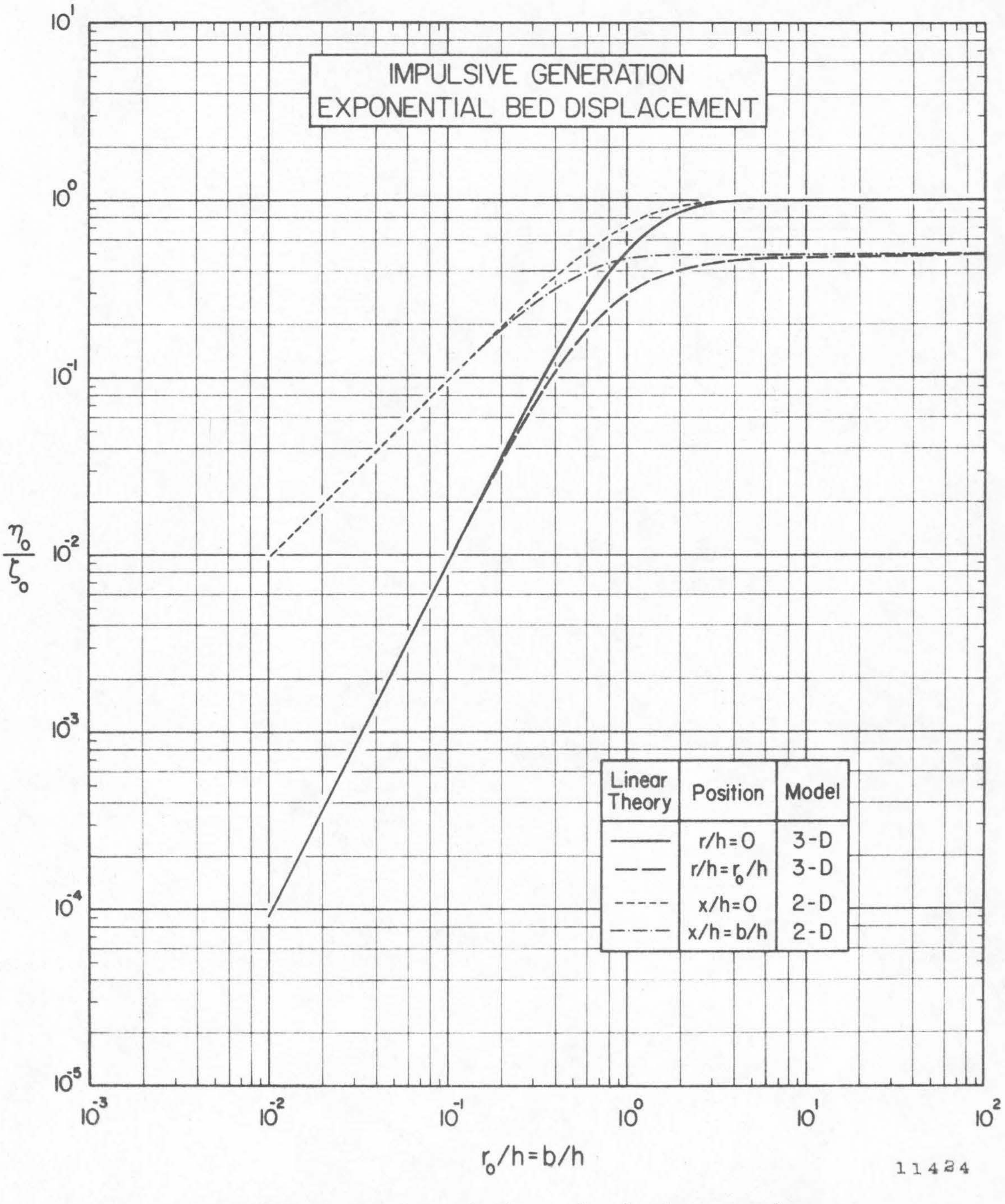

Fig. 5.21 **Theoretical** variation of **relative maximum** wave **amplitude**, η_o/ζ_o, **with the disturbance-size** scale, b/h and r_o/h, for impulsive bed displacements.

At $r/h = 0$, the wave amplitude, η_o, is equal to the bed displacement, ζ_o, for all disturbance-size scales, r_o/h, greater than about four; a similar behavior is observed for the 2-D model at $x/h = 0$. For r_o/h less than four, the relative wave amplitude, η_o/ζ_o, decreases from unity until it becomes proportional to $(r_o/h)^2$ for all size scales less than 10^{-1}, i.e.:

$$\eta_o/\zeta_o \propto (r_o/h)^2 \qquad \text{for } r_o/h < 10^{-1}. \tag{5.6}$$

For the two-dimensional model at $x/h = 0$ the relative wave amplitude became directly proportional to the size scale, b/h, in the region $b/h < 10^{-1}$; hence, a major difference in the behavior of maximum wave amplitudes in the generation region for the two and three-dimensional models occurs for disturbance-size scales less than 10^{-1} when the bed movement is impulsive.

At the leading edge of the circular disturbance, i.e., $r/h = r_o/h$, the ratio, η_o/ζ_o, approaches 0.5 for large disturbance-size scales; however, this value is not actually reached until approximately $r_o/h = 100$. For size scales, r_o/h, which are less than 100, the relative wave amplitude decreases from an asymptotic value of 0.5 with decreasing disturbance-size scale. For $r_o/h < 10^{-1}$ the relative wave amplitudes at both $r/h = r_o/h$ and $r/h = 0$ become equal and continue to decrease in the manner given by Eq. (5.6) with decreasing r_o/h. In the results for the 2-D model at $x/h = 0$, η_o/ζ_o became equal to 0.5 near $b/h = 2$ and for size scales less than two in this model, η_o/ζ_o

decreased until it was directly proportional to the disturbance-size scale for $b/h < 10^{-1}$ (see Eq. 5.1) as well as equal to the relative wave amplitude at $x/h = 0$. Hence, the behavior of the maximum wave amplitudes in the generation region for an impulsive bed movement in both the two and three-dimensional models appears to be identical for disturbance-size scales, b/h or r_o/h, greater than approximately 10^2. The behavior of η_o/ζ_o is almost the same for size scales greater than about four. For size scales less than four the behavior of η_o/ζ_o is quite different between the two models.

Eq. (5.6) may also be written:

$$\frac{\eta_o h^2}{r_o^2 \zeta_o} \propto 1 \qquad \text{for } r_o/h < 10^{-1}, \tag{5.7}$$

which appears to indicate that the displaced water volume at the completion of the impulsive bed movement (which is proportional to $r_o^2\zeta_o$) is located in a region resembling a portion of the upper half of a hemispherical shell with a thickness of η_o and a radius proportional to the water depth, h.

In addition to the maximum wave amplitudes that occur in the generation region of the three-dimensional model, it is also useful to observe the detailed wave profiles in the impulsive, transition, and creeping regions of generation. Fig. 5.22 shows the wave profiles in each region which are calculated by the linear theory, Eq. (3.106), at $r/h = 0$ and $r/h = r_o/h$ for a positive bed displacement. The wave

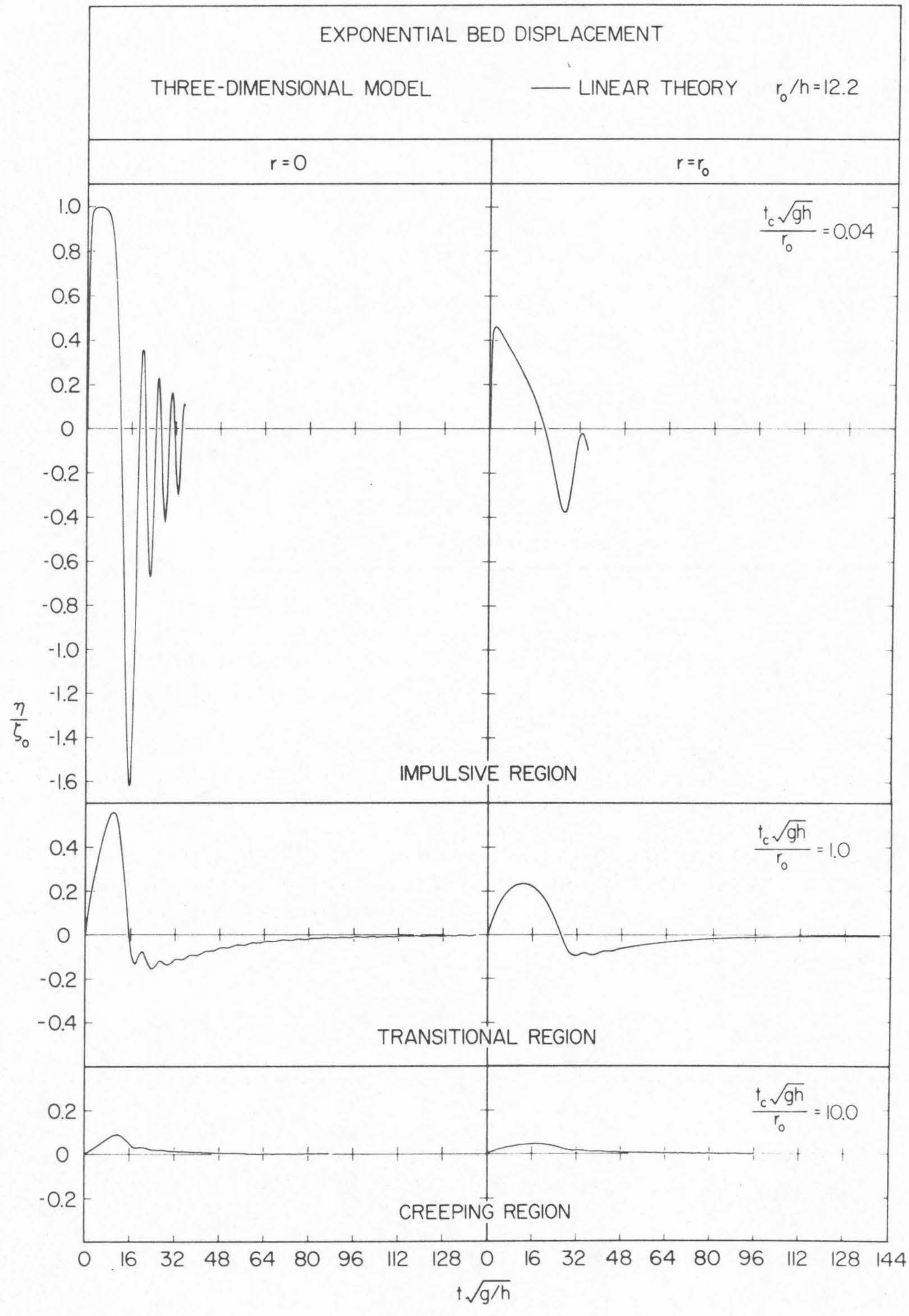

Fig. 5.22 Typical wave profiles in each region of generation at $r/h = 0$ and $r/h = r_o/h$ generated by exponential bed displacements.

amplitude, η, has been normalized by the total bed displacement, ζ_o, and is shown as a function of the nondimensional time, $t\sqrt{g/h}$. A disturbance-size scale of $r_o/h = 12.2$ has been used for each profile in Fig. 5.22 so that a direct comparison with the theoretical waves presented in Fig. 5.8 for an exponential bed movement in the two-dimensional model is possible. (The time-size ratio, $t_c\sqrt{gh}/r_o$, for each profile is indicated in the figure.)

In the impulsive region of generation at $r/h = 0$ the water rapidly rises to an amplitude equal to the total bed displacement, ζ_o, remains constant for an interval of time, and then rapidly decreases to a level of $-1.6\zeta_o$ below the still water level. The water then oscillates in a damped manner about a mean position which appears to be approaching the SWL as time increases. This wave structure behind the leading wave is quite different from the corresponding wave form shown in Fig. 5.8 for the 2-D model in which no large negative waves trail the positive leading wave.

At $r/h = r_o/h$ in the impulsive region of generation the water surface shown in Fig. 5.22 rapidly rises to a maximum amplitude and immediately decreases to the SWL where a large negative wave is formed whose maximum amplitude is approximately equal in absolute value to that reached by the positive leading wave. This wave structure is also different from that observed at $x/h = b/h$ for the impulsive region of generation in the 2-D model which was presented in Fig. 5.8.

For the 2-D model the water rose to a maximum height, η_o, and remained constant for an interval of time before returning to the still water level. The amplitude of the oscillations behind the leading wave for the 2-D case of Fig. 5.8 were found to be small compared to the amplitude of the leading wave. Computations of the wave form for the 3-D model were terminated before the major wave system was fully developed; however, oscillations appear to be forming about a mean level which approaches the SWL asymptotically.

In the transition region of generation shown in Fig. 5.22 the water level at $r/h = 0$ and $r/h = r_o/h$ rises to a maximum amplitude and immediately decreases to the still water level. A negative wave is seen to be trailing the lead wave which appears to approach the still water level in an asymptotic manner. In the transition region of Fig. 5.8 for the 2-D model no negative wave was formed.

In the creeping region of generation in Fig. 5.22 a small positive wave resembling a bore is formed at both $r/h = 0$ and $r/h = r_o/h$. This behavior is similar to the waves generated in the creeping region for the two-dimensional model shown in Fig. 5.8.

In summary, it appears that the simple three-dimensional model of wave generation presented in Chapter 3 results in wave profiles in the generation region which are, in general, different in detailed structure from those produced in the two-dimensional model for analogous generation parameters. In the impulsive region of generation, negative waves of large amplitude trail the positive leading wave produced by a positive bed displacement; hence, positive waves of large amplitude would be expected to result from a negative bed displacement trailing the negative leading wave. This type of behavior was not observed in the two-dimensional model of generation. Hence, the applicability of the two-dimensional model of wave generation appears to be limited, in general, to tectonic earthquakes in which one coordinate dimension of the deformation is very large compared to the other dimension so that locally the wave propagation may be described by a simple 2-D model as presented in Chapter 3.

5.2 THE DOWNSTREAM REGION.

The downstream region is defined as the region of the fluid domain in which the solid boundary is undisturbed for all time; this region is defined in the two and three-dimensional models by $|x| > b$ and $r > r_o$, respectively. Except for very small size scales the water particle motion that occurs in the downstream region is caused by waves propagating from the region of generation. In Chapter 3 the general behavior of waves propagating in the downstream region was discussed and a strategy was suggested for determining wave profiles at any position in this region. A review of this discussion is presented in this section (Subsection 5.2.1) and the suggested strategy is applied to two specific examples of wave generation. This section is concluded (Subsection 5.2.2) with a discussion of energy dissipation present in the experimental measurements made in the downstream region. (No theoretical or experimental results are presented for the three-dimensional model in the downstream region.)

5.2.1 Wave Propagation.

It was shown in Chapter 3 that long wave propagation is characterized by the Ursell Number:

$$\underline{U} = \frac{\eta_o/h}{(h/\ell)^2} = \frac{\eta_o \ell^2}{h^3} , \qquad (5.8)$$

which represents the ratio of nonlinearities to linearities in a propagating wave. When the Ursell Number is much less than unity a linear theory is sufficient in approximating the wave behavior. When the Ursell Number is much greater than unity, amplitude dispersion controls the wave behavior and the linear effect of frequency dispersion may be ignored. For the special case of $\eta_o/h = 0[(h/\ell)^2]$, i.e., the Ursell Number is of order unity, the description of the wave behavior must retain the effect of both frequency and amplitude dispersion. The Korteweg and deVries (KdV) equation was suggested in Chapter 3 as the appropriate model of wave behavior when $\eta_o/h = 0[(h/\ell)^2] << 1$. This special case is of major importance for long waves since the ratio, h/ℓ, must be much less than unity for these waves.

The Ursell Number was also shown in Chapter 3 to provide an excellent indicator for tracing the evolution of a long wave during propagation. Regardless of the magnitude of the Ursell Number for a wave in the downstream region (whose depth is uniform), the wave always evolves into a shape such that $U = 0(1)$. Once this condition is reached, the Ursell Number remains constant during further propagation. The region of the fluid domain in which amplitude and frequency dispersion are of the same order of magnitude, i.e., $\underline{U} = 0(1)$, was termed the far-field. In the far-field the KdV equation appears to be the appropriate description of wave behavior. It was mentioned in Chapter 3 that the asymptotic solution of the KdV equation for any initial condition whose net volume is positive is a train of solitary waves (or solitons) with the amplitude of the waves decreasing toward the rear of the train followed by an oscillatory tail. The number and amplitude of these solitons appear to be a function of the initial profile. When the volume of water in the initial wave is finite but negative, no permanent wave forms are possible. The region of the fluid domain (including the generation region) in which the Ursell Number is changing from its initial value to unity was termed the near-field. A linear near-field was said to exist when the initial value of the Ursell Number is much less than unity; a nonlinear near-field was said to exist when the Ursell Number is initially much greater than unity.

The wave profiles resulting from the bed displacements used in the experimental investigation were shown in Section 5.1.2 to be complex in form, i.e., nonperiodic. For waves of this type, more than one Ursell Number is usually required to describe the entire wave. A definition of the Ursell Number for an appropriate region (which will be defined shortly) of a complex wave was given in Chapter 3 as:

$$\underline{U} = \frac{\eta_o^3}{h^3 ||\eta_x||^2} , \tag{5.9}$$

where η_o is the maximum wave amplitude in the region and $||\eta_x||$ is the maximum value of the slope of the wave profile in that region. An "appropriate" region for a complex wave may be defined as the region of wave structure between points at which the slope of the wave profile becomes zero, i.e., $\eta_x = 0$. Hence, any complex wave may be divided into appropriate regions and characterized by various Ursell Numbers as given by Eq. (5.9). (When Eq. (5.9) is applied to the solitary wave as given by Boussinesq (1872), the Ursell Number is found to be equal to 2.37 in each of the two similar regions of the wave profile.) In deciding on the applicability of the linear theory in predicting the entire wave profile, the Ursell Number with the largest magnitude must be considered. In general, the largest Ursell Number will be found in the leading region of a complex wave, since longer wave components with larger characteristic lengths travel faster than shorter components and thus appear at the front of the wave train. The actual computation of Ursell Numbers by Eq. (5.9) for specific complex wave shapes will be illustrated shortly.

When a linear near-field exists, a possible strategy for finding the wave profile at any downstream position was suggested in Chapter 3. The linear theory may be used until the Ursell Number indicates that nonlinear effects are becoming of the same order of magnitude as the linear effects. At this point the profile calculated by the linear theory may be used as an initial condition for the KdV equation which may then be solved to give the wave profile at any desired position in the downstream region. This is the strategy adopted in this section to investigate wave profiles in the downstream region.

Due to the complexity of the analytical solution of the KdV equation, a numerical solution algorithm is adopted. The numerical model involves the KdV equation in a form given by Eq. (3.80) which was used by Peregrine (1966) to study the development of undular bores. Peregrine found that a straight-forward finite-difference approximation of Eq. (3.80) was stable. Using forward differences in time and central differences in space the finite-difference representation of Eq. (3.80) is:

$$\frac{u_{\delta,\xi+1} - u_{\delta,\xi}}{\Delta t} + \left(1+\frac{3}{2}u_{\delta,\xi}\right)\frac{u_{\delta+1,\xi+1} - u_{\delta-1,\xi+1} + u_{\delta+1,\xi} - u_{\delta-1,\xi}}{4\Delta t}$$

$$= \frac{1}{6\Delta x^2 \Delta t}\left(u_{\delta+1,\xi+1} - 2u_{\delta,\xi+1} + u_{\delta-1,\xi+1} - u_{\delta+1,\xi} + 2u_{\delta,\xi} - u_{\delta-1,\xi}\right), \qquad (5.10)$$

where $u_{\delta,\xi} = u(\delta\Delta x, \xi\Delta t)$, $\delta = 1, 2, \ldots, \underline{n}$, $\xi = 0, 1, 2, \ldots, \underline{m}$, Δx is the nondimensional grid spacing, and Δt is the nondimensional time step. The initial values of the average horizontal velocities, $u_{\delta,\xi}$, can be found from Eq. (3.81) at each of the $\underline{n}$ spatial nodes since the water surface amplitude, η, is known. (For a small initial wave profile the approximation $u_{\delta,0} = \eta_{\delta,0}$ appears to be sufficient.) The velocities at the next time step, i.e., $u_{\delta,1}$, can then be found in terms of the initial values by writing Eq. (5.10) at each of the n nodes which yields a system of n simultaneous algebraic equations in the n unknown velocities. These velocities can then be determined by solving the simultaneous equations using standard techniques of matrix algebra. The values of the water particle velocities at the next time step can be found in a similar manner; hence, this procedure can be repeated for as many time steps as required and the water surface elevation, η, at any time step can be found from the water particle velocities by Eq. (3.81). As in the work of Peregrine, Δx and Δt are taken to be equal for convenience and will be referred to as Δ.

The accuracy of the finite-difference approximation given by Eq. (5.10) over a specific time interval, $m\Delta t$, is easily checked by propagating a solitary wave over the same time interval. Since the solitary wave is an exact solution of Eq. (3.80), the wave profile should propagate unchanged. Changes of the wave profile that do occur represent the inaccuracy of the finite-difference approximation, Eq. (5.10), to the original partial differential equation, Eq. (3.80). A convenient measure of this error (commonly referred to as numerical viscosity or dispersion) is the reduction of the solitary wave amplitude that occurs during wave propagation. The accuracy of the numerical approximation may be improved by decreasing the step size, Δ, (see Peregrine (1966)). In the results that follow, the step size, Δ, was chosen by first propagating a soliton of amplitude comparable to the waves under consideration and reducing the step size until the percentage reduction in the soliton amplitude at the end of propagation was acceptable.

In order to illustrate the use of the Ursell Number for complex waves and to apply the suggested strategy for finding waves whose net volume is positive in the downstream region of the two-dimensional model, an exponential bed displacement with the following generation parameters has been investigated:

$$\zeta_o/h = 0.1, \quad b/h = 12.2, \quad t_c\sqrt{gh}/b = 0.148 . \qquad (5.11)$$

From Fig. 5.1 the time-size ratio in Eq. (5.11) is seen to lie in the impulsive region of generation. Sections 5.1.1 and 5.1.2 also indicate that the linear theory should be applicable in the generation region for these generation parameters; hence, a linear near-field should exist.

The experimental results at the downstream positions: $(x-b)/h = 20, 180,$ and 400 and at the leading edge, $x/h = b/h$ or $(x-h)/b = 0$, are shown in Fig. 5.23a where the wave amplitude, η, is normalized by the water depth, h, and shown as a function of the non-dimensional time, $t\sqrt{g/h} - (x-b)/h$. If the Ursell Number in the leading region of each wave is calculated by taking η_o as the maximum amplitude attained by the leading wave and $||\eta_x||$ to be the maximum slope of the leading face of the wave, then the values shown in Fig. 5.23a are found. (All values of the Ursell Number are rounded to one significant digit since only an order of magnitude is indicated by Eq. (5.9).) No Ursell Number is indicated at $(x-b)/h = 0$ since the water movement at this position is a combination of the generation process and propagation; hence, it is not appropriate to define an Ursell Number for the wave. At $(x-b)/h = 20$ the Ursell Number is found to be 0.7 which is

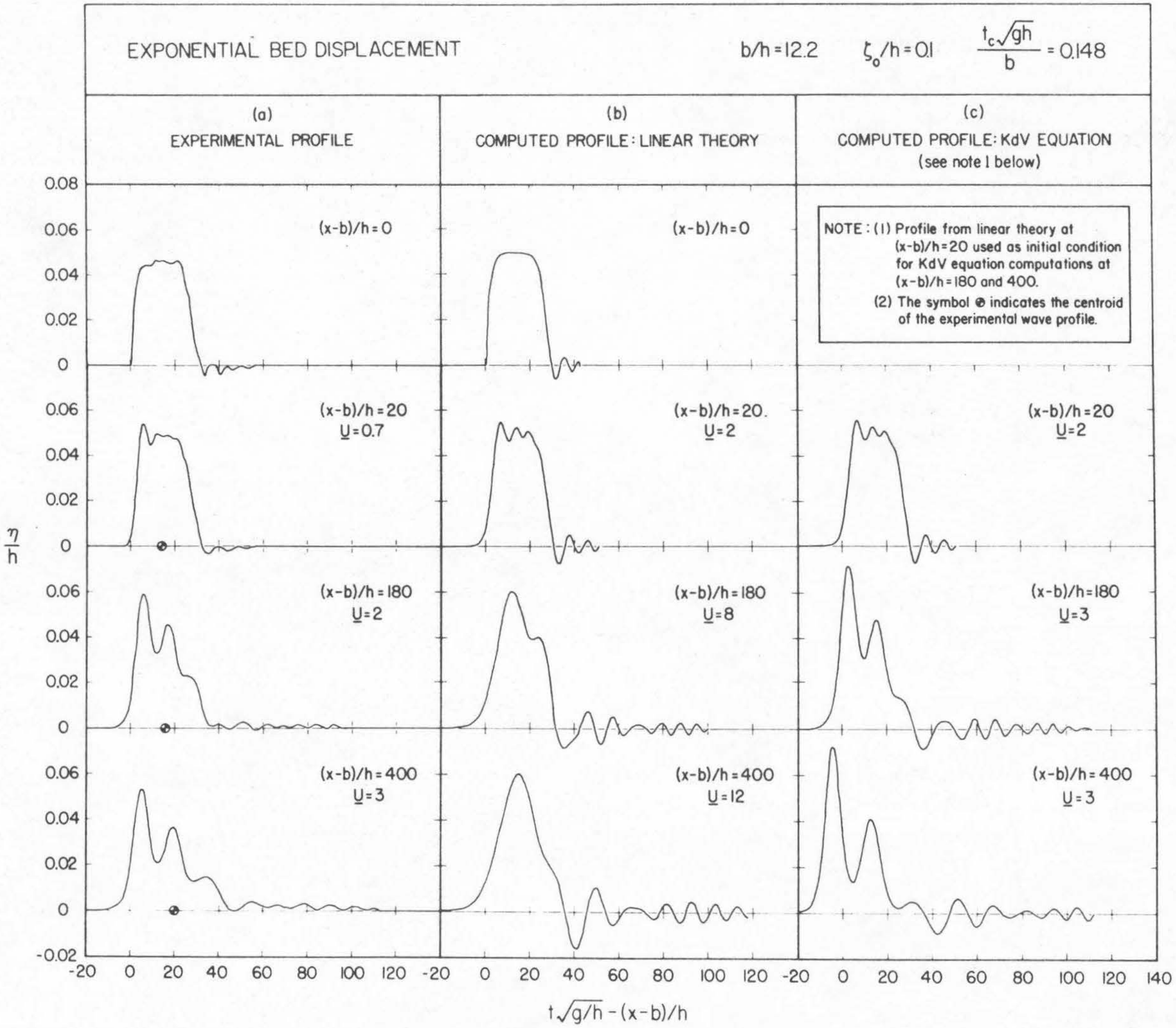

Fig. 5.23 Downstream wave profiles generated by an impulsive exponential bed upthrust; a) measured, b) computed by linear theory, c) computed by KdV equation.

nearly of order unity; hence, within twenty depths of the generation region, amplitude dispersion appears to have become of the same order of magnitude as frequency dispersion. At $(x-b)/h = 180$ and 400 the Ursell Number increases only slightly to values of two and three, respectively. The Ursell Number in the leading region of the wave is thus of order unity at all the downstream positions which indicates that the KdV equation should be used to describe the wave behavior at these positions. (Note that the Ursell Number found at $(x-b)/h = 180$ and 400 is approximately the same as that found for the solitary wave of Boussinesq.)

For the measured wave at $(x-b)/h = 0$, i.e., the leading edge, the water surface rises rapidly to a maximum amplitude $(\eta_o/h \simeq 0.047)$, remains reasonably constant for an interval of time, and then rapidly decreases to the still water level. (This wave profile at the leading edge of the disturbance is characteristic of waves generated by impulsive bed movements for which the size scale, b/h, is greater than approximately two.) At $(x-b)/h = 20$ undulations which are caused by frequency dispersion have formed about the level $\eta_o/h \simeq 0.047$ on the lead wave. At $(x-b)/h = 180$ the nodal period of the leading wave has increased as the wave appears to be separating into individual waves. Note that these individual waves appear to be symmetrical in shape and their troughs do not go below the still water level; to some extent, they resemble solitary waves. Oscillatory waves of small amplitude and short periods are observed to be trailing the lead wave at this position.

At (x-b)/h = 400 the nodal period of the lead wave continues to increase as the separation into individual waves continues. The troughs of the individual waves appear to be moving toward the still water level and the waves remain symmetrical. The trailing waves at (x-b)/h = 400 appear to have increased slightly in amplitude and period.

The wave profiles at each position: (x-b)/h = 0, 20, 180, and 400, as calculated by the linear theory are shown in Fig. 5.23b. At the leading edge, (x-b)/h = 0, the linear theory agrees well with the experimental profile except, as expected, for a small discrepancy in estimating the nodal time. At (x-b)/h = 20 the undulations trailing the lead wave are larger in amplitude than those of the measured profile in Fig. 5.23a. A possible explanation for this discrepancy is indicated by the Ursell Number for the measured profile at (x-b)/h = 20 which is of order unity; hence, amplitude dispersion is approximately equal in magnitude to frequency dispersion and has thus reduced the effects of frequency dispersion for this positive wave.

At (x-b)/h = 180 the temporal variations of the wave predicted by the linear theory no longer agree well with the measured profile. Frequency dispersion, unhindered by amplitude dispersion in the linear theory, has continued to disperse the leading wave into its spectral components as evidenced by the wave groups trailing the lead wave. These wave groups exhibit the well-known beat phenomena found in linear wave theories. At the position furthest downstream, (x-b)/h=400, the differences in the temporal variations between the linear theory and measured profiles have increased as frequency dispersion continues to form wave groups behind the lead wave.

The Ursell Number of the leading wave is also shown for the profiles found from the linear theory in Fig. 5.23b. At (x-b)/h = 20 the Ursell Number has already become of order unity for the linear profile just as indicated by the measured profile in Fig. 5.23a. During further propagation the Ursell Number continues to grow as shown at the downstream positions: (x-b)/h = 180 and 400, where $\underline{U}$ = 8 and 12, respectively. This growth of the Ursell Number during propagation is characteristic of the linear theory since frequency dispersion separates the initial wave into its spectral components with the longer components travelling fastest and thus appearing at the front of the wave train. This behavior suggests that the length of the linear near-field may be found easily by using the linear theory until the Ursell Number in the leading portion of the calculated wave becomes of order unity. For the waves shown in Fig. 5.23b the length of the near-field appears to be on the order of twenty depths from the region of generation.

It is interesting to note that the maximum amplitude of the leading wave computed by the linear theory at the downstream positions agrees well with the maximum amplitudes of the measured waves; however, it should be pointed out that the reduction in the measured wave amplitudes due to viscous energy dissipation is probably quite large. Thus, the agreement between the maximum amplitudes predicted by the linear theory and the measured wave amplitudes is probably coincidental. (The effects of energy dissipation occurring during wave propagation will be discussed in Section 5.2.2.)

Following the suggested strategy for determining wave behavior in the far-field, the linear theory at $(x-b)/h = 20$, (which agrees reasonably well with the measured profile) has been used as the initial condition for the KdV equation. For the numerical propagation of this initial condition, a nondimensional step size, Δ, in space and time, of 0.3 was used. The maximum amplitude of a solitary wave with an initial height of $\eta_o/h = 0.05$ was found to decrease by 14% as a result of numerical dispersion when propagated a distance of 380 depths. It should be noted that numerical dispersion was observed to change the shape of the solitary wave in a manner similar to the effect of frequency dispersion shown in Fig. 5.23b, i.e., waves of smaller amplitude and frequency are left behind the leading wave.

The profiles computed by the KdV equation at the positions $(x-b)/h = 180$ and 400 are shown in Fig. 5.23c. Ursell Numbers for the front region of the lead wave are also shown. The temporal variation of the KdV profile at $(x-b)/h = 180$ more closely resembles the experimental profile at this position than that computed by the linear theory. The leading wave of the KdV profile appears to be separating into individual waves (or solitons) in the same manner as the measured profile in Fig. 5.23a. The major difference in the computed and measured profiles is found in the maximum wave amplitudes which are much larger for the computed wave. (A possible explanation for this behavior will be discussed.) Note that the Ursell Number in the front region of the wave profile computed by the KdV equation has remained of order unity just as in the measured profile.

At $(x-b)/h = 400$ the temporal variation of the leading wave computed by the KdV equation resembles the measured leading wave much better than the variation computed by the linear theory. The leading wave appears to be separating into solitons which are followed by a train of oscillatory waves. The Ursell Number remains constant at a value of three during the propagation by the KdV equation in the same manner as observed in the measured profile.

At the furthest position downstream, $(x-b)/h = 400$, the maximum amplitude of the leading wave computed by the KdV equation is approximately 40% larger than the maximum amplitude of the measured wave profile. If the maximum wave amplitude computed by the KdV equation is increased by 14% to correct for the possible decrease in amplitude resulting from numerical dispersion, the computed wave amplitude becomes approximately 54% larger than the observed wave amplitude. This 54% difference between theoretical and experimental amplitudes of the lead wave is probably a result of energy dissipation due to viscous effects in the laboratory model.

Comparison of the location of the first crest in the leading waves at $(x-b)/h = 400$ in Fig. 5.23a and 5.23c indicates that the wave computed by the KdV equation has an average celerity of approximately 2-1/2% greater than the experimental wave. The average velocity of the computed wave profile between $(x-b)/h = 20$ and 400 is approximately $\sqrt{g(h+\eta_o)} = 71.8$ cm/sec where η_o is the average-maximum wave amplitude over the propagation distance ($\eta_o \simeq 0.25$ cm). The average velocity of the experimental wave between $(x-b)/h = 20$ and 400 is closely approximated by $\sqrt{gh} = 70$ cm/sec. This small discrepancy may be due to measurement error since $\sqrt{g(h+\eta_o)}$ is expected to be a better representation of wave celerities for long waves of finite amplitude.

The positions of the centroid for each measured wave profile at the downstream positions: $(x-b)/h = 20$, 180, and 400, are also indicated in Fig. 5.23a. The centroid position, X, is defined by:

$$X = \frac{\int_{-\infty}^{\infty} x\eta(x;t)dx}{\int_{-\infty}^{\infty} \eta(x;t)dx} , \tag{5.12}$$

which was approximated by numerical integration for each wave record at the downstream locations. In the absence of viscous forces the centroid velocity downstream should remain constant; this behavior has been demonstrated rigorously for water waves recently by Benjamin and Mahony (1971) and can be seen by the direct application of Newton's first principle. When viscous forces are present, the centroid velocity is expected to decrease. The average velocity of the centroid between the positions $(x-b)/h = 20$ and 180 shown in Fig. 5.23a is 69.36 cm/sec and between $(x-b)/h = 180$ and 400 the average velocity is 68.62 cm/sec. Thus, approximately 1% reduction in the average centroid velocity appears to occur between the downstream positions. It should be noted that this slight decrease in the average centroid velocity is probably also within the range of expected error for determining the centroid position from a digitized wave record; hence, definite conclusions cannot be made. However, it does appear that the effect of viscosity on the centroid velocity of a propagating wave is much less than on the wave amplitudes.

It should be noted that the total volume per unit width in the experimental wave profiles at each downstream position in Fig. 5.23a (given by the integral in the denominator of Eq. (5.12)) was never found to vary more than 6% from the known volume of the bed displacement, i.e., $\zeta_o b = 30.5 \text{ cm}^3/\text{cm}$.

It is also of interest to investigate numerically the asymptotic behavior computed by the KdV equation for long waves whose net volume is positive. As stated previously, a train of solitons should evolve from any initial profile of this type. In order to study this behavior, the measured wave profile at $(x-b)/h = 400$ from Fig. 5.23a was chosen as the initial condition and then propagated numerically by the KdV equation a distance of 700 depths further downstream to $(x-b)/h = 1100$. (A nondimensional step in space and time of 0.3 units was chosen. Over the propagation distance of 700 depths a 25% reduction in the amplitude of solitary wave due to numerical dispersion was observed with this nondimensional step size.)

Fig. 5.24 shows the wave profiles computed by the KdV equation at the downstream positions: $(x-b)/h = 600, 800, 1000$, and 1100. The wave amplitude, η, has been normalized by the water depth and is shown as a function of the nondimensional time, $t\sqrt{g/h} - (x-b)/h$. At each position the leading wave continues to separate into individual waves as the peaks gradually separate and the troughs approach the still water level. Each wave remains symmetrical and has the appearance of a solitary wave. The trough behind the third peak actually goes below the still water level at $(x-b)/h = 600$ and continues to drop at the remaining downstream positions. This behavior is probably the result of the numerical dispersion present in the finite-difference approximation since large negative wave amplitudes would not be consistent with the expected asymptotic wave behavior.

The Ursell Number for the leading region of each wave form at $(x-b)/h = 400, 600, 800, 1000$, and 1100 is also indicated in Fig. 5.23. Eq. (5.9) was used in the computation where η_o was taken as the maximum amplitude of the leading wave and the maximum slope of this wave profile is defined as $||\eta_x||$. At every downstream location the Ursell Number remains constant at a value of three, i.e., of order unity. Recall that this asymptotic value of the Ursell Number is approximately equal to that found for a solitary wave ($\underline{U} = 2.37$).

When a negative bed displacement occurs, a wave is generated in which the net volume is negative; hence, no solitons are expected to develop in the downstream region. Amplitude and frequency dispersion

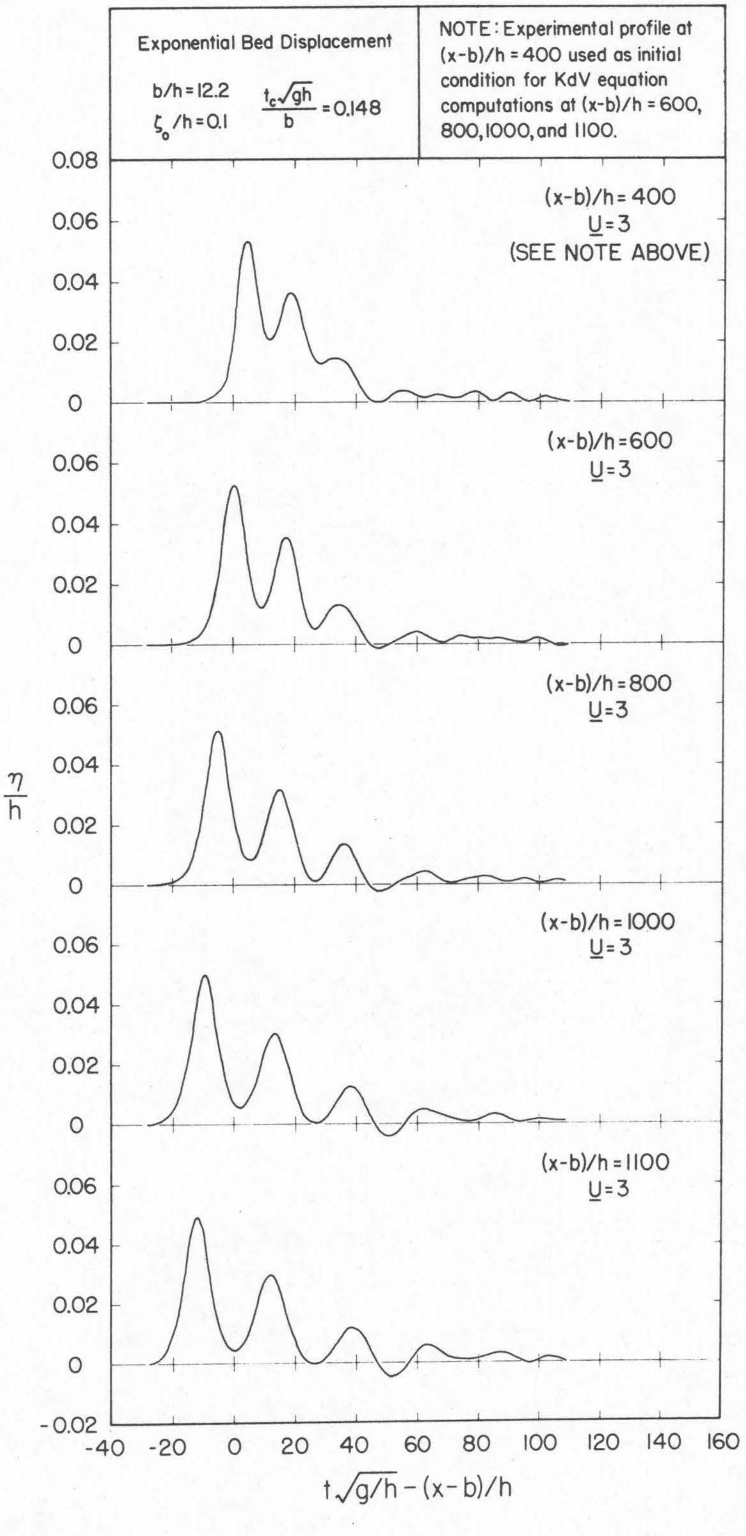

Fig. 5.24 Asymptotic wave behavior computed by the KdV equation for waves with a net positive volume.

in a negative wave ($\eta < 0$) both act to disperse the wave; thus, no permanent form waves are possible even when these two effects are equal in magnitude, i.e., $\underline{U} = 0(1)$. (It should be noted that negative solitary waves are found to be possible when surface energy effects are included in the description of the wave motion; however, for this to occur the water depth must be less than 0.47 cm (see Korteweg and deVries (1895).)

In order to illustrate the downstream behavior of the waves resulting from a negative bed displacement and the application of the suggested strategy for determining downstream wave profiles, an exponential bed movement with the following generation parameters has been investigated:

$$\zeta_o/h = -0.1, \quad b/h = 12.2, \quad \frac{t_c\sqrt{gh}}{b} = 0.093 \; . \tag{5.13}$$

The time-size ratio in Eq. (5.13) can be seen from Fig. 5.1 to lie in the impulsive region of generation. A linear theory is also applicable for describing the wave motion in the generation region for the parameters given in Eq. (5.13) (see Sections 5.1.1 and 5.1.2).

The measured profiles found at the leading edge of the disturbance, $(x-b)/h = 0$ and at the downstream positions of $(x-b)/h = 20$, 180, and 400 are shown in Fig. 5.25a. The wave amplitude, η, has been normalized with respect to the water depth, h, and is shown as a function of the nondimensional time, $t\sqrt{g/h} - (x-b)/h$. Two Ursell Numbers are shown in Fig. 5.25a for each wave profile at the down-

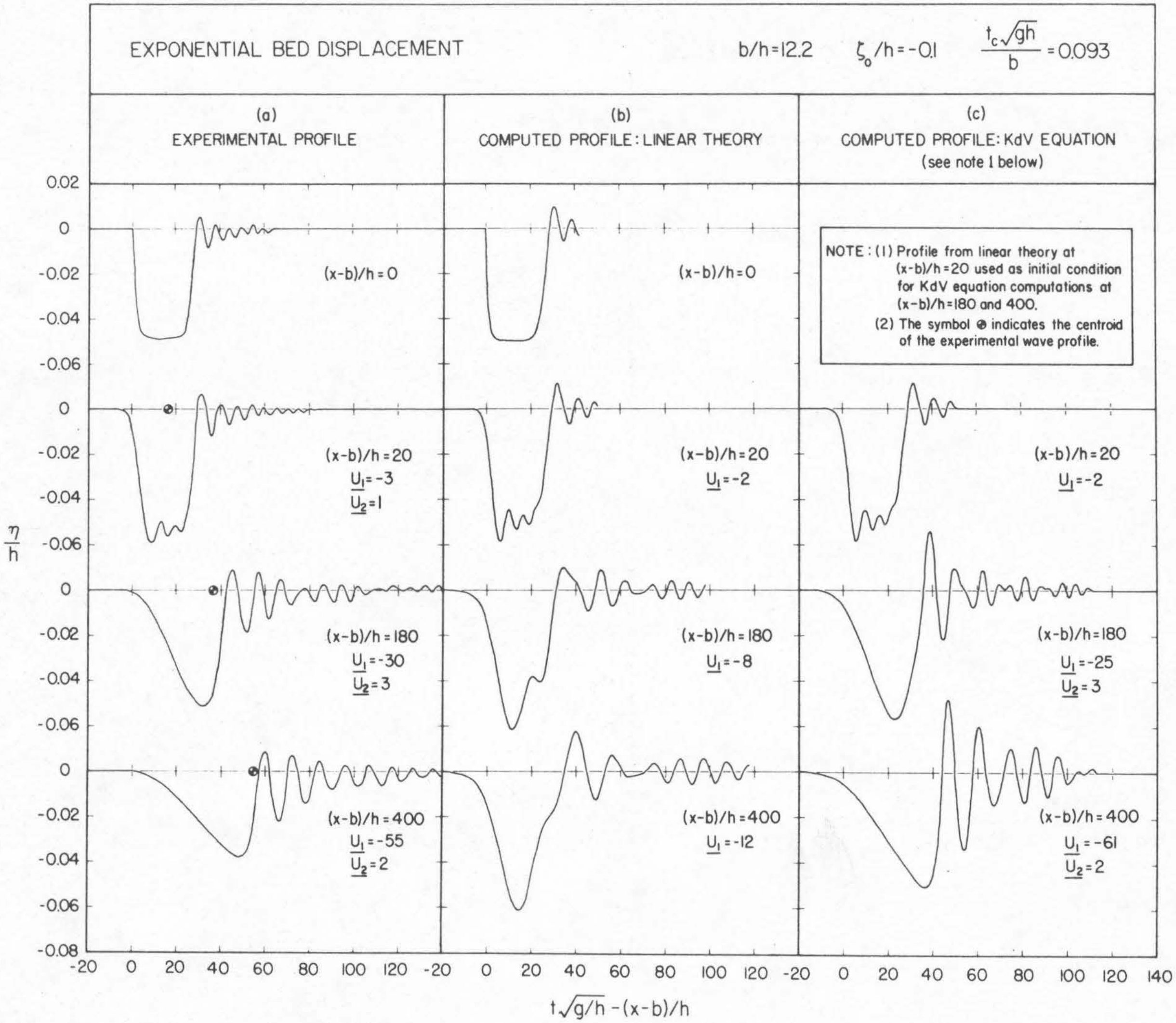

Fig. 5.25 Downstream wave profiles generated by an impulsive, exponential bed downthrow; a) measure, b) computed by linear theory, c) computed by KdV equation.

stream positions $(x-b)/h = 20$, 180, and 400. The first Ursell Number, $\underline{U}_1$, corresponds to the front region of the lead wave and is based on the maximum negative amplitude of this wave, η_o, and the maximum slope reached by the water surface in decreasing to that elevation. The second Ursell Number, $\underline{U}_2$, corresponds to the rear region of the lead wave and is based on the total change in water level from $-\eta_o$ until the slope of the water surface becomes zero again and the maximum slope of the rear face of the leading wave. Note that the Ursell Number, $\underline{U}_1$, is negative since the change in water level is negative in the front region of the leading wave while $\underline{U}_2$ is positive since the water level is increasing in the rear region of the wave. The reason for computing two Ursell Numbers for the leading wave will become evident shortly.

At the leading edge of the disturbance, $(x-b)/h = 0$, in Fig. 5.25a the water level rapidly decreases to a maximum amplitude, $\eta_o/h \simeq -0.05$, remains constant for an interval of time, and then rapidly rises to the still water level about which it oscillates in a damped manner. This profile is similar to all profiles at $(x-b)/h = 0$ created by a negative bed movement which is impulsive (see Section 5.1.2). Ursell Numbers are not calculated for this wave since the water movement here is a combination of the generation process and propagation.

At $(x-b)/h = 20$ the water level rapidly decreases to a minimum elevation, oscillates about this elevation for an interval of time, and then rapidly rises to the still water level about which it oscillates in a damped manner. The Ursell Numbers in both the front and rear regions of the lead wave are of order unity; hence, amplitude and frequency dispersion are of the same order of magnitude after only twenty depths of propagation. Comparison of this profile with the measured profile at $(x-b)/h = 20$ for the case of bed uplift in Fig. 5.23a indicates that the two profiles are nearly the mirror image of one another. The major difference bewteen these two profiles exists in the oscillatory waves trailing the lead wave which are larger and more numerous for the case of bed downthrow. This difference is probably due to the presence of amplitude dispersion which is acting to decrease the effect of frequency dispersion for the positive wave and is increasing the dispersion process for the negative wave.

At $(x-b)/h = 180$ in Fig. 5.25a the Ursell Number, $\underline{U}_1$, has increased (in absolute value), an order of magnitude to a value of minus thirty; hence, in the front region of the leading wave amplitude dispersion is dominating wave behavior. This is evident by the increase in distance (or time) required for the water level to decrease from the still water level to the maximum negative elevation. In the rear region of the leading wave the Ursell Number has remained of order unity ($\underline{U}_2 = 1$); hence, amplitude and frequency dispersion are remaining of the same order of magnitude. Large-amplitude oscillatory waves are forming behind the negative leading wave. Comparison of this wave profile and the corresponding profile in Fig. 5.23a for a positive bed movement shows that the two wave profiles are no longer the mirror image of each other. The difference in the two profiles is the result of the opposite action of amplitude dispersion between positive and negative waves.

At $(x-b)/h = 400$ the Ursell Number in the front region of the leading wave has increased to $\underline{U}_1 = -55$ as amplitude dispersion continues to dominate frequency dispersion and the "stretching" of the front face of the negative wave continues. The Ursell Number in the rear region of the leading wave is still of order unity $(\underline{U}_2 = 2)$. The train of oscillatory waves following the negative lead wave appear to be increasing in crest-to-trough amplitude as propagation continues.

Wave profiles at $(x-b)/h = 0$, 20, 180, and 400 calculated by the linear theory for the generation parameters given by Eq. (5.13) are shown in Fig. 5.25b where the normalized wave amplitude, η/h, is shown as a function of the nondimensional time, $t\sqrt{g/h} - (x-b)/h$. The Ursell Number in the front region of the leading wave at each downstream position is also shown. (No Ursell Numbers have been calculated in the rear region of the leading wave.) At $(x-b)/h = 0$ and 20 the profiles computed by the linear theory agree well with the measured profiles at the corresponding downstream positions in Fig. 5.25b. The Ursell Number in the front region of the leading wave computed by the linear theory has already become of order unity (and negative) at $(x-b)/h = 20$; hence, the linear near-field has ended within twenty depths of the generation region. This behavior was also indicated by the measured profile in Fig. 5.25a.

At $(x-b)/h = 180$ the temporal variations and the amplitudes of the profile calculated by the linear theory no longer agree well with the measured profile in Fig. 5.25a. The differences are a result of amplitude dispersion as indicated by the Ursell Numbers, $\underline{U}_1$. For the computed profile $\underline{U}_1 = -8$ whereas $\underline{U}_1 = -30$ for the measured profile. The increase in $\underline{U}_1$ (in absolute value) from $(x-b)/h = 20$ to 180 indicated for the wave profile computed by the linear theory is a result of the decomposition of the wave into its spectral components by frequency dispersion.

At $(x-b)/h = 400$ the differences between the temporal variations and amplitudes of the wave profile computed by the linear theory and the measured profiles increase as amplitude dispersion continues to affect the actual wave behavior. The Ursell Number for the computed wave has increased to $\underline{U}_1 = -12$ at this position which alone suggests that the linear theory is no longer descriptive of wave behavior as is observed.

Following the suggested strategy for computing wave profiles in the downstream region, the wave profile computed by the linear theory at $(x-b)/h = 20$ has been used as the initial condition for the KdV equation and then propagated numerically to $(x-b)/h = 400$. The Ursell Number for the linear profile indicated that amplitude and frequency dispersion had become of the same order of magnitude at $(x-b)/h = 20$; hence, the far-field has been reached and the KdV equation should now be used to propagate the wave. Again a nondimensional time and size step, Δ, of 0.3 has been used for the finite-difference approximation of the KdV equation (Eq. (5.10)). Recall that a solitary wave with an initial amplitude, $\eta_o/h = 0.05$, was found to decrease in amplitude by 14% when propagated a distance of 380 depths as a result of numerical dispersion.

The profiles computed by the KdV equation at $(x-b)/h = 180$ and 400 are shown in Fig. 5.25c where the normalized amplitude, η/h, is shown as a function of the nondimensional time, $t\sqrt{g/h} - (x-b)/h$. The Ursell Numbers, $\underline{U}_1$ and $\underline{U}_2$, for the leading wave of the computed profiles are also indicated in the figure. At $(x-b)/h = 180$ the temporal variation of the leading wave computed by the KdV equation agrees well with the measured wave shown in Fig. 5.25a. The agreement is indicated further by the Ursell Numbers which are given by $\underline{U}_1 = -25$ and $\underline{U}_2 = 3$ for the computed profile and $\underline{U}_1 = -30$ and $\underline{U}_2 = 3$ for the measured profile. Hence, the KdV equation appears to properly model the stretching of the front face of the leading wave and the balance of frequency and amplitude dispersion in the rear region of this wave.

At $(x-b)/h = 400$ in Fig. 5.25c the profile computed by the KdV equation continues to agree well with the measure profile in its temporal variation. In the front region of the computed leading wave the Ursell Number has grown to $\underline{U}_1 = -61$ compared to $\underline{U}_1 = -55$ for the measured profile. In the rear region of the leading wave, the Ursell Numbers are equal and of order unity for both the measured and computed profile.

The major difference between the measured and computed profiles at (x-b)/h = 180 and 400 is found in the amplitudes of the leading waves and the trailing train of oscillatory waves. The measured leading wave amplitude at (x-b)/h = 400 is 36% smaller (in absolute value) than the amplitude of the wave computed by the KdV equation at this position. If the leading wave amplitude is increased in absolute value by 14% to correct for numerical dispersion, the difference in measured and computed amplitudes increases to 50%. (Recall that a 54% difference between measured and computed leading wave amplitudes was found at (x-b)/h = 400 in Fig. 5.23a and Fig. 5.23c.) It should be noted that when the leading wave amplitude computed by the KdV equation is increased by 14% to correct for numerical dispersion, the wave amplitudes behind the leading wave must be decreased in a like manner in order to satisfy the requirement of the conservation of wave volume. Hence, the large amplitude oscillatory waves behind the computed leading wave in Fig. 5.25c would be reduced in amplitude and would then agree better with the measured oscillatory waves. As indicated in the discussion of Fig. 5.23, the difference between the computed and observed amplitudes is probably a result of energy dissipation due to viscous effects in the experimental measurements.

It can be seen from Figs. 5.25a and 5.25b that the wave computed by the KdV equation arrives at (x-b)/h = 400 before the measured profile. The arrival time of the measured wave at this location indicates that the wave has propagated with an average velocity of $\sqrt{gh} = 70$ cm/sec between $(x-b)/h = 20$ and 400. The difference in the arrival times of the measured and computed profiles indicate that the average velocity of the computed profile is approximately 3% larger than the observed velocity of measured profile. A similar difference in average velocities was found for positive wave propagation in Figs. 5.23a and 5.23c.

The centroid of each measured profile in the downstream region is also indicated in Fig. 5.25a. The average centroid velocity between $(x-b)/h = 20$ and 180, and $(x-b)/h = 180$ and 400, was found to be 62.8 cm/sec and 63.7 cm/sec, respectively. The centroid velocity thus appears to be relatively constant during propagation. A similar behavior was also found for the centroid velocity of the positive waves in Fig. 5.23a; hence, the effect of viscous forces on centroid velocity again appears to be small compared to the effect of energy losses on wave amplitudes.

In order to investigate further downstream behavior of waves created by a negative bed displacement, the measured wave profile at $(x-b)/h = 400$ has been used as the initial condition for the KdV equation and then propagated numerically a distance of 700 depths similar to the case of the positive disturbance. A step size of $\Delta = 0.3$ was used for the numerical propagation which resulted in a 25% reduction in amplitude of a solitary wave with an initial amplitude of $\eta_o/h = 0.05$ for 700 depths of propagation. The results of the propagation are shown in Fig. 5.26 where the normalized wave amplitude, η/h, is shown as a function of the nondimensional time, $t\sqrt{g/h} - (x-b)/h$, at $(x-b)/h = 600$,

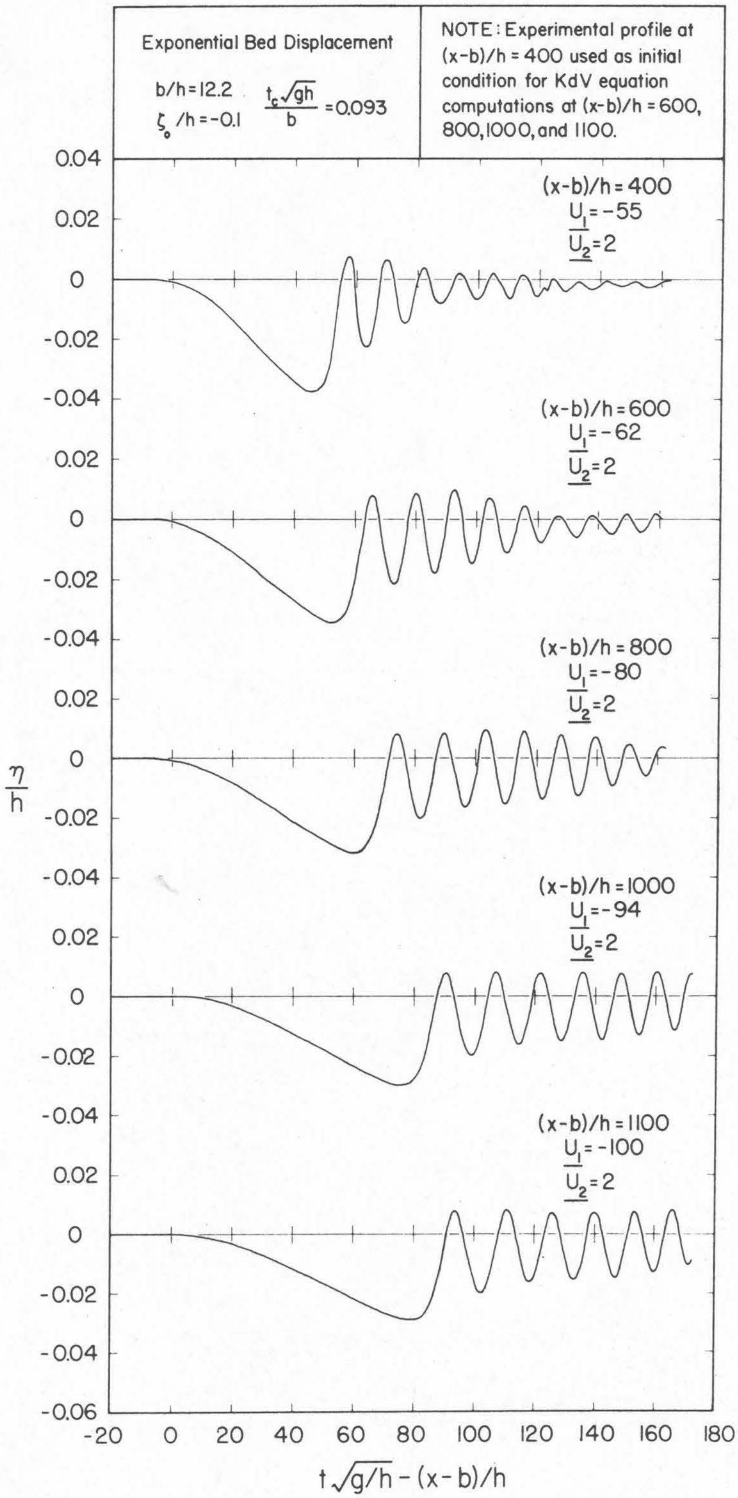

Fig. 5.26 Asymptotic wave behavior computed by the KdV equation for waves with a net negative volume.

800, 1000, and 1100. Ursell Numbers are also shown at each location for the front ($\underline{U}_1$) and rear ($\underline{U}_2$) regions of the lead wave.

At each downstream position the front face of the leading wave continues to stretch as the Ursell Number in this region grows from $\underline{U}_1 = -55$ at $(x-b)/h = 400$ to $\underline{U}_1 = -100$ at $(x-b)/h = 1100$. In the rear region of the leading wave the Ursell Number remains constant ($\underline{U}_2 = 2$) and of order unity at each downstream position. The trailing train of oscillatory waves appear to spread behind the leading wave during propagation as their period increases. The amplitudes of each of these oscillatory waves appear to vary less between adjacent waves as propagation continues. No solitary waves (or solitons) are formed.

For the waves created by a positive bed displacement in Fig. 5.23a and the waves created by a negative bed displacement in Fig. 5.25a, the linear near-field was found to be approximately twenty depths in length. The bed displacement used to generate each series of waves was impulsive and the disturbance-size scale, b/h, was equal to 12.2. In the discussion of the growth rate of nonlinearities in Chapter 3, it was found that for impulsive bed movements the length, β, of the linear near-field behaved like $(b/h)^{-3}$, (see Eq. (3.77)). Hence, for size scales greater than 12.2 the length of the linear near-field would appear to be appreciably less than twenty depths, and the linear theory would then appear to be even more limited in its ability to adequately treat a propagated wave.

In summary, the KdV equation appears to be the appropriate model for finding the temporal variation of the wave profiles in the far-field of the downstream region. The major difference between the measured profiles and the profiles computed by the KdV equation in the far-field occurs in maximum wave amplitudes; the measured amplitudes always were smaller than the computed amplitudes. This discrepancy is probably due to the effect of viscosity in the experiments and will be discussed in the following section (Section 5.2.2). The length of the linear near-field was found to be determined easily by observing the Ursell Number in the front region of the leading wave computed by the linear theory. When this Ursell Number became of order unity, the far-field had been reached. Up to and including this position the linear theory was found to agree well with the measured wave profiles. The linear theory appears to be quite limited in its ability to propagate a wave generated by an impulsive bed displacement over any large distance when the disturbance-size scale is also large.

For positive bed displacements a series of solitons followed by a group of oscillatory waves was found to be the asymptotic solution for the waves in the far-field. For negative bed movements no solitons were found; in the far-field the front face of the negative lead wave stretched with time and numerous oscillatory waves whose amplitude were of the same order of magnitude as the lead waves were observed following the negative leading wave. In regions of the wave where the Ursell Number was negative, the Ursell Number was found to become more negative during propagation while in wave regions where the Ursell Number was positive, the Ursell Number tended toward unity and remained constant during further propagation.

5.2.2 Energy Dissipation in the Downstream Region.

The presence of viscosity in the experimental model has been cited in Section.5.2.1 as a possible cause of the difference between wave amplitudes computed in the downstream region by the KdV equation and the measured wave amplitudes. As indicated in Section 5.1.4, viscosity causes boundary layers to form around the wetted perimeter of the wave tank and at the free surface of the fluid. Energy losses in these boundary layers causes a decrease in wave amplitudes during propagation.

Keulegan (1948) has investigated the damping of long waves of translation due to energy dissipation arising from the boundary layers adjacent to the solid boundaries of a wave tank. Assuming the boundary layers to be laminar, the energy dissipation was calculated using the well-known dissipation function (see e.g., Batchelor (1967, p. 153)). The total energy loss was shown to consist of two components: energy loss in the laminar layer directly beneath the wave, and kinetic energy left behind as the wave propagates. For a solitary wave of initial height η_{o_i} at x = 0, in water of depth, h, and in a wave tank of width B, Keulegan developed the following expression for the height, η_o, of the solitary wave at a downstream position relative to the initial height η_{o_i}:

$$\frac{\eta_o}{\eta_{o_\ell}} = \left[1 + \frac{1}{12}\left(\frac{x}{h}\right)\left(\eta_{o_\ell}/h\right)^{\frac{1}{4}}\left(1 + \frac{2h}{B}\right)\left(\frac{\nu^2}{gh^3}\right)^{\frac{1}{4}}\right]^{-4}, \qquad (5.14)$$

where g is the acceleration of gravity and ν is the kinematic fluid viscosity.

Laboratory experiments have been conducted to check the validity of Eq. (5.14) by several authors. These are summarized by French (1969, p. 170) who also includes his own data from experiments which were conducted in the same wave tank which was used in the current study. The different data shown by French (1969) show considerable scatter when compared to Eq. (5.14); however, the data of French appear to agree reasonably well with Keulegan's equation. Although the range of water depths used in the current study varied more than those of French, Eq. (5.14) appears to be a convenient expression for estimating the effect of viscous boundary layers developed along the wetted perimeter of the wave tank.

Fig. 5.27 shows the decrease in the ratio, η_o/η_{o_ℓ}, computed by Eq. (5.14) as a function of the downstream distance, $(x-b)/h$ for the four water depths: h = 5, 10, 30, and 50 cm, which were used in the experiments with the larger bed unit (b = 61 cm). At each water depth, curves have been computed for three values of the initial relative wave amplitude, η_{o_ℓ}/h = 0.1, 0.5, and 1.0. (The curve for $\eta_{o_\ell}/h = 1.0$ is of little practical value since waves are known to break when their amplitude approaches the same order of magnitude as the water depth.)

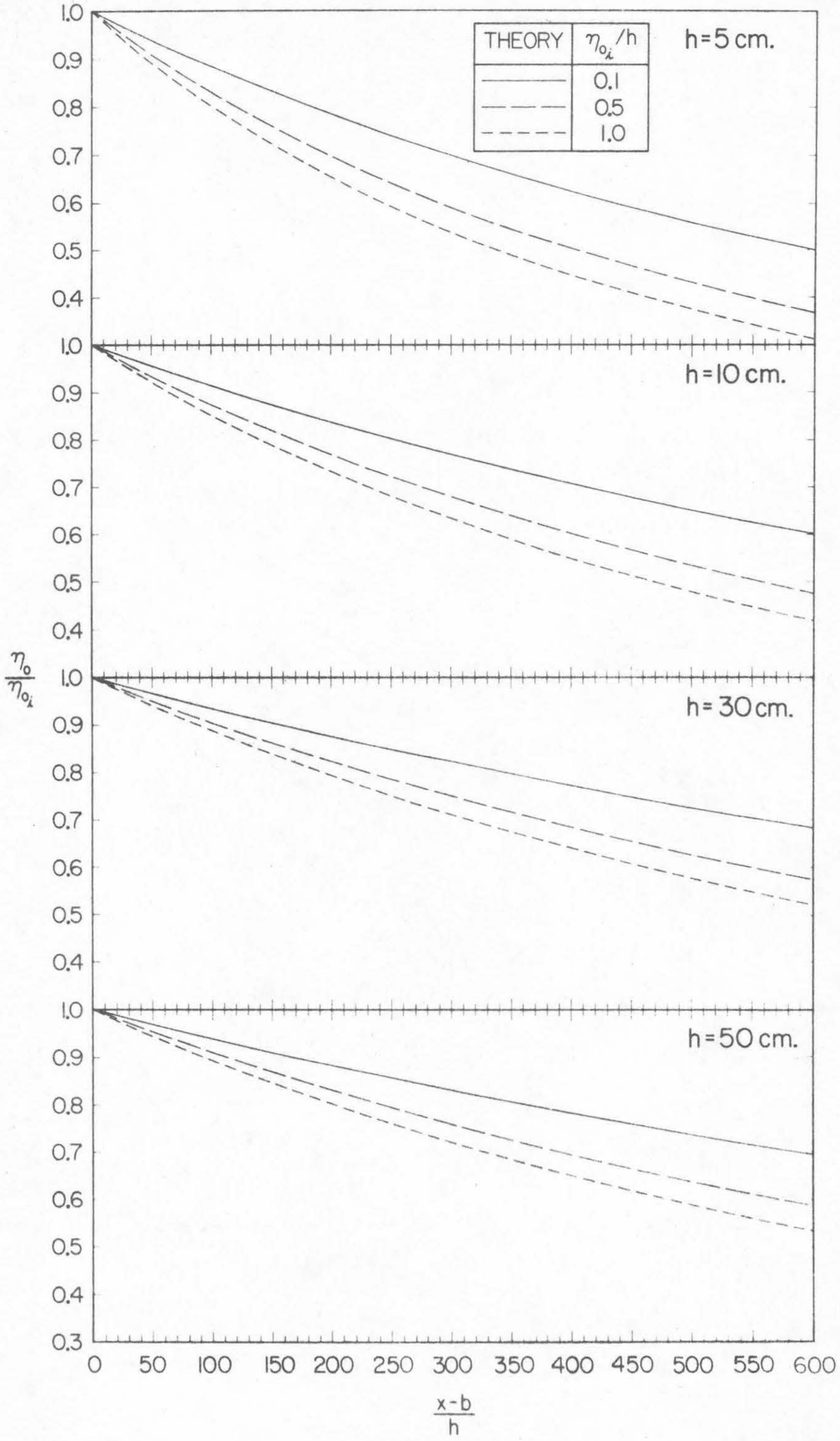

11430

Fig. 5.27 Amplitude decay of a solitary wave during propagation based on the equation of Keulegan (1948).

As would be anticipated, Fig. 5.27 shows that small depths and large wave amplitudes lead to more energy dissipation in the boundary layers and thus to greater damping of the wave amplitude.

Fig. 5.27 can be used to estimate the effect of boundary dissipation of the experimental waves shown in Figs. 5.23a and 5.25a. For these profiles the ratio of the initial wave amplitude to the depth (h = 5 cm) was approximately 0.1. From Fig. 5.27 Keulegan's equation is observed to predict approximately a 38% decay in wave amplitude after 400 depths of propagation, i.e., at (x-b)/h = 400. Recall that the observed difference between the measured and computed profiles was approximately 50-54%; hence energy losses in the boundary layer around the wetter perimeter of the wave tank do not appear to be sufficient to account for the total difference between theory and experiment.

Energy losses also occur in the boundary layer developed at the free surface. (Note that Keulegan's study does not consider losses in this layer.) In a study of the energy dissipation in the free-surface boundary layer, Van Dorn (1966) found that for low frequency oscillatory waves, the total energy loss in the surface layer was often as large or larger than the energy dissipation around the tank side walls. This surprisingly large dissipation is due to variations in surface energy which result from the contamination of the water surface invariably present under laboratory conditions unless the surface is specially treated. Since energy losses in the surface layer may be so large, it is reasonable to assume that these losses may account for the additional 12-16% decay in the experimental wave amplitudes at $(x-b)/h = 400$ indicated by the theoretical computations. Hence, the KdV equation appears to be an accurate model of wave propagation in the downstream region in the absence of viscous effects.

Another source of energy dissipation that occurred in some experiments resulted from the phenomenon of wave breaking. When the bed displacement was negative such that $|\zeta_o/h| \geq 0.5$ and the time-size ratio small, the positive wave immediately following the leading negative wave was found to break at a distance of ten to twenty depths from the generation region. This phenomenon occurred for both the exponential and half-sine bed displacements when the time-size ratio was less than 1.5 and 6.0, respectively.

Fig. 5.28 shows the positive wave immediately behind a negative leading wave breaking in the downstream region. The generation parameters for this wave are identical to those given by Eq. (5.5) for the negative, half-sine bed displacement used in the photographic sequence of Fig. 5.13. The energy loss due to wave breaking appears to have little effect on the downstream wave profiles since the breaking wave is small relative to the leading wave where most of the propagating energy is contained. No wave breaking occurred when the bed displacement was positive for the full range of generation parameters investigated.

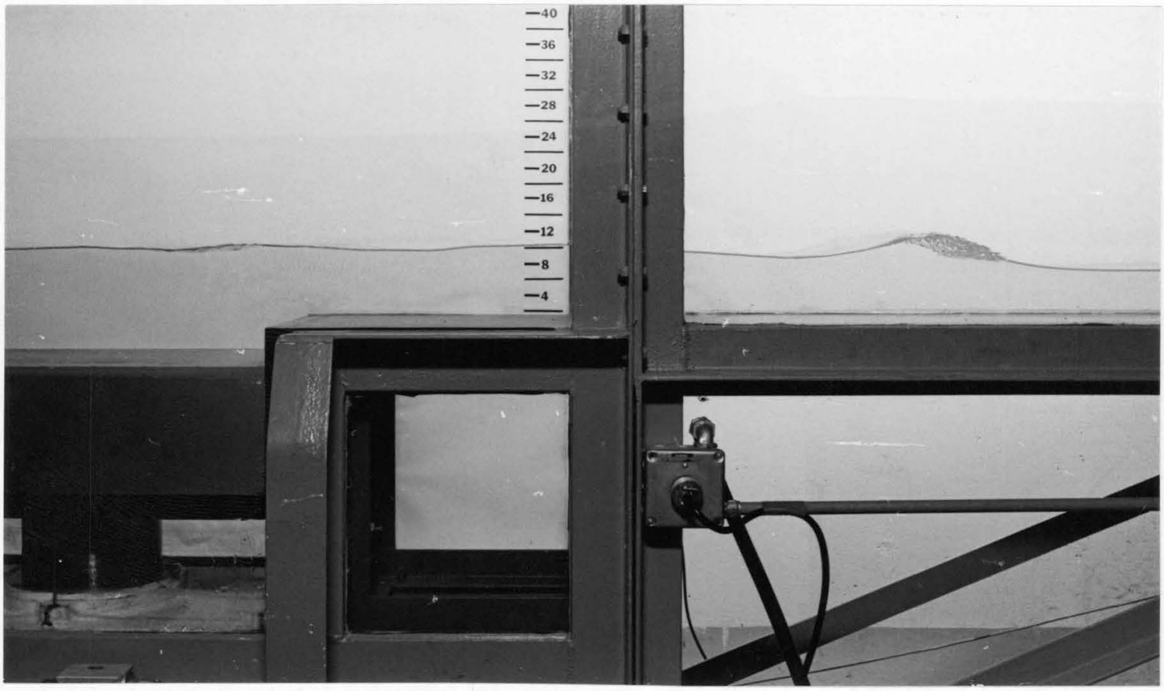

11431

Fig. 5.28 Wave breaking in the downstream region for negative bed displacements.

5.3 OSCILLATING BED MOTIONS WITH A MEAN DISPLACEMENT.

In the preceding sections only two simple time-displacement histories of the bed movement were considered. For each of these displacements the bed section rose or fell from its initial position to a prescribed elevation, ζ_o, in a manner such that its velocity, ζ_t, never changed sign during the movement. In order to observe experimentally the effect of a more general time-displacement history of the bed movement on the wave behavior, a system was constructed whereby an oscillating motion could be superposed on the half-sine or exponential bed displacements. The oscillating motion (or dither) began at the same instant as the mean motion and was automatically stopped as the bed unit neared the prescribed permanent displacement, ζ_o. Both the period, τ, and the crest-to-trough amplitude, ζ_1, of the dither could be varied. Experiments were conducted for the half-sine mean motion in which the period of the dither was varied from 10% to 50% of the characteristic time of the mean motion, i.e., $0.1 \le \tau/t_c \le 0.5$, and the amplitude of the dither was varied from 20% to 50% of the characteristic amplitude of the mean motion, i.e., $0.2 \le \zeta_1/\zeta_o \le 0.5$.

Figs. 5.29a, 5.29b, and 5.29c shows the results for three experiments in which the half-sine mean motion had the following generation parameters:

$$\zeta_o/h = 0.2, \quad b/h = 12.2, \quad t_c\sqrt{gh}/b = 1.10 \ . \tag{5.15}$$

From Fig. 5.2 the time-size ratio of the mean motion is observed to lie at the boundary between the impulsive and transition regions of generation. In Fig. 5.29a the actual time-displacement history of the bed for the mean motion and the resulting waves are shown at the positions: $(x-b)/h = -b/h$, 0, 20, 180, and 400. In Fig. 5.29b the time-displacement history of the bed and the resulting waves at similar positions are shown when a dither with a period of $\tau = 0.5\ t_c$ and an amplitude of $\zeta_1 = 0.5\ \zeta_o$ is superposed on the mean motion. The time-displacement history of the bed and resulting waves at $(x-b)/h = -b/h$, 0, 20, 180, and 400 are shown in Fig. 5.29c when a dither of period $\tau = 0.1\ t_c$ and amplitude $\zeta_1 = 0.5\ \zeta_o$ is superposed on the mean motion. In each case the wave amplitude, η, has been normalized by the water depth, h, and is shown as a function of the non-dimensional time: $t\sqrt{g/h} - (x-b)/h$.

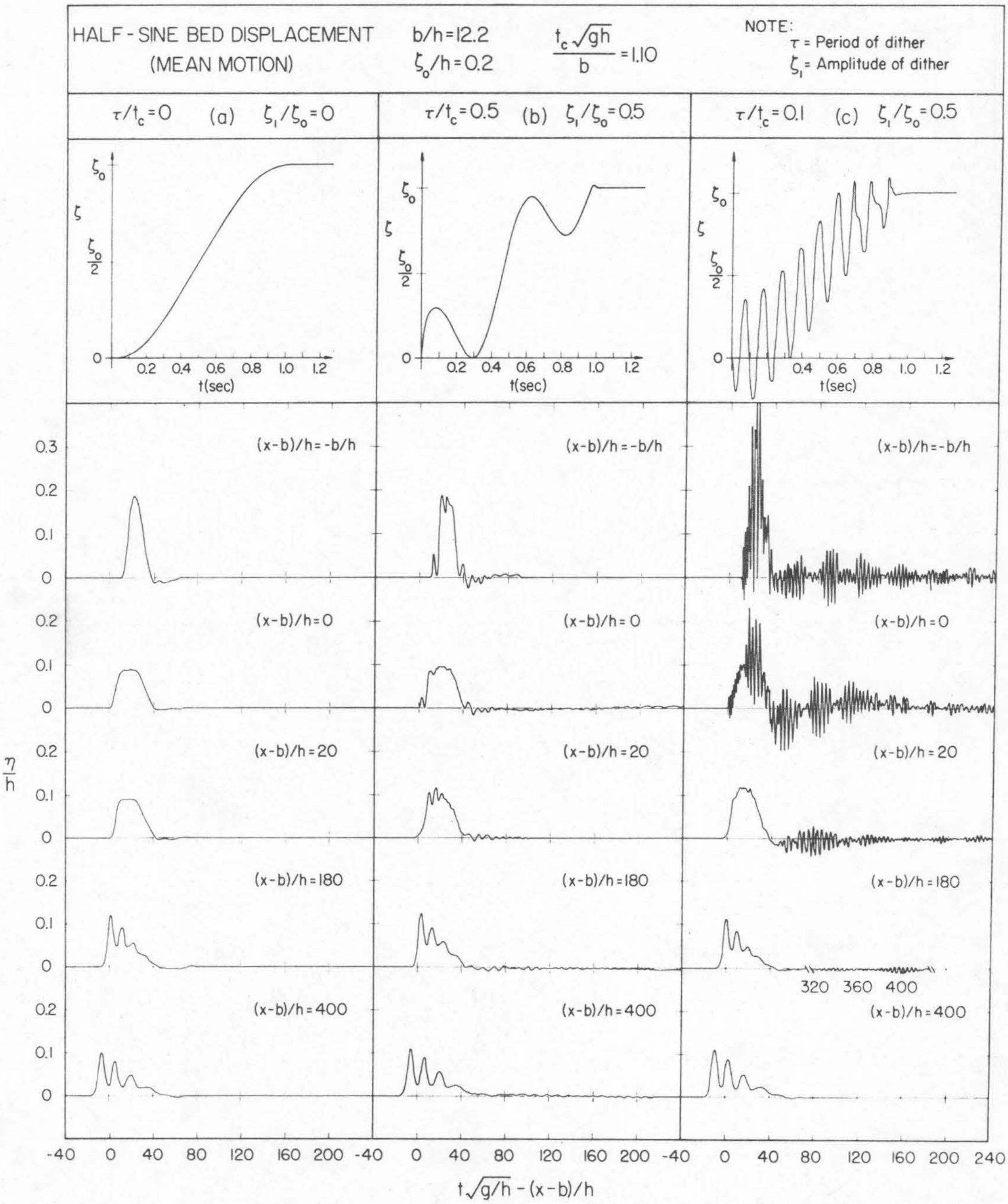

Fig. 5.29 Measured wave profiles; a) an impulsive half-sine mean motion, b), c) half-sine mean motion with a superposed oscillation.

The wave profile at the backwall, i.e., $(x-b)/h = -b/h$, in Fig. 5.29a rapidly rises to a maximum elevation, $\eta_o/h = 0.2$, (or $\eta/\zeta_o = 1$ since $\zeta_o/h = 0.2$) and immediately decreases to the still water level where a small amplitude negative wave results which has a nodal time of the same order of magnitude as the positive leading wave. At the leading edge of the disturbance, $(x-b)/h = 0$, the water rises to a maximum elevation, $\eta_o/h = 0.1$, remains at this level for an interval of time, and then decreases to the still water level where a small negative wave is formed. At $(x-b)/b = 20$ the wave has changed very little from the profile observed at the leading edge of the disturbance. Further downstream at $(x-b)/h = 180$ the positive leading wave has begun to separate into solitons similar to the behavior of the waves shown previously in Fig. 5.23a. The separation of the leading wave into solitons continues at $(x-b)/h = 400$ as the crests of the individual waves separate and the troughs approach the still water level.

When a dither with an amplitude of $\zeta_1 = 0.5\ \zeta_o$ and a period of $\tau = 0.5\ t_c$ is superposed on the mean motion (Fig. 5.29b) the change in water level at the backwall, $(x-b)/h = -b/h$, follows the actual time-displacement history of the moving bed up to a maximum elevation equal to that reached by the mean motion in Fig. 5.29a. The superposed dither is responsible for generating small amplitude oscillatory waves whose period and amplitude are proportional to τ and ζ_1, respectively. After reaching a maximum elevation the water level at the backwall immediately decreases toward the still water level where oscillations are also observed to occur. At the leading edge of the moving bed the change in water level again follows the actual time-displacement history of the moving bed up to a maximum elevation equivalent to that observed for the mean motion alone in Fig. 5.29a. A small oscillatory wave is observed to be preceding the primary leading wave. The maximum water level is maintained for an interval of time and then begins to decrease to the still water level where small oscillatory waves occur. At $(x-b)/h = 20$ the water level rises to a maximum elevation about which small oscillations occur before the water level begins to decrease to the still water level. Small oscillatory waves are observed to be following the lead wave. It appears that the small wave preceding the primary leading wave at $(x-b)/h = 0$ has now been overtaken by the primary wave which is propagating with a larger celerity. At $(x-b)/h = 180$ the leading wave is observed to be separating into solitons just like the corresponding wave in Fig. 5.28a which was created by the mean motion alone. The oscillatory waves created by the superposed dither have now been left behind by the longer leading wave which is apparently generated by the mean motion only. This behavior is seen more clearly at $(x-b)/h = 400$ where the leading wave has continued to separate into solitons and resembles very closely the corresponding wave in Fig. 5.29a. The only difference between these two profiles occurs in the trailing portion of the wave profiles where very small oscillatory waves can be seen in the experiment in which the dither was superposed on the mean motion. It thus appears that this superposed dither has little effect on the downstream wave profiles for this experiment.

For the wave measurements shown in Fig. 5.29c the period of the superposed dither has been reduced to $\tau = 0.1\ t_c$ while the amplitude of the dither has been maintained at $\zeta_1 = 0.5\ \zeta_o$. The water movement at the two positions in the generation region, $(x-b)/h = -b/h$ and 0, is drastically altered from that observed in Fig. 5.29b where $\tau = 0.5\ t_c$. At the backwall the water level initially follows the time-displacement history of the moving bed but suddenly large amplitude oscillations with a small period occur. Some of these oscillations have a maximum amplitude, η_o/h, greater than 0.4 which corresponds to an amplitude greater than twice the total bed displacement, ζ_o. These large waves are caused by the formation of cross waves in the generating region, i.e., waves propagating laterally across the wave tank. Cross waves are known to sometimes form during the forced oscillation of a fluid region as a result of a nonlinear instability (see e.g., Lin and Howard (1960)). Cross waves were found to occur in the present experiments when both ζ_1/ζ_o approached unity and τ/t_c became very small. For example, no cross waves occurred when the period of the dither was maintained at $\tau = 0.1\ t_c$ and the amplitude of the dither was reduced to $\zeta_1 = 0.2\ \zeta_o$. The cross waves at the backwall continue to reflect from the tank sidewalls after the displaced water volume propagates from the generation region.

The effect of the cross wave pattern is clearly shown at the leading edge of the disturbance, $(x-b)/h = 0$. Initially the water level rises and oscillates just as the bed unit but suddenly large amplitude waves develop. These cross waves which develop continue to propagate back-and-forth across the wave tank long after the longitudinal waves created by the bed motion have propagated from the generation region.

At the first downstream position, $(x-b)/h = 20$, the long wave which is apparently created by the mean motion arrives first and resembles very closely the wave form recorded at the same position in Fig. 5.29a where only the mean motion was used. The effect of the cross waves in the generation region can also be seen at $(x-b)/h = 20$ in Fig. 5.29c where groups of oscillatory waves are observed to be following the longer leading wave. These oscillatory waves which are propagating longitudinally in the wave tank are two-dimensional and have apparently been generated by the longitudinal pressure gradients induced by the cross wave pattern in the generation region.

At $(x-b)/h = 180$ the leading wave is separating into solitons just as the leading waves at the same position in Figs. 5.29a and 5.29b. The oscillatory wave pattern following the leading wave at $(x-b)/h = 180$ is now approximately 360 nondimensional time units behind the leading wave. (Note that the time axis has been broken in order to show this trailing wave group.) The maximum amplitude of the oscillatory waves of the first wave group has decreased by approximately 80% between

$(x-b)/h = 20$ and $(x-b)/h = 180$; probably as a result of the combined effect of energy dissipation due to viscosity and frequency separation.

At $(x-b)/h = 400$ the leading wave continues to separate into solitons and is almost identical to the wave profiles at this downstream position in Figs. 5.29a and 5.29b. The trailing wave groups have been left so far behind by the leading wave at this position that they were not recorded before the leading wave reflected from the end of the wave tank and returned to the position of the wave gage.

Fig. 5.29 thus demonstrates that when the mean motion of the bed displacement is impulsive, the same leading wave results during propagation, regardless of the details of the actual bed displacement. (Recall that the time-size ratio of the mean motion used in Fig. 5.29 was at the boundary of the impulsive and transition regions of generation.) This behavior of the downstream waves is extremely important in the practical application of the results obtained in Sections 5.1 and 5.2 for the simple family of bed displacements, i.e., the half-sine and exponential motions. (Application of these results will be discussed in Section 5.4.)

In Section 5.1.2 it was shown that the waves resulting when the time-size ratio of the bed displacement was in the creeping region of generation were highly dependent on the actual time-displacement history of the bed movement. Hence, if an oscillation is superposed on the mean motion of a creeping bed displacement the resulting waves would be expected to differ accordingly. A half-sine mean motion with the following generation parameters has been used to investigate this suggested behavior:

$$\zeta_o/h = 0.4, \quad b/h = 12.2, \quad t_c\sqrt{gh}/b = 16.75. \tag{5.16}$$

Fig. 5.30a and Fig. 5.30b show, respectively, the waves resulting for the mean motion alone and for the mean motion with a superposed dither which has a period of $\tau = 0.1\ t_c$ and an amplitude of $\zeta_1 = 0.5\ \zeta_o$. The wave amplitude, η, has been normalized with respect to the water depth, h, and is shown at the positions $(x-b)/h = -b/h$, 0, 20, 180, and 400, as a function of the nondimensional time: $t\sqrt{g/h} - (x-b)/h$. The actual time-displacement histories of the bed motion are also shown above each sequence of wave profiles.

The wave created by the mean motion alone in Fig. 5.30a is similar at each position of measurement in the generation region. The water rises slowly to a maximum elevation and then decreases to the still water level forming a symmetric wave form. During propagation the front face of the wave begins to steepen as a result of amplitude dispersion.

When the dither is superposed on the mean motion, the water in the generation region is observed in Fig. 5.30b to move in the same manner as the bed, forming a train of oscillatory waves whose amplitude is much larger than the waves created by the mean motion alone. During propagation each of these oscillatory waves begins to disperse and interact to form a complex train of waves which do not resemble in any manner the single wave created by the mean motion. Hence,

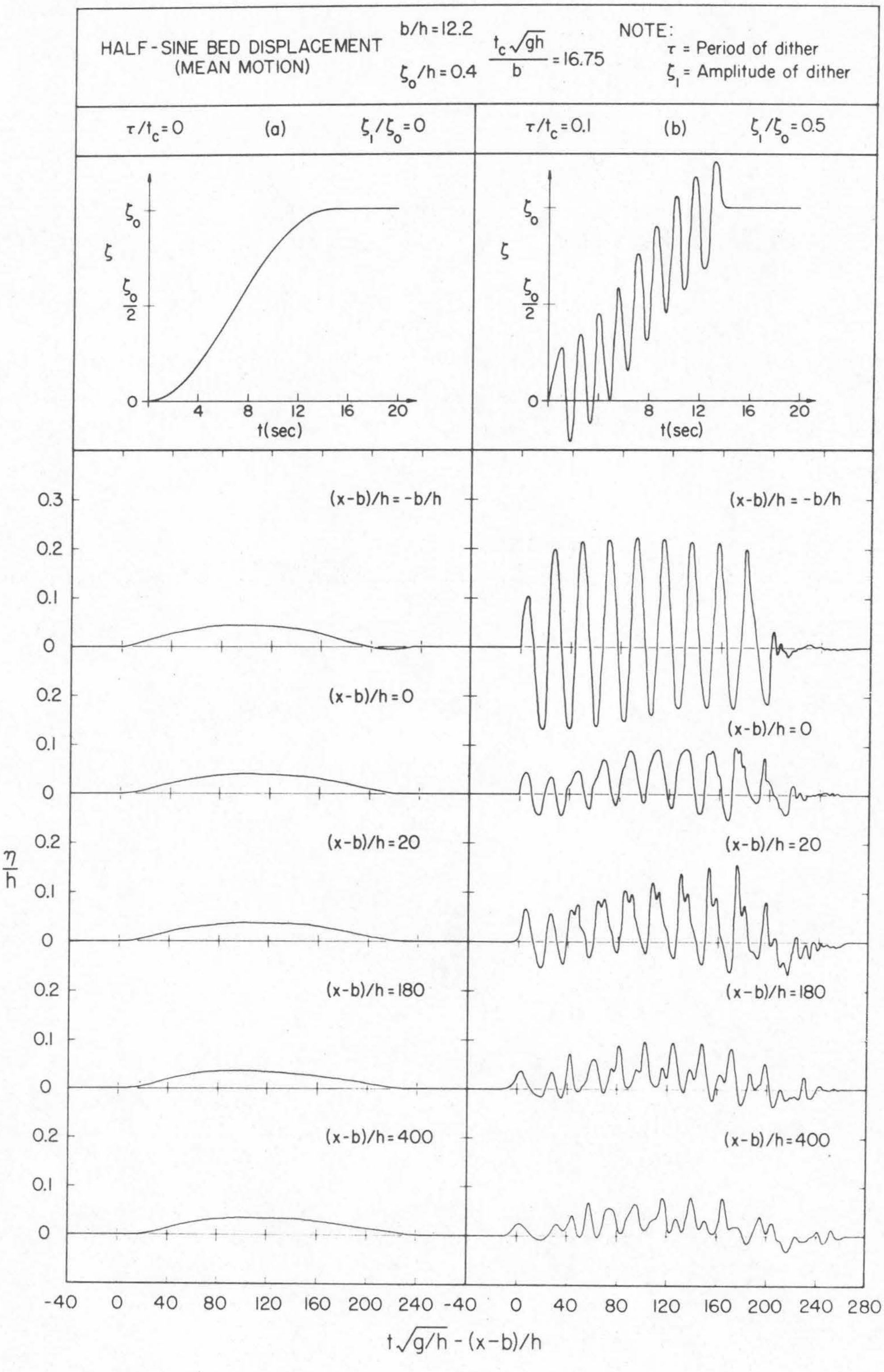

Fig. 5.30 Measured wave profiles; a) a creeping half-sine mean motion, b) half-sine mean motion with a superposed oscillation.

when the mean motion of a bed displacement lies in the creeping region of generation, the detailed time-displacement history of the movement is extremely important in determining wave behavior. (No cross waves developed in any experiments for which the mean motion was in the creeping region of generation.)

In summary, it appears that the superposition of an oscillating movement on an impulsive mean motion has little effect on the wave profiles measured in the downstream region. Some small oscillatory waves are generated by the dither but these are quickly left behind by the larger (and longer) wave which is apparently created by the mean motion alone. When the mean motion is in the creeping region of generation, the superposed dither has a major effect on the observed waves in the downstream region. The oscillating motion generates a series of long waves which have maximum amplitudes that are somewhat larger than the amplitude of the wave created by the mean motion alone; hence the oscillatory waves are traveling at a slightly larger velocity than the wave created by the mean motion.

5.4 APPLICATION OF RESULTS TO THE ALASKAN EARTHQUAKE OF 27 MARCH 1964.

The results presented in Sections 5.1, 5.2, and 5.3 for a simple two-dimensional model of tsunami generation indicate that three parameters of bed deformation are important in determining the characteristics of the generated wave. These three parameters are: (1) the disturbance-amplitude scale, ζ_o/h, (2) the disturbance-size scale, b/h, and (3) the time-size ratio, $t_c\sqrt{gh}/b$, which incorporates the disturbance-time scale, $t_c\sqrt{g/h}$. It is of primary importance to investigate an actual tsunamigenic earthquake in order to determine characteristic values of these nondimensional ratios and thus to infer certain characteristics of the generated tsunami.

Although numerous tsunamigenic earthquakes have occurred (mainly in the Pacific Ocean), very little information is available in the literature regarding the actual tectonic deformations of the sea bed which are responsible for generating tsunamis. The detailed form of submarine tectonic displacements is extremely difficult to determine since the deformations cannot be observed directly and in most cases the preearthquake bathymetry is unknown so that postearthquake soundings are of little value. In fact, submarine bed deformations resulting during an earthquake appear to be generally inferred from available tsunami signatures recorded at various tide gage stations that are affected.

The only tsunamigenic earthquake for which a reasonably accurate description of the submarine tectonic deformations exists appears to be the Alaskan earthquake of 27 March 1964. This disasterous earthquake had a Richter magnitude of 8.4 (Pasadena seismograph station) and was accompanied by crustal deformations of land and sea bottom in south-central Alaska covering an area probably in excess of 110,000 square miles (Plafker, 1969). A tsunami was generated by the sea bed deformations which caused extensive damage and loss of life along the Alaskan coastline and at locations as far away as Crescent City, California. Because of the location of numerous offshore islands in the coastal region affected by the earthquake, and the knowledge of preearthquake bathymetry in portions of the coastal region, this earthquake provided an exceptional opportunity to determine the submarine tectonic deformations responsible for generating the ensuing tsunami. The tectonics of the Alaskan earthquake have been discussed extensively by Plafker (1969) from which most of the following description has been taken.

The epicenter of the Alaskan earthquake was located somewhat north of Prince William Sound (lat. 61.06° N., long. 147.44° W.) as indicated in Fig. 5.31 which has been adapted from Plafker (1969). The initial rupture apparently propagated in a predominantly south-westerly direction for a distance of 375-500 miles (600-800 km). The propagation of the rupture appears to have occurred in a complex series of bursts (Wyss and Brune, 1967) with an average velocity of 2 miles/sec (3 km/sec). The observed and inferred tectonic deformations are postulated by Plafker (1969) to have resulted primarily from a relative seaward displacement and uplift of the seaward portion of the effected area and a simultaneous horizontal extension and subsidence of the landward portion of the effected area. This dipolar movement of the earth's crust was centered along a "hinge line" running from the northern portion of Prince William Sound in a southwesterly direction to Trinity Islands (see Fig. 5.31). Isobase contours of the vertical tectonic

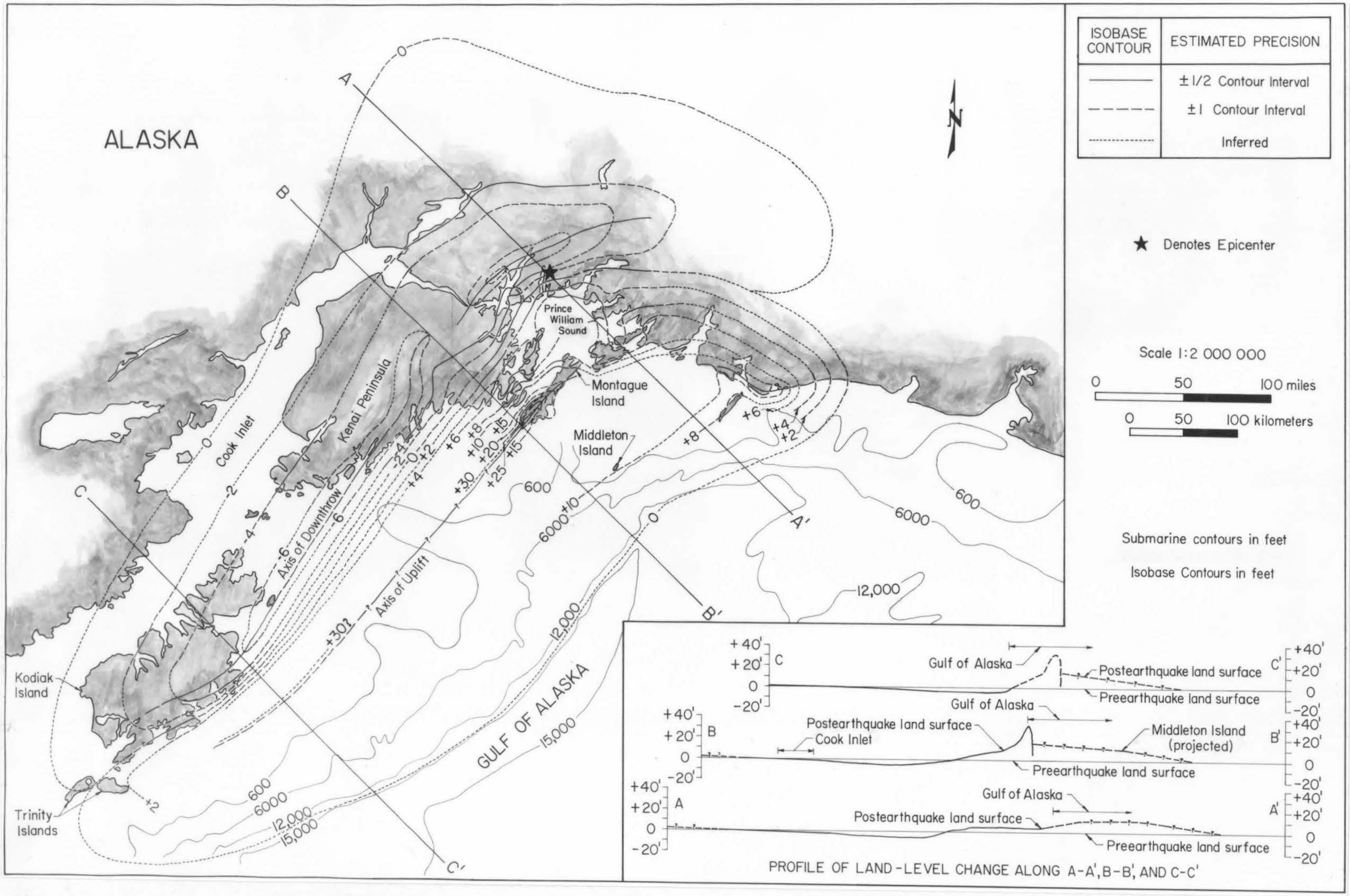

Fig. 5.31 Vertical ground deformations resulting from the Alaskan earthquake of 27 March 1964 (adapted from Plafker (1969)).

displacements (which indicate the amount of vertical deformation relative to the preearthquake land elevation) have been constructed by Plafker (1969) and are shown in Fig. 5.31. The major area of uplift is observed in Fig. 5.31 to occur in an arcuate region encompassing the Continental Shelf and possibly portions of the continential slope with a length of approximately 375 miles and a maximum width of 150 miles. The maximum measured uplift was found to be 38 ft which occurred in a northwest trending belt about 6 miles wide along the Continental Shelf and was exposed on Montague Island in the southwestern portion of Prince William Sound. The major zone of subsidence occurred partially in the embayed coastal areas and along the Alaskan mainland. The maximum measured land downthrow appears to be approximately 8 ft.

The vertical displacements along three cross-sections through the effected region are also shown in Fig. 5.31; these deformations are measured from the preearthquake land elevation denoted by the zero base line. Along Section A-A' an approximately uniform uplift of 5-10 ft occurs in a submarine region with a cross-sectional length of approximately 150 miles; a corresponding downthrow with a maximum amplitude of 6 ft occurs on the landward side of this cross-section. From the cross-section B-B', the sea bed is observed to have uplifted in an approximately linear manner to an elevation of approximately 17 ft at a distance of 30 miles seaward of the hinge line of the dipolar crustal deformation. The sea bed then lifted to a maximum elevation of 30 ft in a narrow belt approximately 6 miles wide. This region is followed by a zone of nearly uniform uplift of 15 ft for a distance of 50 miles to the projected position of Middleton Island. The remaining uplift occurred in a region over the continental slope and apparently decreased to zero near the foot of the slope. (Note that Middleton Island appears to be located at the edge of the Continental Shelf.) The negative displacement along Section B-B' occurs mainly on land and does not exceed approximately 6 ft. The inferred zone of uplift along Section C-C' closely resembles the profile at Section B-B' even though these two cross-sections are separated by approximately 200 miles along the major axis of the region affected by the earthquake. As observed before, most of the uplift along Section C-C' occurs on the Continental Shelf and decreases to zero along the continential slope.

Plafker suggests that the axis of sea bed uplift along the Continental Shelf, shown in Fig. 5.31, is also the axis of the source region for the tsunami generated by the earthquake. Independent evidence of this suggested source region was also determined by Van Dorn (1964) with the use of wave refraction diagrams constructed from known arrival times of the Alaskan tsunami at different tide gage locations around the Pacific Ocean. It thus appears that the tectonic deformation responsible for the Alaskan tsunami consists of an elongated belt which extends approximately 350 miles from the vicinity of Montague Island to the area offshore of the Kodiak Island group in which a typical vertical bed displacement is illustrated by the cross-section B-B' in Fig. 5.31.

The average width of the belt of uplift appears to be approximately 125 miles. (It should be noted that the seaward thrust of the earth movement during the Alaskan earthquake created horizontal displacements of approximately 64 ft; however, these movements are apparently discounted by Plafker (1969) as a mechanism for large ocean wave generation since the bathymetry of the sea bed was not sufficiently steep in the region of these horizontal displacements to generate a large wave.)

As stated by Plafker (1969), no instrument records exist which would indicate the time or rate of the tectonic movements occurring during the Alaskan earthquake; hence, no time-displacement history of the bed uplift in the source region of the generated tsunami is known. Eyewitness reports indicate that the major portion of the tectonic movements occurred during the 1-1/2 to 5 minutes of violent tremors. Van Dorn (1964) suggests that the vertical displacements must have occurred very rapidly (from 2 to 6 minutes) due to the presence of an atmospheric gravity wave measured at La Jolla, California which was apparently generated by the vertical movements of the land and ocean.

From the preceding discussion of the source mechanism for the Alaskan tsunami, a two-dimensional model of the generation would appear to be applicable at least locally since the region of generation is elongated with a length of approximately three times the width. If the deformed bed profile shown at the cross-section B-B' in Fig. 5.31 is indeed typical of the general bed displacement responsible for the Alaskan tsunami, then a characteristic size, b, may be defined. The total width of the region of uplift excluding the region over the continental slope is approximaely 100 miles; hence, the half-width of the region is $b \simeq 50$ miles. (It seems appropriate to neglect the region of uplift over the continental slope, i.e., seaward of Middleton Island in Section B-B', since the water depth in this region is increasing rapidly and the uplift is decaying to zero.) The average water depth in the region of uplift landward of Middleton Island is of the order of 600 ft as seen in Fig. 5.31; hence, a characteristic disturbance-size scale becomes: $b/h \simeq 450$.

In order to determine the time-size ratio, $t_c\sqrt{gh}/b$, of the generation process, a characteristic time, t_c, of the bed displacement is required. As indicated earlier, the best estimate of the total time of ground movement (which is a convenient characteristic time) appears to be two to six minutes. Using these times and an average water depth of $h = 600$ ft, yields a range of possible time-size ratios given by:

$$0.06 < \frac{t_c\sqrt{gh}}{b} < 0.18 . \qquad (5.17)$$

Since the probable range of time-size ratios given by Eq. (5.17) is much less than unity, the bed displacement of the Alaskan earthquake appears to be impulsive. This suggested behavior can be seen directly from Fig. 5.1 or Fig. 5.2 if the results determined for an exponential or half-sine bed displacement in Section 5.1 are applied to the Alaskan earthquake.

Since the bed uplift (and water depth) along B-B' in Fig. 5.31 is not uniform, the disturbance-amplitude scale, ζ_o/h, must vary along this cross-section. The maximum uplift of approximately 30 ft occurs in a narrow region in which the water depth is approximately 300 ft. (Detailed contours of the water depth in this region are given by Wilson and Tørum (1968, p. 53) from which this depth was determined.) Outside this narrow belt the amplitude of the vertical deformation decreases while the water depth is generally greater than 300 ft; hence, the maximum value of the disturbance-amplitude scale along B-B' appears to be: $(\zeta_o/h)_{max} = 0.1$.

From the preceding discussion, possible values of the important parameters of generation for the Alaskan tsunami appear to be:

$$\zeta_o/h < 0.1, \quad b/h \simeq 450, \quad 0.06 < \frac{t_c\sqrt{gh}}{b} < 0.18 \; . \qquad (5.18)$$

The small amplitude scale of Eq. (5.18) suggests that a linear theory provides an adequate description of the initial wave behavior; since the time-size ratio indicates an impulsive generation, the actual time-displacement history of the bed movement is not expected to be of critical importance in determining the general characteristics (e.g., the maximum amplitude, η_o, the rise time, t_r, the fall time, t_f, and the nodal time, t_n) of the lead wave propagating from the region of generation. Hence, it is of interest to examine the predicted general features of the lead wave of the Alaskan tsunami in light of the results determined in Section 5.1 by the linear theory for waves generated by two specific bed movements. Since the bed uplift or water depth in the generation region is not uniform or symmetrical about the centerline of the uplift region, the wave which propagates out of the generation region toward the Alaskan mainland would not be expected to resemble in detail the wave which propagates seaward of the uplift region. The following discussion will be primarily concerned with the wave which propagates seaward of the region of uplift.

As suggested previously, the leading edge of the generation region on the seaward side of the uplift may be taken as the projected position of Middleton Island shown on the cross-section B-B' in Fig. 5.31. The characteristics of the wave which propagates past this position are probably dominated by the 50 miles of nearly uniform uplift of 15 ft which occurs between the narrow belt of maximum uplift and Middleton Island. As a first approximation it is useful to assume that the uplift along the entire cross-section is uniform with a total displacement, ζ_o, of approximately 15 ft; under this assumption, the results presented in Section 5.1 may be directly applied. It should be recalled from the discussion in Section 5.1.1 that the maximum amplitude ratio, η_o/ζ_o, of the leading wave in the generation region was found to become constant and independent of the time-size ratio in the impulsive region of generation. The asymptotic value of η_o/ζ_o for impulsive bed movements was found to be independent of size scale for $b/h > 4$; hence, the results presented in Section 5.1.1 may be used for the very large size scale ($b/h = 450$) of the Alaskan tsunami. It was determined in Section 5.1.3 that for each type of bed movement investigated, the rise-time ratio, t_r/t_c, and the nodal-time ratio, t_n/t_c, did not vary appreciably between the size scales of b/h = 12.2 and b/h = 100. In the impulsive region of generation where the rise and fall-time ratios are not equal, the ratio of the nodal and fall times, i.e., t_n/t_f, was observed to decrease toward unity as the size scale increased from b/h = 12.2 to b/h = 100. Hence, it appears to be appropriate to apply the results computed for b/h = 100 in Section 5.3.1 to this case. Since the characteristic time, t_c, for the Alaskan earthquake has been estimated as the total time of the bed deformation, the results for the half-sine bed displacement would appear to be more appropriate than the corresponding results for the exponential bed movement; however, both types of motion will be considered in this discussion.

The inferred characteristics (η_o, t_r, t_f, and t_n) of the leading wave of the Alaskan tsunami at the projected position of Middleton Island on the cross-section of B-B' of Fig. 5.31 are presented in Table 5.1. Column (1) indicates the type of bed motion from which the characteristic features of the wave have been determined while Columns (2) and (3) indicate the assumed characteristic time, t_c, and the resulting time-size ratio, respectively. Columns (4), (5), (6), and (7) indicate the nondimensional time ratios of the leading wave where the values in Column (4) have been found from Fig. 5.6a for the exponential bed movement and from Fig. 5.6b for the half-sine bed movement. Columns (5),

(1)	(2)	(3)	(4)	(5)	(6)	(7)	(8)	(9)	(10)	(11)
BED MOTION	t_c (min)	$\frac{t_c\sqrt{gh}}{b}$	η_o/ζ_o	t_r/t_c	t_f/t_c	t_n/t_c	η_o (ft)	t_r (min)	t_f (min)	t_n (min)
Exponential	2	0.06	0.5	5	32	38	7.5	10	64	76
	6	0.18	0.5	5	11	13	7.5	30	66	78
Half-Sine	2	0.06	0.5	1	32	34	7.5	2	64	68
	6	0.18	0.5	1	11	12	7.5	6	66	72

Table 5.1 Inferred characteristics of the leading wave of the Alaskan tsunami (27 March 1964) near Middleton Island.

(6), and (7) have been determined from Fig. 5.17 for the exponential bed movement and from Fig. 5.18 for the half-sine bed movment. (The theoretical curves for $b/h = 100$ in Fig. 5.18 must be extrapolated to the small time-size ratio of $t_c\sqrt{gh}/b = 0.06$.) Column (8) has been computed using $\zeta_o = 15$ ft which is the assumed uplift. Columns (9), (10), and (11) indicate the rise, fall, and nodal times of the leading wave, respectively, which were computed from the characteristic time, t_c, presented in Column (2) and the time ratios presented in Columns (5), (6), and (7).

The rise times of the leading wave are observed in Table 5.1 to vary between 2-6 minutes for the half-sine displacement and 10-30 minutes for the exponential movement. As suggested earlier, the results for the half-sine motion are probably more appropriate since the total time of bed deformation has been used to estimate the characteristic time, t_c. The fall time of the leading wave is estimated in Column (10) to be 64-66 minutes regardless of the type of bed movement. The nodal time of the leading wave is found in Column (11) to be in the range of 68-72 minutes by the half-sine results and 76-78 minutes by the exponential results. The type of bed motion thus appears to have little effect on the fall and nodal times. The profile of the leading wave of the Alaskan tsunami is thus suggested by the results of Section 5.1 to resemble the shape of the nondimensional profiles shown in Fig. 5.8 or Fig. 5.9 at $x/h = b/h$ in the impulsive region of generation; the suggested dimensional characteristics of the leading waves are:

$\eta_o \simeq 7.5$ ft, $t_r \simeq 2$-6 minutes, $t_f \simeq 64$-66 minutes, and $t_n \simeq 68$-78 minutes.

The characteristics of the leading wave which are suggested above are based on the assumptions of uniform bed uplift and uniform water depth which are not completely valid assumptions. The variable uplift would be expected to affect η_o to some degree; however, no wave amplitude greater than 15 ft, i.e., one-half the maximum bed uplift, would be expected to propagate from the generation region. The variation in the water depth would affect the temporal variations of the wave profile to some extent; however, the indicated values are expected to suggest at least the correct order of magnitude of these times. The suggested nodal time of more than 1 hour is in relative agreement with the leading wave periods found by Wilson and Tørum (1968) from the subjective analysis of marigrams of the Alaskan tsunamis recorded at tide gage stations near Alaska. This large nodal time is also in agreement with the leading wave period found from the deep-water signature of the Alaskan tsunami which was recorded at Wake Island and presented by Van Dorn (1964).

The very large size scale indicated by Eq. (5.17) suggests that the effects of nonlinearity will very quickly become of the same order of magnitude as the linear effects of frequency dispersion during wave propagation. However, it should be noted that the wave propagating seaward of the generation region immediately enters the region of the continental slope where the water depth increases rapidly; hence, the effects of frequency dispersion which are indicated by $(h/\ell)^2$ would increase while the effects of nonlinearity indicated by η_o/h would decrease. Thus a linear theory which incorporates a variable water depth might be useful to propagate the wave over the continental slope; however, at some point past the continental slope (if not before), the nonlinearities would become of equal importance as the linearities and a theory such as that given by the KdV equation would be necessary to adequately model the wave behavior. (Recall that the KdV equation used in this study is only applicable for wave propagation in a fluid domain of uniform depth.)

Regardless of the actual time-displacement history of the bed uplift in the Alaskan earthquake, the results of Section 5.3 indicate that the leading wave reaching positions outside the generation region would resemble the wave generated by the mean motion only. Any high frequency waves generated by high frequency oscillations of the moving bed would be left behind during propagation by the longer lead wave.

If the Alaskan earthquake is indeed typical of a major tsunamigenic earthquake, the general characteristics of the tsunami generated by this earthquake, which have been described above, would appear to be applicable to most tsunamis. The major limitation of the two-dimensional model of tsunami generation presented in this study appears to result from the assumption of uniform depth in the downstream region of propagation. Tsunamigenic earthquakes in the Pacific Ocean usually occur in the shallow water along the Continental Shelf; hence a proper description of wave propagation must consider the large changes in depth which occur across the continental slope. The two-dimensionality of the model appears to be sufficient in determining local wave behavior; however, for wave propagation over large distances from the source region, a three-dimensional model should be used.

CHAPTER 6

CONCLUSIONS

The major objective of the present study has been to investigate, both theoretically and experimentally, the generation of tsunamis initiated by a simple family of bed deformations in a fluid domain with a uniform depth. Both a two and three-dimensional model of generation have been investigated theoretically; experiments have been conducted to check the validity of the two-dimensional model. The study of the wave behavior was presented by dividing the fluid domain into two regions: a generation region above the moving bed section and a downstream region in which the bed remained in its initial position for all time. Wave behavior in the downstream region has also been investigated using a theory which considers in an approximate manner both linear and nonlinear effects which affect the wave during propagation.

The following major conclusions can be drawn from this study for the region of generation:

1. Three nondimensional parameters of the bed deformation are important in defining the characteristics of the waves which are generated: ζ_o/h, which represents an amplitude scale of the disturbance, b/h, which represents a size scale of the disturbance, and the time-size ratio,

$t_c\sqrt{gh}/b$, which incorporates a time-scale, $t_c\sqrt{g/h}$, of the disturbance.

2. The time-size ratio is useful in defining three general types of bed deformations for both the two and three-dimensional models: an impulsive bed deformation (for $t_c\sqrt{gh}/b$ very small) where the maximum amplitude ratio, η_o/ζ_o, of the leading wave becomes constant (independent of the time-size ratio), a creeping bed movement (for $t_c\sqrt{gh}/b$ very large) where η_o/ζ_o becomes inversely proportional to the time-size ratio, and an intermediate or transition region of generation for time-size ratios between the impulsive and creeping range.
3. The linear theory, which was developed for the two-dimensional model, adequately predicts the wave structure in the generation region (including the maximum amplitude and certain temporal variations such as the rise, fall, and nodal times of the leading wave) for impulsive or transition bed movements whenever the absolute value of the amplitude scale of the disturbance is less than 0.2, i.e., for $|\zeta_o/h| < 0.2$; the linear theory accurately predicts the wave structure for creeping bed movements over the full range of amplitude scales, i.e., $|\zeta_o/h| \leq 1$;
4. The general shape of the lead wave propagating across the boundary between the generation and downstream

region for an impulsive bed movement does not depend significantly on the actual time-displacement history of the bed; in the creeping region of generation the wave profiles are strongly dependent on the actual time history of the bed movement.

5. The detailed structure of the waves generated by an impulsive bed movement for the two and three-dimensional models of generation differ in one main respect; large amplitude negative waves can result from a positive bed movement in the three-dimensional model (and vice versa) whereas no large negative waves result from a positive bed movement in the two-dimensional model (or vice versa) for comparable generation parameters.

The following major conclusions can be drawn from the results determined for the downstream region of the two-dimensional model:

6. The Ursell Number as defined by Eq. (3.72) provides an excellent indicator for tracing the evolution of a long wave during propagation; when the maximum Ursell Number of a complex wave profile is less than unity then the linear theory provides an adequate description of wave behavior; when the Ursell Number becomes of order unity then the linear theory is no longer applicable; positive Ursell Numbers tend toward a value of unity during propagation and remain of this order during further propagation;

negative Ursell Numbers grow indefinitely in absolute magnitude during propagation.

7. The Korteweg and deVries equation (Eq. (3.80)) provides an adequate description of wave behavior (in the absence of viscous forces) once the Ursell Number has become of order unity; hence, wave profiles in the region of propagation where the linear theory is no longer valid may be determined by using a wave profile computed by the linear theory in its region of validity as the initial condition for the KdV equation and solving this equation for the wave profile at any downstream position.
8. Asymptotic numerical solutions of the KdV equation suggest that any initial wave with a net positive volume eventually results in a train of permanent-form solitary waves (or solitons) with decreasing amplitude toward the rear of the train followed by a tail of oscillatory waves; initial waves whose net volume is negative do not result in any waves of permanent form.
9. In the downstream region the same leading wave profile results for impulsive bed movements whose mean motions are similar regardless of the actual time-displacement history of the movement; this leading wave is apparently generated by only the mean motion of the bed displacement.

The Alaskan earthquake of 27 March 1964 was examined in detail in order to apply the results and determine the limitations of the generation models investigated in this study. The following major conclusions can be drawn from the examination of the Alaskan earthquake:

10. The probable generation parameters of the Alaskan tsunami indicate that a linear theory is applicable for determining the initial wave behavior and that the bed movement of this earthquake was impulsive so that a detailed knowledge of the actual time-displacement history of the movement probably is not required to predict certain features of the wave propagating from the generation region.
11. A two-dimensional model of wave generation is applicable for describing local wave behavior since the source region of the Alaskan tsunami was elongated with a length of approximately three times the average width.
12. The major limitations found in applying the results of the models investigated in this study to the Alaskan tsunami are caused by the assumptions of a uniform bed displacement and a uniform water depth in the downstream region; in order to determine more detailed structure of the wave propagating from the region of uplift, the variable uplift must be considered; the large changes in water depth

which occur at the continental slope must be considered to adequately model the wave behavior during propagation.

If the Alaskan earthquake is typical of large tsunamigenic earthquakes, then conclusions (10) to (12) may be applied to tsunamis in general.

LIST OF REFERENCES

1. Batchelor, G.K. (1967), An Introduction to Fluid Dynamics, Cambridge University Press, London.

2. Benjamin, T.B., and Mahony, J.J. (1971), "On An Invariant Property of Water Waves", Journal of Fluid Mechanics, Vol. 49, Part 2, pp. 385-389.

3. Binnie, A.M., and Orkney, J.D. (1955), "Experiments on the Flow of Water from a Reservoir Through an Open Horizontal Channel. II. The Formation of Hydraulic Jumps", Proceeding, Royal Society of London, Vol. 230, pp. 237-246.

4. Boussinesq, J. (1872), "Theorie des ondes et des remous qui se propagent le long d'un canal rectangulaire horizontal, en communiquant au liquide contenu dans ce canal des vitesses sensibilement pareilles de la surface au fond", Journal de Mathematiques Pures et Appliquees, 2nd Serie, Vol. 17, pp. 55-108.

5. Buckingham, E. (1914), "On Physically Similar Systems", Physical Review, Vol. 4, pp. 354-376.

6. Carrier, G.F. (1966), "Gravity Waves on Water of Variable Depth", Journal of Fluid Mechanics, Vol. 24, Part 4, pp. 641-659.

7. Churchill, R.V. (1958), Operational Mathematics, McGraw-Hill Book Company, Inc., New York.

LIST OF REFERENCES (Cont'd)

8. Courant, R., and Friedrichs, K.O. (1967), Supersonic Flow and Shock Waves, Interscience Publishers, Inc., New York.

9. French, J. A. (1969), "Wave Uplift Pressures on Horizontal Platforms", Report No. KH-R-19, W.M. Keck Laboratory of Hydraulics and Water Resources, California Institute of Technology.

10. Fung, Y.C. (1965), Foundations of Solid Mechanics, Prentice-Hall, Englewood Cliffs, New Jersey.

11. Gardner, C.S., Greene, J.M., Kruskal, M.D., and Miura, R.M. (1967), "Method for Solving the Korteweg-deVries Equation", Physical Review Letters, Vol. 19, No. 19, pp. 1095-1097.

12. Hendrickson, J.A. (1962), "Asymptotic Solution to Surface Profile of Tsunamis Created by Rectangular Upthrust of Sea Bed at Large Distance from the Source", from Appendix 2 of The Nature of Tsunamis, Their Generation and Dispersion in Water of Finite Depth, Technical Report No. SN 57-2, National Engineering Science Co.

13. Honda, H., and Nakamura, K. (1951), "The Waves Caused by One-Dimensional Deformation of the Bottom of Shallow Sea of Uniform Depth", Science Report, Tohoku University, Sendai, Japan, Vol. 3, No. 3, pp. 133-137.

LIST OF REFERENCES (Cont'd)

14. Hwang, L.S., Butler, H. L., and Divoky, D., (1971), "Rat Islands Tsunami Model: Generation and Open-Sea Characteristics", Tetra Tech Report TC-239, Tetra Tech, Inc., Pasadena, California.

15. Hwang, L.S., and Divoky, D. (1970), "Tsunami Generation", Journal of Geophysical Research, Vol. 75, No. 33, pp. 6802-6817.

16. Ichiye, T. (1950), "On the Theory of Tsunami", Oceanographical Magazine, Vol. 2, No. 3, pp. 83-100.

17. Ichiye, T. (1958), "A Theory of the Generation of Tsunami by an Impulse at the Sea Bottom", Journal of the Oceanographical Society of Japan, Vol. 14, No. 3, pp. 41-44.

18. Japanese Organization for Tsunami Investigation (1962), "The Annotated Bibliography of Tsunamis (1889-1962)", Earthquake Research Institute, Tokyo University, Tokyo.

19. Jeffreys, H., and Jeffreys, B.S. (1946), Methods of Mathematical Physics, First Edition, Cambridge University Press, London.

20. Kajiura, K. (1963), "The Leading Wave of a Tsunami", Bulletin, Earthquake Research Institute, Tokyo University, Vol. 41, pp. 535-571.

21. Keller, J.B., (1963), "Tsunamis – Water Waves Produced by Earthquakes", International Union of Geodesy and Geophysics, Monograph No. 24, pp. 154-166.

LIST OF REFERENCES (Cont'd)

22. Keulegan, G.H. (1948), "Gradual Damping of Solitary Waves", Research Paper RP 1895, Journal of Research of National Bureau of Standards, Vol. 40, No. 6, pp. 487-498.

23. Korteweg, D.J., and deVries, G. (1895), "On the Change of Form of Long Waves Advancing in a Rectangular Canal, and on a New Type of Long Stationary Waves", London, Edinburgh, and Dublin Philosophical Magazine, Series 5, Vol. 39, pp. 422-443.

24. Kruskal, M.D., Miura, R.M., Gardner, C.S., and Zabusky, N.J. (1970), "Korteweg-deVries Equation and Generalizations. V. Uniqueness and Nonexistence of Polynominal Conservation Laws", Journal of Mathematical Physics, Vol. 11, No. 3, pp. 952-960.

25. Lamb, H. (1945), Hydrodynamics, Sixth Edition, Dover Publications, New York.

26. Lax, P.D. (1968), "Integrals of Nonlinear Equations of Evolution and Solitary Waves", Communications on Pure and Applied Mathematics, Vol. 21, pp. 457-290.

27. Lighthill, M.J., and Whitham, G.B. (1955), "On Kinematic Waves I. Flood Movement in Long Rivers", Proceedings, Royal Society of London, Series A, Vol. 229, pp. 281-316.

LIST OF REFERENCES (Cont'd)

28. Lin, J.D., and Howard, L.N. (1960), "Nonlinear Standing Waves in a Rectangular Tank Due to Forced Oscillation", Technical Report No. 44, Hydrodynamics Laboratory, M.I.T.

29. Madsen, O.S., and Mei, C.C. (1969), "Dispersive Long Waves of Finite Amplitude Over and Uneven Bottom", Report No. 117, Hydrodynamics Laboratory, M.I.T.

30. McCowan, J. (1891), "On the Solitary Wave", London, Edinburgh, and Dublin Philosophical Magazine, Series 5, Vol. 32, pp. 45-53.

31. Miura, R.M. (1968), "Korteweg-deVries Equation and Generalizations. I. A Remarkable Explicit Nonlinear Transformation", Journal of Mathematical Physics, Vol. 9, No. 8, pp. 1202-1204.

32. Miura, R.M., Gardner, C.S., and Kruskal, M.D. (1968), "Korteweg-deVries Equation and Generalization. II. Existence of Conservation Laws and Constants of Motion", Journal of Mathematical Physics, Vol. 9, No. 8, pp. 1204-1209.

33. Momoi, T. (1964), "Tsunami in the Vicinity of a Wave Origin", Bulletin, Earthquake Research Institute, Tokyo University, Vol. 42, pp. 133-146.

34. Nakamura, K. (1953), "On the Waves Caused by the Deformation of the Bottom of the Sea, I", Science Report, Tohoku University, Sendai, Japan, 5th Series, Vol. 5, pp. 167-176.

LIST OF REFERENCES (Cont'd)

35. Peregrine, D.H. (1966), "Calculations of the Development of an Undular Bore", Journal of Fluid Mechanics, Vol. 25, Part 2, pp. 321-330.

36. Plafker, G. (1969), "Tectonics of the March 27, 1964 Alaska Earthquake", Geological Survey Professional Paper 543-I.

37. Raichlen, F. (1965), "Wave-Induced Oscillations of Small Moored Vessels", Report KH-R-10, W.M. Keck Laboratory of Hydraulics and Water Resources, California Institute of Technology.

38. Raichlen, F. (1970), "Tsunamis: Some Laboratory and Field Observations", Proceedings of the Twelfth Coastal Engineering Conference, Washington, D.C., pp. 2103-2122.

39. Rayleigh, Lord (1876), "On Waves", London, Edinburgh, and Dublin Philosophical Magazine, Vol. 1, No. 4, pp. 257-279.

40. Sano, K. and Hasegawa, K. (1915), "On the Wave Produced by a Sudden Depression of a Small Portion of the Sea Bottom", Bull. Cent. Met. Obs. Japan, Vol. 2, No. 3, pp. 1-30.

41. Sneddon, I. N. (1951), Fourier Transforms, McGraw-Hill Book Company, Inc., New York.

42. Sokolnikoff, I.S. (1946), Mathematical Theory of Elasticity, McGraw-Hill Book Company, Inc., New York.

43. Stoker, J.J. (1957), Water Waves, Interscience Publishers, Inc., New York.

LIST OF REFERENCES (Cont'd)

44. Stokes, G.G. (1847), "On the Theory of Oscillatory Waves", Transactions, Cambridge Philosophical Society, Vol. 8, pp. 441-455.

45. Stokes, G.G. (1891), "Note on the Theory of the Solitary Wave", London, Edinburgh, and Dublin Philosophical Magazine, Series 5, Vol. 31, pp. 314-316.

46. Su, C.H., and Gardner, C.S. (1969), "Korteweg-deVries Equation and Generalizations. III. Derivation of the Korteweg-deVries Equation and Burgers Equation", Journal of Mathematical Physics, Vol. 10, No. 3, pp. 536-539.

47. Syono, S. (1936), "On the Wave Caused by a Sudden Deformation of a Finite Portion of the Bottom of a Sea at Uniform Depth", Geophysical Magazine of Japan, Vol. 10, pp. 21-42.

48. Takahasi, R. (1942), "On Seismic Sea Waves Caused by Deformations of the Sea Bottom", Bulletin, Earthquake Research Institute, Tokyo University, Vol. 20, No. 4, pp. 375-400. (in Japanese)

49. Takahasi, R. (1945), "On Seismic Sea Waves Caused by Deformations of the Sea Bottom, 2nd Report", Bulletin, Earthquake Research Institute, Tokyo University, Vol. 23, pp. 23-35. (in Japanese).

50. Takahasi, R. (1947), "On Seismic Sea Waves Caused by Deformations of the Sea Bottom, 3rd Report", Bulletin, Earthquake Research Institute, Tokyo University, Vol. 25, pp.5-8.

LIST OF REFERENCES (Cont'd)

51. Takahasi, R. (1963), "On Some Model Experiments on Tsunami Generation", International Union of Geodesy and Geophysics, Monograph No. 24, pp. 235-248.

52. Takahasi, R., and Hatori, T. (1962), "A Model Experiment on the Tsunami Generation from a Bottom Deformation Area of Elliptic Shape", Bulletin, Earthquake Research Institute, Tokyo University, Vol. 40, pp. 873-883.

53. Tranter, C.J. (1966), Integral Transforms in Mathematical Physics, Methuen and Co. Ltd., London.

54. Tuck, E.O., and Hwang, L.S. (1972), "Long Wave Generation on a Sloping Beach", Journal of Fluid Mechanics, Vol. 51, Part 3, pp. 449-461.

55. Ursell, F. (1953), "The Long-Wave Paradox in the Theory of Gravity Waves", Proceedings, Cambridge Philosophical Society, Vol. 49, pp. 685-694.

56. Van Dorn, W.G. (1964), "Source Mechanism of the Tsunami of March 28, 1964 in Alaska", Proceedings of Ninth Conference on Coastal Engineering, Lisbon, Portugal, pp. 166-190.

57. Van Dorn, W.G. (1966), "Boundary Dissipation of Oscillatory Waves", Journal of Fluid Mechanics, Vol. 24, Part 4, pp. 769-779.

58. Webb, L.M. (1962), "Theory of Waves Generated by Surface and Sea-bed Disturbances", from Appendix I of The Nature

LIST OF REFERENCES (Cont'd)

of Tsunamis, Their Generation and Dispersion in Water of Finite Depth, Technical Report No. SN 57-2, National Engineering Science Co.

59. Wilson, B.W., and Tørum, A. (1968), "The Tsunami of the Alaskan Earthquake, 1964: Engineering Evaluation", Technical Memorandum No. 25, U.S. Army, Corps of Engineers, Coastal Engineering Research Center.

60. Wyss, M., and Brune, J.N. (1967), "The Alaska Earthquake of 28 March 1964 - A Complex Multiple Rupture", Bulletin, Seismological Society of America, Vol. 57, No. 5, pp. 1017-1023.

61. Zabusky, N.J., and Galvin, C.J. (1971), "Shallow-water Waves, the Korteweg-deVries Equation and Solitons", Journal of Fluid Mechanics, Vol. 47, Part 4, pp. 811-824.

62. Zabusky, N.J., and Kruskal, M.D. (1965), "Interactions of 'Solitons' in a Collisionless Plasma and the Recurrence of Initial States", Physical Review Letters, Vol. 15, No. 6, pp. 240-243.

LIST OF SYMBOLS

Ai( )	The Airy function.
a_1, a_2	Arbitrary limits of integration.
B	Width of wave tank.
b	Half-width of the bed deformation.
C_1, C_2, C_3	Denotes characteristics in the solution of the dam-break problem.
D	Denotes the fluid domain.
e	The base of the Naperian logarithm.
g	Acceleration of gravity.
H( )	The Heavyside step function.
h	The uniform water depth.
I	Denotes the integrand of an integral.
i	$\sqrt{-1}$
J_o, J_1	Bessel functions of the first kind and of order zero and one, respectively.
j	The number of fundamental dimensions.
k	Parameter of the Fourier transform.
ℓ	A characteristic length scale of a wave during propagation.
$\underline{m}$	The total number of time steps used in the finite-difference solution of the KdV equation.
n	An integer.
$\underline{n}$	The total number of spatial nodes used in the finite-difference solution of the KdV equation.
O( )	Indicates order of magnitude.
P	Pressure in the fluid domain.

LIST OF SYMBOLS (Cont'd)

p	Arbitrary parameter of an integral transform of a function.
Q_1, Q_2, . . .	Independent variables.
$\vec{q}$	The velocity vector.
r	Coordinate axis in the radial direction of the three-dimensional model.
r_o	Radius of bed deformation in three-dimensional model.
S_b	The solid boundary of the fluid domain.
S_f	The free surface of the fluid domain.
s	Parameter of the Laplace transform.
T	The total time of a bed deformation.
t	Time.
t_c	A characteristic time of a bed deformation.
t_f	The fall time of the lead wave.
t_n	The node to node time of the lead wave.
t_o	A specified time after wave generation.
t_r	The rise time of the lead wave.
t'	Time measured from midpoint of half-sine bed movement.
Δt	Nondimensional length of time steps used in finite-difference solution of the KdV equation.
$\underline{U}$	The Ursell Number.
$\underline{U}_1$	The Ursell Number in the front region of the lead wave.
$\underline{U}_2$	The Ursell Number in the rear region of the lead wave.
u	Horizontal component of the water particle velocity.

LIST OF SYMBOLS (Cont'd)

u_2	Horizontal water particle velocities under the bore generated in the dam-break problem.
V	The bore velocity in the dam-break problem.
v	Vertical component of velocity of a water particle.
X	Horizontal position of the centroid of a wave profile.
x	Coordinate axis in the horizontal direction of the two-dimensional model.
Δx	Nondimensional spatial steps used in finite-difference solution of KdV equation.
y	Coordinate axis in the vertical direction of the two-dimensional model.
z	Coordinate axis in the vertical direction of the three-dimensional model.
α	The time constant of the exponential bed movement.
β	Nondimensional length of the linear near-field.
Γ	A real number denoting the imaginary axis location of the Bromwich contour.
Δ	Denotes $\Delta x = \Delta t$.
δ	Index notation of spatial nodes used in the finite-difference solution of the KdV equation.
ϵ	A small parameter.
ζ	The bed displacement from its initial position.
ζ_o	The total bed displacement.
ζ_1	Amplitude of the dither superposed on the mean motion of the bed displacement.
ζ_t	Total bed displacement at a nonzero forcing frequency.

LIST OF SYMBOLS (Cont'd)

ζ_{t_o}	Total bed displacement at a forcing frequency of zero.
ζ'	Bed displacement measured from midpoint of half-sine bed movement.
ζ_e	Denotes the exponential bed displacement.
ζ_s	Denotes the half-sine bed displacement.
η	Displacement of the water surface from its initial position.
η_o	Maximum wave amplitude.
η_{o_i}	The maximum amplitude of a solitary wave before propagation.
Θ	Angular coordinate direction in the three-dimensional model.
θ	Angle of expansion fan in the dam-break problem.
$\varkappa$	π/T.
Λ	A characteristic length scale of the deformed water surface during generation.
λ	Nondimensional integration variable, kh.
μ	A positive number denoting the real location of the Bromwich contour.
ν	The kinematic viscosity of the fluid.
ξ	Index notation of the temporal step used in the finite-difference solution of the KdV equation.
π	3.14159 . . . .
ρ	The fluid density.
τ	Period of the dither superposed on the mean motion of the bed displacement.
φ	The velocity potential.

LIST OF SYMBOLS (Cont'd)

χ	A characteristic vertical length scale of the water surface movement during generation.
ψ	The nondimensional time interval after wave generation in which the Ursell Number remains less than unity.
ω^2	gk tanh kh.
Ω	Characteristic length of a stress distribution applied to an elastic solid.
$\lvert\ \rvert$	Denotes absolute value.
$\lVert\ \rVert$	Denotes maximum value.
∇	Gradient operator.
∇^2	Laplacian operator.
$\nabla \cdot (\ )$	Divergence of a vector.
$(\ )_x, (\ )_t, \ldots$	Denotes differentiation with respect to the subscripted variable.
$*$	Sometimes used to denote dimensional quantity.
$-$	(Overscore) denotes Fourier transform.
$\sim$	(Overscore) denotes Laplace transform.
$\wedge$	(Overscore) denotes Hankel transform.
$\int_{Br.}$	Denotes Laplace inversion integral around Bromwich contour.

Additional Symbols Referred to in Chapter 2: Literature Survey

K, R, L, M	Arbitrary constants appearing in the assumed velocity of the bed deformation (Syono, 1936).
$\forall$	The volume of the bed deformation (Takahasi, 1942).

LIST OF SYMBOLS (Cont'd)

N	Arbitrary constant in temporal variation of the velocity of the bed deformation (Ichiye, 1960).
A, x_1, t_1	Arbitrary constants appearing in the assumed velocity of the bed deformation (Honda and Nakamura, 1951).
A, R, t_1	Arbitrary constants appearing in the assumed velocity of the bed deformation (Nakamura, 1953).
P_b	A parameter for indicating the decay rate of the leading wave of a tsunami (Kajiura, 1963).
a, c	Arbitrary constants appearing in the assumed velocity of the bed deformation (Carrier, 1965).
b_o	Characteristic size of the bed deformation (Tuck and Hwang, 1972).
α_o	The slope of the bed (Tuck and Hwang, 1972).